DESIGN, MODELING AND CONTROL OF 4-AXIS ELECTRO-OPTICAL DIRECTOR FOR HIGH ENERGY LASER APPLICATION

A THESIS SUBMITTED TO
THE GRADUATE SCHOOL OF NATURAL AND APPLIED SCIENCES
OF
MIDDLE EAST TECHNICAL UNIVERSITY

BY

AHMET MAVUŞ

IN PARTIAL FULFILLMENT OF THE REQUIREMENTS
FOR
THE DEGREE OF MASTER OF SCIENCE
IN
MECHANICAL ENGINEERING

DECEMBER 2019

Approval of the thesis:

DESIGN, MODELING AND CONTROL OF 4-AXIS ELECTRO-OPTICAL DIRECTOR FOR HIGH ENERGY LASER APPLICATION

submitted by **AHMET MAVUŞ** in partial fulfillment of the requirements for the degree of **Master of Science in Mechanical Engineering Department, Middle East Technical University** by,

Prof. Dr. Halil Kalıpçılar
Dean, Graduate School of **Natural and Applied Sciences** _____

Prof. Dr. M. A. Sahir Arıkan
Head of Department, **Mechanical Engineering** _____

Prof. Dr. Tuna Balkan
Supervisor, **Mechanical Engineering, METU** _____

Examining Committee Members:

Assist. Prof. Dr. A. Buğra Koku
Mechanical Engineering, METU _____

Prof. Dr. Tuna Balkan
Mechanical Engineering, METU _____

Prof. Dr. Y. Samim Ünlüsoy
Mechanical Engineering, METU _____

Assist. Prof. Dr. Ali Emre Turgut
Mechanical Engineering, METU _____

Assist. Prof. Dr. Melih Çakmakcı
Mechanical Engineering, Bilkent University _____

Date: 05.12.2019

I hereby declare that all information in this document has been obtained and presented in accordance with academic rules and ethical conduct. I also declare that, as required by these rules and conduct, I have fully cited and referenced all material and results that are not original to this work.

Name, Surname: Ahmet Mavuş

Signature :

ABSTRACT

DESIGN, MODELING AND CONTROL OF 4-AXIS ELECTRO-OPTICAL DIRECTOR FOR HIGH ENERGY LASER APPLICATION

Mavuş, Ahmet
M.S., Department of Mechanical Engineering
Supervisor: Prof. Dr. Tuna Balkan

December 2019, 153 pages

With the development of laser technology, high power applications increasingly play significant roles in industry, military, and communication fields. Thus, handling large payloads, precisely steering laser beams comes into prominence. Achieving appropriate stiffness in mechanical design, optimal actuator and sensor selection, successful control strategy, and elaborative testing are factors involved in determining the system performance. In this study, firstly, a thorough literature review is conducted. Next, steps on sizing and selection of actuators, choosing sensors, and structural design are taken. Then, supported by the measurements, a detailed system model is created including friction, unbalance, cogging, and cable torques, structural dynamics altering with elevation angle along with electronics delays and noise. Finally, control architecture is proposed, and overall performance is evaluated against potential targets.

Keywords: High Power Laser Beam Control, Electro Optic Director Design, Simulink Modeling, Real-Time Control via xPc Target, Cascade Control Strategy, Target Tracker

ÖZ

YÜKSEK GÜÇLÜ LAZER UYGULAMASI İÇİN 4 EKSENLİ ELEKTRO-OPTİK YÖNLENDİRME BİRİMİ TASARIMI, MODELLENMESİ VE KONTROLÜ

Mavuş, Ahmet
Yüksek Lisans, Makina Mühendisliği Bölümü
Tez Yöneticisi: Prof. Dr. Tuna Balkan

Aralık 2019 , 153 sayfa

Lazer teknolojilerindeki gelişmelerle, yüksek güçlü uygulamalar endüstri, askeri ve haberleşme alanlarında kayda değer roller edinmiştir. Bu nedenle, yüksek faydalı yükler altında lazer hüzmelerinin hassas yönlendirilmesi önem arz etmektedir. Yüksek rijitlikli mekanik, uygun eyleyici ve sensör, başarılı kontrolcü ve özenli testler performans üzerinde belirleyicidir. Bu çalışmada öncelikle kapsamlı bir litaratür taraması gerçekleştirilmiştir. Akabinde, eyleyicilerin hesabı, sensörlerle birlikte seçimi ve yapısal tasarım adımları atılmıştır. Bu adımları, sürtünme, dengesizlik, vuruntu ve kablo momenti, yükseliş açısı ile değişen yapısal dinamik ve elektronik bozucu faktörlerini içeren, ölçümlerle desteklenmiş detaylı modelleme izlemiştir. Son olarak, kontrol mimarisi tasarlanmış ve muhtemel hedefler karşısında performans değerlendirilmiştir.

Anahtar Kelimeler: Lazer Hüzme Kontrolü, Elektro-Optik Yönlendirme Birimi, Simulink Benzetim, xPc Target Gerçek Zamanlı Kontrol, Kaskat Döngü, Hedef Takip

To My Family

ACKNOWLEDGMENTS

First of all, I would like to thank my supervisor Prof. Dr. Tuna Balkan for his priceless guidance, suggestions and encouragement throughout this study. The door to Prof. Balkan office was always open whenever I ran into a trouble spot or had a question about my research or writing. His knowledge and feedbacks always steered me in the right direction to complete this work.

I sincerely would like to express my gratitude to my director Mr. Eray Yasan and my managers Mr. Atakan Dura and Mr. Enis Naci Özkan for their invaluable support and advices. Above all, there are two people whose efforts deserve particular recongition. I am thankful to my co-workers Mr. Fatih Işık and Mr. Suphi Taylan Tatar for their companionship and mentorship throughout thw whole process under which all planning and development came to fruition. I would also like to express my appreciation to all other contributors; in particular Mr. Ömer Çakmak, Mr. Bilal Canatar, and Mr. Mustafa Aydoğan for being dedicated teammates.

I am also grateful to my thesis buddy İlim Karaçal for sharing and facing together up this belated thesis writing experience.

Lastly, I would like to thank my family: my parents Nurefşan and Türker Mavuş, for trusting and supporting me for every choice I made throughout my life, my sister Zeynep Mavuş for giving me valuable support and being an inspiration source with her strength and tenacity.

TABLE OF CONTENTS

ABSTRACT v

ÖZ vi

ACKNOWLEDGMENTS viii

TABLE OF CONTENTS ix

LIST OF TABLES xii

LIST OF FIGURES xiii

LIST OF ABBREVIATIONS AND SYMBOLS xxi

CHAPTERS

1 INTRODUCTION 1

1.1 Motivation and Problem Definition 1

1.2 Literature Survey 4

1.2.1 Lasers 4

1.2.2 Optical Train 9

1.2.3 Actuation Systems 24

1.2.4 Control Strategies 46

1.3 Objective of the Thesis 48

1.4 The Outline of the Thesis 48

2 DESIGN 51

2.1 Servomechanism Component Selection 52
2.1.1 Motor Selection 52
2.1.2 FSM Selection 59
2.1.3 Gyro Selection 60
2.1.4 Encoder Selection 61
2.2 Servomechanism Design 62
2.3 Servoelectronics Design 70
2.3.1 Servo Drive Selection 70
2.3.2 Power Supply Selection 72
3 SYSTEM IDENTIFICATION AND MODELING 73
3.1 SYSTEM IDENTIFICATION 73
3.1.1 Gimbal 73
3.1.1.1 Friction, Unbalance, Springness and Cogging Tests . . . 73
3.1.1.2 Dynamic Response Tests 80
3.1.2 FSM 93
3.1.2.1 Impedance Tests 93
3.1.2.2 Dynamic Response Tests 94
3.2 MODELING 97
3.2.1 Gimbal 97
3.2.1.1 Friction, Unbalance, Springness and Cogging Modeling 97
3.2.1.2 Dynamic Response Modeling 102
3.2.2 FSM 106
3.2.2.1 Dynamic Response Modeling 108

3.2.3 Atmospheric Disturbance . . . 110
3.2.4 Cameras and Target Tracking Algorithms . . . 111
3.2.5 Targets . . . 113
3.2.5.1 Pressurized Tank on Rail . . . 114
3.2.5.2 Drone . . . 115
4 CONTROL . . . 117
4.1 Velocity Controller Design . . . 117
4.1.1 Elevation Axis . . . 117
4.1.2 Azimuth Axis . . . 120
4.2 Position Controller Design . . . 123
4.2.1 Elevation Axis . . . 124
4.2.2 Azimuth Axis . . . 126
4.3 Coarse Tracking Controller Design . . . 127
4.3.1 Elevation Axis . . . 129
4.3.2 Azimuth Axis . . . 132
4.4 Atmospheric Disturbance Compensation . . . 136
5 CONCLUSIONS . . . 137
REFERENCES . . . 139
APPENDICES
A REMAINING SIMULATION MODEL DETAILS . . . 149
B AZIMUTH VELOCITY MEASUREMENT EULER TRANSFORMATION 153

LIST OF TABLES

TABLES

Table 2.1 Natural Frequencies (Hz) 68

Table 3.1 Hysteresis Characteristics Identification Tests Plan 75

Table 3.2 Kick-off Test Plan on Readily Available Motion Controller 81

Table 3.3 Azimuth Axis Dynamic Response Identification Tests Plan 82

Table 3.4 Elevation Axis Dynamic Response Identification Tests Plan 83

Table 3.5 Estimated Steady State Friction Parameters 99

Table 4.1 Velocity Controller Performance with Respect to Elevation Angles . 120

Table 4.2 Velocity Controller Performance with Respect to Elevation Angles . 123

Table 4.3 Position Controller Performance with Respect to Elevation Angles . 126

Table 4.4 Coarse Tracker Controller Performance with Respect to Elevation Angles 129

Table 4.5 Coarse Tracker Controller Performance with Respect to Elevation Angles 133

LIST OF FIGURES

FIGURES

Figure 1.1 HEL Weapon Components (Adapted from [3]) 2

Figure 1.2 Laser Principle Parts and Working Process Schematic Diagram [7] 4

Figure 1.3 Laser Characteristic Properties [8] 5

Figure 1.4 Laser Applications [10, 11, 12, 13] 6

Figure 1.5 HEL History of the U.S. Navy [15] 7

Figure 1.6 Today's Laser Applications [17, 18] 8

Figure 1.7 Demonstrative Schematic of Beam Guidance Optical Train [13] . 9

Figure 1.8 Closed Loop Operation of Adaptive Optics System [21] 10

Figure 1.9 Deformable Mirror Architecture [22] 11

Figure 1.10 WaveFront Sensors Operation Principles [25][26] 12

Figure 1.11 Closed Loop Block Diagram of Adaptive Optics System [27] . . 13

Figure 1.12 Fast-Steering Mirror (FSM) [31][32] 14

Figure 1.13 Piezoelectric Fast-Steering Mirror (FSM) Operation Details [35][36] 15

Figure 1.14 FSM Cascaded Control Loop [41] 17

Figure 1.15 Resistive SG [42] 17

Figure 1.16 Resistive Strain Gauge Integration [44][45] 18

Figure 1.17 Wind Velocity and C_n^2 Change with Altitude Gain [51] 20

Figure 1.18 Power Spectral Density of Atmospheric Turbulence Components [51] 20

Figure 1.19 Atmospheric Propagation Effects [55][56][57][58] 21

Figure 1.20 Beam Combining Technique Principles [19] 22

Figure 1.21 Reflector Telescopes Configurations [63] 23

Figure 1.22 Several Stabilization and Pointing Systems Configurations [65] . 24

Figure 1.23 Stabilized Gimbal Examples [64] 25

Figure 1.24 Nested Gimbal Formation [64] 25

Figure 1.25 Electric Motor Classification [66] 26

Figure 1.26 Electric Motor Components [66] 27

Figure 1.27 Motor Operating Principles [66] 27

Figure 1.28 Electrical Drive Block Diagram [69] 28

Figure 1.29 PWM Output Waveform [72] 29

Figure 1.30 PWM Drive Circuitry [72] 29

Figure 1.31 Motor Commutation Algorithms [76] 30

Figure 1.32 A Data Link Layer Frame Example [74] 32

Figure 1.33 Motor Sizing & Selection Process [80] 33

Figure 1.34 Disturbance Sources [81] 35

Figure 1.35 Application Operation Points on Motor Performance Graph [80] 36

Figure 1.36 Gyroscope Classification [83] 38

Figure 1.37 Logarithmic Allan Variance Plot [84] 38

Figure 1.38 Bias Stability Application Requirements and Gyro Specifications[86] 39

Figure 1.39 Optical Gyro Classification [86] 40

Figure 1.40 Working Principles of Optical and Magnetic Encoder [88] 41

Figure 1.41 Schematics of Several Angular Position Measurement Devices [87] 43

Figure 1.42 Isolation, Pointing, and Suppression (IPS) System Details [92] . 45

Figure 2.1 Design Team Structure [68] 51

Figure 2.2 Design Process Flow Chart [68] 52

Figure 2.3 Azimuth Axis Performance and Functions Required Displacement Curve 53

Figure 2.4 Springness Effect Characterization Works 54

Figure 2.5 Azimuth Motor Selection Simulink Model 55

Figure 2.6 Azimuth Motor Torque Profile 55

Figure 2.7 Elevation Motor Selection Simulink Model 56

Figure 2.8 Elevation Motor Torque Profile 56

Figure 2.9 Azimuth Motor Duty Cycle for Acceleration Requirements Profile 57

Figure 2.10 Azimuth Motor Properties and Performance 57

Figure 2.11 Elevation Motor Duty Cycle for Acceleration Requirements Profile 58

Figure 2.12 Elevation Motor Properties and Performance 58

Figure 2.13 Atmospheric Disturbance $PSD(f)$ Graph 60

Figure 2.14 Preliminary Design FEA Model Details 63

Figure 2.15 Preliminary Design FEA Results 64

Figure 2.16 Preliminary Design FEA Results cont. 65

Figure 2.17 Preliminary Azimuth Design Flexible Dynamic Analysis Results 66

Figure 2.18 Preliminary Elevation Design Flexible Dynamic Analysis Results 67

Figure 2.19 Final Model Main Analysis Alignments 68

Figure 2.20 First Third Mode Shapes of Final Design for Alignments 45°Apart 69

Figure 2.21 Servo Drive Properties and Performance 71

Figure 3.1 Friction, Unbalance, Springness and Cogging Torque Measurement Procedure Technical Details [81] 74

Figure 3.2 Test Technique Verification on Azimuth Torque Table 76

Figure 3.3 Azimuth Friction Torque vs. Angular Velocity 77

Figure 3.4 Azimuth Hysteresis Curve for Different Angular Velocities . . . 78

Figure 3.5 Elevation Hysteresis Curve for Different Angular Velocities . . . 78

Figure 3.6 Elevation Friction Torque vs. Angular Velocity 79

Figure 3.7 Dynamic Linear System Input-Output Relationship 80

Figure 3.8 Dynamic Response Test Setup 81

Figure 3.9 Results of Benchmark and Verification Tests via the Available Drive 84

Figure 3.10 Results of Benchmark and Latency Tests via the Selected Drive . 85

Figure 3.11 The Result of Latency Test on the Selected Drive via Current Probe 86

Figure 3.12 Azimuth Axis Torque to Velocity Transfer Functions (Elevation @0°) 87

Figure 3.13 Azimuth Axis Torque to Velocity Transfer Functions (For Elevation Angles 10°Apart) 88

Figure 3.14 Azimuth Axis Torque to Elevation Axis Velocity Cross Axis Transfer Functions 89

Figure 3.15 Azimuth Axis Torque to Position Transfer Functions 89

Figure 3.16 Comparison of Synthesized and Test Product Elevation Axis Torque to Velocity Transfer Functions 91

Figure 3.17 Elevation Axis Torque to Velocity Transfer Functions (For Elevation Angles Approximately 10°Apart) 92

Figure 3.18 Elevation Axis Torque to Position Transfer Functions 92

Figure 3.19 Results of the Impedance Measurements for both Axes 94

Figure 3.20 R_x and R_y Axes Closed Loop Transfer Functions Performed with 500μrad PTP Sine-sweep Input at FAT 95

Figure 3.21 R_x and R_y Axes Closed Loop Transfer Functions Performed with 500μrad PTP Sine-sweep Input on Assembly 96

Figure 3.22 R_x and R_y Axes Closed Loop Transfer Functions Performed with 1000μrad PTP Sine-sweep Input on Assembly 96

Figure 3.23 Elevation and Azimuth Axes Presiliding Regime Behaviors . . . 97

Figure 3.24 Azimuth Axis Friction Torque vs. Velocity Mappings 99

Figure 3.25 Elevation Axis Friction Torque vs. Velocity Mappings 99

Figure 3.26 Bristle Interpretation of Friction Micromechanism with LuGre Model 100

Figure 3.27 The LuGre Friction Model Simulink Implementation 101

Figure 3.28 Cogging, Unbalance, and Springness Models Simulink Implementation 101

Figure 3.29 Comparison of Fitted and Test Product Azimuth Axis Torque to Velocity Transfer Functions 102

Figure 3.30 Comparison of Fitted and Test Product Elevation Axis Torque to Velocity Transfer Functions 103

Figure 3.31 Simulink Transfer Function Model with Varying Coefficients . . 103

Figure 3.32 $Pcoff_n$ vs. Elevation Angle Fitted Curves for Azimuth Axis . . 104

Figure 3.33 Final Version of 2-Axis Simulink Gimbal Model 105

Figure 3.34 Azimuth Axis Hysteresis Curve Comparison at Constant 15 °/s Rate 105

Figure 3.35 Elevation Axis Hysteresis Curve Comparison at Constant 15 °/s Rate 106

Figure 3.36 Additional Effects on Piezoelectric Effector Performance [98] . . 106

Figure 3.37 Drawbacks of Several Preloading Mechanisms [98] 107

Figure 3.38 Piezo Ceramic Stress-Strain Diagram [98] 107

Figure 3.39 Final Version of Elevation Axis FSM Simulink Model 109

Figure 3.40 Comparison of FSM Elevation Axis Model Output and Test Result 110

Figure 3.41 Comparsion of Phase Screens Analysis and Tyler Approximation on Atmospheric Turbulence Time Data Generation 111

Figure 3.42 Course Video Tracker Simulink Model Segment 112

Figure 3.43 Timing Routine for Fine Tracking System 112

Figure 3.44 Fine Tracker Algorithm Output against Disturbance Created by FSM 113

Figure 3.45 Pressurized Tank as Moving Target on Rail System 114

Figure 3.46 On Rail Target Velocity Profile 115

Figure 3.47 Drone Path During Data Acquisition 116

Figure 3.48 Drone Velocity Profile 116

Figure 4.1 Detail View of On Rail Target Velocity Profile 118
Figure 4.2 MATLAB Control System Designer app Bode Plot Editor Interface 119
Figure 4.3 Elevation Axis Torque to Velocity Transfer Functions 119
Figure 4.4 Detail View of Drone Velocity Profile 121
Figure 4.5 Azimuth Axis Torque to Velocity Transfer Functions 121
Figure 4.6 MATLAB Control System Designer app Bode Plot Editor Interface 122
Figure 4.7 Cascaded Position Control Loop Topology 123
Figure 4.8 Position Loop Forward Path Nonlinear Terms 124
Figure 4.9 Elevation Axis Position Loop Step Response 124
Figure 4.10 Elevation Axis Positioning Accuracy 125
Figure 4.11 Elevation Axis Position Profile Tracking Accuracy 125
Figure 4.12 Azimuth Axis Position Loop Step Response 126
Figure 4.13 Azimuth Axis Position Profile Tracking Accuracy 127
Figure 4.14 Target Tracking Architecture 127
Figure 4.15 MATLAB Control System Designer app Bode Plot Editor Interface 129
Figure 4.16 Elevation Axis Coarse Tracking System Error Against on-Rail Target 130
Figure 4.17 Elevation Axis Coarse Tracking System Error Against Drone Threat 130
Figure 4.18 Elevation Axis Fine Tracking System Error Against on-Rail Target 131
Figure 4.19 Elevation Axis Fine Tracking System Error Against Drone Threat 132
Figure 4.20 MATLAB Control System Designer app Bode Plot Editor Interface 132

Figure 4.21 Azimuth Axis Coarse Tracking System Error Against on-Rail Target 133

Figure 4.22 Azimuth Axis Coarse Tracking System Error Against Drone Threat 134

Figure 4.23 Azimuth Axis Fine Tracking System Error Against Drone Threat 134

Figure 4.24 Azimuth Axis Fine Tracking System Error Against on-Rail Target 135

Figure 4.25 Compensation of Atmospheric Disturbance Components 136

Figure A.1 Simulink EOD Simulation Model General View 149

Figure A.2 Model Inlet and Outlet Means 150

Figure A.3 Coarse Tracking System (Except From End Effector) 150

Figure A.4 Fine Tracking System 151

Figure A.5 Tracker Random Jitter Model 151

Figure A.6 Stabilization System Model 151

Figure A.7 Positioning System Model 152

Figure A.8 Elevation Angle Dependent Structural Dynamics 152

Figure B.1 Real-time IMU Axis Transformation Model Segment 153

LIST OF ABBREVIATIONS AND SYMBOLS

ABBREVIATIONS

EOD	Electro-Optical Director
IR	Infrared
HEL	High Energy Laser
APFSDS	Armor-Piercing, Fin-Stabilized, Discarding Sabot
HEAT	High-Explosive, Antitank
FSM	Fast Steering Mirror
FOV	Field of View
FLIR	Forward-Looking Infrared
DTV	Daytime Video
Nd:YAG	Neodymium-doped Yttrium Aluminum Garnet
DF	Deuterium Fluoride
COIL	Chemical Oxygen Iodine Laser
NACL	Navy-ARPA Chemical Laser
MIRACL	Mid-Infrared Advanced Chemical Laser
ABL	Airborne Laser
LaWS	Laser Weapon System
MLD	Maritime Laser Demonstrator
AO	Adaptive Optics
DM	Deformable Mirror
MEMS	Micro Electro-Mechanical System
CILAS	Compagnie Industrielle des Lasers
WFS	WaveFront Sensing

S-H	The Shack-Hartmann
CCD	Charge-Coupled Detector
SiC	Silicon Carbide
PSD	Position-Sensitive Detector
ID	Imaging Detector
SG	Strain Gauge
SBC	Spectral Beam Combining
ISP	Inertially Stabilized Platform
LoS	Line of Sight
AC	Alternating Current
DC	Direct Current
MOSFET	Metal-Oxide-Semiconductor Field-Effect Transistor
IGBT	Insulated Gate Bipolar Transistor Current
PWM	Pulse-Width Modulation
EMI	Electromagnetic Interference
ADC	Analog-to-Digital Converter
IEC	International Electrotechnical Commission
PLC	Programmable Logic Controller
STO	Safety Torque Off
OSI	Open Systems Interconnection
DTE	Data Terminal Equipment
DCE	Data Communication Equipment
NRZ	Non-Return-to-Zero
CAN	Controller Area Network
IT	Information Technology
EtherCAT	Ethernet for Control Automation Technology
ETG	EtherCAT Tehcnology Group

CoG	Center of Gravity
CAD	Computer Aided Design
RMS	Root Mean Square
ARW	Angle Random Walk
AVAR	The Allan Variance
IEEE	Institute of Electrical and Electronics Engineers
FOG	Fiber Optic Gyroscope
RLG	Ring Laser Gyro
RVDT	Rotary Variable Differential Transformer
IMU	Inertial Measurement Unit
INS	Inertial Navigation System
IEPE	Integrated Electronics Piezo-Electric
TEDS	Transducer Electronic Data Sheet
EMA	Experimental Modal Analysis
FRF	Frequency Response Function
FEA	Finite Element Analysis
SILOS	Structurally induced line of sight
IPS	Isolation, Pointing, and Suppression
PID	Proportional+Derivative+Integral
MPC	Model Predictive Control
LQG	Linear Quadratic Gaussian
TF	Transfer Function
OLTF	Open Loop Transfer Function
QFT	Quantitative Feedback Theory
NC	Nichols chart
ZOH	Zero Order Hold
BD	Backward Differences

COTS	Commercial off-the-Shelf
HV	High Voltage
CLTF	Closed Loop Transfer Function
LCM	Least Common Multiple
PTP	Peak to Peak
FAT	Factory Acceptance
LuGre	Lund Institute of Technology and INPG Grenoble
RAM	Random Access Memory

SYMBOLS

D	Clear Aperture Diameter
r_0	Coherence Length
ζ	Zenith Angle
λ	Light Wavelength
C_n^2	Structure Constant
W	Wind Speed
z	Altitude
f_c	Atmospheric Cut-off Frequency
f_G	Greenwood Frequency
α	Angular Acceleration
ω	Angular Velocity
θ	Angular Displacement
t_{total}	Total Period of Motion
J	Equivalent Mass Moment of Inertia
T_i	Inertial Torque
T_m	Motor Torque

T_d	Disturbance Torque
T_n	Noise Induced Torque
T_{PS}	Stall Peak Torque
T_{PR}	Rated Peak Torque
T_{CS}	Stall Continuous Torque
T_{CR}	Rated Continuous Torque
σ_R	Rated Speed
σ_{max}	Maximum Speed
τ	Averaging Time
$\sigma(\tau)$	Allan deviation
J	Equivalent Mass Moment of Inertia
J_a	Azimuth Axis Mass Moment of Inertia
J_e	Elevation Axis Mass Moment of Inertia
T_f	Friction Torque
T_u	Unbalance Torque
T_s	Springness Torque
T_c	Cogging Torque
$\mathcal{T}_{cogging}$	Cogging Period
$\hat{\nu}$	Effective Wind Speed
r_0	Fried's Parameter
$\boldsymbol{M}$	Mass Matrix
$\boldsymbol{C}$	Damping Matrix
$\boldsymbol{K}$	Stiffness Matrix
$\vec{X}$	Nodal Displacement Vector
$\vec{F}(t)$	Forcing Function
$T_{HeatSink}$	Integral Heat-Sink of the Drive Temperature
$T_{Ambient}$	Ambient Temperature

$P_{Dissipation(W)}$	Dissipated Heat Power
R_θ	Thermal Resistance
K_s	Springness Constant
$PSD(f)$	Power Spectral Density Function
$\|G(f)\|$	Transfer Function Magnitude
$\angle G(j\omega)$	Transfer Function Phase
σ_2	Viscous Friction Coefficient
σ_0	Bristle Stiffness Term
σ_1	Bristle Damping Term
z	Bristle Deformation
$s(\dot{\theta})$	Stribeck Function
θ_s	Stribeck Displacement
δ	Stribeck Shape Factor
T_{Static}	Static Friction Torque Component
$T_{Coulomb}$	Coulomb Friction Torque Component
$T_f(\dot{\theta}, z)$	Rate and Bristle Deformation Dependent LuGre Friction Torque
$T_{f(ss)}(\dot{\theta})$	Rate Dependent Steady-State LuGre Friction Torque
$Pcoff_n$	nth Modal Participation Factor
ω_n	Natural Frequency
ξ	Structural Damping Factor
$e^{-st_{delay}}$	Transport Lag
S	Strain Term
T	Stress Term
D	Induction Term
E	Field Term
s^E	Constant Field Compliance
d	Piezoelectric Strain per Unit Field
ε^T	Constant Stress Permittivity

CHAPTER 1

INTRODUCTION

1.1 Motivation and Problem Definition

Against traditional and asymmetric military threats from air, land, or sea, Electro-Optical Director (EOD) Systems are widely used for Gun Sight, Surveillance, and Target Acquisition Applications. EOD Systems are generally composed of Laser Rangefinder, visible light, and Infrared (IR) camera which are housed in a motorized and stabilized gimbal with capabilities of target detection and tracking, ballistic prediction and gun control, remote operability, and harsh environment usage [1]. Another emerging technology adds EOD totally different role as a sole gun on top of being gun director namely High Energy Laser (HEL) Weapons.

Differently from conventional ammunition, which takes the advantage of high-velocity kinetic energy such as Armour-piercing, fin-stabilized, discarding sabot (APFSDS) or energy released in an explosion such as high-explosive, anti-tank (HEAT) warhead, HEL Weapons direct light energy to damage their target. Engagement to the target at speed of light, no ballistics correction requirement, and low incremental cost per shot compared to conventional projectile weapon systems make HEL Weapons one of the most challenging military applications in future battlefields and become main sources of motivation for their design [2].

HEL EOD design necessitates addressing some challenging problems. The definition of these problems goes back to laser fundamentals. Laser beam quality is degraded by atmospheric aberrations and deformable mirrors correct degradations to a great extent. One of the significant atmospheric propagation effects, turbulence has the largest component in the tip-tilt removable form, and it could be compensated via a

simpler solution, i.e., fast steering mirror (FSM). However, in any case, an agile orthogonal axes couple is required for atmospheric corrections. These piezo actuators could not fulfill both beam correcting and directing functionalities due to their low strokes. Hence, collaboration with a prime mover, namely, an outer gimbal is essential. Inner piezo-axes are not the only payload to be handled by the gimbal, but also, sub-units such as telescope, beam combiner, and sensors are present as demonstrated in Figure 1.1. On telescope clear aperture, and so on its total size, diffraction limit is determinative. Beam combiner enlarges proportionally to its output power due to increment in contained collimators. Thus, as its payloads are increased in number and getting heavier, gimbal design becomes bulkier in order to ensure required stiffness for keeping platform-based jitters as low as possible.

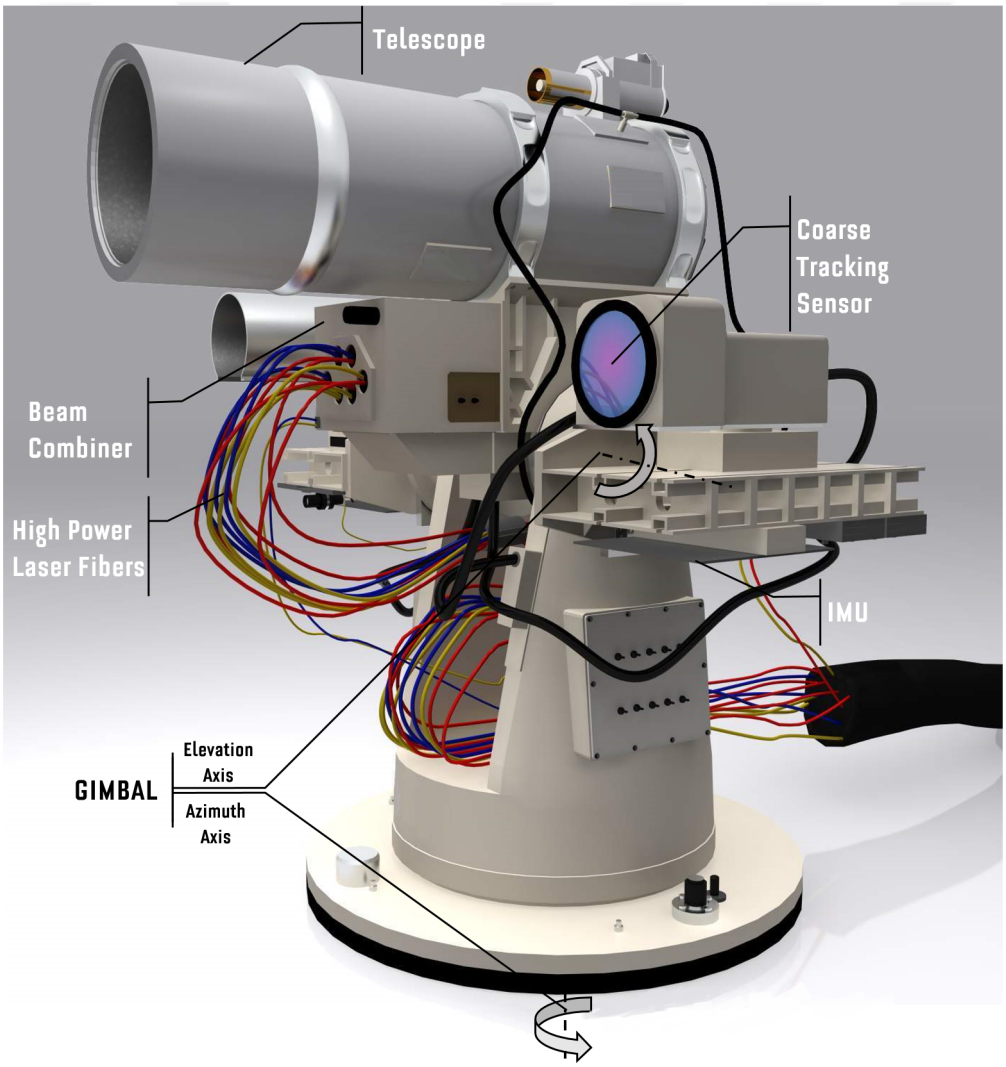


Figure 1.1: HEL Weapon Components (Adapted from [3])

As well as structural dynamics, disturbance torque components such as friction, unbalance, and cable restraint could be problematic on EOD performance with expanding sizes of gimbals. In the design phase, selecting appropriate bearing and seals, balancing in static and dynamic manners, and guiding flexible elements helps dealing with friction, unbalance, and springiness based problems, respectively. Nevertheless, testing these physical properties throughout the assembly phases for verification, improvement, and fault diagnostic purposes is essential. Also, on actuator selection, influence coefficients of these factors, along with moment of inertia, become more dominant as the characteristics system dimension is getting bigger. Required high torque values and backlash-free, precision operation, typically, entail high voltage motor and drive elements, which bring along handling problems.

During operation, generated HEL beam passes through optical train and is focused on distant target via telescope in order to concentrate as much as energy. Laser beam is directed to and tracks a target via gimbal with the assist of fast steering mirror, several sensors and, electronics units. Laser beam spot cross-section area on target aim-point has to be small enough to create damage in a short time [4]. Moreover, tracking performance has to be high enough to achieve that laser beam wavefront keeps on aim-point with low jitter during fire. However, in addition of aforementioned platform vibrations and atmospheric turbulence, large variety of factors, ranging from tracker jitter to sensor noise, from electronics delays to boresight errors, might decrease effectiveness of HEL weapons [5]. Compensating all these factors, essentially, poses the key design and control problems.

Target tracking and all other operation modes necessitate dedicated control loops. For instance, when a threat acquired via radar, EOD is expected to point its location immediately, which is known as slew to cue mode. In order to fulfill this task, agile and low overshoot position loop has to be created with absolute encoder as feedback element. When target becomes visible in field of view (FOV) of forward-looking infrared (FLIR) or daytime video (DTV) camera, video tracker comes into operation. Combination of camera and tracker electronics, which can be named as tracking system, are feedback elements of tracker control loops. Target tracking accuracy plays key role on system legality. Therefore, performance maximization problem evolves into keeping peak and mean errors considerably low via proper control strategies.

1.2 Literature Survey

1.2.1 Lasers

Laser is acronym for "Light Amplification of Stimulated Emission of Radiation" and single wavelength narrow beam of light, in which constituent waves are in phase. Stimulated emission of electromagnetic radiation at proper frequency results in optical amplification, and each electron is triggered to emit. This is the key dynamics for laser operation and named as stimulated emission.

Between two optically parallel mirrors, one of which is highly reflective and the other one is partially permeable, active/gain medium is presented in principle for all laser systems as depicted in Figure 1.2. As long as it amplifies the amplitude of light wave by stimulated emission, solid, liquid, or gas state gain media can be utilized. Besides, in order to pump active medium an energy source is required. Pumping can be electrical, optical or via chemical reaction. While moving back and fort between mirrors, light attains amplification in each passage through active medium, and after a threshold energy, it is sent out on partially permeable mirror [6].

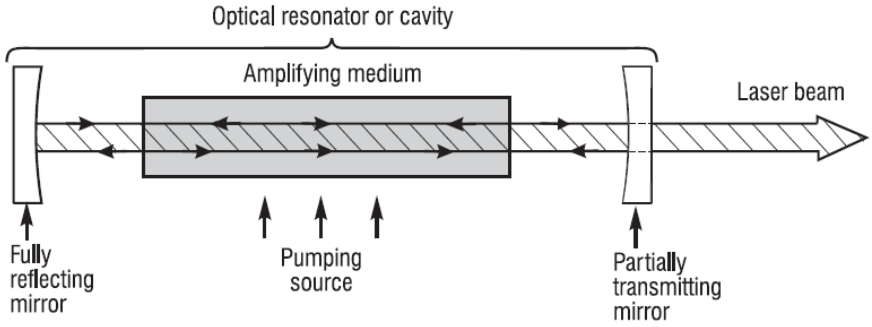


Figure 1.2: Laser Principle Parts and Working Process Schematic Diagram [7]

Laser characteristics is essentially defined by monochromaticity, coherence, and collimation properties as illustrated in Figure 1.3. The light production capability at a definite wavelength is described as monochromaticity. Coherence represents the degree of in-phaseness for all emitted photons in a single laser beam. Collimation property reflects the parallelism of light waves. Intensity or irradiance is also worth mentioning value indicating amount of energy, which can be directed in unit time [8].

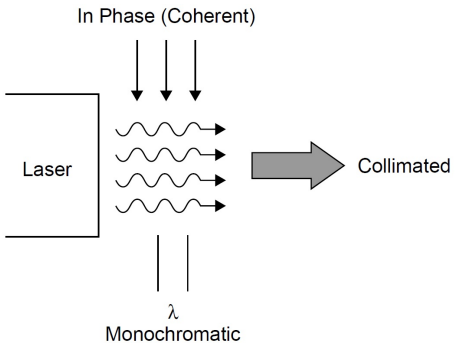
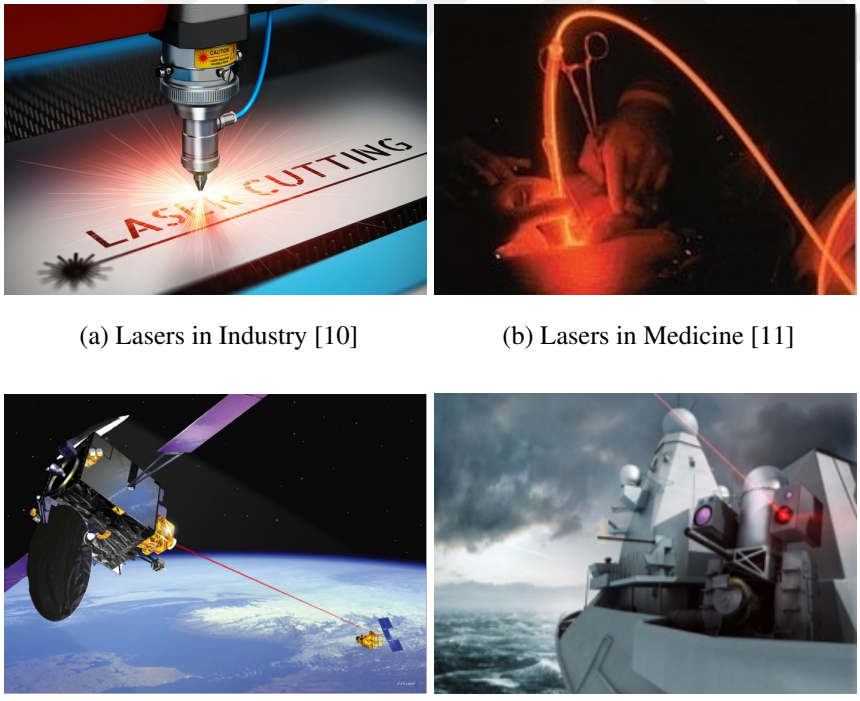


Figure 1.3: Laser Characteristic Properties [8]

Based on state of active media, lasers are mainly classified as solid, liquid, and gas. Solid state laser mediums are produced by embedding ions as impurities into insulating host lattice such as glass or crystal. This process is called as doping and plays significant role on population inversion, which is indispensable for stimulated emission. One of the most commonly utilized laser medium is Neodymium-doped Yttrium Aluminum Garnet (Nd:YAG). By using optical devices such as flash lamps pumping is performed. Unlike solid-state lasers, mixture of gases, such as helium and neon, filled into glass tube constitutes gas laser mediums and, they may be atomic, ionic or molecular. Pumped by electrical discharge and accelerated through electrical field, electrons are collided with active medium atoms, ions, or molecules, and transition to higher energy levels occurs. This dynamic underlies the working principle and paves the way for stimulated emission by enabling population inversion. When long coherence and high beam quality is required, gas lasers come to the forefront, plus they are available in a wide range of wavelengths and energy levels. Above-mentioned helium-neon laser is the most popular example to atomic lasers. Among molecular gas lasers' mediums, particularly, when high-power is the concern, CO_2 is the most effective element. Highly toxic and corrosive content is the limiting factor especially for UV gas lasers such as Excimer. As against gases, liquid active mediums contain larger volume of active atoms. In addition to that, their homogeneity is higher than solid ones. Dye laser are examples to liquid lasers whose gain media is obtained by blending organic compounds such as rhodamine, DCM with appropriate solvents. Laser beam is produced from optically excited energy states of organic dyes molecules. Low fabrication difficulties, easy heat removal, and replaceability characteristics are favorable aspects of liquid lasers [6].

Because of the aforecited unique properties, lasers are used in a great variety of applications including medicine, military, communications, and industries as exemplified in Figure 1.4. From removing kidney stones and tumors to curing lung, liver diseases and eye lens curvature aberrations, lasers are increasingly utilized for diagnosis and treatment in the medical field. In the communication field, weak signals are strengthened, and signal loses through long runs are prevented by solid state amplifiers. As well as laser light is used in fiber optical communications, laser signals are used in free-space optical communication for direct connection to satellites. In especially industrial production, welding, hole drilling, marking, micromachining, cutting, photolithography, etc. are some examples for manufacturing techniques made use of lasers. Touching briefly on laser cutting, since this technology offers minimal thermal material influence, no surface finish requirement in many cases, non-contact and force-free machining, laser cutters are used widely. Even if there is no cutting force exerted, depending on the workpiece, significantly high focused cutting power may require to be applied.The most common laser cutters are of the gaseous CO_2 with powers of up to 50 kW and Nd:YAG with typical powers of 5 kW [9].



(a) Lasers in Industry [10]

(b) Lasers in Medicine [11]

(c) Lasers in Communication [12]

(d) Lasers in Military [13]

Figure 1.4: Laser Applications [10, 11, 12, 13]

In military field high power lasers are used in directed energy weapon systems as microwave and particle beam alternatives. While low power lasers are preferred in target designation, range finding and countermeasure military applications, high power lasers are utilized for jamming and destruction purposes depending on power grade [13]. Generally, lasers with power rating less than 1 kW are used for sensor jamming and destruction. Lasers from 10 kW to 100 kW power ratings are effective against unmanned air vehicles, improvised explosive devices, mortars etc. threats. Lasers, which generate power greater than 100 kW might cause massive damage on even to armor steel. Extensive research on HEL weapons has been carried out by many countries including US, Russia, Germany for many years. Just after 5 years from invention of laser, first HEL development project was kicked off in USSR. For their contribution to laser invention, Nobel Prize awarded scientists Basov and Prokhorov were individually appointed in charge of two projects Terra-3 and Omega, respectively. While Terra-3 was for specifically ballistic missiles, aim of Omega was ground to air threats. Because the light pulses on the order of mega joule was noticed to be insufficient for eliminating missile threats, contrary to main envisagement of project, Terra-3 was terminated in 1978. Since Russia has been continuing HEL weapon development projects under privacy for years, very few details are known publicly [14].

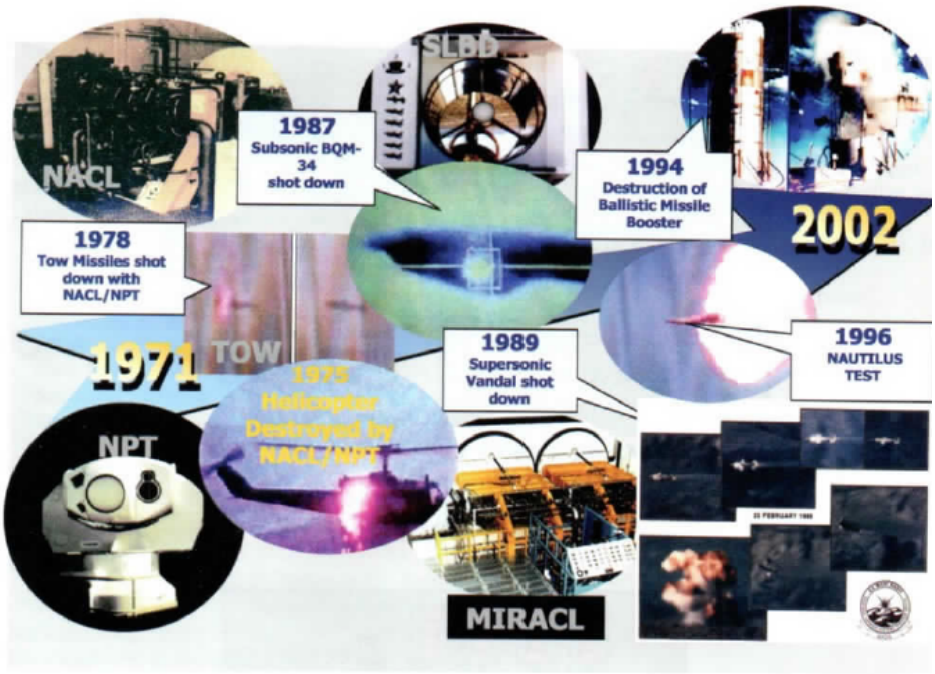


Figure 1.5: HEL History of the U.S. Navy [15]

In the U.S., HEL development progress started by Ed Garry's the gaseous CO_2 laser with 138 kW power in 1968. In 1972, project Delta was launched as ground based air defense system. To mobilize project Delta via integrating onto truck, MTU project was started in 1974. Since the gaseous CO_2 lasers are absorbed in a great extent on ground level and hard to focus on long distances because of the high wavelength, they are left then and supplanted by deuterium fluoride (DF) lasers. After this step, projects followed each other under auspices of the U.S. Navy in quick succession as visualized in Figure 1.5. Although some military successes was achieved by these projects such that Navy-ARPA Chemical Laser (NACL) intercepted TOW missile in 1978 and Mid-Infrared Advanced Chemical Laser (MIRACL) was effective on supersonic missiles, this laser technology is slipped into background because of toxicity, corrosive nature, and emerged logistics difficulties [14]. With the advances in Chemical Oxygen Iodine Laser (COIL), focusing laser beam on smaller points, and achieving longer ranges became possible. Integrating COIL laser onto Boeing 747-400F and intercepting ballistic missiles on boost phase ABL (Airborne Laser) project was initiated and it cost around $5 Billion. Ultimately, because of underperformance and removal of ballistic missile threat against the U.S., ABL project was canceled as its predecessors ended up after almost 15 years [16]. At the present time, the U.S. HEL development activities proceed extensively. Presented in Figure 1.6, Laser Weapon System (LaWS) and Northrop Grumman Maritime Laser Demonstrator (MLD) might be stated as noteworthy examples. Shifting threat perception from ballistic missiles to asymmetric war makes bulk and fiber lasers, which are variations of solid state lasers, have come to forefront for both the U.S. and Europe HEL applications.



(a) LaWS [17] (b) MLS [18]

Figure 1.6: Today's Laser Applications [17, 18]

1.2.2 Optical Train

Optical train might be basically described as optical component arrangement of lens, prism, filter, mirror, etc. in order to guide light rays and generally fulfills tasks such as projecting scene on optical sensor, zooming, and focusing. Due to their high susceptibility towards optical aberrations and atmospheric distortions, HEL optical trains are specifically designed by taking these factors into consideration [19]. A demonstrative schema of beam guidance optical train for HEL application is presented in Figure 1.7.

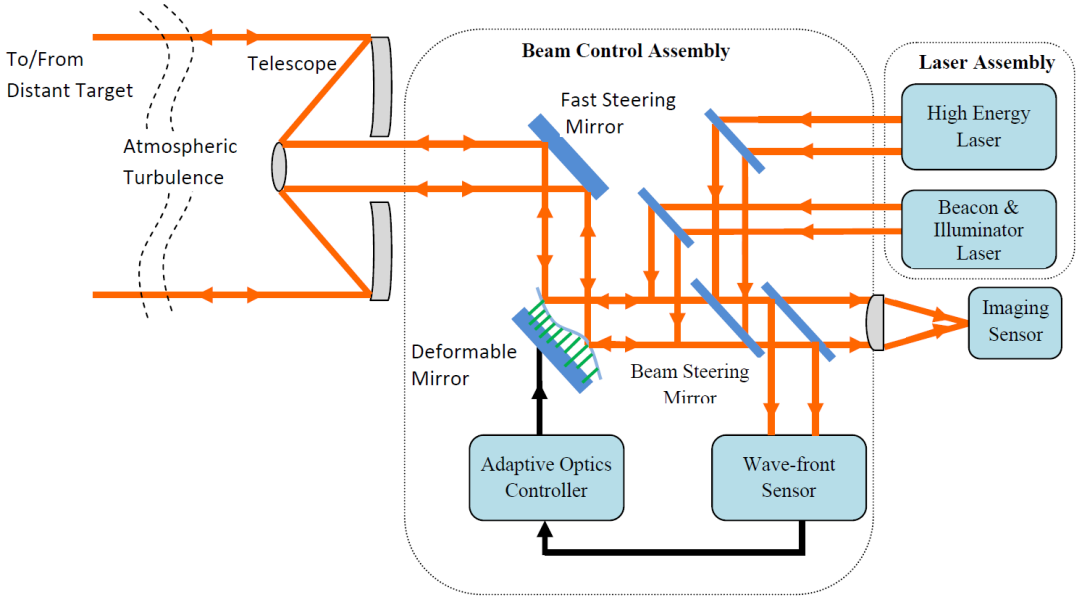


Figure 1.7: Demonstrative Schematic of Beam Guidance Optical Train [13]

Reflective and refractive components of HEL applications must be designed to withstand high temperatures, since they are subjected to higher power densities than ordinary optics. Optical path deviations by heat-induced aberrations, which is termed as thermal lensing, are mainly driven by power absorption, element's physical and thermal properties, and temperature gradient. It is worth noting that because of heat flow throughout medium, beam quality degradation is more severe for refractive components than reflective ones, which are just subject to surface level exposure. In order to compensate thermal lensing in a passive manner, good thermal management and tandem arrangement of optical components with reverse speed of light-temperature dependencies are practiced. Active compensation is achieved via adaptive optics [19].

Adaptive optics is a real-time optical aberration compensation and blur reduction technique, based on that reflecting mirror is taken the phase reverse shape of incoming wavefront, and outgoing wavefront is flattened; hence phase-error is removed [20].

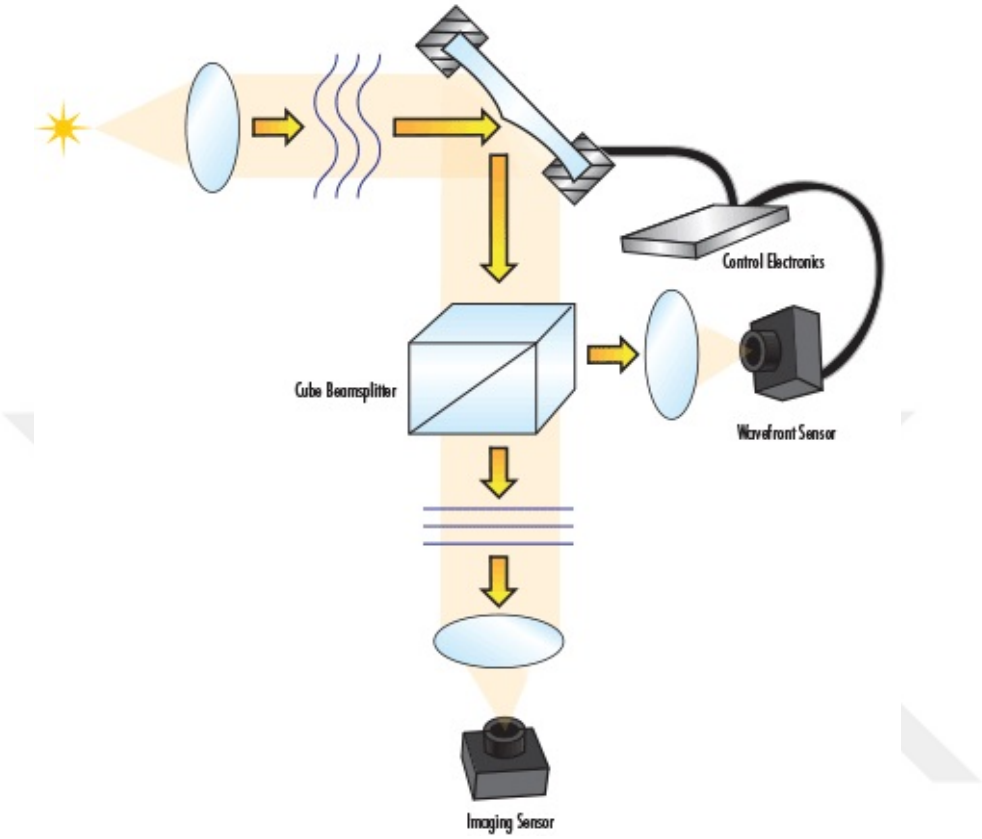
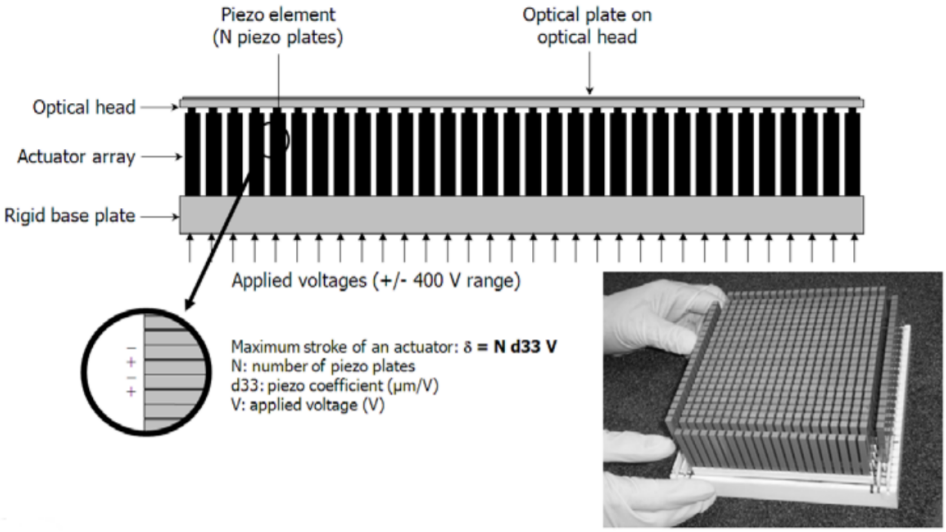


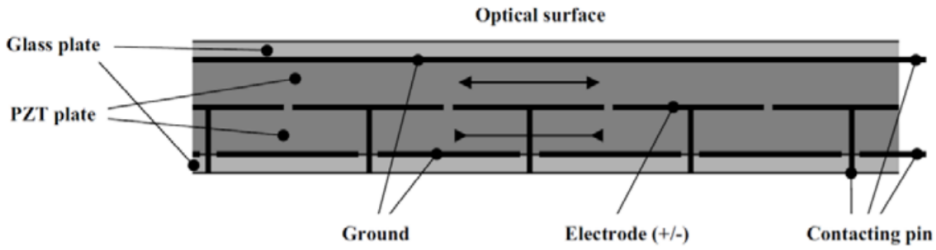
Figure 1.8: Closed Loop Operation of Adaptive Optics System [21]

As shown in diagram (Figure 1.8), deformable mirror (DM) and wavefront sensor, which are functioning as actuator and feedback sensor, respectively, are the key elements of adaptive optics system. DMs are wavefront correctors. Parameters, derived from requirements such as, number of actuators, which is specified by required degree-of-freedom to be corrected, actuator pitch, which is distance between actuators, actuator mechanical stroke, which is peak excursion value of single actuator, and temporal response, which is indicator of DM control loop bandwidth, has driven the development process of various types since 1970s. As illustrated in Figure 1.9, DMs are mainly classified as segmented mirrors, which are composed of triangular, square or hexagon stacked mirror array each with 1 stroke plus optionally 2 tilt axis degree of freedom, bimorph mirrors, which are formed by bonding flat piezoelectric disks as ac-

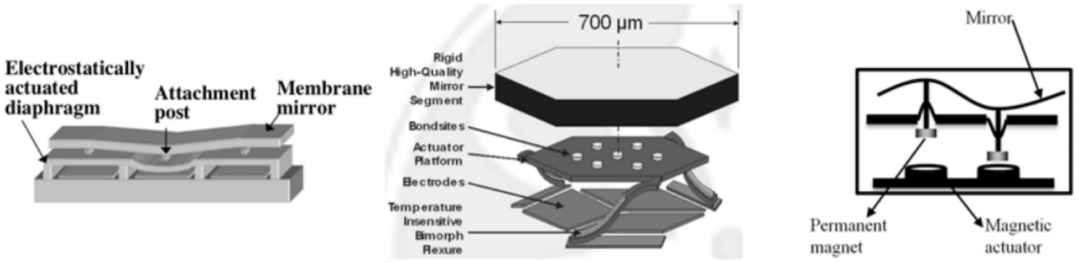
tuators onto faceplate backside and function based on transverse piezoelectric effect principle, and MEMS (Micro Electro-Mechanical System) Mirrors, which are produced by micromachining techniques as an intermediate flexible structure supported thin mirror membrane and actuated under effect of electromagnetic field. Compagnie Industrielle des Lasers (CILAS) and Xinetics are pacesetters of DM market [22][23].



(a) Segmented Mirror Architecture



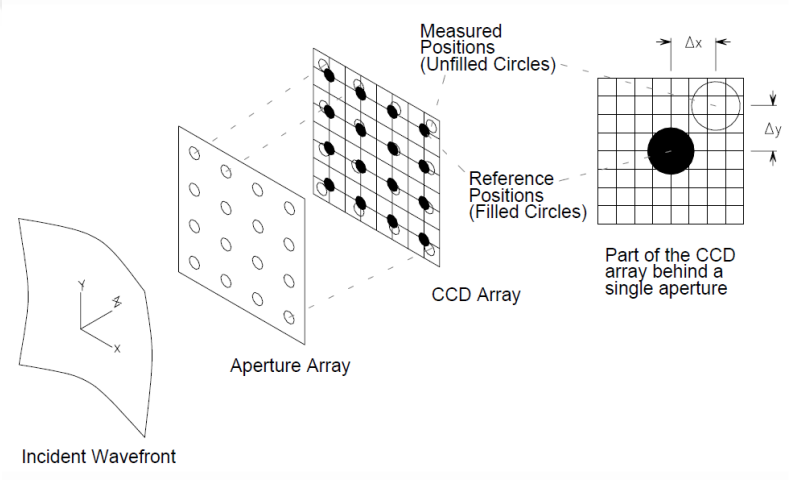
(b) Bimorph Mirror Architecture



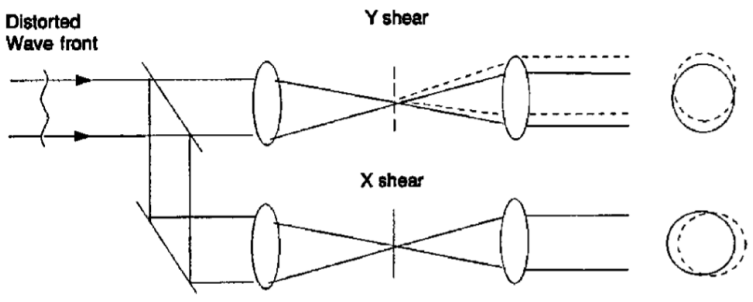
(c) Several MEMS Mirror Architectures

Figure 1.9: Deformable Mirror Architecture [22]

The other key element of AO system is wavefront sensing (WFS), which is an effective group of measurement methods to determine optical wavefront shape itself or its deviation from ideal form. These methods fall mainly 3 groups, namely interferometric methods, which are based on creating two copies of wavefront and comparing them continuously for lateral displacement or shear as shearing interferometer, image-plane sensing methods, which are based on wavefront deduction from intensity distribution of reference source in video frame, and wavefront slope or curvature measurement methods, which are based on dividing wavefront into independent subaparture array and simultaneously measuring slope for each as Shack-Hartmann (S-H) wavefront sensor. Invented a century ago, the time-honored practice the Shack–Hartmann wavefront sensor and shearing interferometer operation principles are schematically illustrated in Figure 1.10 [23][24].



(a) Shack Hartmann Wavefront Sensor [25]



(b) Shearing Interferometer [26]

Figure 1.10: WaveFront Sensors Operation Principles [25][26]

(S-H) wavefront sensors have become standard unit for adaptive optics applications by virtue of their stability, reliability, and ease of implementation. Main disadvantages of (S-H) sensors are their tilt sensitivity and dynamic range inflexibility, whereas flexibility on these aspects is the primary advantage of shearing interferometers. Although there are fundamental differences among optical means, in all wavefront sensors a photodetector exists to capture incident photons. Charge-coupled detector (CCD) arrays are one of the most preferred photon sensor offering high percentage of input photons to corresponding current generation ratio, mechanical stability, and wide size range. Photomultiplier arrays and intensified silicon diode arrays are some examples to other types of photodetectors. Readings from each independent photodetector pixel are required to be reconstructed for constituting a meaningful whole such that the edges of adjoining spatial slope segments touch before control action taken as illustrated in Figure 1.11.This process is termed as wavefront reconstruction. Due to the fact that measurement errors, noise content etc. factors are accumulating throughout the process, wavefront reconstruction is complicated and entails significant computational effort plus short processing time [23].

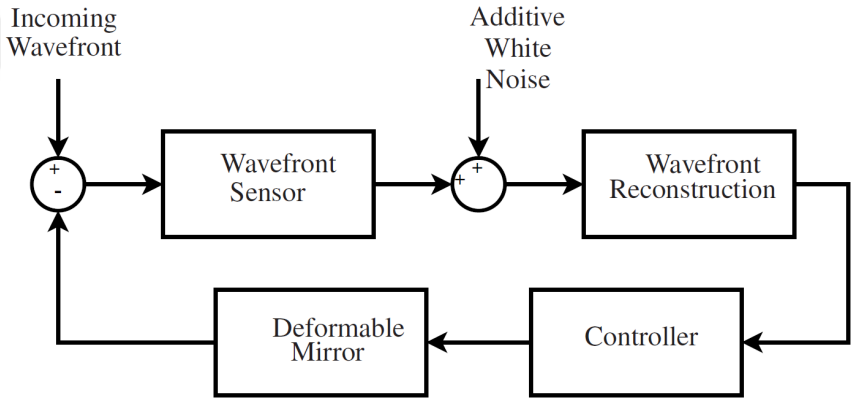
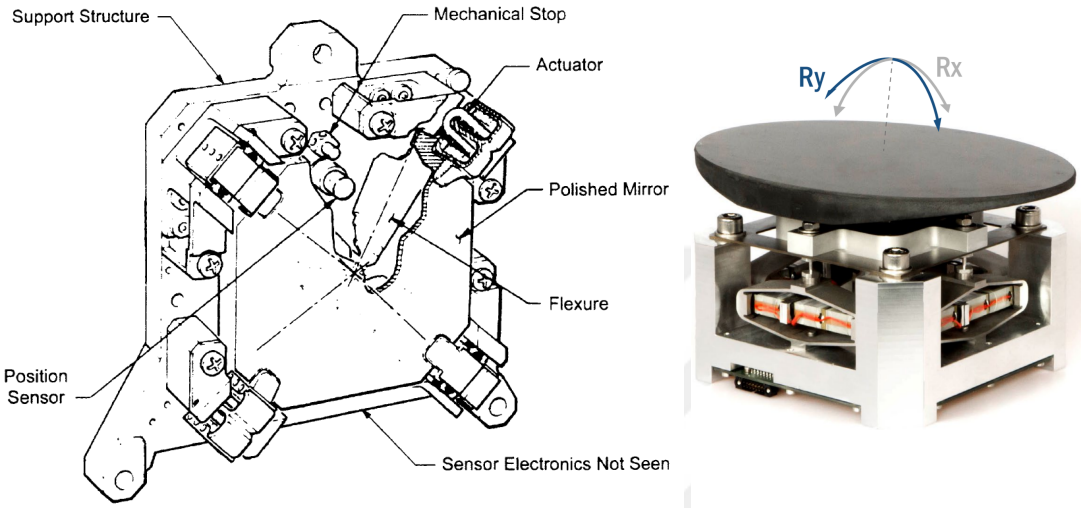


Figure 1.11: Closed Loop Block Diagram of Adaptive Optics System [27]

Yet to be mentioned, component from Figure 1.8 Closed Loop Operation of Adaptive Optics System, the Cube Beamsplitter is an optical component for branching incoming beam into two separate beams at a specific reflection/transmission ratio. Reversely, to combine two separate beams into a single beam, beamspliters can also be utilized. One other class is Plate Beamsplitters, which are lightweight and inexpensive compared to cubic ones [28].

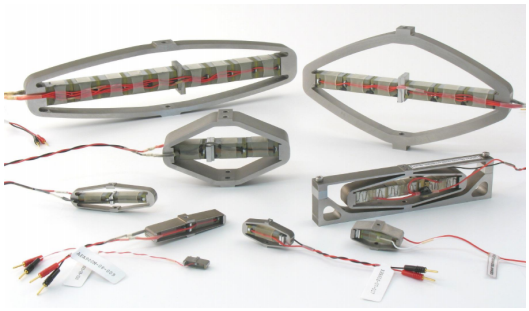
Adaptive optics are already expensive and as larger strokes and shorter response times are demanded, more sophisticated and costly units are required [29]. When DM works in tandem with FSM which corrects tip-tilt component of total wavefront error, its workload decreases significantly [23]. As illustrated in Figure 1.12, FSM is an optical platform, in which mirror is mounted on complaint mechanism and actuated by fast, precise actuators in order to point beam accurately [30].



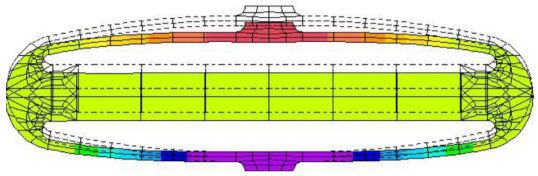
(a) Main FSM Constituents [31] (b) An FSM Platform Example [32]

Figure 1.12: Fast-Steering Mirror (FSM) [31][32]

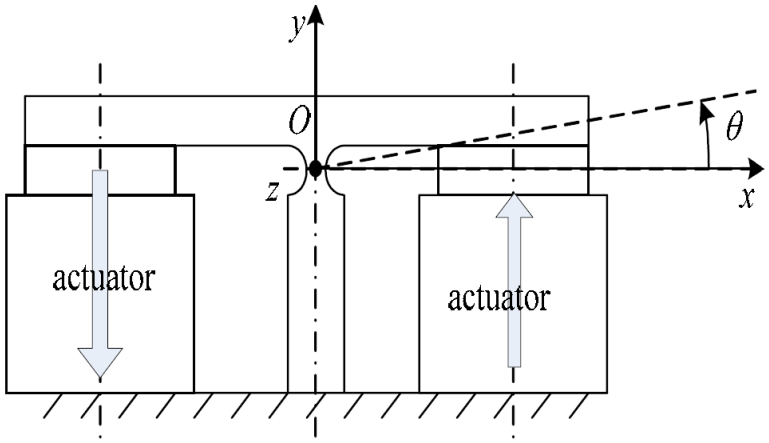
Motion is generated by deflection of flexible elements in compliant mechanisms. When compared to their rigid peers in order to fulfill the same task, complaint mechanisms require less components. No matter linear or slider conventional bearings, springs, pins, fasteners etc. mechanical parts are not taken place in the design of complaint mechanisms, that brings advantages such as manufacturing and assembly easiness, low costs, no wear, friction and backlash based precision loss, no need for lubrication and, miniaturizability whereas fatigue performance, due to nonlinear nature analysis and design difficulties, undesirable energy storage, and limited motion range pose challenges [33]. Along with the complaint structure design, the other important factor on FSM performance is actuators, where voice coil and piezo technologies are widely preferred [34]. When piezoelectric crystals and ceramics undergo electric field, they deform, push against the flexure; hence mirror is tilted.



(a) Piezoactuator Examples [35]



(b) Piezoactuator Operation Principle [35]



(c) FSM Operation Principle [36]

Figure 1.13: Piezoelectric Fast-Steering Mirror (FSM) Operation Details [35][36]

Based on these dynamics, piezoelectric FSM functions as detailed in Figure 1.13 [30]. Although piezo actuators have high bandwidth, hysteresis and creep phenomena have to be handled. Besides, short motion range and high-voltage requirement may be regarded as unfavorable aspects, whereas voice coil actuators offer larger motion range, lower-voltage requirement, and no hysteresis [34]. Sharing with loudspeakers the same working principle of Lorentz force, voice coil actuator is a direct drive motion device that uses permanent magnet, and current flowing through electromagnet interaction produces force to achieve push-pull action. Voice coil actuators are affected by magnetic flux and have lower bandwidth compared to piezo peers [30]. Servo bandwidth is an important performance issue, however, alone is not enough. Travel range, operation modes such as stabilization, slew position, accuracy with all its subtitles such as jitter, positioning plus position reporting accuracy, turn-on characteristics and optical quality are other critical specifications, which have to be matched [37].

Speaking of optical quality, it is closely related with mirror design. On mirror design a compromise has to be reached for mechanical and optical parameters. To be on the safe side for achieving optical requirements and high stiffness, proposed bulky mirrors necessitate larger actuators in order to keep agility high. Hence, size limitations might be violated, and costs might escalate. Glass mirrors offer low prices and high surface finishes yet are not formable as metal peers. Metal mirror stiffness to mass ratios are generally lower than required to achieve compactness in concurrence with stiffness. Since the mass and stiffness properties govern first natural frequency, in turn closed-loop bandwidth, some special and expensive materials are utilized such as Beryllium or Silicon Carbide (SiC). One other reason why Beryllium and SiC are preferred is their high thermal conductivity. Excessive heat load may distort mirror, which poses an beam alignment error and decreases image quality. Mirror mount to flexures entails similar risks such that if thermal expansion coefficients of mating parts does not match, stress is induced and warpage occurs [38].

Along with nonuniform thermal expansion, geometric and alignment-based errors such as eccentricity, nonorthogonality stem from mirror mounting. These factors can be minimized by tight tolerances and calibration, moreover, compensated by the aid of position-sensitive (PSD) or imaging (ID) detectors as feedback element. No matter whether CCD or ID is used, orthogonality-like intrinsic to its own reference frame faults lose their influences because FSM is driven down to zero the incoming feedback error, which is produced according to a different reference frame than mirror's. To detail optical detectors, PSD is position sensor, which locates and reports the centroid of incoming beam onto its surface by exploiting photoelectric effect. For indicating centroid quadrant detectors and measuring displacement, lateral-effect photodiodes are mostly used PSD types. Quadrant detectors, which are 2x2 cell array of photodiodes, derive position information based on relative signal power of each cell. Lateral-effect photodiodes, which are made up of single photodiode with embedded resistive layers, deduce beam centroid point from resistance path-passing through photocurrent relation. Maximum sensitivity and accuracy demanding applications employ IDs such as CCDs [39]. If there is no reference or guidance as laser beacon, video tracking and therefore CCD usage becomes obligatory. However, camera frame-rate, exposure, and processing time delays are major restrictions on high bandwidth gains [40].

In order to compensate the decrease in bandwidth due to delays posed by CCD internal dynamics, as a common practice, loop controller gains are increased, however, this affects stability, adversely. Also, shortening CCD exposure times and predictive or delay reduction algorithmic solutions all fall short of performance especially under severe atmospheric turbulence, and because of nonlinear piezoactuator dynamics. Creating a fast inner feedback loop via strain gauges (SG), as depicted in Figure 1.14, is proposed for performance enhancement. Here, inner strain gauge loop corrects hysteresis effects, builds dynamic response up; hence, facilitates outer CCD loop's work. This facilitation can also be in the form of getting rid of nonlinear dynamics and eventual predictive algorithm performance improvement [41].

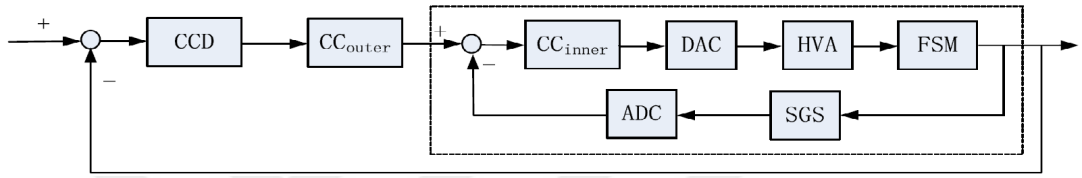


Figure 1.14: FSM Cascaded Control Loop [41]

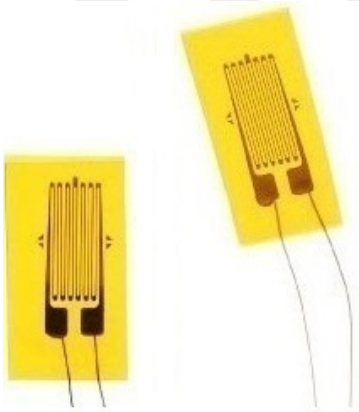
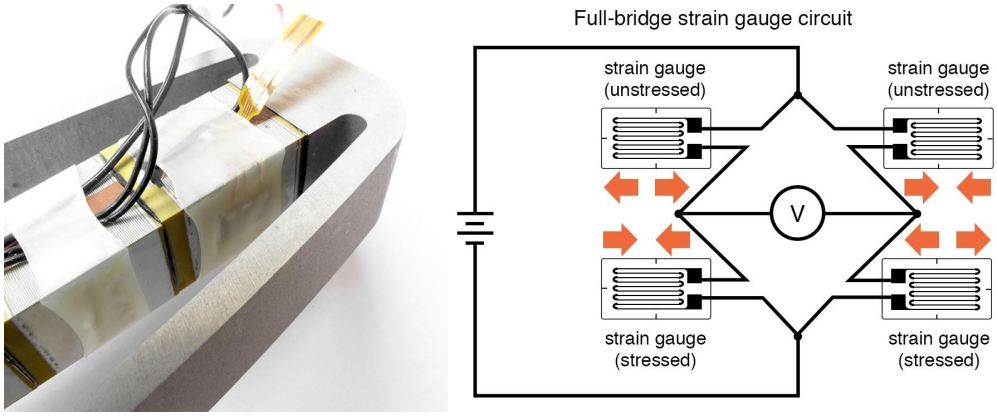


Figure 1.15: Resistive SG [42]

SGs are not always auxiliary components, and thanks to their compactness, low price and high precision, they are the primary feedback sources for considerable number of piezoactuator applications as the one sketched in Figure 1.12. Represented in Figure 1.15, a resistive foil strain gauge is essentially constructed from a long, thin piece of metal folded back on itself, or zig-zag and sandwiched between insulating layers. The underlying operating mechanism is the change of resistance due to expansion or contraction under load.

SG is mechanically integrated to actuator by attaching on its surface. Special attention is paid on surface preparation and sensor orientation. Electrical integration is implemented in Wheatstone bridge formation due to its temperature insensitivity. Sole SG is susceptible to temperature variations, and bridge circuitry removes their adverse effects by virtue of symmetry [43]. Integration details are presented in Figure 1.16.



(a) Mechanical Integration [44] (b) Electrical Integration [45]

Figure 1.16: Resistive Strain Gauge Integration [44][45]

In 1954, by the invention that silicon and germanium have resistance change toward strain up to two fold of conventional metal fold strain gauges, piezoresistive strain gauges have started to be offered in the field. In addition to their actuator role, piezoelectric crystals and ceramics are utilized as strain sensor by exploring their electric field creation under strain property. Although they introduce large drifts, piezoelectric sensors have lowest high frequency noise characteristics among peers [43]. Strain gauges are known to achieve tip/tilt angle measurements in the order of sub-µrad accuracies, in some cases they bring non-minimum phase dynamics; hence, fall behind optical detectors in performance. Because of the right hand plane zero presence, non-minimum phase systems initially move on opposite direction of command in response to step input [46]. When direct optic measurement is infeasible, along with strain-based means, however, distinctively as non-contact methods, capacitive and inductive transducers are widely used. Inductive sensors are also called as Eddy-Current sensors, and operate based on the course that induced current on mirror mount side creates opposing magnetic field along sensing coil whose magnitude depends upon the gap in-between. Within their air-gap inductive sensors are highly tolerant to dust and pollutants, however, due to their disadvantages such as high temperature dependency and excessive minimum achievable range for nanopositioning, they do not have field of application as large as capacitive sensors'. Capacitive sensors rely on the principle of two conducting surfaces' capacitance change with their distance proportionality, and offer short range, low cost, good linearity & resolution, and high bandwidth [43].

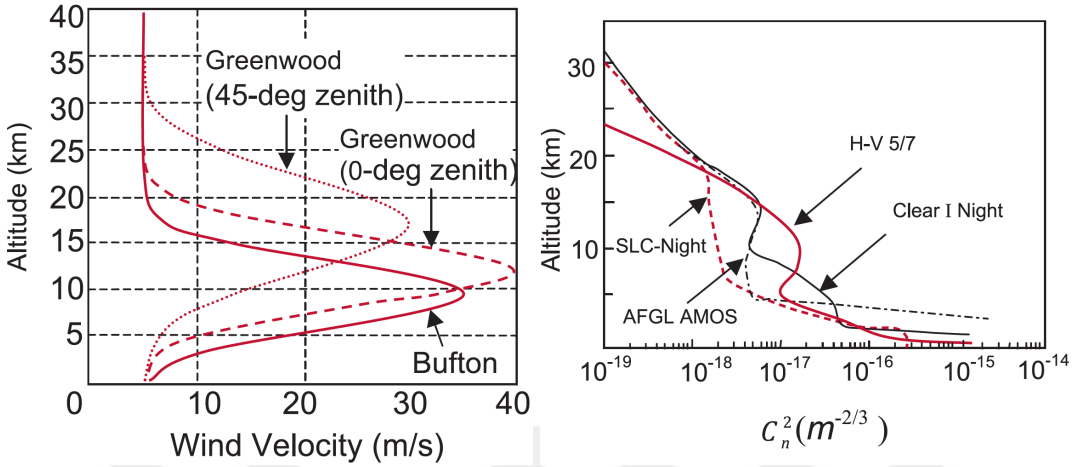
As mentioned above, DM offloads its tip-tilt motion content to FSM in some practices. Tip-tilt correction is required for low-order atmospheric turbulence and residual tracking error. Low-order aberrations as in the form of wavefront slope constitute 87% of total disturbance energy and have detrimental effects on performance [47]. For $D/r_0 \leq 1$, AO correction is not required and if on the order of magnitude $D/r_0 = 2$ weak turbulent is present, a significant performance is achieved via only FSM, however, as from moderate to strong turbulence conditions appear, need for DM becomes imperative [48]. Coherence length (r_0) is also known as Fried's parameter and the key to characterize the level of present turbulence at a particular site. Due to local density variations throughout the atmospheric medium, refractive index inhomogeneities arise in a random manner. For this reason, beam spatial coherence diminishes while propagation and largest effective telescope light collecting region, i.e., aperture (D) diameter is limited to (r_0) as formulated in Equation 1.1 where ζ is zenith angle, $k = 2\pi/\lambda$ for a fixed wavelength λ, and C_n^2 is structure constant [49].

$$r_0 = \left[0.423k^2 \sec\zeta \int_{path} C_n^2(z)dz\right]^{-3/5} \tag{1.1}$$

Fried's parameter is calculated essentially by taking path integral of C_n^2, which is a turbulence strength measure. Although C_n^2 is denoted as constant, actually it varies instantaneously depending on temperature, moisture, wind, and altitude. While air gets colder and becomes less denser, turbulence affects decay [49]. Within the atmospheric surface layer, C_n^2 ranges from 10^{-12} to 10^{-16} $m^{-2/3}$. Indicated by visual blurring and wavy lines seen on hot paved road, intensive convective heat transfer between ground surface and ambient-air on a clear, dry, and sunny day is resulted in unstable atmospheric conditions and the highest C_n^2 values on the order of 10^{-12} $m^{-2/3}$. Sunrise, sunset, and windy or cloudy weather creates adiabatic process, i.e., no heat or mass transfer occurrence, and ensures low C_n^2 readings between 10^{-16} to 10^{-15} $m^{-2/3}$ [50]. Above jet streams layer, particularly polar jets, C_n^2 drops off to 10^{-18} $m^{-2/3}$ level as a result of relationship between wind speed (W), altitude (z), and C_n^2, which is expressed by Hufnagel-Valley Boundary Model as Equation 1.2 and Figure 1.17 [49].

$$C_n^2(z) = 5.94 \times 10^{-23} z^{10} e^{-z}(W/27) + 2.7 \times 10^{-16} e^{-2z/3} + Ae^{-10z} \tag{1.2}$$

Since C_n^2 is highly site-dependent, besides Hufnagel-Valley Boundary Model (H-V 5/7), Clear 1 Night, SLC-Night&-Day etc. models are proposed, accordingly, in literature. They follow similar trends considering their profiles in Figure 1.17b [49].



(a) Wind Velocity vs. Altitude

(b) C_n^2 Profile vs. Altitude

Figure 1.17: Wind Velocity and C_n^2 Change with Altitude Gain [51]

As well as strength of turbulence, its time rate of change is also a key factor on determining system performance. Greenwood frequency (f_G) is a change of rate measure, which relates it to the required compensating servo loop bandwidth [51].

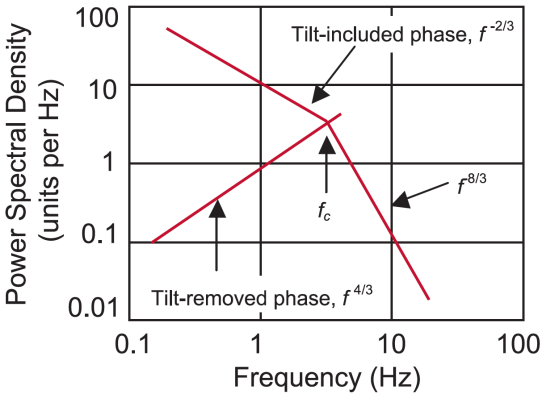
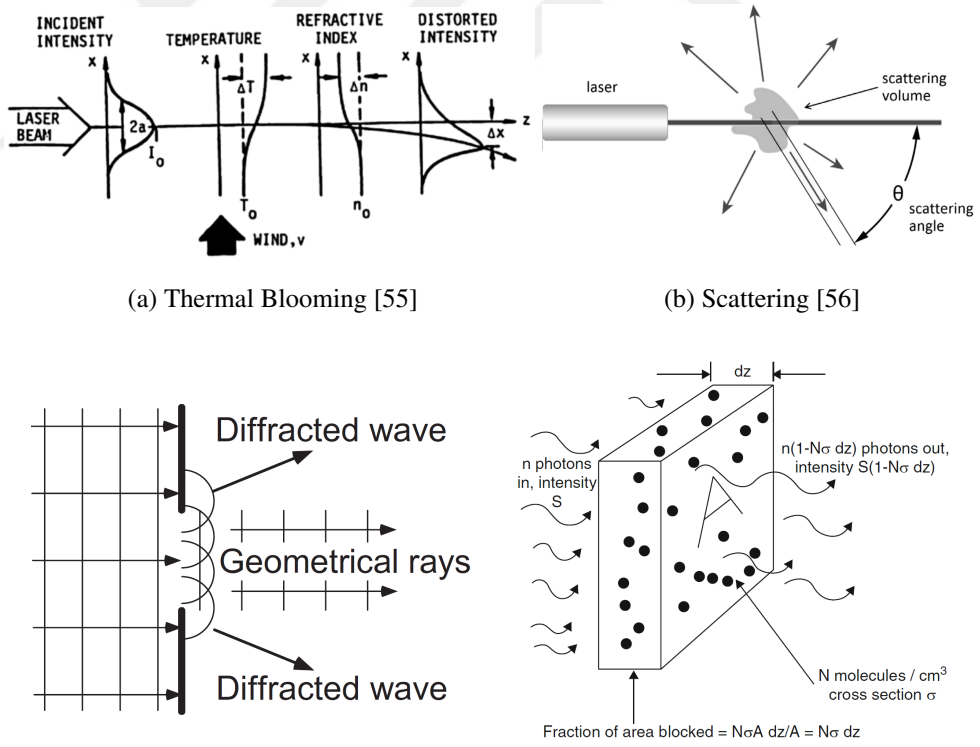


Figure 1.18: Power Spectral Density of Atmospheric Turbulence Components [51]

Atmospheric turbulence components, which vary in frequencies lower than cut-off (f_c) contain mainly tip-tilt content and have downward trend of ($f^{-2/3}$). With tip-tilt compensation, low frequency trend turns out to be ($f^{4/3}$) as demonstrated in Figure 1.18 [51]. In his article (1977) Darryl Greenwood suggested a method to calculate ideal servo cut-off frequency, subsequently named as Greenwood frequency [52]. Despite hypothetical shortages on proper estimation in practice, 10 fold of f_G is considered as optimal bandwidth projection [53].

In addition to turbulence, diffraction, scattering, and absorption are other significant atmospheric propagation effects as illustrated in Figure 1.19. Diffraction is spreading out tendency of beam while propagation. Diffraction phenomenon poses fundamental limit for focusable smallest spot size proportional to λ/D ratio where λ is wavelength and D is aperture diameter. As wavelengths get shorter or apertures become larger, diffraction influence dampens. On the other hand, with shortening wavelengths, scattering becomes more dominant. Scattering is deviation of laser beam from its straight path due to non-uniformity posing particles such as tiny water droplets, dust, and molecules. Particles in atmospheric medium also cause removal of beam energy during propagation. Atmospheric composition, strongly related with time, place, weather condition, and water vapor content e.g. maritime environment is the key determinant on absorption level and spectrum. Particularly for high power lasers, as air volume within beam absorbs energy, expansion and dependently density decrease occur while air at beam vicinity remains intact. Emergent reflective index gradient behavior as if weak lens and defocusing laser beam is termed as thermal blooming [54].



(a) Thermal Blooming [55]

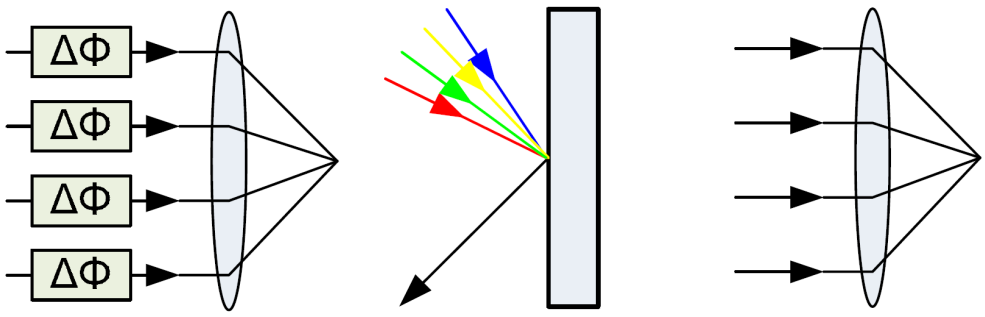
(b) Scattering [56]

(c) Diffraction [57]

(d) Absorbtion [58]

Figure 1.19: Atmospheric Propagation Effects [55][56][57][58]

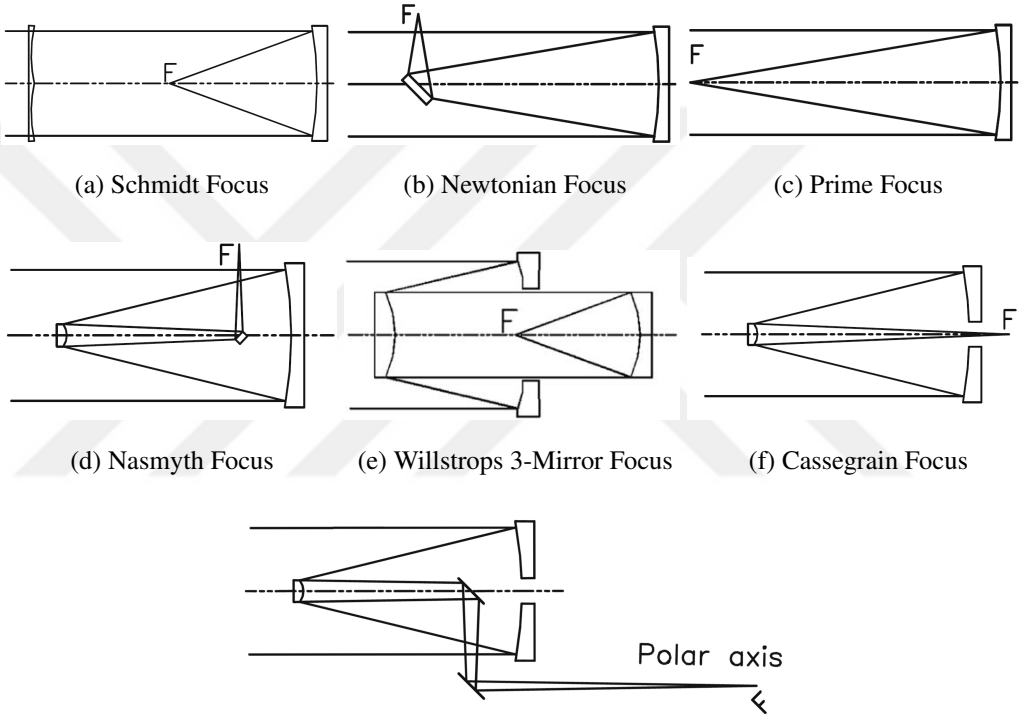
As much as atmospheric factors, beam combining practice is also influential on laser beam quality. In order to reach required high energy levels efficiently, robustly, compactly, and with low maintenance requirement, individual laser sources are combined. Coherent, incoherent (geometric), and spectral coupling are beam combination concepts. As aforementioned laser characteristic property, coherence herein implies all combined beams' possessing the same wavelength and phase. Coherent combining requires high phase and wavelength stability; hence, complex design. Due to applications challenges, as spectral combining, it is still under fundamental and feasible design phase [19]. Coupling many incoherent laser beams with different wavelengths by the use of angular dispersion with prism or grating is mainstay of Spectral Beam Combining (SBC). SBC is additive power scaling technique, which refers no performance loss in case of single laser source failure, on the other hand, this property is not valid for coherent combining [59]. Both techniques preserve beam quality while incoherent coupling degrades it with the number of individual sources' square root law. Larger aperture requirement is counted as another drawback. In spite of all shortages, design simplicity, wavelength independency and conformity to today's industrial lasers make incoherent coupling widely used technique [19]. Technical principles are shown in Figure 1.20. One of the most commonly used beam combining elements is dichroic mirror, which allows certain wavelengths pass through while reflects the rest of spectrum. Wavelengths to be passed are governed by composite non-translucent glass substrate and optical coating. In particular, for high power laser applications, coherent beam combining is implemented effectively by adjusting beam phases to obtain destructive and constructive interfaces with the aid of mirror [60].



(a) Coherent Coupling (b) Spectral Coupling (c) Incoherent Coupling

Figure 1.20: Beam Combining Technique Principles [19]

Each individual laser beam's expansion and on target orientation by means of a separate FSM incoherently combine fiber lasers [61]. In order to reduce beam spot size on target and unite laser optical path with scene's, telescopes are utilized. Traditionally, optical telescopes are distant object observation instruments and divided into two main categories as refractors and reflectors according to lens or mirror based design. Due to lens focusing failures, i.e., chromatic aberration, transmission losses, and fabrication difficulties, reflector telescopes are more advantageous with their maximum reflectivity and easy manufacturability nature. Reflector telescope configurations are presented in Figure 1.21 [62].



(a) Schmidt Focus (b) Newtonian Focus (c) Prime Focus

(d) Nasmyth Focus (e) Willstrops 3-Mirror Focus (f) Cassegrain Focus

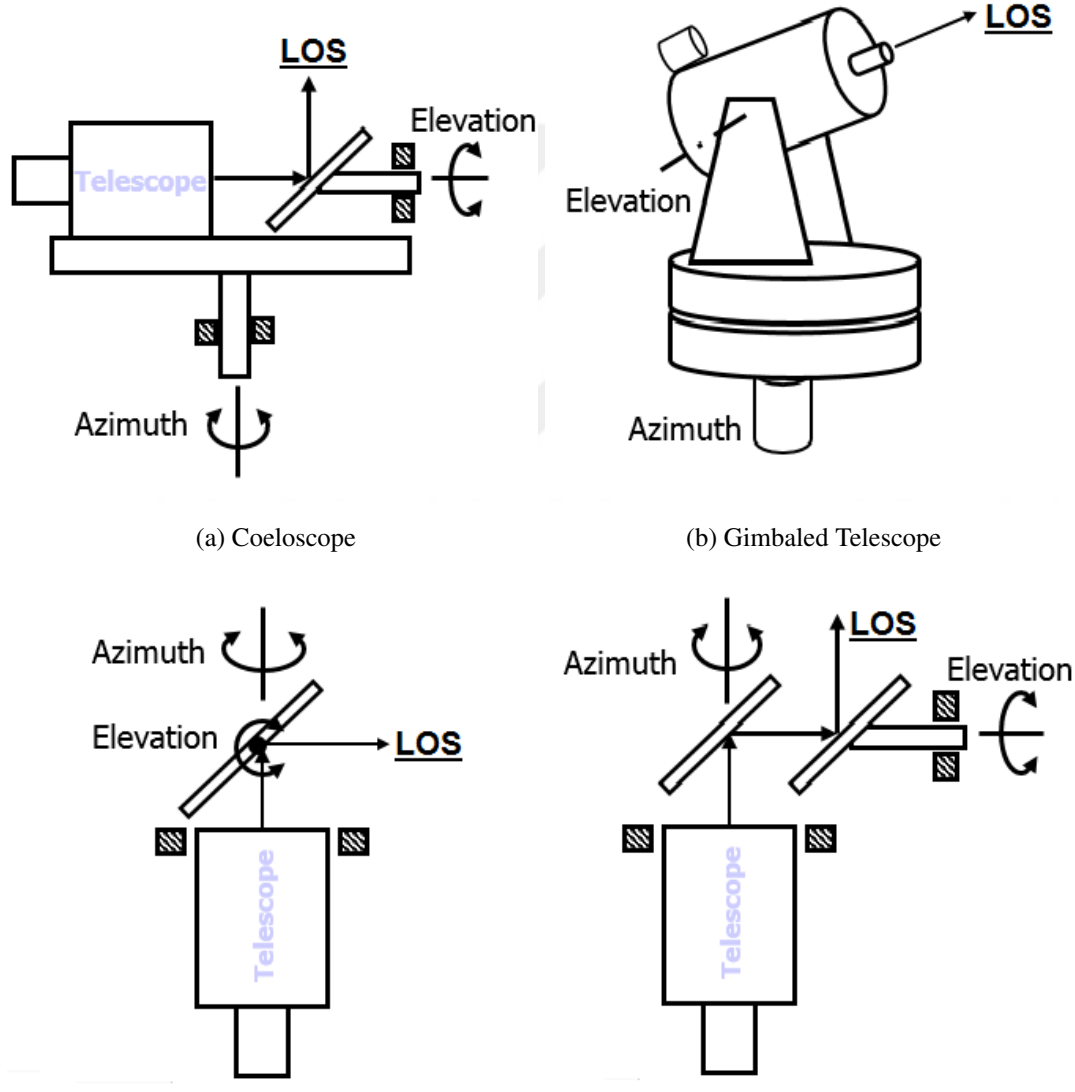
(g) Coude Focus

Figure 1.21: Reflector Telescopes Configurations [63]

The Schmidt system is not only reflecting, but also refracting, i.e., catadioptric, and have numerous disadvantages, most distinct of which is difficulties in aspherical correction [63]. The remaining configurations are almost comprised of primary and secondary mirrors. Cassegrain telescope, as a widely used configuration, functions such that parabolic primary mirror reflects to prime focus and secondary convex hyperbolic mirror reflects back through main mirror center hole [62].

1.2.3 Actuation Systems

Maintaining the orientation of a broad array of sensors, cameras, telescopes, and weapon systems via base platform motion compensation is termed as inertial stabilization. Inertially stabilized platform (ISP) is generally composed of structure assembly, motors, drive electronics, encoders, and gyros [64]. In order to stabilize and point payloads, a diverse range of electromechanical configurations is available, e.g., gimbal, heliostat, coeloscope, coelostat etc., as demonstrated in Figure 1.22 [65].



(a) Coeloscope

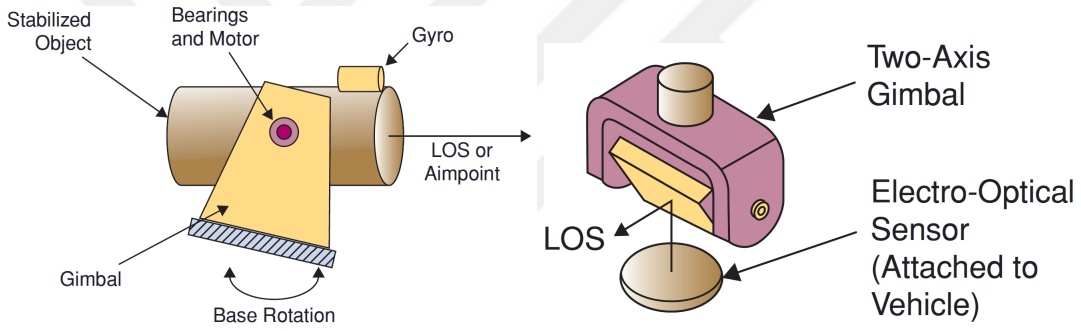
(b) Gimbaled Telescope

(c) Heliostat

(d) Coelostat

Figure 1.22: Several Stabilization and Pointing Systems Configurations [65]

In principle, sensors such as thermal camera in a direct manner or its scene with the aid of optics is stabilized and pointed as graphical comparison is presented in Figure 1.23. For heliostat and coelostat, telescope is off gimbal, whereas telescope is mounted on coeloscope azimuth axis. Heliostat and coelostat are good for scanning and have compact structure. On the other hand, posing difficulties in control and requiring more precision optical design with more than one large optics make them disadvantageous. As direct stabilization and pointing means, gimbaled telescopes could take multiple forms such as azimuth-elevation or elevation-elevation. Elevation-elevation form is advantageous for overhead coverage, however, could not move to low angles of elevation. Among all, elevation over azimuth is the most common form, offering good hemispherical coverage along with ease of manufacturing and stabilizability, although it is exposed to lower bandwidth limitation inherent on direct sensor stabilization and gimbal lock phenomena in overhead alignment [65].



(a) Sensor Stabilization (b) Mirror Stabilization

Figure 1.23: Stabilized Gimbal Examples [64]

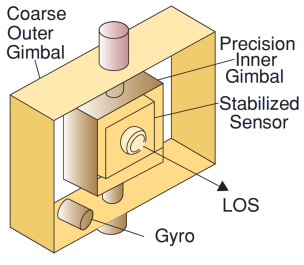


Figure 1.24: Nested Gimbal Formation [64]

Gimbals are typically designed to point and stabilize imaginary straight line joining sensor focal plane and target, i.e., Line of Sight (LoS) in 2 or more orthogonal axes. In order to achieve better isolation and less LoS jitter, nested gimbals configuration is deployed with inner and outer gimbals as shown in Figure 1.24 [64]. Outer gimbal fulfills course stabilization and position heading functionality with low control bandwidths, whereas inner gimbal is in charge of fine stabilization with broader motion spectrum.

Each gimbal axis has its own actuation mean. As prime mover, whether direct or indirect manner, an electric motor is an indispensable axis component. Electric motors are classified into two broadest groups, namely, Alternating Current (AC) and Direct Current (DC). AC motors are subdivided into Synchronous and Asynchronous (induction) designs, whereas DC motors are sub-classified based on excitation as self and separately excited which is charted in Figure 1.25 with all sub-classes [66].

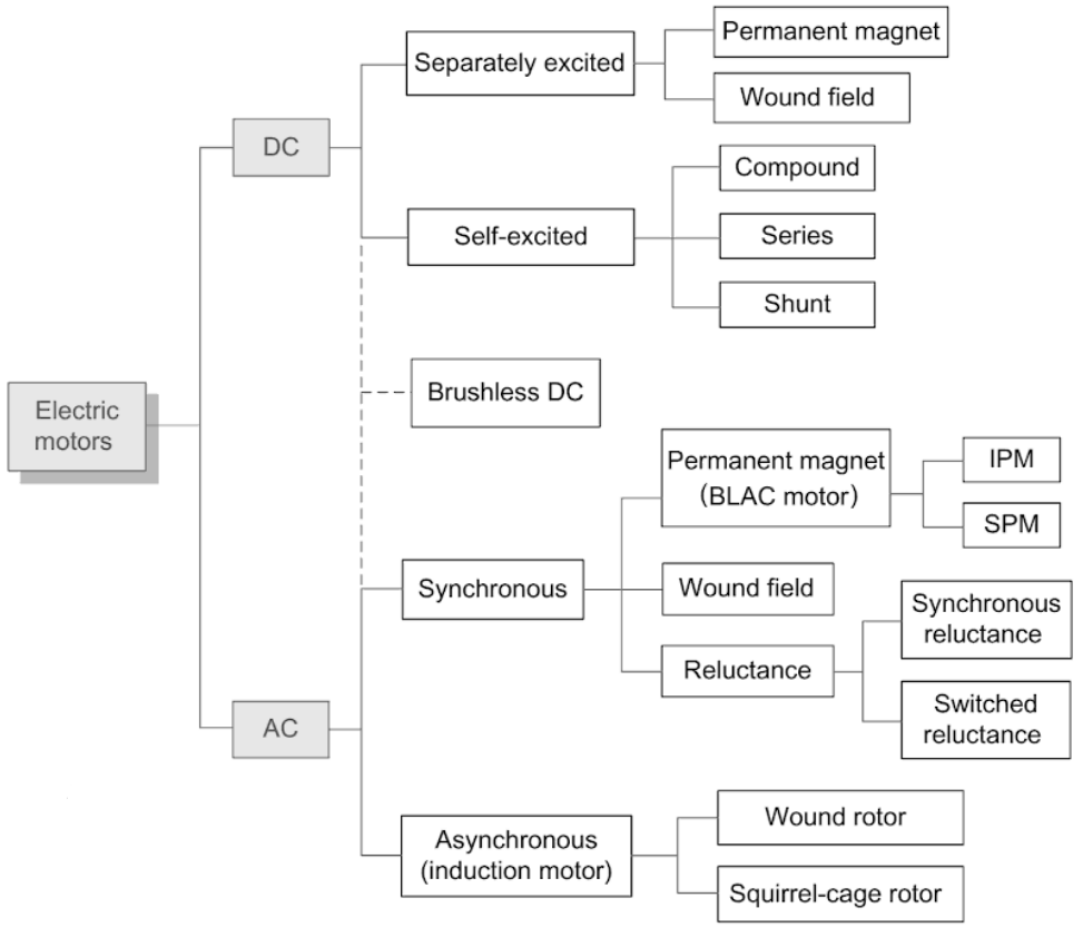


Figure 1.25: Electric Motor Classification [66]

Electric motors are mainly composed of stationary and rotary parts, which are named as stator and rotor, respectively. Winding current flowing through iron core slots creates magnetic flux, which leads to electromagnetic interactions, and thus forces are arisen. Magnetic field is created by the aid of permanent magnets in certain motor types. Fundamental motor parts are illustrated graphically in Figure 1.26 [66].

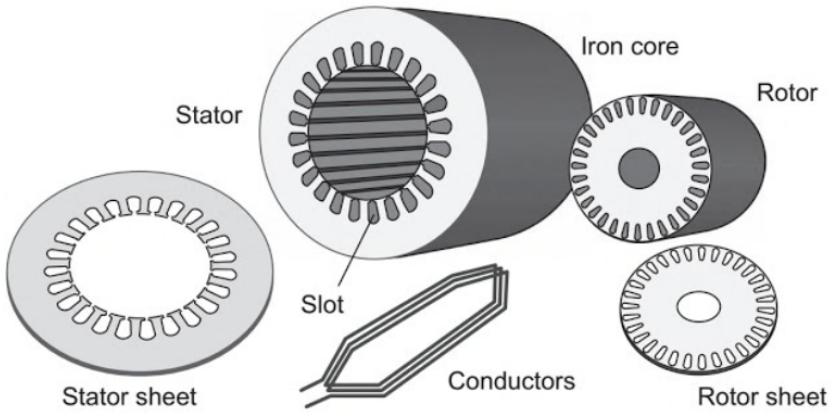
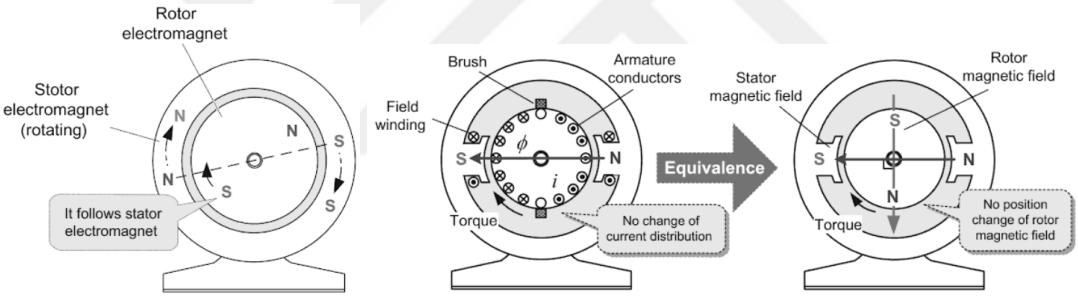


Figure 1.26: Electric Motor Components [66]

Interaction of two stationary magnetic fields, one of which is produced by field winding or permanent magnet in stator, and the other in rotor is originated from current carrying conductors, rotates DC motors. In AC motors, both rotor and stator magnetic fields rotate at the same speed as if they stand relatively still [66].



(a) AC Motor (b) DC Motor

Figure 1.27: Motor Operating Principles [66]

Among all, as marked with dash line in Figure 1.25, brushless DC motors are not exactly fit in classification such that its formation is quite similar to permanent magnet synchronous AC motor while electrical characteristics is similar to DC motors. Brush is used to ensure electrical contact between static and rotary parts. Despite simple design and low cost, brush puts forward major drawbacks such as noise, decreased life time due to wear and low efficiency, which is undesirable in mission critical applications [66]. Thereby brushless DC motors, particularly direct drive, have become one of the most deployed drive mean in defense and aerospace applications [67].

Having ideal form factor and eliminating error sources such as backlash, ripples, and low frequency resonant peaks (gear-inherent) could be added to the factors making brushless direct drive torque motors preferable in stabilization and pointing. Generally, geared drives are used when high torque is required without performance expectation such as outer gimbal of nested gimbal configuration. For inner gimbal, agile components such as limited angle torque motors, rotary voice coil, and piezo actuators are prominent candidates [68]. Regardless of area of utilization, all drive means with different complexity levels require power modulator, supply, and control unit along with motor as illustrated in Figure 1.28 [69]. Above-mentioned brush in conjuction with commutator split-ring fulfills commutation mechanically such that as rotor turns synchronously switches, i.e., commutates winding currents in order to keep torque continuity up for brush type DC motors [70]. Brushless DC motors require elaborate electronic commutation with the hall sensors or encoder feedback [67].

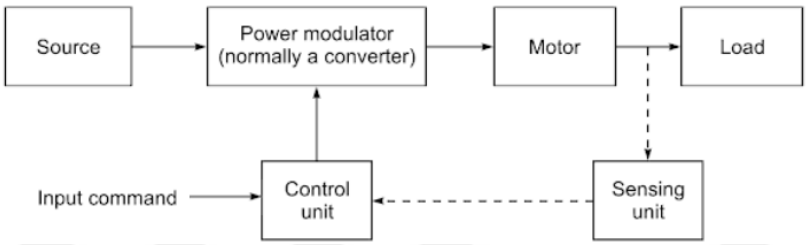


Figure 1.28: Electrical Drive Block Diagram [69]

Availability of thyristor by the late 1950s, which is a four-layered, three terminal semiconductor device and has controlled current flow between two electrodes by the third, was followed by development of superior semiconductor devices such as Metal-Oxide-Semiconductor Field-Effect Transistor (MOSFET), which has the ability to change conductivity based on applied voltage level for switching or amplifying signals and Insulated Gate Bipolar Transistor (IGBT), which is high power rating version of MOSFET with high switching speed and low conductance loss; thus, a major breakthrough is achieved on power electronics [69]. Using these semiconductor components in circuitry, converter, variable impedance, and switching power modulation functionalities are implemented. One or three-phase AC input rectification to DC with self commuted devices, e.g., IGBTs are exemplary of AC to DC conversion with voltage and current output operating modes as one or two quadrant [71].

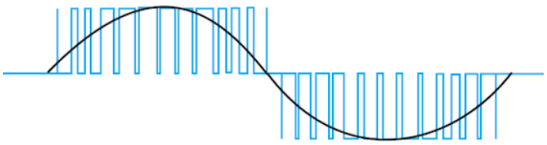


Figure 1.29: PWM Output Waveform [72]

Among the families of power modulators, Pulse-Width Modulation (PWM) inverters offers ability of DC voltage pulse width modification in proportional to control input and simulates sinusoidal voltage output with variable duty-cycle pulses as shown in Figure 1.29 [71]. Low-speed torque pulse elimination by virtue of negligible low-order harmonics make PWM drives ideal solution for a broad speed range. Other advantages of PWM drives is low switching loss and nearly 98% power efficiency, which is highly dependent on switching frequency. A few hundred hertz of switching frequency is barely achieved via thyristor based design, whereas IGBT circuity (Figure 1.30) increases switching capacity to range of 1-40 kHz. It is elevated even higher order of multiple MHz by MOSFET deployment [73].

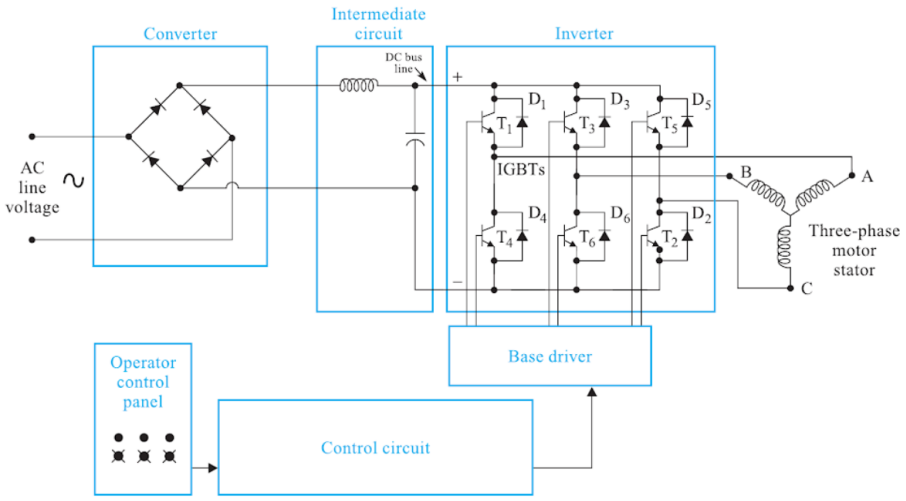


Figure 1.30: PWM Drive Circuitry [72]

Directly or by converting to DC, power is supplied via AC sources for most drives. Under 1 kV, three phase (3ϕ) and single phase (1ϕ) AC mains electricity supplies vary between 50/60 Hz and 380/220-400/230 V in the World. 1ϕ sources feed low power drives, and 3ϕ supplies facilitate running of high power loads. Portable systems are powered by DC batteries with 6 V, 12 V, 28 V etc. ratings [71]. Nonlinear circuitry dynamics' resultant harmonics and electromagnetic interference (EMI), which stem from sensitive data and measuring circuits interference through unintended coupling path, are supply-based detrimental factors on drive operation [74].

Power modulator control is fulfilled by control unit. The control unit may be composed of gate drivers formed by transistors, and linear and digital integrated circuits. Microprocessors are preferred when more complicated control actions are implemented [71]. To exemplify, as presented in Figure 1.30, each IGBT pair of 3ϕ bridge structure is responsible for $120°$-angled phase switch of motor, and generating PWM pulses, inverter is commuted by control unit. Motor commutation algorithms are summarized in Figure 1.31. Trapezoidal commutation is the simplest among its cluster, however, susceptible to low velocity torque ripples, whereas sinusoidal control ensures smooth operation. Vector control, calculating voltage and current vectors based on motor current feedback, provides high efficiency and precise dynamic control [75].

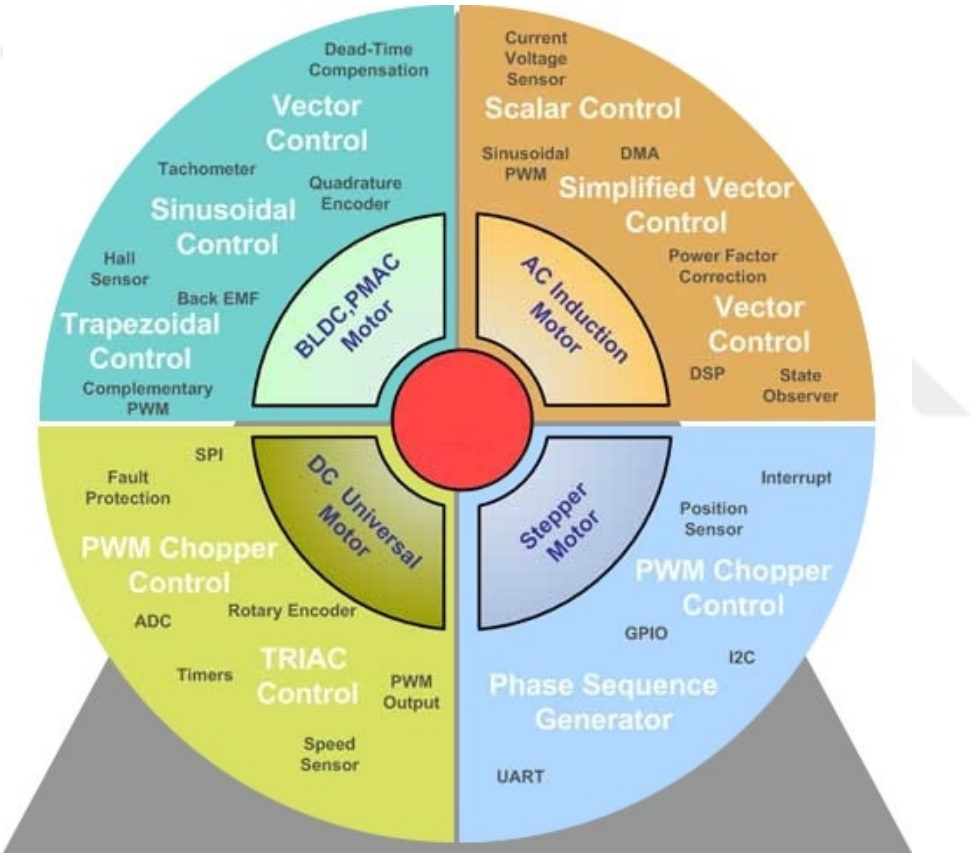


Figure 1.31: Motor Commutation Algorithms [76]

The control unit is also required to operate contactors for interchanging motor lines and reversing motor direction. In order to avoid undesirable states during motion reversal, including short circuit and simultaneous contactor energization, mechanical, push-button (electrical), and auxiliary interlocking mechanisms are featured [77].

Communicating with sensing unit and acquiring input commands are the other critical control unit functionalities. Analog reference input entails conversion, which is restricted by analog-to-digital converter (ADC) resolution and poses quantization errors. Moreover, analog signals are more susceptible to noise. Special precautions have to be taken for isolation such as differential circuitry and screened cable (especially as receiver and sender become farther). Based on IEC (International Electrotechnical Commission) 61131-2 standard, properly isolated simple digital interfaces could be used in direct I/O connection to programmable logic controller (PLC) or mission computer etc. mainframe for conveying on the order of 67 µs fast and high priority single bit messages, e.g., Inhibit/Enable motion, Safety Torque Off (STO). Sending larger size messages such as encoder position reading, mode of operation, commanded torque etc. one by one or completely, serial digital interfaces as serial communication or fieldbus systems are appropriate choices. Today, as the controllers are digitalized, communication protocols gain importance. Furthermore, in modern motor controllers, velocity and position loop implementation on PC software makes the significance of digital interfaces more apparent. Internationally agreed Open Systems Interconnection (OSI) Reference Model is used to relate the features and design elements of communication networks based on seven layers, namely physical, data link, network (so far three of which are media layers and developed for industrial utilization), transport, session, presentation, application from button to top. Concerned with raw bit-wise transfer, physical layer is comprised of palpable components such as wiring, connectors, and interface circuitry. Serial ports, available in some PCs, support RS-232 data terminal equipment (DTE) to data communication equipment (DCE) connection standard. Single-ended design brings high noise susceptibility and short transmission distance. In addition to these limitations, allowing data rates just up to 20 kbps causes RS-232 to never be used as main communication mean, just offered as auxiliary port in modern drives. Differential signaling has solved most of the RS-232 inherent problems; thus, RS-422/RS-485 standards have unveiled. In even high-end applications, RS-422 output gyros are reliably used thanks to high data rates up to 10 Mbps and long distance links. In full or half duplex arrangement, RS-485 allows data transfer among multiple units over single pair of wire [78]. Bitstream sent on interface circuits has to be encoded, and non-return-to-zero (NRZ), NRZ-Inverted and succeeding Manchester are popular encoding mechanisms [74].

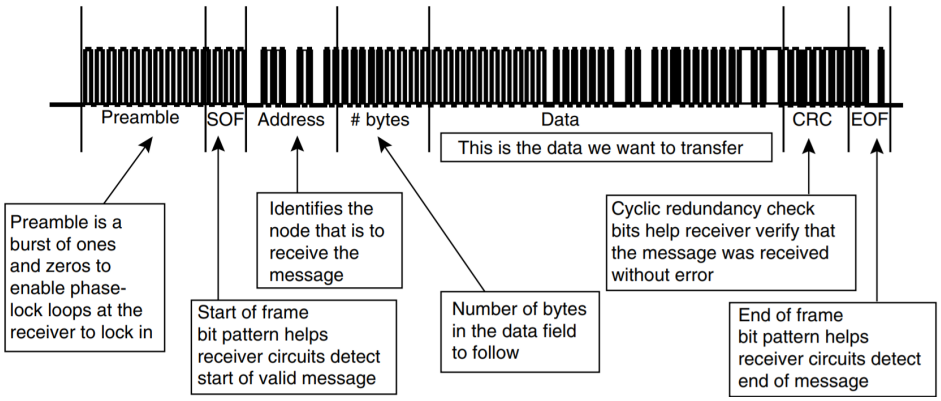


Figure 1.32: A Data Link Layer Frame Example [74]

Encapsulated digital information into message frames, which is exemplified and detailed in Figure 1.32, are reliably transferred under Data Link Layer responsibility. To fulfill its tasks, several affairs are addressed such as data routing, identification, arbitration, error handling etc. Wasting communication effort and considerable bandwidth, data routing is carried out in source-destination network by all nodes' receiving the same message on a one-on-one basis, whereas with producer-costumer network all nodes simultaneously access the same data. Identification is performed via addressing. Another affair is media access control in a shared medium, defining agreement mechanisms on which node use the bus, i.e., arbitration. Controller Area Network (CAN) bus is a communication system, which successfully operates producer–consumer model up to 2047 data objects, is extensively used in automotive, and implements bitwise arbitration based on message priority. Along with CAN bus, Profibus-DP, DeviceNet and Modbus are also popular industrial device-level Fieldbus standards. With the advent of low-cost IP-ready hardware and several Ethernet software layers' upgrades, Ethernet-based Fieldbuses were born and are growing at a fast pace to dominate industrial networking technology in near future, according to industry needs such as deterministic performance and cost-effectiveness. Designed for Information Technology (IT), Ethernet did not meet the real-time operation need of motion control until Modbus TCP/IP development in 1999, which is followed by PROFINET and EtherCAT. Nowadays Ethernet for Control Automation Technology (EtherCAT) interface is offered by most of the top motion controller producers such as Elmo, Kollmorgen and Copley. EtherCAT is originally developed by Beckhoff GmbH and now developments are maintained by EtherCAT Technology Group (ETG) [74].

Along with topological flexibility and synchronization easiness, unique on the fly processing property of EtherCAT enables high speed and efficient operation. Short cycle times of around 50 µs and communication jitter lower than 1 µs make EtherCAT preferred for precision, process and repeating accuracy requiring applications [79]. In addition to communication performance, there are variety of factors effecting drive and motor preference ranging from steady state and transient operation, source requirements to maintenance and reliability needs, space and weight restrictions [71].

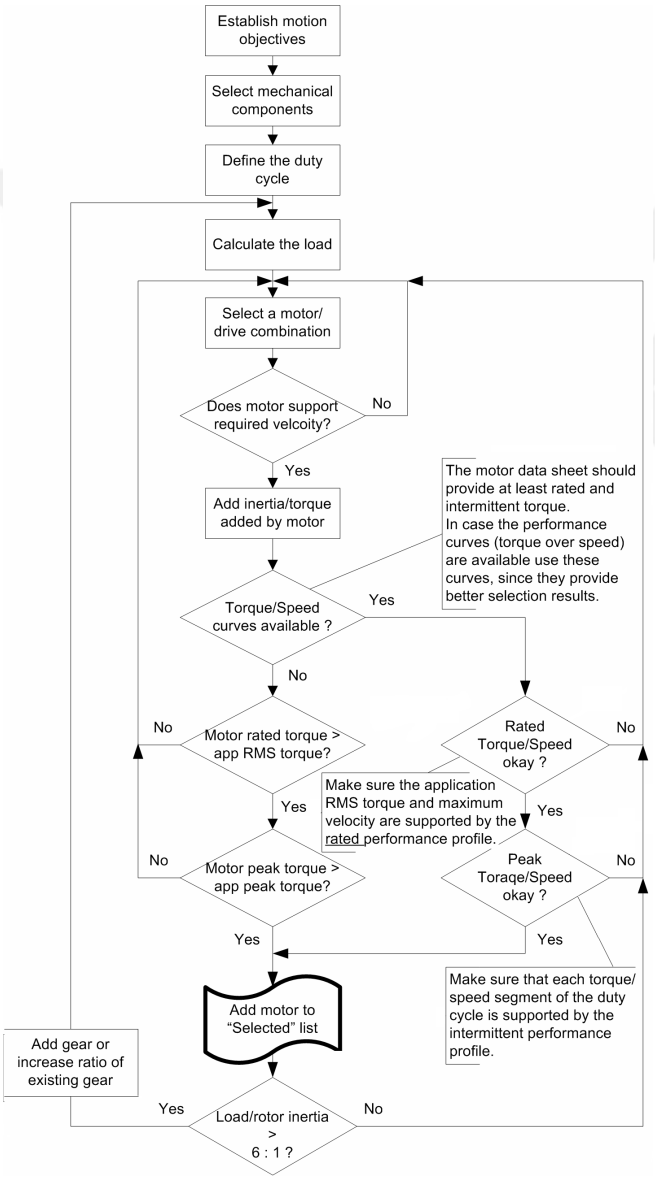


Figure 1.33: Motor Sizing & Selection Process [80]

The motor sizing and selection process involves establishment of motion objectives, mechanical component selection, load (duty) cycle definition, load calculation, and motor selection steps as flow-charted in Figure 1.33. Putting forward the required positioning, tracking and stabilization accuracy, repeatability parameters, defining operational conditions, disturbance profiles etc. main motion objectives are set. Hence, into mechanical component selection stage is moved. Questions such as "Are standard components adequate or special designs required?", "Can requested accuracy levels be achieved with belt drive or is direct drive imperative?", "Are brake and mechanical limits supposed to be integrated?" are discoursed and the appropriate action is taken [80].

After high level design review, duty cycle and load calculation steps are attained. Based on the application, acceleration and deceleration profile takes numerous forms such as triangular and trapezoidal. Owing to exertion of all available torque as theoretically the fastest way of point to point motion, triangular profile is comprised of acceleration and immediate deceleration after reaching maximum velocity, whereas trapezoidal profile contains constant pace movement, i.e., slew rate for a certain period of time between acceleration and deceleration [80][81]. To illustrate, an envisaged system is based on scenario such that in a naval platform, EO sight is required to engage two distinct targets 180°apart in 3 seconds of short time and track during 6 seconds with the lowest possible jitter in order to neutralize successfully. Required motion profile in this scenario includes high acceleration pointing, subsequently nearly constant velocity tracking, and eventually high deceleration to head reverse direction, put it differently, almost trapezoidal profile. Under ideal circumstances for theoretically minimum cycle time, acceleration (α) peak of triangular profile is kinematically calculated via rearrangement of $\theta = \frac{1}{4}\alpha t_{total}^2$ where displacement (θ) is half cycle and t_{total} total period of motion. More complex motion profiles necessitate more elaborate calculations. As the shaper of intermittent operation regime, peak acceleration values are linked to inertial torque by the dynamical equation of $\alpha = \frac{4\alpha}{t_{total}^2} = \frac{T_i}{J}$, and total torque budget $\sum \frac{T}{J}$ via Equation 1.3 where T_m is motor , T_d is disturbance , and T_n is noise induced torques, normalized by equivalent inertia term J division [81].

$$\frac{T_m}{J} = \sum \frac{T}{J} = \frac{T_i}{J} + \sum \frac{T_d}{J} + \sum \frac{T_n}{J} \tag{1.3}$$

Commonly encountered disturbance torques are friction, unbalance, kinematic coupling, aerodynamics torques, spring torques, product of inertia, and onboard shaking forces. Accompanying unbalance, structural flexibility originated aniso-elastic torques are also disturbance component. In closed loop operation, to compensate motor cogging and erroneous sensor readings, e.g., drift or high-freq noise, it is possible to spend a significant torque budget portion such that sinusoidal noise having 1 μrad amplitude and 500 Hz frequency corresponds to 10 rad/sec^2 of acceleration content. All mentioned disturbance and noise-induced torque components are summarized in Figure 1.34. Taking them into account, even if it is approximately, might prevent oversizing, which is ended up with bulky design, or disastrous undersizing [81].

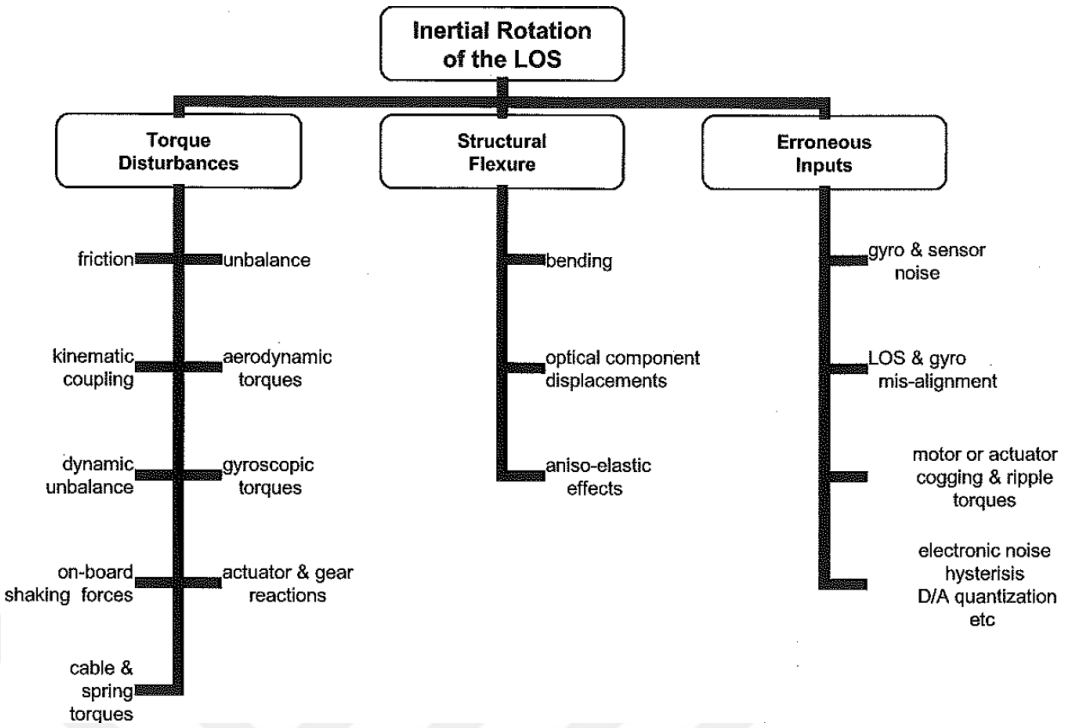


Figure 1.34: Disturbance Sources [81]

Bearings, seals, slip-rings, and motor brushes create friction. Frictional behavior is strongly dependent on temperature, geometric tolerancing, and vibration content. Especially at low speed operation, friction may cause steady-state errors and stick-slip oscillations. In order to prevent a vast portion of total torque budget to be spent by friction, necessary precautions such as fine tolerancing and precision machining of moving parts, operational environment conditioning and low friction component selection are taken in design phase. Using brushless motor and teflon O-ring along with angular contact ball bearings instead of cross-roller bearings, if the trade-off between rigidity and friction is acceptable, or non-contact ones, e.g., air and magnetic bearings exemplify low friction component selection. Moreover, balancing axes, i.e., shifting center of gravity (CoG) to rotation centers decreases unbalance percentage in disturbance torque budget. Since balancing via counterbalances increases total weight and inertia, bearing and motor capacities are required to be monitored throughout the design. In conjunction with symmetrically elastic structure, balancing reduces anisoelastic torques too. Symmetrical form not only elasticity-wise but also geometrical basis, aerodynamically optimized silhouette, and proper cable and hose routing weaken dynamic unbalance, aerodynamic torques and spring effects, respectively [68].

Eventually, reviewed motor technologies suitable for application, gathered data about available disturbance torques, and calculated load inertia from computer aided design (CAD) model, motor selection phase is reached. Basic selection criteria are based on rated and intermittent torque, load-rotor inertia ratio, and rated speed as most of the motor catalogs conform. Rated speed and torque represents root mean square (RMS) values over duty cycle, and for gear or belt driven axes, required dynamical and kinematic conversions are made beforehand [80]. In practice, because of creating lost motion due to backlash, bringing additional friction and causing transmission error, conventional geared drives are less preferable in precision applications. With anti-backlash gears, several servo techniques employing dual transducers, special gear meshes such as harmonics drive or worm and bevel gears combination, however, higher performances could be achieved. Eliminated backlash and even lowered transmission error with steel ones, noteworthy performance levels are also reached by belt drives [81]. In spite of specified merits of gear and belt, direct drives generally surpasses if considering precision.

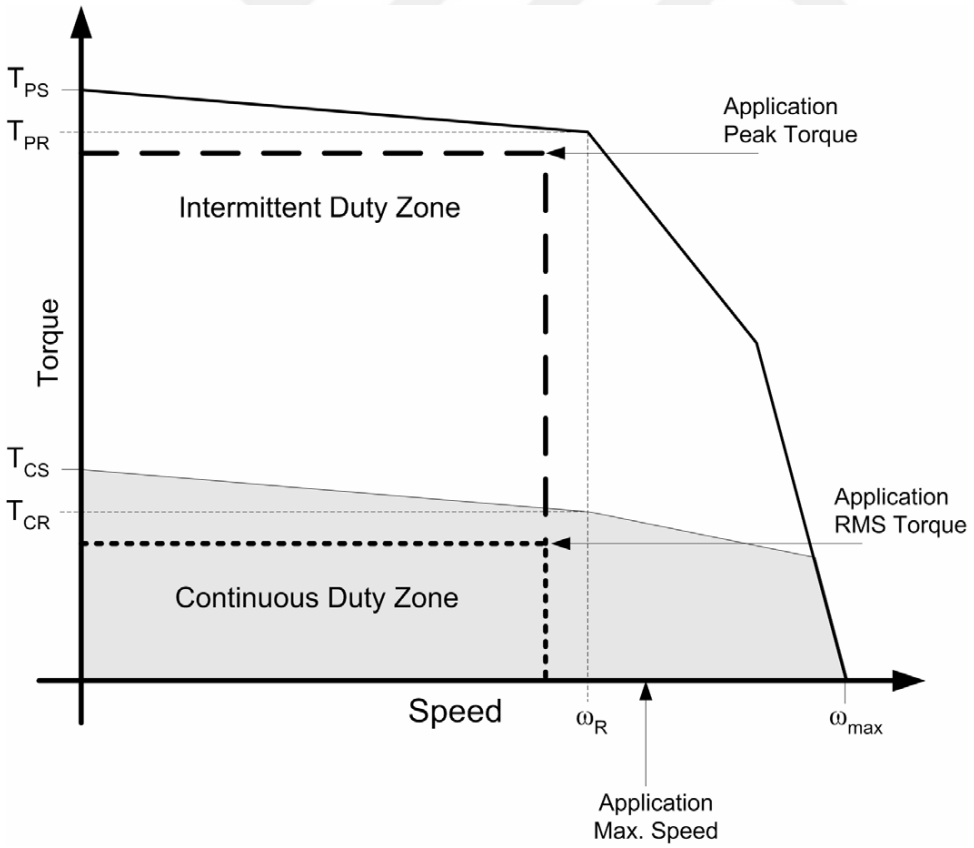


Figure 1.35: Application Operation Points on Motor Performance Graph [80]

Gear trains are used in some practices to match rotor and load inertia. According to Bosch Rexroth, load with twofold inertia of rotor is good for quick positioning applications, with five-fold moderate positioning performance is achieved, and with ten-fold servo loop tunable limit value is exceeded. Mismatched load and rotor inertia could also cause oscillations, motor overheating, decreased cost effectiveness regarding to inertia ratio [80]. In spite of this, inertia ratio matching with application requirements is the key to achieve desired performance and coupling selection along with motor structure turn into important parameters. Removing mechanical components between motor and load, disposing inertia matching criticality, compactness, and rigidity make frameless motors advantageous and extensively used [82].

Assuring that load and motor rotor inertia matches as well as operational points, which corresponds to rated speed-rated torque and peak speed-peak torque are mapped onto intermittent and continuous duty zones of performance graph, respectively, motor selection is completed. Performance curves are issued by motor suppliers or derived from datasheets. Marked peak and RMS operation points of an example application, a typical torque vs. speed performance curve is shown in Figure 1.35 [80].

Together with appropriate motor selection, appropriate feedback sensor selection is another important factor on actuation system performance. In pointing, tracking, and stabilization applications gyro, tachometer, and rotary position transducer feedback sources measure inertial rate, relative velocity and angular position, respectively [67]. Accelerometers are utilized in acceleration-based feedforward compensation.

Gyroscopes can be split into two groups depending on the physical principles of their construction namely mechanical gyros and quantum (wave) gyros as presented with sub-classes in Figure 1.36 [83]. Gyro dynamics and noise characteristics play a crucial role on overall system performance and control bandwidth. For this reason gyros, their selection, and integration are of paramount importance. Important gyro selection parameters are bandwidth, output rate, processing delay, high and low frequency noise, maximum rates, scale factor, cross coupling, size, cost, and reliability [68]. Low frequency noise is characterized with bias offset and instability. High frequency white noise content of gyro output is described by Angle Random Walk (ARW). Both high and low frequency noise components are vibration and shock sensitive [84].

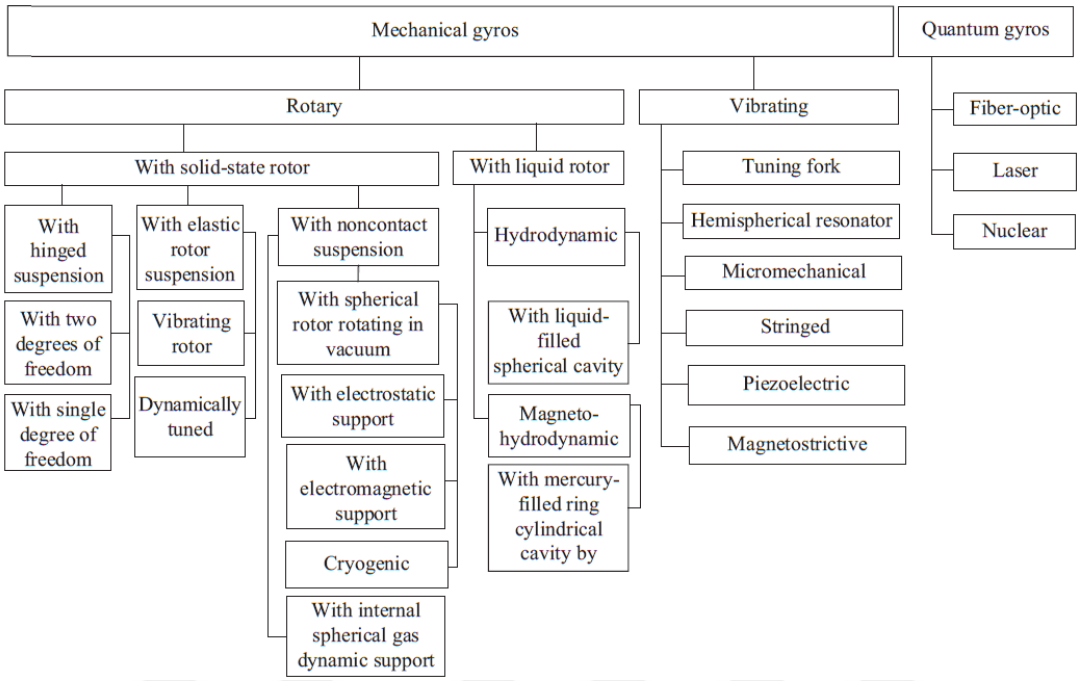


Figure 1.36: Gyroscope Classification [83]

Accepted by the Institute of Electrical and Electronics Engineers (IEEE) as gyro specifications standard by virtue of computational and interpretation simplicity along with applicability to any signal, The Allan Variance (AVAR) time domain analysis technique is originally proposed for estimating clock and oscillator stability against different noise processes. Averaging time function of (τ) RMS noise components $\sigma(\tau)$ are appeared on AVAR plot with distinguishable slopes as exemplified in Figure 1.37 [85]. Systematic errors such as temperature and vibration are not directly reflected on AVAR plot; alter noise components with respect to their sensitivity instead [84].

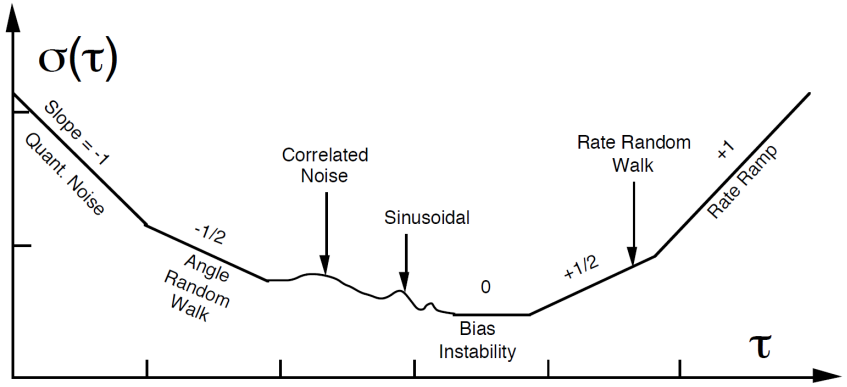


Figure 1.37: Logarithmic Allan Variance Plot [84]

As the lowest flat region of AVAR curve, bias instability indicates the fluctuation trend of bias offset from its mean. For long runs, bias instability causes larger LoS deviations; thus, poor performance particularly in case of tracker unavailability. Several gyro technologies' bias instability values and application requirements are represented in Figure 1.38. Touching upon high frequency noise component in Allan Variance curve, active elements is fiber optic gyroscope (FOG) laser and photo diodes as well as MEMS gyro silicon or quartz crystal based vibrating beam and detection circuitry create noise, which substantially dominate the (-½) slope regime within short averaging times [84].

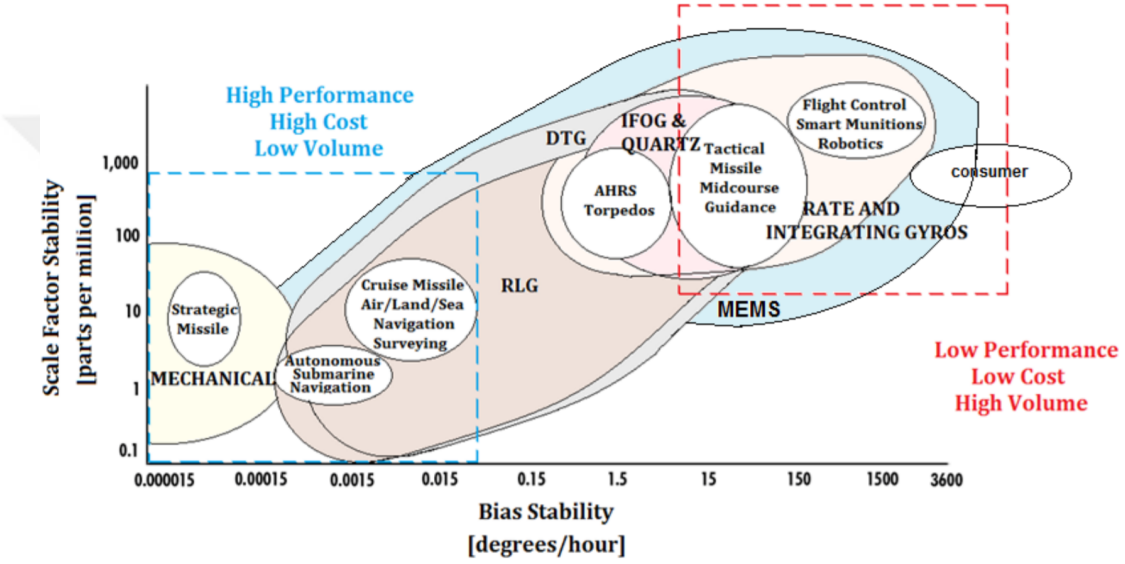


Figure 1.38: Bias Stability Application Requirements and Gyro Specifications[86]

Detailed with tree chart in Figure 1.39, above-mentioned FOG is placed in a subgroup of optical gyroscopes in which propagating optical beams in precisely opposite directions is used for rotation measurement interferometrically by exploiting the Sagnac effect. FOG functions based on phase difference measurements of beams propagating through fiber in two directions. Another subgroup of optical gyros, Ring Laser Gyros (RLG) vary from FOGs such that beam is propagating in cavity. RLGs offer high precision, however, the resonant cavity is expensive. If ultra-high precision is demanded, mechanical gyros gets ahead of RLG. Built based on conservation of angular momentum principle, mechanical gyro fundamental component spinning mass experiences precession phenomenon in reaction to rotation, and proportional to external torque, angular rotation is derived displacement or rate wise since the 19th century [86].

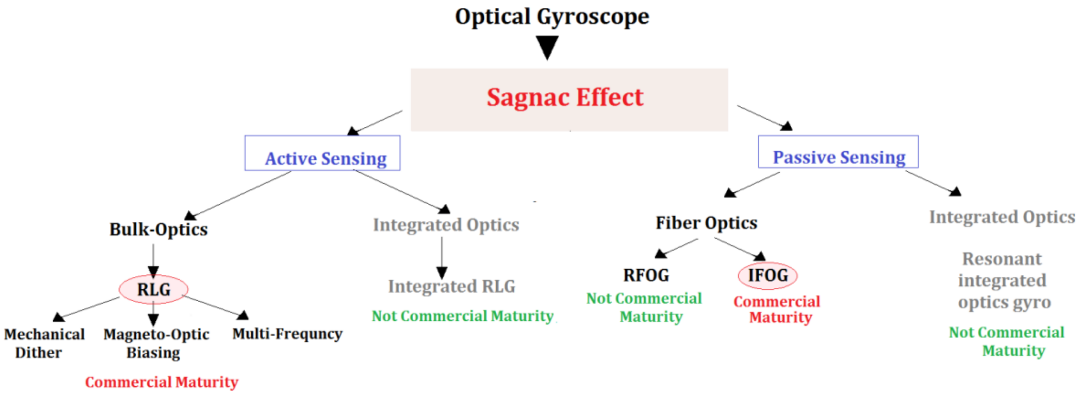


Figure 1.39: Optical Gyro Classification [86]

Besides utilizing precession phenomena, Coriolis effect is exploited for mechanical transduction of inertial angular rate, which is underlying MEMS vibratory gyroscope operating principle [86]. High non-operational shock endurance, compact form along with lowest power consumption and cost make MEMS technology ideal among all gyroscopes for up to industrial grade applications. Nevertheless, high ARW and thermal sensitivity are considered as weaknesses in stabilization and positioning which entail within 0.1–300°/h band bias stability [84][86]. Yet, still MEMS gyros are used in tactical applications requiring around 1-30°/h bias stability such as rockets guidance and smart munitions. Analog Devices, Inc. with MEMS gyro, KVH Industries, Inc. with FOG products are examples to gyroscope market prominent players [86].

Tachometers are angular velocity measurement devices as well as gyroscopes. The difference is that gyroscopes measure inertially, whereas tachometers transduce rotational velocity relative to base frame. Digital tachometers function based on optical, inductive and magnetic sensing. Optical tachometers, yielding best accuracy in its class, operate based on light pulse, through or reflected from rotating disc, counting during unit time for calculating instantaneous velocity. For inductive and magnetostrictive tachometers, similar configurations are employed, governed by number of marks around rotating disc circumference, whereas analog tachometer structure is more identical to power generator in AC and DC types with full-scale reading inaccuracies of 1% and 0.05%, respectively. Measurement limit, on the order of 6000 rpm for AC and DC tachometers, is elevated up to 15000 rpm in eddy-current tachometer, which utilizes induced eddy currents as magnet carrying spindle rotates [87].

Time integral of rotational velocity, relative to base frame, yields rotational displacement. Generating angular position data, specialized electro-mechanical devices such as encoders, resolvers, potentiometers, and rotary variable transformers (RVDT) are used [67]. Encoders could be absolute or incremental and functioning based on optical and magnetic sensing, whose working principles are illustrated in Figure 1.40.

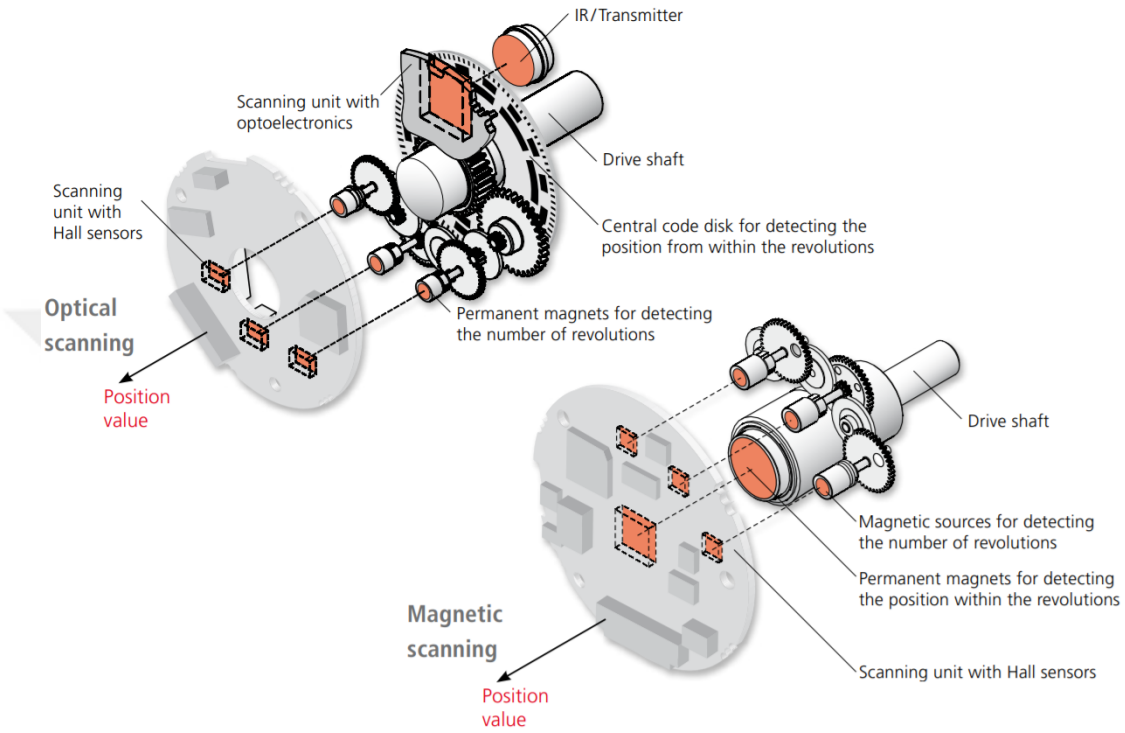
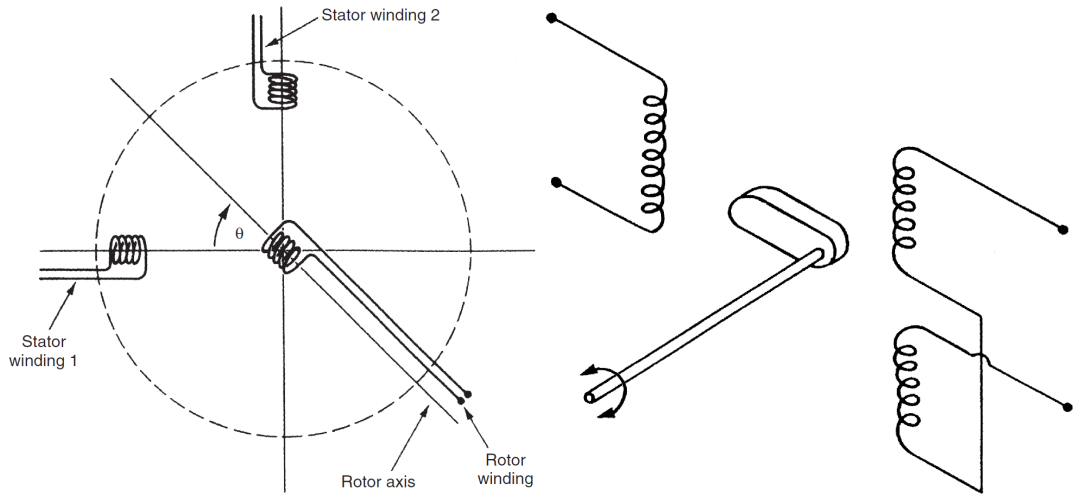


Figure 1.40: Working Principles of Optical and Magnetic Encoder [88]

Fundamentally, incremental encoders consist of rotating disc between transmitter and receiver. Optical encoder rotating disc is coded by window arrangements in order to transmit light beam on photodetector in a controlled manner. In magnetic encoder, rotating disc is a ferrous gear. As disc rotates, magnetic flux, emitted by permanent magnet, changes and is sensed by pick-up circuit. Most commonly, with two output channels (A and B), emerged optical and magnetic pulse count is used as angular position measure. Positioned 90° out of phase, two code tracks with sectors in quadrature encoder is also utilized for direction of rotation sensing. Distinctively, absolute encoders have more complex disc patterns with extra outer track, i.e., antiambiguity track or special coding such as the Gray code for increased resolution, absolute position reporting, and overcoming fabrication and alignment based errors [67][87].

Along with resolution, parameters such as accuracy, repeatability, form factor, and level of ruggedness are used in encoder specifications. Resolution values reach up to 1 in 20000 for incremental encoders (when inner tracks of windows is included) and even 1 in 10^6 for absolute encoders, whereas ranging 1° to 10-20 arc-seconds, resolvers fall behind. Performing reliable and frictionless operation, physical formation of resolvers is quite similar to small AC motors with 10-100 mm diameter. Resolvers acquire measurements in analog format as a product of 2-winding transformer action. The synchro shares the same structure and working principle with resolvers apart from having 3-winding configuration. Offering robustness under shock and disturbance, as high accuracy levels as digital encoders achieve, and as low errors as 1 arc-seconds, synchros are preferred particularly in military applications such as tactical gimbals. Also, resolvers and synchros have low temperature dependency when especially compared with potentiometers. Not requiring external excitation, potentiometers are absolute angular position measurement elements of typically low cost and accuracy applications. The measurement range of circular potentiometers depends on track formation such as full or part circle. When multi-turn operation is required, helical potentiometers are preferred, although they increase the cost due to structural and mechanical complexity. Mechanical details such as bore sizes, shaft tolerances, their concentricity, and bearing run-out are effective on measurement linearity. Moreover, wear of sliding surfaces limits lifetime. Rotary variable differential transformer (RVDT) exhibits no wear behavior by means of structure similar to 2-winding transformer which employs a cam type iron-core. Although RVDTs assure maintenance-less operation and harsh environment conformity, because of the difficulties on secondary windings symmetry establishment and iron-core machining, minimum accuracy of 1% is barely achieved for even 40° excursion. Schematic representations of resolver, potentiometer, and RVDT are shown in Figure 1.41 [67][87].

Compared with angular rate and position measurements, angular acceleration is not widely utilized in gimbal control systems. Only in high velocity aircraft and missile guidance, angular accelerometers are used in order to accomplish high agility by putting one time derivative order higher than angular velocity into loop. Sharing the same working principle with angular accelerometers, linear counterparts have larger area of usage ranging from unbalance feedforward control to vibration measurements.



(a) Resolver

(b) RVDT

(c) Circular Potentiometer

(d) Helical Potentiometer

Figure 1.41: Schematics of Several Angular Position Measurement Devices [87]

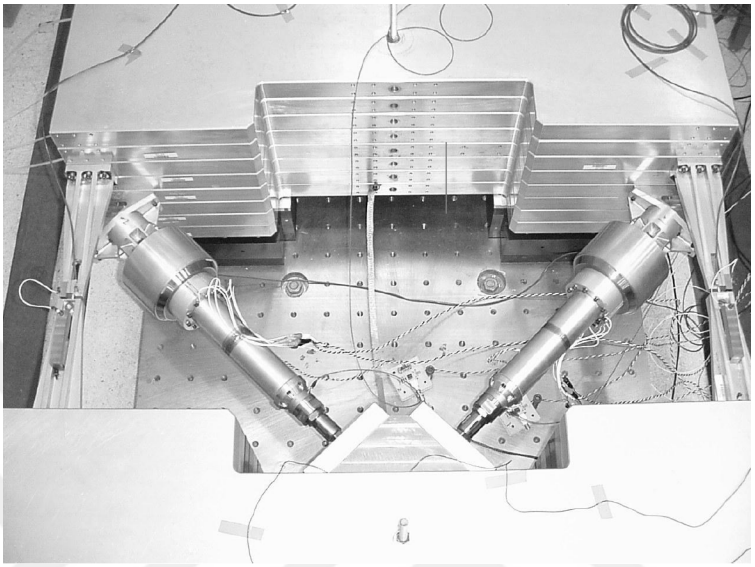
Fundamental formation of accelerometers is enclosed mass-spring-damper system. Exploiting spring/dashpot behavior of piezoelectric crystals, quite compact accelerometers are produced. Piezoelectric accelerometer measurement range varies from 0.03 g to 1000 g with typical resolution of 0.1% and inaccuracy of 1%, however, by its very nature, constant or slowly time-varying accelerations could not be sensed properly. Resistive potentiometer-based accelerometers are used for measuring slowly varying acceleration content instead. Mainly, for this class, acceleration data is inferred from mass displacement, which is read on potentiometer, and up to 50 g range along with resolution of 0.25% could be reached. Furthermore, cross-sensitivity, as an important characteristic defining sensitivity to perpendicular accelerations, is typically 1% [87].

As well as low cross-sensitivity, high sensitivity and linearity, good frequency response and temperature characteristics, and compactness are important merits such that from triad of compact and precise accelerometers along with triad of gyroscopes, inertial measurement unit (IMU), which is the core of inertial navigation system (INS), are developed. Additionally, acoustic and intrinsic noise, magnetic field, and vibration and shock levels are important factors on accelerometer performance [89].

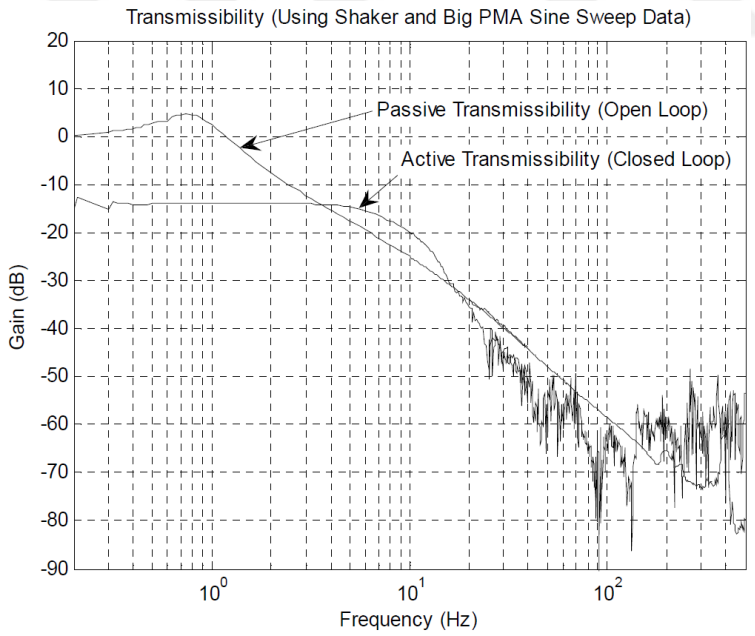
Vibration measurement is made not only in operational manner but also throughout design, analysis, and test phases. Balancing, shock testing, vibration monitoring, and modal analysis are some examples to areas of accelerometer utilization for electromechanical system development. Today, miniature Integrated Electronics Piezo-Electric (IEPE) accelerometers with Transducer Electronic Data Sheet (TEDS) are frequently used for experimental modal analysis (EMA) [89]. Herein, modal data is acquired by data logger upon exciting structure by impact hammer or shaker. Thus, frequency analyzer or vibration analysis software yield frequency response function (FRF), which contains modal parameters, i.e., natural frequencies, damping coefficients, and mode shapes. Building appropriate CAD model ahead of analysis along with ensuring good signal quality, optimum windowing, and punctual triggering constitute the basis for modal parameter identification and visualization. EMA has to match up with finite element analysis (FEA) in order to ensure that projected structural rigidity is attained [90]. Combined with optical coefficients, FEA might yield more realistic results. Structurally induced line of sight (SILOS) jitter could be much greater than rigid body vibrations, cause gyro or motor driver saturation and not be compensated by control system; thus, global and radical changes are required, particularly after all is assembled. For this reason, the importance of structural considerations could not be overlooked. Accordingly, design restrictions has to be taken into account as they are, e.g., specific stiffness is revised as elastic modulus to density cubed ratio in case application poses weight limit. Moreover, base motion along with self-excitation sources such as cyrogenic coolers has to be handled properly.

In order to assist disturbance handling by attenuating base vibration, passive, semi-active, or active isolators could be used. Isolator utilization brings along expanded volume, complicated boresight, and unintended servo interactions; hence, might cause worse dynamic response. Nevertheless, reduced weight, minimized high frequency

content, and lessened unbalance effects are attained [91]. New generation hybrid isolation systems offer both base disturbance rejection and assistance for payload pointing. Utilizing voice coils in conjunction with struts, far better suppression up to 16 dB at low frequencies, and approximately 50 nm RMS error pointing performance is achieved as presented with details in Figure 1.42 [92].



(a) Bipod Arrangement of IPS Struts



(b) IPS Active and Passive Transmissibility Comparison

Figure 1.42: Isolation, Pointing, and Suppression (IPS) System Details [92]

1.2.4 Control Strategies

Stabilization and control of gimbals have been studied and practiced extensively for many years. According the system operation modes, designing control system, which fulfills performance criteria and withstands disturbances, could be a challenging task. Based on powerful idea of feedback, classical and modern, i.e. state-space control techniques are broadly deployed in industrial and military fields such that more than 90% of controllers are in PID (Proportional+Derivative+Integral) form. Model predictive control (MPC), as an advanced control strategy, is typically takes supervisory position to PID controller and could yield major performance improvement in coordination required multi variable systems. Another advanced control method fuzzy logic is distinguished with easiness and enriched control law functionalities such as adding logic, spare input and nonlinear dynamics. As a consequence of linear characteristics, availability of severe nonlinear dynamics limits the performance of PID controller even if it is supported with gain scheduling [93]. Although during design phase required precautions, such as selecting high precision components and proper tolerancing, are taken, nonlinear terms, particularly friction and vibration, exist in some extent. Degree of their severity dictates the sophistication level of the controller, therefore, addition to MPC and fuzzy logic, advanced techniques such as optimal linear quadratic Gaussian (LQG) regulators, adaptive filters, state observers, and robust controllers are utilized. For instance, Kalman filter supported LQG is reported to increase stabilization performance of a gimbal when compared with PI controller with notch filters via rejecting hysteresis and stiction more effectively. Herein, the effectiveness of LQG algorithm is strongly dependent on plant model [94]. Principally, modeling is a critical step for control system analysis and design. Linear modeling include deriving differential equations, making linear approximations, taking the Laplace transforms, obtaining transfer functions (TFs), and drawing block diagrams or signal flow models. Based on the model and performance specifications control system is designed. Closed loop stability, disturbance rejection, bandwidth, speed of response, and robustness are some of performance indices. In order to assure required performance, controller parameters are chosen via root locus or open loop transfer function (OLTF) gain is manipulated via loop shaping. Lead and lag compensators, increasing the phase margin at crossover frequency and decreasing the

steady-state error, respectively, are major elements in compensator structure repertoire for loop shaping. Quantitative feedback theory (QFT) is a robust loop shaping technique, which takes plant loop gain variations within a specified frequency region into consideration and utilizes the Nichols chart (NC). On the other side, using a quadratic performance index, designing control system is converted into an optimization problem via LQ and LQG design methods. Their H_2 formulation allows frequency domain based design with frequency dependent weighting functions. H_∞ optimization minimizes the peak closed-loop transfer function magnitude with frequency response shaping in an effective manner and assuring robustness straightly against plant uncertainty. Extension of H_∞, μ-synthesis, accomplishing joint robustness and performance optimization, attempts to deal with structured uncertainty by reducing the peak value of the structured singular value [95]. Upon analytical continuous control system design and stability evaluation via criteria such as Routh-Hurwitz or Nyquist, controller is discretized with zero order hold (ZOH), backward differences (BD), Euler, and Tustin approximations in order to be implemented in digital motion controller. Feedback system stability do not degraded by feedforward path, which anyway could be designed independently, moreover, general performance could be increased significantly. Even a reduced-order, single-state disturbance observer, which is applied to inertially stabilized LoS control application, is reported to improve disturbance rejection capability by a factor of more than 3. Furthermore, tolerance to plant parameter variations within a considerable extent and implementation easiness, such that a couple of code segments are added in control system source code, are strengths, whereas it could make gyro noise coupling more severe and its efficiency is highly dependent on disturbance frequency content [96]. As well as feedforward controllers, prefilters are located outside of feedback loop and have numerous advantages ranging from steady-state reduction to overshoot elimination, when properly designed. Another overshoot attenuation element is anti-windup filters. Due to integral term, a significant error could be accumulated in case of large setpoint variation or input saturation. Even if the error decreases, the residual large integrator output detains total controller action to return expected response. To prevent this phenomenon and assure compensator stability, several anti-windup algorithms are available such as bounding integrator output within pre-determined limits or disabling integrator functionality until controlled variable falls within controllable region.

1.3 Objective of the Thesis

Focusing a laser beam on a point over distances is a tough problem. What harder is keeping the laser spot on the same point under motion. The principle purpose of this thesis study is to develop a 4-Axes EOD for high power laser application in order to fulfill this functionality. Herein, the first milestone is conducting an elaborative literature research. Understanding fundamentals of lasers and optics along with their correlations between EOD design and performance, and reviewing all trends in actuation systems and subsystems such as gyroscopes, piezo-actuators, as well as control architectures are the key roadmap to get first milestone. Then, in the light of gained knowledge and past experiences, designing mechanics, sizing actuators, and selecting sensors are the steps to be taken for meeting project performance objectives. Upon EOD assembly, system identification phase proceeds with the main aims of diagnosing problems beforehand and acquainting with dynamic behaviors. Retrieved data from identified system feeds detailed simulation model, which is established for creating control architecture, foreseeing the performance against several threat scenarios as well as angles, and analyzing impacts of subsystem dynamics on overall performance. Ultimate control goal is conveying system to desired tracking accuracy levels for both reality and simulation. On the road to ultimate goal, stability analysis and response assessment play fundamental roles. Finally, performing target tracking tests on the final system and simulations on the model, thus, verifying both is the goal line.

1.4 The Outline of the Thesis

This chapter begins with the motivation behind HEL weapons and related design steps along with challenges. Afterward, an elaborative literature research takes place including lasers, optical train, actuation systems, and control strategies sub topics. Within this framework, laser fundamentals, characteristic properties, and applications are reviewed, at first. High-energy laser dynamics and tactical history are, distinctively, covered. Following, upon the literature of components involved in formation of optical trains such as wavefront sensors, telescopes, FSMs, DMs, and cameras, is touched. As one of the major disturbance sources, on atmospheric disturbance, its

modeling, and compensation, special attention is paid. Lastly, detailing the rest of atmospheric propagation effects, i.e., diffraction, scattering, and absorption, actuation systems subsection proceeds. Ranging from director system configurations, gimbal formations, electric motors along with their sizing and selection methodology, motion controller interfacing to even disturbance torque sources, precision sensors such as gyros encoders, a large variety of topics are dealt under actuation systems heading. Laying emphasis on control architecture and stability background, literature review section is finalized. Then, stating the objectives of thesis study and drawing a detailed outline, whole introduction chapter is concluded.

Second chapter covers the design process. Serving design approach at the beginning, to servomechanism component selection subsection is moved. Herein, system performance and functional requirements are considered separately from dynamic environment and design constraints. Subsequently, taking inertial, frictional, unbalance, and springness terms into account, a detailed torque analysis and resultant motor selection practice is reported. Motor selection is followed by selection of remaining servomechanism elements, i.e., FSM, gyro, and encoder, thus, component selection part is completed and on servomechanism design topic is passed. Defining subrequirements, structural analysis details are explained for both preliminary design and final payload. Finally, under servoelectronics design title, to motor driver and power supply selection analyses are covered.

Third chapter is divided into two main sections as system identification and modeling. System identification section begins with gimbal friction, unbalance, springness, and cogging test procedures along with the results. Afterwards, a wide coverage is given to gimbal axes dynamic response tests, their routine and outputs. Following gimbal, system identification process for FSM is presented under impedance and dynamic response tests titles. Upon concluding system identification section, explanations on data driven modeling studies starts with gimbal. Gimbal unbalance, springness, cogging, the LuGre friction, and elevation angle dependent plant dynamic response submodel details are explained. Later, review onto piezoelectric dynamics of FSM and its modeling technicalities are stated. With the modeling practices of camera and tracking algorithms, on rail and drone target sets, and atmospheric disturbances, this chapter is completed.

Chapter four is comprised of velocity, position, and coarse tracker controller designs. Deriving design requirements back from target maneuvers, PI velocity controllers were designed for both elevation and azimuth axes on bode plots, graphically. Elevation angle dependent stability and bandwidth persistency analyses were performed, and the results are tabulated. Owing to system type along with posed functional requirements, for cascaded position loops P control law was considered as enough, and design was carried based on step response, accordingly. Elevation angle dependent azimuth position controller performance along with each of axes hard limit to limit positioning and position profile tracking accuracy assessments were also conducted within the context of position controller design section. Different from position control, coarse track control necessitates PI law in order to yield zero steady-state error for constant velocity target motion. PI coarse tracker controllers were synthesized on bode plot, graphically, and elevation angle dependent stability was measured, as well. Coarse tracking system performance against on-Rail target and drone threat were evaluated via simulations and real-time tests. Convergence of the results, eventual requirement fulfillment, and the benefits of active tracker assistance were depicted, quantitatively. Lastly, atmospheric disturbance compensation was included as test data and simulation results. Disturbance model was observed to consistent with real-life atmospheric phenomena, and the first order content was removed as envisaged.

Lastly, in conclusions chapter all the project outcomes are summarized. Upon touching gained invaluable experiences such as a large scale multi axes EOD development, FSM application, and configuring concurrent tracking system, final chapter begins. After that, provided benefits of extensive literature research is highlighted and conclusions on identification phase proceeds. The coherence within each of gimbal and FSM axes' identification tests and their conformity to the design is expressed. Accumulated data via identification process is stated to take an important place on modeling success. From plant-wise to closed loop control system levels, simulation and test results are depicted to be convergent. Drone and on-rail target tracking accuracy levels are put forward to be better than required as both model outputs and real-time tests converge. Finally, praising requirement driven design's fruitage, future work projections are mentioned. In this context, naval platform integration and FSM replacement with a head-mirror are specified as the first steps that spring to mind.

CHAPTER 2

DESIGN

Stabilization, pointing and tracking system design process includes multidisciplinary engineering tasks. Major technologies involved are mechanism design, servoelectronics design, and servomechanism component selection. Mechanism design comprises selection of component, material, and manufacturing technique, gimbal design and measurement system deployment. Servoelectronics design deals with all electronic components, power amplifiers, signal conditioning, filters and compensators. As their combination, servomechanism design is, substantially, seizing and selection of actuators, transducers and others, such as sliprings and twistgaps. In order to fulfill all tasks, design teams are established, as their structure in illustrated in Figure 2.1. Moreover, design workflow is demonstrated with Figure 2.2 [68]. Within context of this chapter, design works, which was gotten involved in, would be addressed.

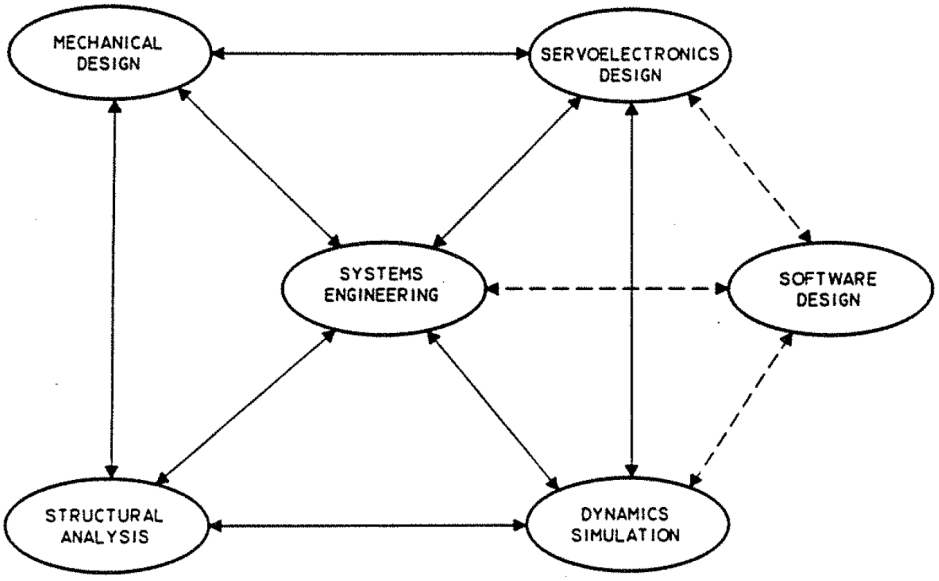


Figure 2.1: Design Team Structure [68]

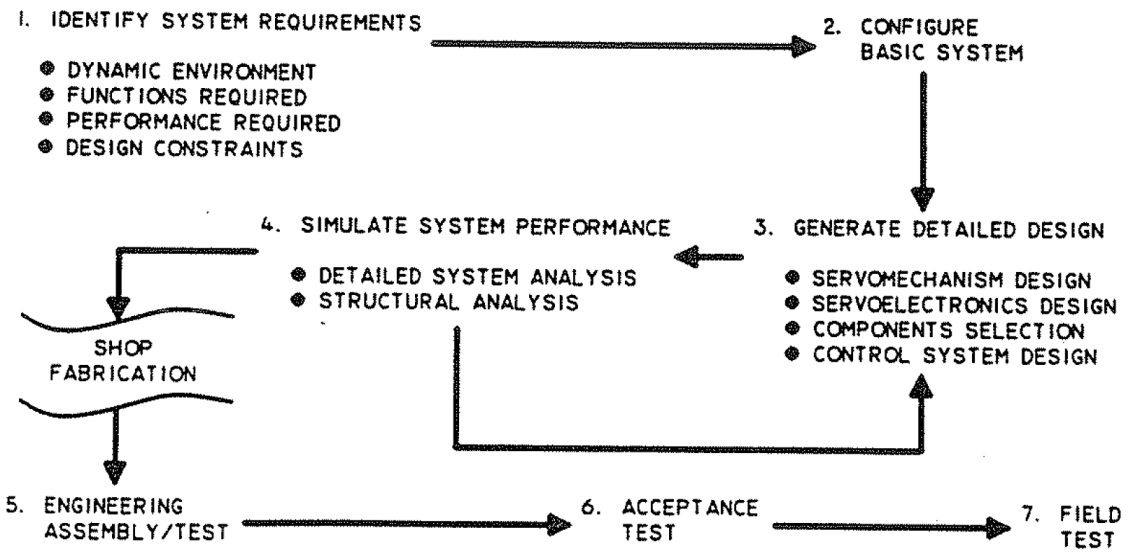


Figure 2.2: Design Process Flow Chart [68]

2.1 Servomechanism Component Selection

2.1.1 Motor Selection

System Requirements:

1. Performance and Functions Required (Within the frame of below listed requirements, motion profile, represented in Figure 2.3 is derived.)

   - Maximum Acceleration: 90 °/s^2
   - Maximum Velocity: 60 °/s
   - Suddenly moving 180°in azimuth axis, engaging a target moving, relatively, with a constant lateral velocity, and, subsequently, tracking at least 6 seconds with lowest possible jitter during high-power lasing.
   - Suddenly moving to azimuth home position, engaging a target moving, relatively, with a constant lateral velocity, and, subsequently, tracking at least 6 seconds with lowest possible jitter during high-power lasing.
   - Low-cogging operation
   - Natural convection cooling

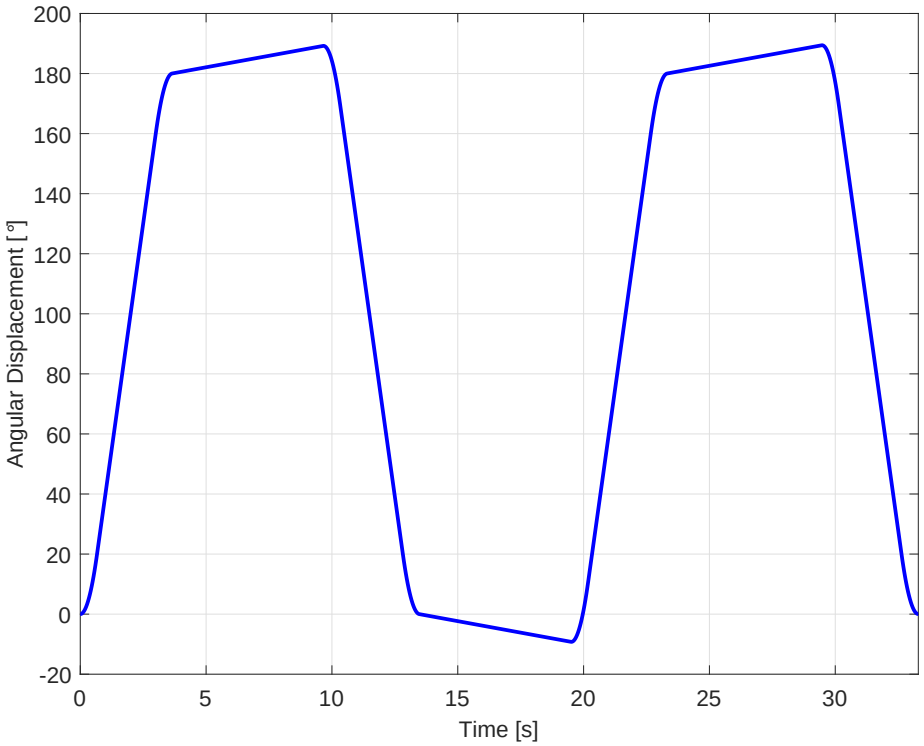


Figure 2.3: Azimuth Axis Performance and Functions Required Displacement Curve

2. Dynamic Environment and Design Constraints

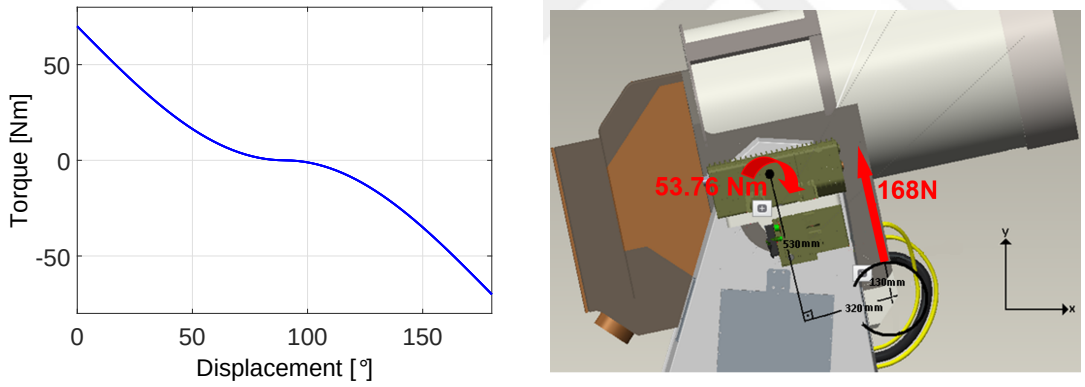
- **Mass Moment of Inertia:** From the latest version of CAD model, in which all payloads with mass properties are available, mass moment of inertiae are deduced as 194 kgm^2 and 640 kgm^2 for elevation and azimuth axes, respectively.

- **Friction Torque:** Experiences from past projects, equivalent torque table datasheets, information taken from bearing and seal manufacturers made friction torque assumption convergent to 100 Nm for elevation axis and 80 Nm to azimuth axis. In order to cover further friction effects, which could probably be arisen from machining tolerance and bearing installation, these values are multiplied by safety factor of 1.3.

- **Unbalance Moment:** Although CAD model points out unbalance moment of 350 Nm on elevation axis, this value could be lowered to a considerable extent with counterbalance weights. Considering past experiences

along with decreased rigidity and unbalancing azimuth axis trade-offs of balancing, minimum achievable unbalance moment is assumed not to excess 50 Nm. Nonetheless, in order to be on the safe side, safety factor of 1.3 is utilized, too.

- **Springness Effect:** Laser fibers, cooling hoses, and power cables, whose total number is 16, bend with elevation axis movements. In order to investigate this effect thoroughly, for several bending radii, one by one for fibers, hoses, and cables, forces are measured via mechanical force gauge and flexibility data are extracted. As illustrated in Figure 2.4b, combining with CAD model for several elevation angles, torque calculations are carried out. Accordingly, depending on level arm to elevation axis pivot point and severity of bending, experiencing more than 50 Nm springness torque is highly possible when safety factor of 1.3 is taken into account. Springness torque profile is approximated by sinusoidal fit, which conforms to nonlinear nature quite well, as plotted in Figure 2.4a.



(a) Springness Torque Profile

(b) Model-Aided Springness Torque Calculation

Figure 2.4: Springness Effect Characterization Works

- **Torque due to High Pressure Water through Hoses:** High pressure water acts as straightener on hoses and, eventually, a torque source. As again calculated with the aid of CAD model and Bernoulli's Equations, water flow, at 50 kPa and 2.65 m/s rate, creates approximately 0.32 Nm torque on single hose. Causing small torque even 4 hoses, this factor is neglected.

Detailed Analysis:

1. Azimuth Axis: For the largest torque demand scenario, azimuth motor torque (T_m) profile is calculated via Equation 2.1 where J_a azimuth axis mass moment of inertia, α angular acceleration, and T_f friction torque. In order to solve Equation 2.1 for performance and functions acceleration requirements profile, which is derived from Figure 2.3, Simulink model is created (Figure 2.5). Resultant motor torque profile, which is represented in Figure 2.6, yields that motor, which is to be selected, has to fulfill requirements:

   - **RMS Torque:** 529.3 Nm
   - **RMS Speed:** 5.9 RPM
   - **Peak Torque:** 1401.0 Nm

$$T_m = J_a\alpha + T_f \tag{2.1}$$

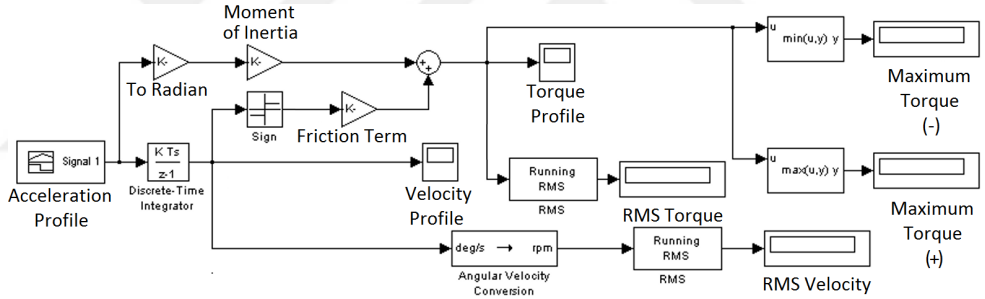


Figure 2.5: Azimuth Motor Selection Simulink Model

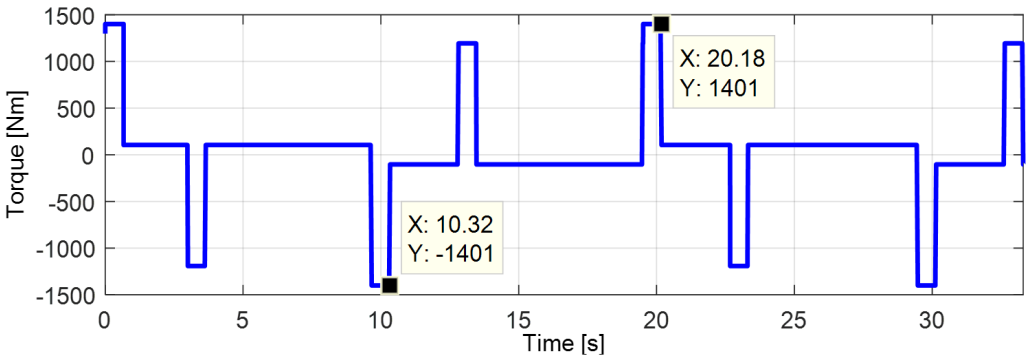


Figure 2.6: Azimuth Motor Torque Profile

2. Elevation Axis: For the largest torque demand scenario, elevation motor torque (T_m) profile is calculated via Equation 2.2 where J_e elevation axis mass moment of inertia, α angular acceleration, T_f friction torque, T_u unbalance torque, and T_s springness torque. For elevation axis there is no acceleration requirements profile to define duty-cycle. In order to be consistent and considering it as a reasonable scenario, azimuth axis profile is used in Simulink model (Figure 2.7), for solving the Equation 2.2. Resultant motor torque profile, which is represented in Figure 2.8, yields that motor, which is to be selected, has to fulfill requirements:

- **RMS Torque:** 244.2 Nm
- **RMS Speed:** 5.9 RPM
- **Peak Torque:** 421.1 Nm

$$T_m = J_e\alpha + T_f + T_u + T_s \tag{2.2}$$

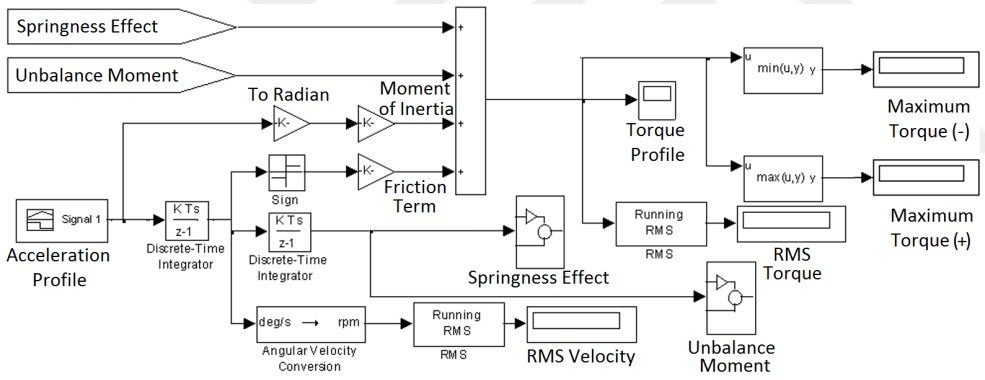


Figure 2.7: Elevation Motor Selection Simulink Model

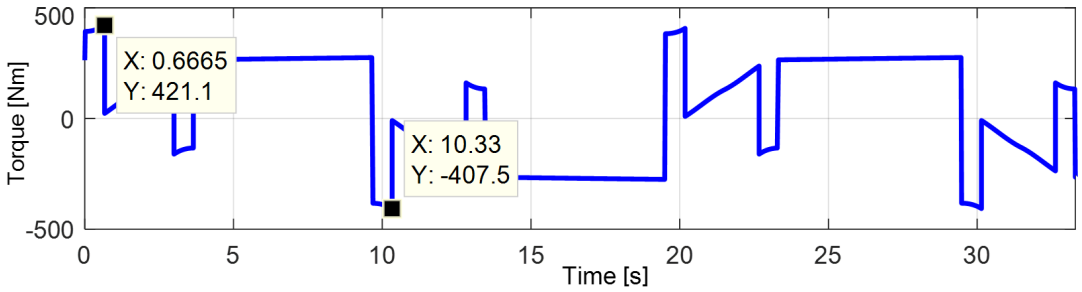


Figure 2.8: Elevation Motor Torque Profile

Component Selection:

1. Azimuth Axis: Based on the requirements and the detailed analysis results motor selection was completed. Although RMS torque requirement is slightly higher than motor capability, reconsidering initial assumptions and distinguishing operation points on motor performance graph (Figure 2.10a), selected motor seems as an optimized choice. During duty cycle, operation in continuous and intermittent regimes are presented in Figure 2.9). Elapsed 0.6 s in intermittent regime is quite lower than maximum rule of thumb value of 3 s. Also, following cooling period is sufficient for convection.

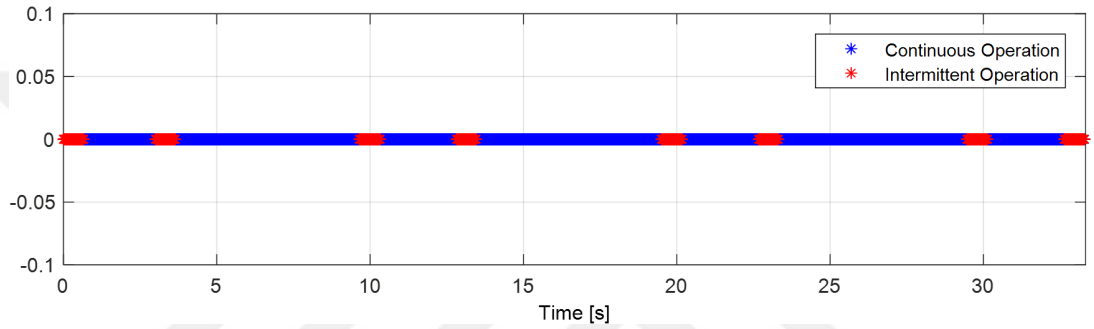
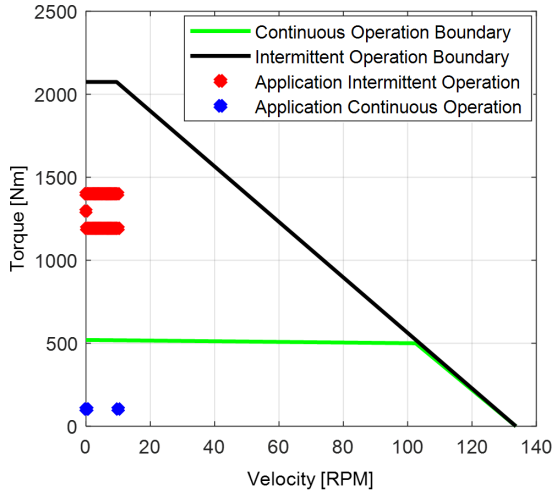


Figure 2.9: Azimuth Motor Duty Cycle for Acceleration Requirements Profile



(a) Operation Points on Motor Performance Graph

NATURAL CONVECTION					
Rated speed		rpm	50	600	
Continuous torque	(1)(4)	N.m	520		
Current at continuous torque	(1)	A	13.9	91.5	
Peak torque	(2)(3)	N.m	2304		
Current at peak torque	(2)	A	70	443	
Rated power	(1)	KW	2.6	25.2	
Inertia		10^{-3}kg.m²	649		
Weight		kg	58		
Thermal time constant	(1)	s	2153		
Thermal resistance	(1)	°C / W	0.072		
Phase resistance at 20°C	(2)	Ω	1.83	0.046	
Phase inductance at I continuous		mH	17	0.42	
Electrical time constant	(2)	ms	9.3		
Back emf constant (line to line)	(2)	V/rad.s	26.28	4.15	
Power cable square section	(7)	nxmm²	4x1.5	4x16	
Power cable diameter	(7)	mm	Ø8	4xØ11	
Number of poles			36		

(b) Motor Datasheet

Figure 2.10: Azimuth Motor Properties and Performance

2. Elevation Axis: Based on the requirements and the detailed analysis results motor selection was completed. Continuous and intermittent torque capacity values of selected motor seems adequate considering required RMS and peak values, along with operation points of motor performance graph (Figure 2.12a). Additionally, regarding continuous and intermittent operation regimes on time domain, as shown in Figure 2.11, natural convection cooling interval seems even longer than azimuth axis operation. To note that, even if the same acceleration requirements profile is applied with azimuth axis, by means of supporting effect of unbalance and springness to motor on elevation axis, the resultant operation regimes are totally different.

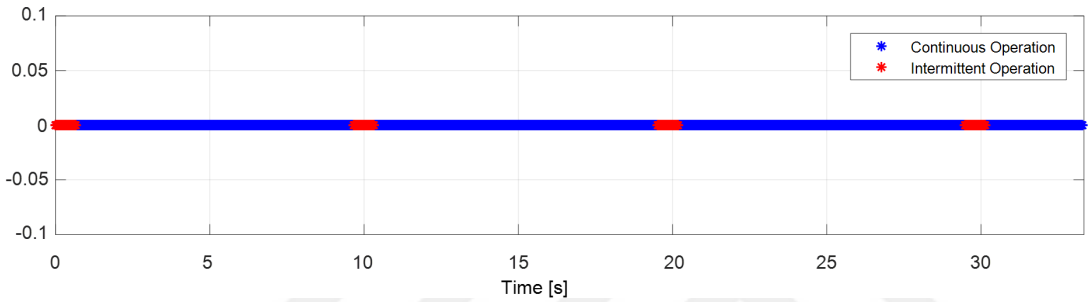
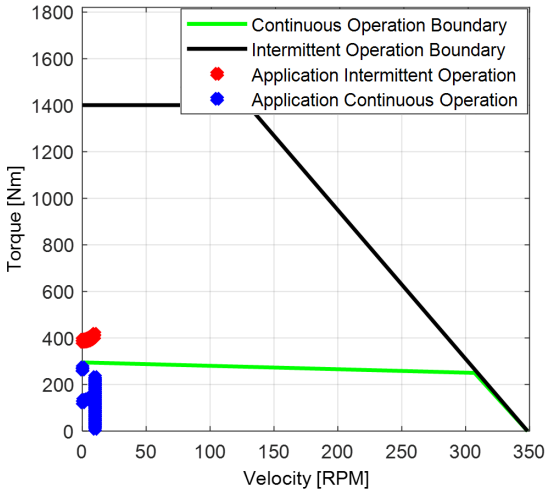


Figure 2.11: Elevation Motor Duty Cycle for Acceleration Requirements Profile



(a) Operation Points on Motor Performance Graph

NATURAL CONVECTION				
Rated speed		rpm	200	800
Continuous torque	(1)(4)	N.m	295	
Current at continuous torque	(1)	A	20.3	69.5
Peak torque	(2)(3)	N.m	1548	
Current at peak torque	(2)	A	133.1	425.8
Rated power	(1)	KW	5.25	15.12
Inertia		10^{-3}kg.m²	211	
Weight		kg	57	
Thermal time constant	(1)	s	2097	
Thermal resistance	(1)	°C / W	0.1	
Phase resistance at 20°C	(2)	Ω	0.534	0.052
Phase inductance at I continuous		mH	5.5	0.53
Electrical time constant	(2)	ms	10.2	
Back emf constant (line to line)	(2)	V/rad.s	10.04	3.14
Power cable square section	(7)	nxmm²	4x2.5	4x10
Power cable diameter	(7)	mm	Ø9.6	4x Ø9.5
Number of poles			18	

(b) Motor Datasheet

Figure 2.12: Elevation Motor Properties and Performance

2.1.2 FSM Selection

System Requirements:

1. Performance and Functions Required
   - Compensating atmospheric disturbance up to C_n^2 of 10^{-14} $m^{-2/3}$
   - Maximum tip & tilt stroke no less than 1 mrad in order to be compliant with optical design
2. Dynamic Environment and Design Constraints
   - **Payload Capacity:** No less than 0.5 kg in order to be compliant with mirror design

Detailed Analysis:

Control Bandwidth: Formulated by set of Equations 2.3, Tyler approximation simplifies the determination process of turbulence power spectrum at low and high frequencies via the assumption of single dominant layer with effective wind speed. Hence, no elaborative phase screen analysis is required and data, which are convergent to the ones in SPIE Field Guide to Adaptive Optics, are obtained [53]. Calculated centroid motion $PSD(f)$ via Tyler approach, for $\hat{\nu}$ = 20 m/s as effective wind speed, λ = 808 nm as wavelength, and C_n^2 = 10^{-14} $m^{-2/3}$ is represented in Figure 2.13. Herein, as the intersection point of low and high frequency regimes, Greenwood frequency (f_G) is 8 Hz. Aforementioned in optical train chapter, 10 fold of f_G is considered as optimal bandwidth projection. Thus, required FSM closed loop bandwidth is 80 Hz.

$$
\begin{aligned}
PSD_{low}(f) &= 0.096\left(\frac{r_0}{\hat{\nu}}\right)^{\frac{1}{3}}\left(\frac{\lambda}{r_0}\right)^2 f^{-\frac{2}{3}}\left[\frac{arcsec}{Hz^2}\right] \\
PSD_{high}(f) &= 0.0013\left(\frac{D}{\hat{\nu}}\right)^{-\frac{8}{3}}\left(\frac{\lambda}{r_0}\right)^2\left(\frac{D}{r_0}\right)^{-\frac{1}{3}} f^{-\frac{11}{3}}\left[\frac{arcsec}{Hz^2}\right] \\
\text{where } r_0 &= 0.185\left(\frac{4\pi^2}{C_n^2(3\pi/8)(2\pi/\lambda)^2}\right)^{3/5} \text{ as Fried's parameter}
\end{aligned}
\tag{2.3}
$$

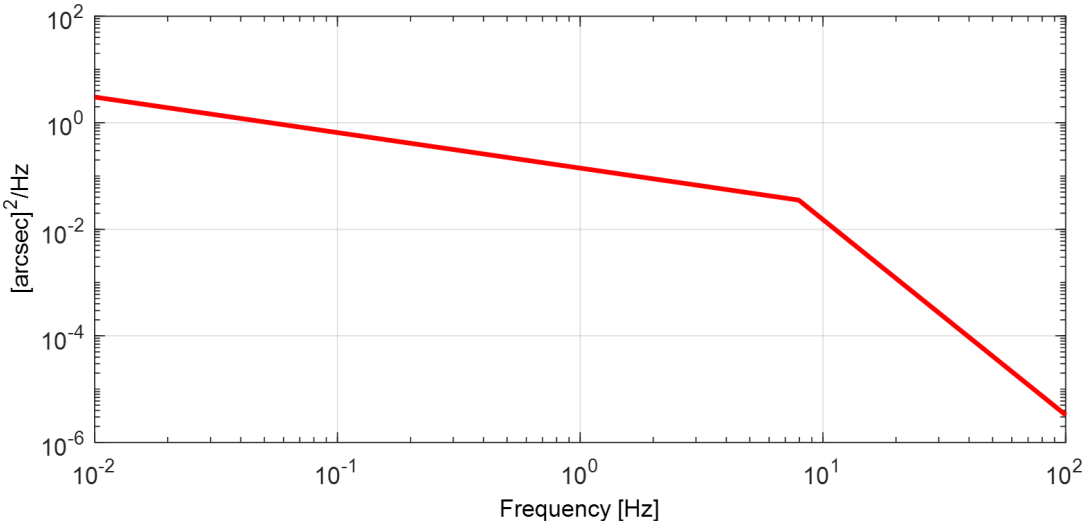


Figure 2.13: Atmospheric Disturbance $PSD(f)$ Graph

Component Selection: A COTS (commercial off-the-shelf) solution was not available. A custom design unit was ordered.

2.1.3 Gyro Selection

System Requirements: For the initial phase, there is no stabilization performance requirement. However, at a later stage it is possible to integrate the system to a base platform on the move. In order to get the gyro hardware and software substructure ready and smooth servo loop operation, gyro deployment is planned. Herein, requirement derivation could be initialized via RMS stabilization accuracy. The smallest FOV value of camera is 1°x 1°and the resolution is 640 x 480 pixels, yielding IFOV values of 27.27 μrad and 36.36 μrad for elevation and azimuth, respectively. During stabilization, in order to keep motion within single pixel of 27.27 μrad, required 1 σRMS accuracy is calculated as 9.64 μrad from $\pm 13.64/\sqrt{2}$. Aforesaid ARW value, which is calculated by multiplying 1 σRMS stabilization accuracy value with $\sqrt{2}$ and dividing the resultant to square root of RMS Data Duration, is $0.015°/\sqrt{hr}$. In accordance with ARW requirement and in order to prepare acceleration based feedforward infrastructure, an IMU was selected. In addition, previous project experiences, low group delay, and large bandwidth, make selected IMU more distinguished.

2.1.4 Encoder Selection

System Requirements:

1. Performance and Functions Required
    - Absolute orientation measurement within 320°azimuth and -10°to 90°elevation motion envelope
    - Adjustable soft limits
    - Cued pointing capability
    - Masking restricted zones to position
    - Position Measurement Resolution: <3 μrad
2. Dynamic Environment and Design Constraints
    - **Mechanical Interfaces:** Fitted on hollow azimuth and elevation shafts and placed properly assuring trouble-free motor commutation
    - **Electronics Interfaces:** Output protocol is supported by digital servo drive

Detailed Analysis:

IFOV of the camera, which is placed on high-power laser optical path is 2.045 μrad. For precise boresight, quarter pixel measurement resolution is adequate value, i.e., 0.511 μrad. Hence, absolute encoder resolution has to be at least 24 bits. Further to that, neither cued pointing nor masking or soft-limits necessitates better precision.

Component Selection:

Based on the requirements and the analysis result, an absolute encoder with 26 bits resolution and BiSS interface were selected. BiSS C-mode (uni-directional) protocol is largely supported by modern digital servo drives.

2.2 Servomechanism Design

System Requirements:

1. Performance and Functions Required

   - Position Limits: 320°(For Azimuth) and -10°to 90°(For Elevation)
   - Payload Capacity: >250 kg
   - Positioning Repeatability: <25 μrad
   - Positioning Accuracy: <75 μrad
   - Reference Input Tracking Accuracy: <125 μrad
   - Smooth servo operation

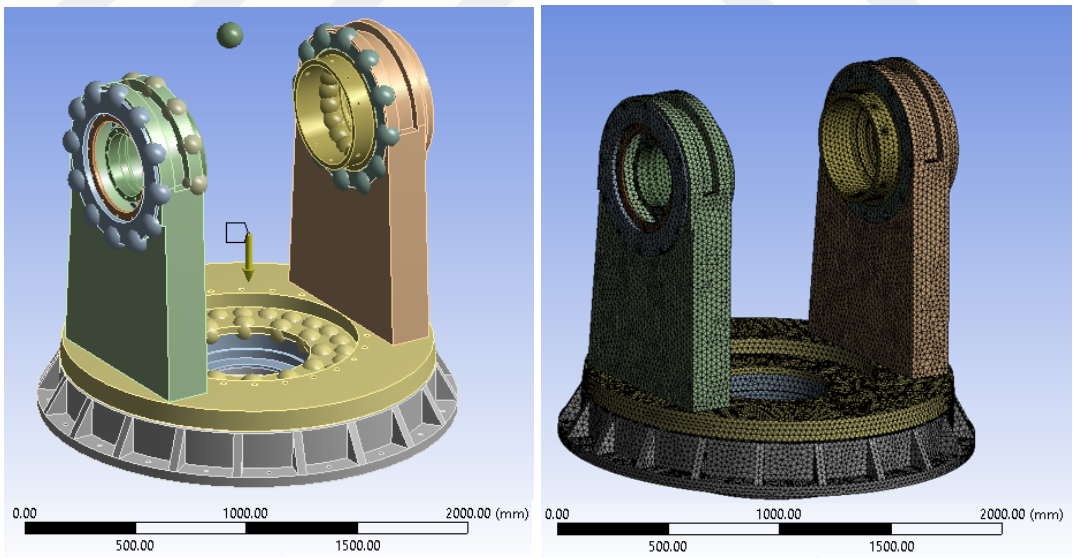
2. Dynamic Environment and Design Constraints

   - **Mass Moment of Inertia:** High inertia improves stabilization performance. Since there is no stabilization requirement for initial phase, inertiae are required to be optimized such that lower power rating motors are adequate.
   - **Friction Torque:** In order to achieve lowest friction torque, tight tolerances, precision seals and bearings, and craftmanly installation are required to be applied.
   - **Unbalance Moment:** Since there is no base excitation, unbalance tilts elevation axis when motor or break is unenergized at the worst and degrades control performance to a certain extent. At least up to friction torque holds it stationery, elevation axis is required to be balanced.
   - **Springness Effect:** Laser fibers, cooling hoses, and power cables are required to be guided with carriers such as the ROBOTRAX, properly. After leaving a motion margin, hanging the rest on azimuth frames is required to get springness behavior acting on elevation axis under control.
   - **Structural Dynamics:** Due to lack of structural data available on motor selection phase, this term is neglected with the assumption that rigid-body acceleration term on torque budget covers by far. However, structural

weaknesses have drastic impacts on overall performance, from low control bandwidth to even saturated controller, driven by sensed-by-gyro structural oscillations. It is required that transmissibility between gyro, motor and optics has to be highest possible. From preliminary payload model to final payload model, structurally strengthening upgrades are required to be carried out, progressively.

Structural Analysis: Conventional metallic structures are approximated as lumped multi element system of mass-spring-damper by means of their linear nature, as general formulation is represented via Equation 2.4 where $\boldsymbol{M}$, $\boldsymbol{C}$, and $\boldsymbol{K}$ are mass, damping, stiffness matrices, respectively, $\vec{X}$ is displacement vector of nodes, and $\vec{F}(t)$ is time function of excitation. This formulation also forms the basis of FEA and helps designers to predict transfer functions along with stress distributions of structures throughout design process.

$$\boldsymbol{M}\ddot{\vec{X}} + \boldsymbol{C}\dot{\vec{X}} + \boldsymbol{K}\vec{X} = \vec{F}(t) \tag{2.4}$$

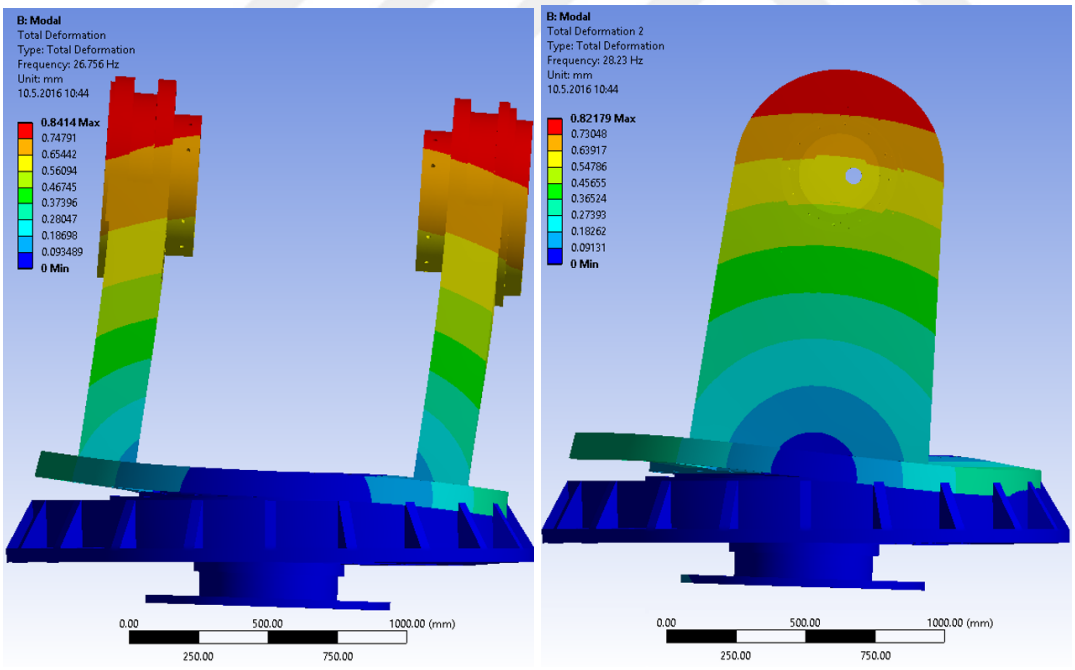


(a) Point Mass and Connection Details

(b) Fine Meshing Details

Figure 2.14: Preliminary Design FEA Model Details

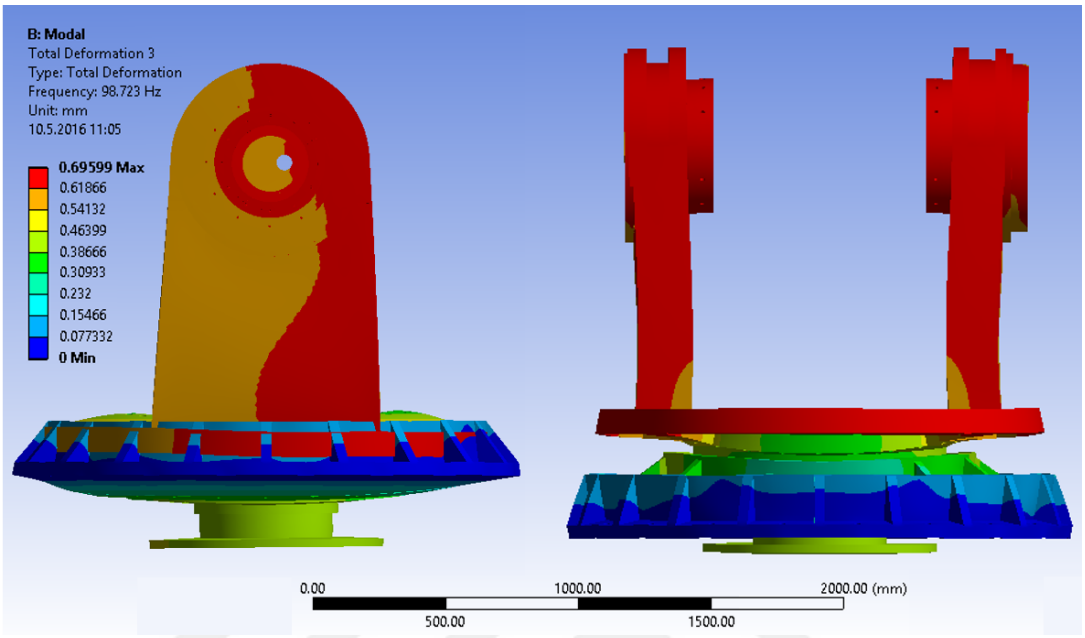
◇ Preliminary Payload Model: Since the payload details on elevation axis were not determined at that stage, total elevating mass was considered as point mass in the analysis. Moreover, as well as point mass to elevation supports interfaces, rigid connections were assigned to all joints interconnecting mechanical parts and assemblies as presented with balls in Figure 2.14a. As represented in Figure 2.14b, fine meshing was done with 770000 nodes and 440000 elements. Herein, in order to verify the model accuracy, mesh convergence was performed and optimum nodal point number was concluded. By the use of ANSYS FEA software packages, modal analysis is conducted, and the results indicate that first and second natural frequencies are at 26.7 Hz and 28.2 Hz, respectively (Figure 2.15). By means of approximate equivalent inertia along two orthogonal axes on azimuth bearing face plane, first two natural frequencies are convergent and arising from azimuth bearing flexibility. Considering the first natural frequencies' order of magnitude, for such a large system it could be stated that they are high enough to achieve noteworthy bandwidths.



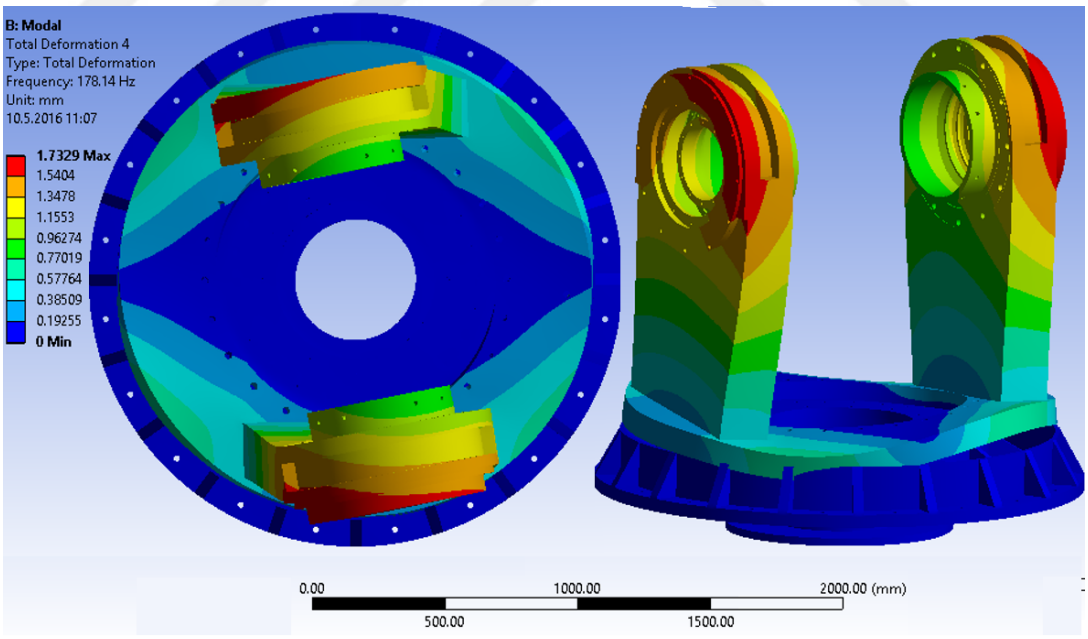
(a) First Mode Shape @26.7 Hz (b) Second Mode Shape @28.2 Hz

Figure 2.15: Preliminary Design FEA Results

One critical point to stress on is that the low mode oscillations are in the same direction with elevation axis operation. Third and more natural frequencies, which are detailed with Figure 2.16, are high enough not to play a significant performance role.



(a) Third Mode Shape @98.7 Hz



(b) Second Mode Shape @178.1 Hz

Figure 2.16: Preliminary Design FEA Results cont.

Flexible dynamic analysis was carried out, too. For this purpose, a model, for which all mechanical sub-gimbal parts were modeled via MSC.Patran & MSC.Nastran in an elastic manner, were reduced via Craig-Bampton method and, eventually, became ready for MSC.Adams. Although ANSYS analysis provided valuable data for validating structural design of preliminary work, MSC.Adams analysis assured more thorough insight on force interactions and inter-analyses cross-checking. Herein, in place of elevation and azimuth motors, by one by, sine-sweep torque excitation is applied between 5-600 Hz and velocity response is logged. As cross-checked on the torque to velocity FRF graphs for both azimuth (Figure 2.17) and elevation (Figure 2.18) axes, natural frequencies are located at closer points with ANSYS analysis. The source of slight difference is the co-location of motor and sensor for the analysis. Availability of anti-resonance is proves that phenomenon. For different lay-outs, due to the flexibility between motor and sensor, quite different responses are possible.

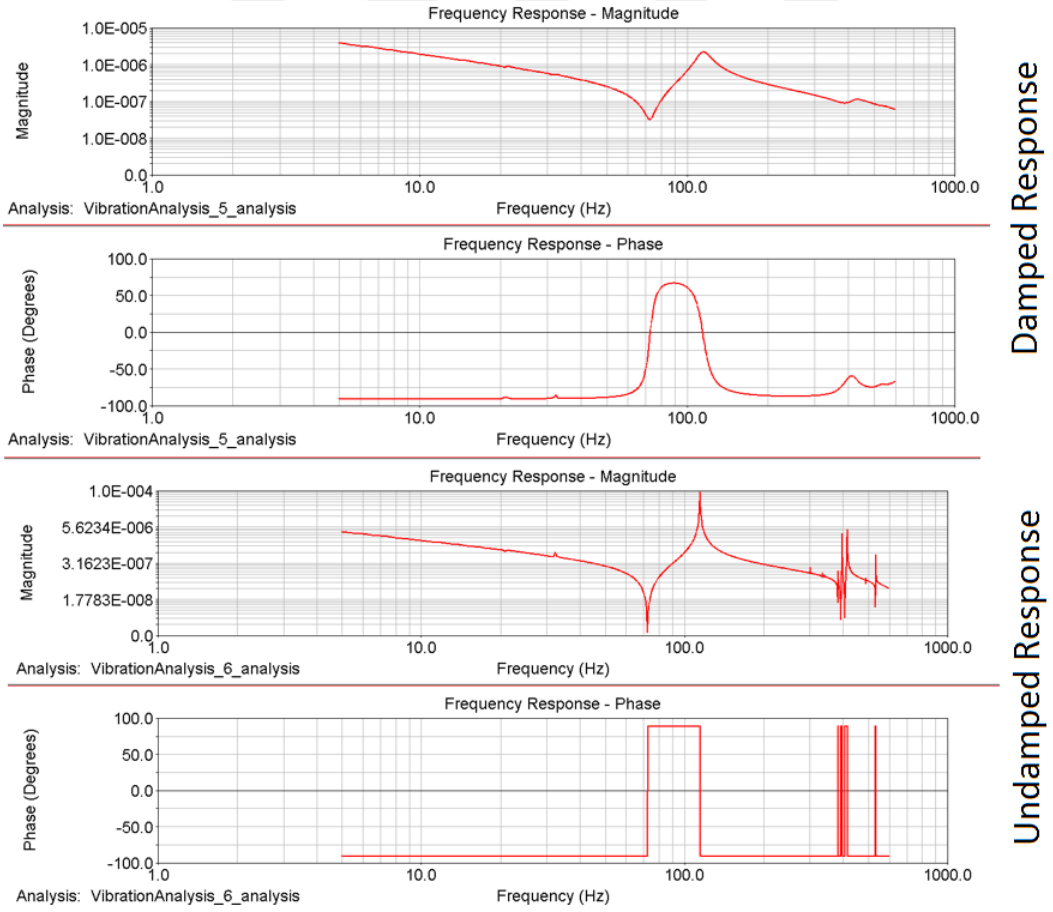


Figure 2.17: Preliminary Azimuth Design Flexible Dynamic Analysis Results

Since in preliminary design phase the exact position of gyro was not decided yet, more realistic transfer function could not been obtained. Accordingly, using this data set, further analyses, such as Simulink control design, were postponed to the final phase. Gyro, necessarily, would be placed at a rigid location of elevation axis on final design, and general structural rigidity level did not seem to pose future weaknesses when elevation axis details become clear. Considering the design rule of thumb that with 1/3 or less than first torsional interactive mode, bandwidth is, typically, limited, preliminary design was expected to assure around 8 Hz bandwidth velocity loop [81]. For such a large unit, this bandwidth value is quite high when compared with equivalent ones in size. At that point, ground connection details became more of an issue, such that even if gimbal is rigid enough, due to lack of stand structural rigidity, underperformance could be experienced. In order to avoid this, stand alternatives, singly and gimbal-mounted, were finite element analyzed and verified before production.

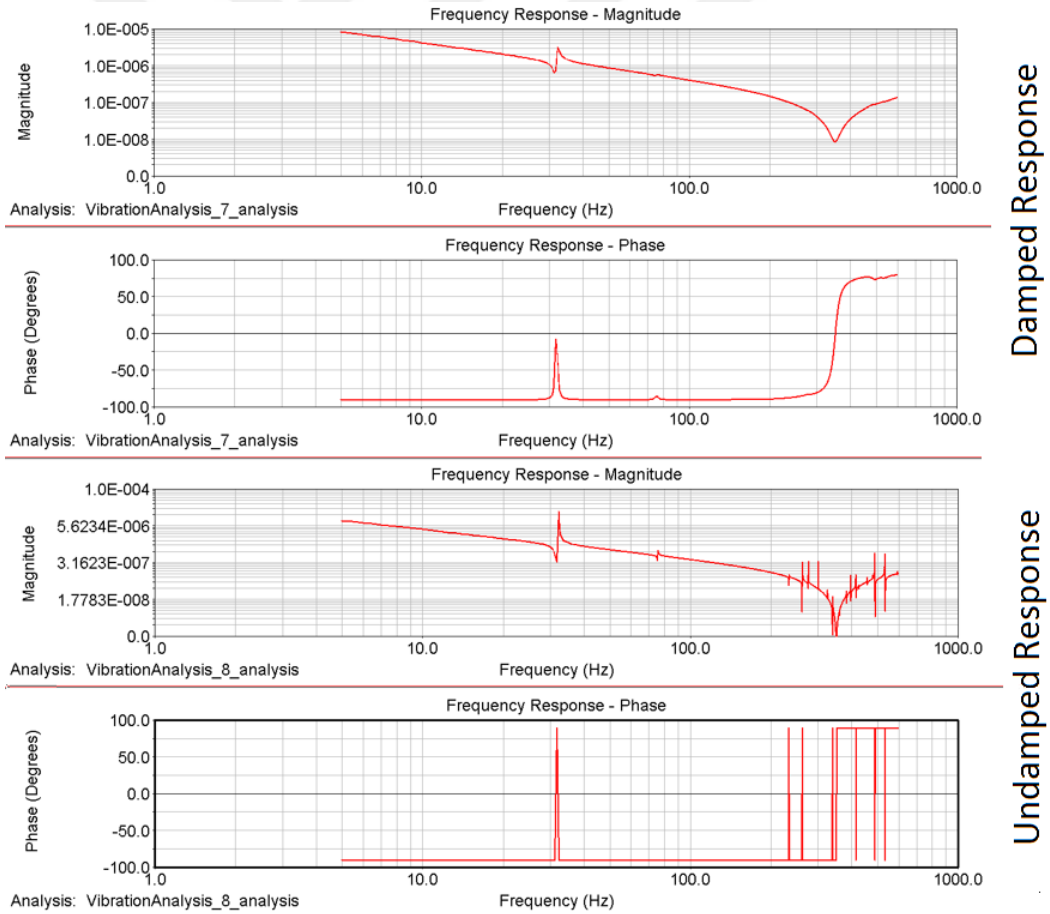
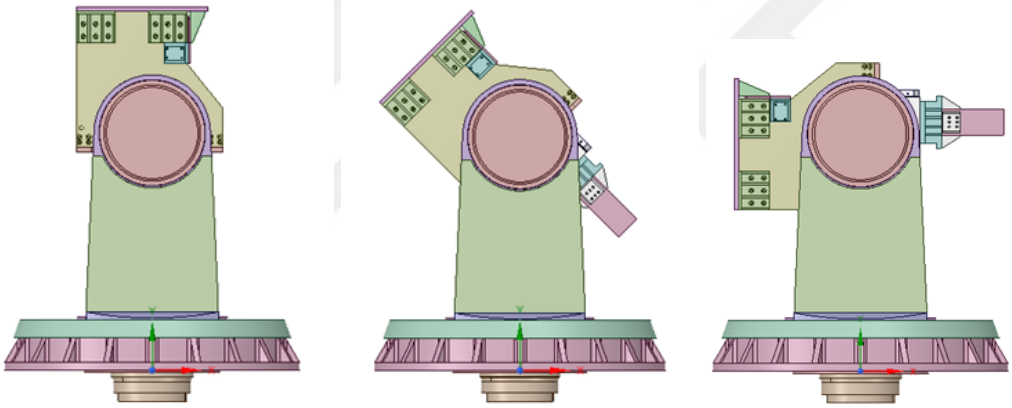


Figure 2.18: Preliminary Elevation Design Flexible Dynamic Analysis Results

◇ Final Payload Model:As the elevation payload details became clear, it was realized that counterbalances limit the upper motion limit. To fulfill functional requirement of elevation motion range, supports were required to be extended at the risk of lowered natural frequencies. Along with the new modes of vibration, stemming from elaborate elevation axis mechanics, lowered former modes and their interaction could accompany with performance loss. In order to prevent this, optimization was carried out and the reached natural frequencies on final design is presented in Table 2.1 for elevation alignments 45°apart (Figure 2.19). In addition, corresponding mode shapes are demonstrated in Figure 2.20. The first could be named as vertical bending mode. Although it was the lowest, due to its oscillation travel direction, it was not expected to be an interactive mode. It could, instead, cause arching of beam over target without large angular shift.

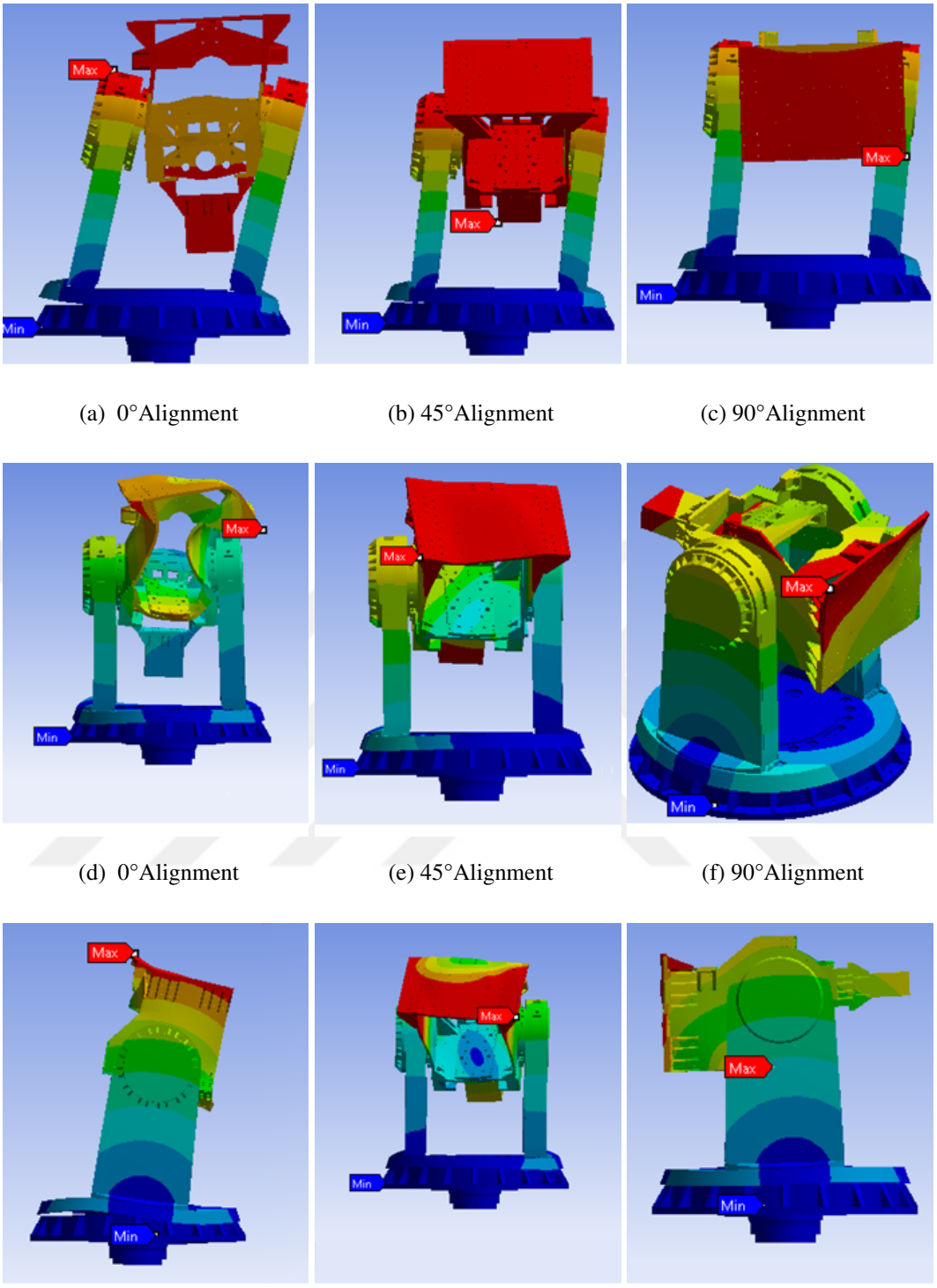


(a) 0°Alignment (b) 45°Alignment (c) 90°Alignment

Figure 2.19: Final Model Main Analysis Alignments

Table 2.1: Natural Frequencies (Hz)

Mode of Vibration #	@0°	@45°	@90°
1	10.0	11.0	11.9
2	16.6	18.3	18.1
3	17.4	20.7	23.9



(a) 0°Alignment (b) 45°Alignment (c) 90°Alignment

(d) 0°Alignment (e) 45°Alignment (f) 90°Alignment

(g) 0°Alignment (h) 45°Alignment (i) 90°Alignment

Figure 2.20: First Third Mode Shapes of Final Design for Alignments 45°Apart

Having torsional characteristics, the second and third modes could pose fundamental system limitation on bandwidth. Although, interactive modes were lowered by the final design, they remained within allowable limits for more than 2000 kg heavy system. The cause of natural frequency changes with respect to elevation alignment was linked with variance of stress distribution and they are considered as reasonable. Within system identification activities, this subject is studied thoroughly.

2.3 Servoelectronics Design

2.3.1 Servo Drive Selection

System Requirements:

1. Performance and Functions Required
   (a) Sub-requirements from motors and motion scenarios
      - Output Voltage: 400 VAC (for both of the gimbal axes)
      - Output RMS Current: 14.2 A (for azimuth) & 16.8 A (for elevation)
      - Output Peak Current: 42.6 A (for azimuth) & 36.2 A (for elevation)

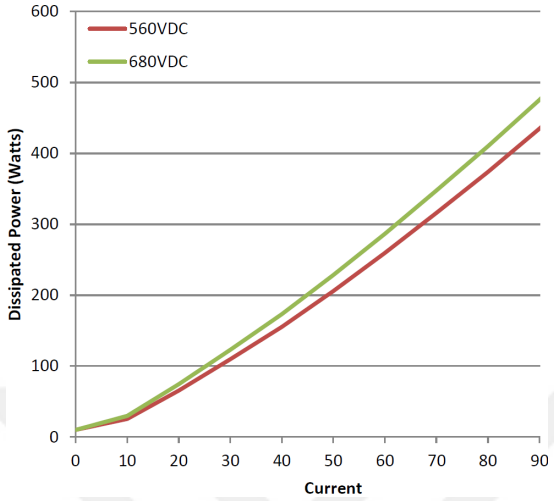
   (b) Sub-requirements from encoders
      - BiSS C-mode (uni-directional) protocol support

   (c) Sub-requirements for interfacing
      - EtherCAT protocol support
      - USB or RS-232 based computer interface with tuning software

Detailed Analysis and Component Selection:

Based on the requirements, the same commercial servo drive was selected for both axes. As stated in the datasheet (Figure 2.21b), based on the commutation type, continuous current output of the drive could reach up to 100 A. Peak acceleration values are planned to be limited in the first plan for protecting delicate optics, therefore, drive current level is sufficient.

By means of a special mechanism, motion controller could maintain 1.5 fold of continuous current, i.e., 150 A for long times, regardless of load. Hence, even if in the future it is required to use motors at their full capacity, it will also be possible.



(a) Heat Dissipation vs. Current Graph

Feature	Units	
Minimum supply voltage	VDC	95
Nominal supply voltage	VDC	560 for 400 VAC 680 for 480 VAC
Maximum supply voltage	VDC	780
Maximum continuous power output	kW	65
Efficiency at rated power	%	> 98
Auxiliary supply voltage option	VDC	18 to 30 VDC
Auxiliary power supply	VA	7
Continuous current limit (Ic) Amplitude sinusoidal/DC trapezoidal commutation	A	100
Continuous RMS sinusoidal (Ic) commutation current limit	A	71
Peak Current	A	No Peak

(b) Servo Drive Datasheet

Figure 2.21: Servo Drive Properties and Performance

For 400 VAC, nominal suppy voltage of 560 VDC is required and on heat dissipation vs. current graph for 14.2 A (for azimuth axis) around 40 W and 16.8 A (for elevation axis) around 50 W are read. Free air convection thermal resistance is given as 8 °C/W. Based on thermal equation $T_{HeatSink} = T_{Ambient} + P_{Dissipation(W)} R_{\theta}$, where $T_{HeatSink}$ is the integral heat-sink of the drive temperature, $T_{Ambient}$ is ambient temperature and $P_{Dissipation(W)} R_{\theta}$ is dissipated power times thermal resistance, for $T_{Ambient}$ = 40°, $T_{HeatSink}$ elevates up to 80°, which is limit value for proper servo operation, and 86°is thermal shutdown level. The integral heat sink has the dissipation capacity of almost 20 W, however, with the addition of external no fan heat sink, this value could be increased to more than 100 W. External heat sink could yield thermal resistance of 0.07 °C/W and with a a thermal foil, the thermal resistance could even be lowered to 0.03 °C/W. Although no fan solutions seems sufficient, for prototype development, considering extensive tests, it is decided to use the most influential cooling mean, i.e., built-in fan assembly, which dissipates up to 600 W at ambient temperature of 40 °C.

2.3.2 Power Supply Selection

System Requirements:

1. Performance and Functions Required
   (a) Sub-requirements from servo motor driver
      - Output Voltage: 560 VDC
      - Output RMS Current: 17.2 A (with driver power loss compensation)
      - Output Peak Current: 43.5 A (with driver power loss compensation)
   (b) Sub-requirements from technological and safety infrastructure
      - Direct-to mains operation
      - Fault detection and Enable Features

Detailed Analysis and Component Selection:

Based on the requirements, the same power supply was selected for both axes. 3ϕ-380 VAC mains is rectified by supply, and $380\sqrt{2}$ = 540 VDC output is obtained, which is quite appropriate value. The selected supply could power multiple drives and also has 30 A continuous - 60 A peak output current capacity. (14.2 + 16.8) / 0.98 = 31.6 A_{RMS} and (42.6 + 36.2) / 0.98 = 80.4 A_{peak} total current from all axes, including drive losses, are required for the motion scenario. Considering rare occurrence of dual axes peak in-rush current demand, even single supply deployment could be sufficient. In case of rapid deceleration, due to motor shaft's back energy regeneration on drive, bus voltage could increase to cause irreversible damage. In order to prevent and dissipate energy, shut resistors are used, and Elephant supply has 6.7 kW shunt power capacity. In the worst case scenario, at peak velocity and torque for both axes at the same time, mechanical power to be dissipated is 1.9 kW and far below 6.7 kW value. Having 5-6 °C/W free air convection resistance, when drive calculations are regarded for the same limit of 80 °C, supply is not expected to pose overheating risk. Nevertheless, by means of cooling and programmability features, an adjustable bench high power DC supply was planned to be used at the initial extensive test period.

CHAPTER 3

SYSTEM IDENTIFICATION AND MODELING

3.1 SYSTEM IDENTIFICATION

3.1.1 Gimbal

By the finalizing of the design, manufacturing and assembly of sub-units began. In a parallel manner, testing activities were initiated for both identifying system dynamics and diagnosing probable faults beforehand. After assembling all gimbal sub-units, full assembly level tests were carried out with dummy payloads. Eventually, by the disposability of ultimate payloads, final system identification tests were performed.

3.1.1.1 Friction, Unbalance, Springness and Cogging Tests

In constant velocity motion, since there is no inertial torque, all motor torque (T_m) is equal to the resultant of friction (T_f), unbalance (T_u), and springness ($K_s\theta$) torques (Equation 3.1a). Depending on this relation, the resultant torque is measured via driving an axis back and forth between the same angular limits, while synchronously logging motor current and position values. Current times motor torque constant (K_t) yields motor torque, whose plot against gimbal angle is a hysteresis curve. As exemplified with Torque Equation Set 3.1, for complete characterization, the procedure is repeated at 6 orthogonal orientations, i.e., $\pm\overrightarrow{X}$, $\pm\overrightarrow{Y}$, and $\pm\overrightarrow{Z}$, where gravity on -$\overrightarrow{Z}$.

$$(@0^\circ)T_m = T_f - T_u + K_s\theta \tag{3.1a}$$

$$(@180^\circ)T_m = T_f + T_u + K_s\theta \tag{3.1b}$$

Measurement technique details are presented in Figure 3.1. The half difference between upper and lower bounds of hysteresis curve gives friction torque value. Adding Torque Equation Set 3.1 side by side yields $T_u = (T_{m@0^\circ} + T_{m@180^\circ})/2$, in other words, half difference between upper bounds of 180°apart two gimbal orientations' hysteresis curves gives unbalance torque over bearing (Bng). Springness torque diagonally pulls hysteresis curve by means of gimbal angle dependent nature. In addition to these, cogging torque (T_c) is inferred from hysteresis curve by means of its period, which is calculated via relation $\mathcal{T}_{cogging} = 360^\circ / LCM(\#Sloth)(\#Pole)$, where LCM stands for least common multiple of motor sloth and pole numbers .

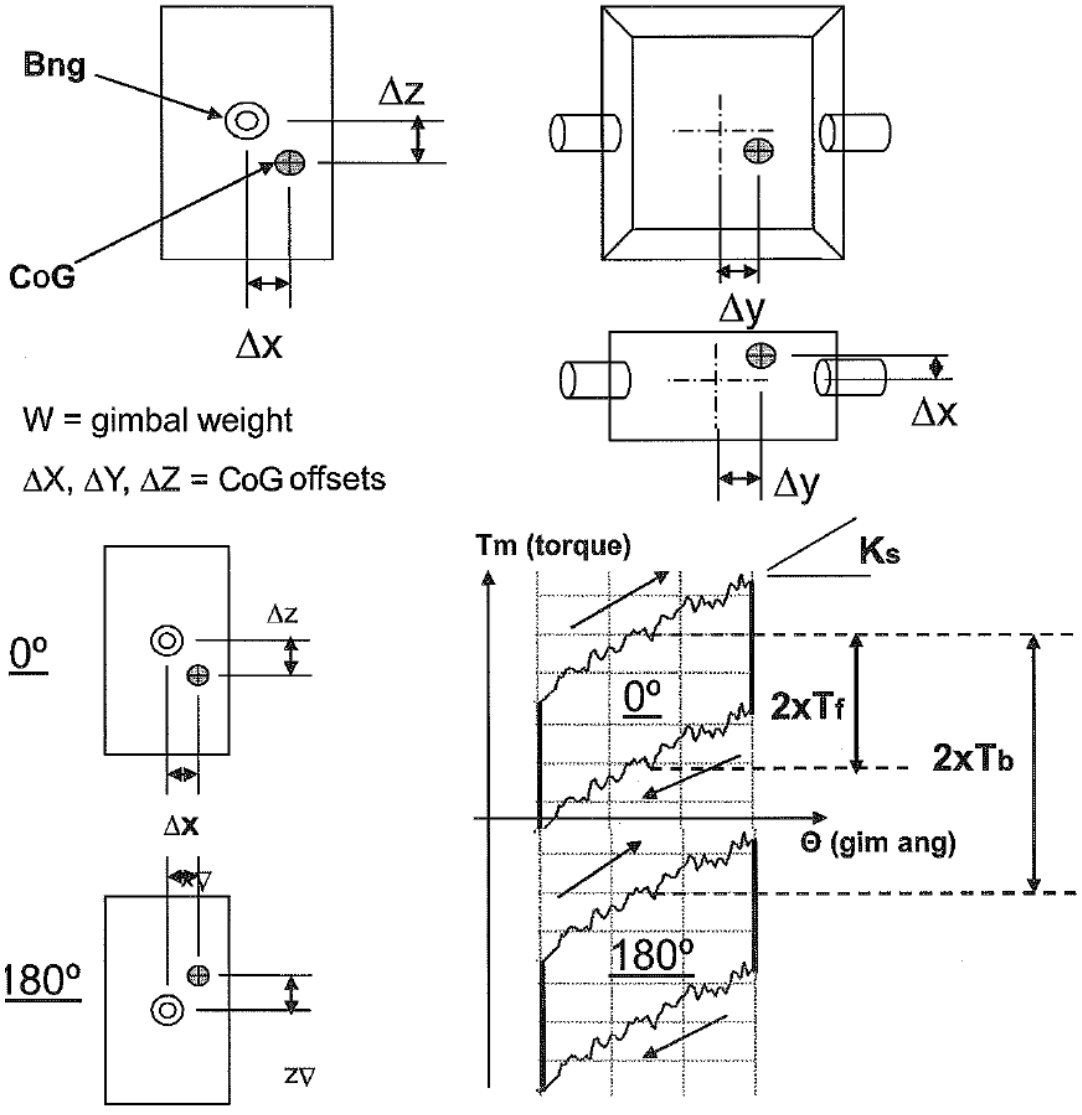
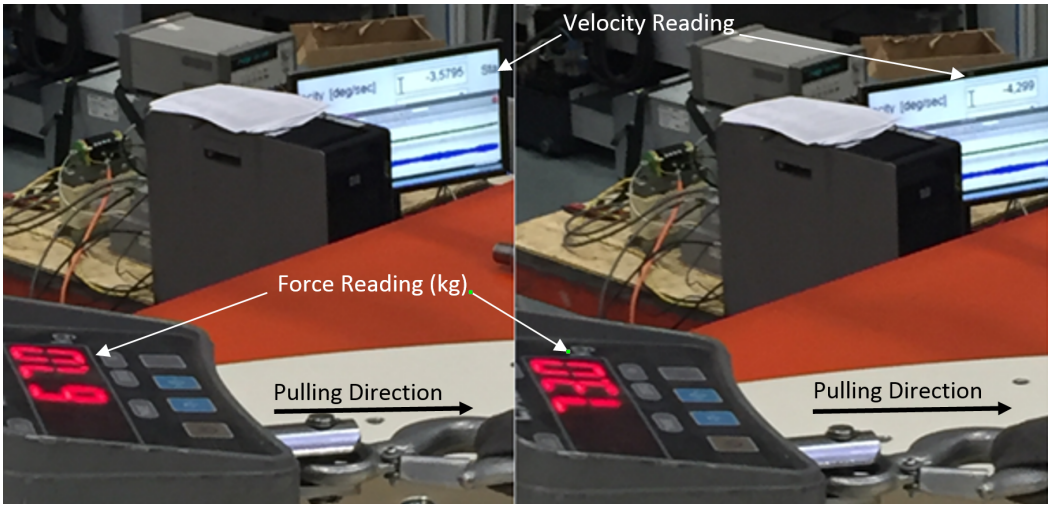


Figure 3.1: Friction, Unbalance, Springness and Cogging Torque Measurement Procedure Technical Details [81]

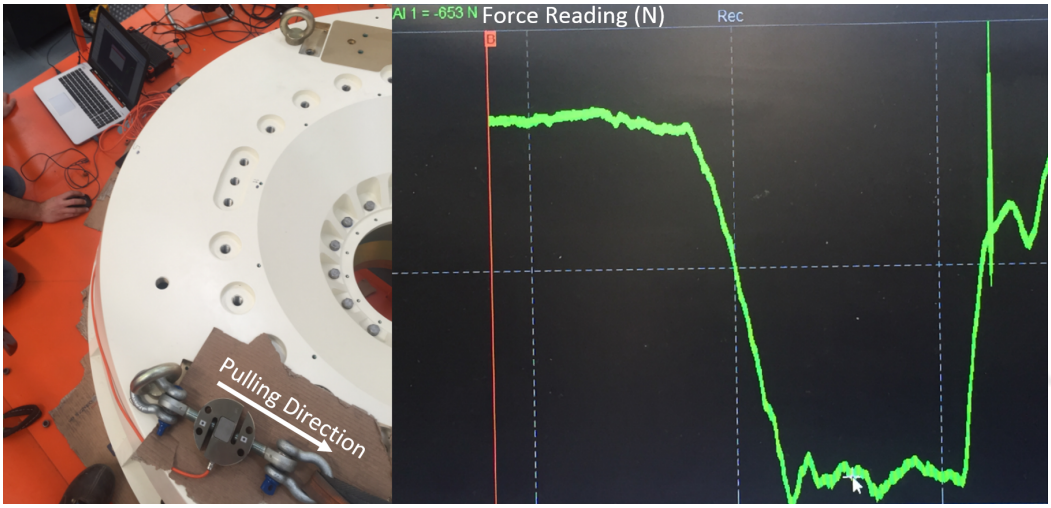
Table 3.1: Hysteresis Characteristics Identification Tests Plan

	Velocity (°/s)				
	2	10	20	40	60
Azimuth Axis as Torque Table	✓	✓	✓	✓	✓
Azimuth Axis as Torque Table + Elevation Axis Supports	✓	✓	✓	✓	✓
Azimuth Axis with Equivalent Elevation Axis Payload	✓	✓	✓	✓	✓
Elevation Axis with Equivalent Payload	✓	✓	✓	✓	✓

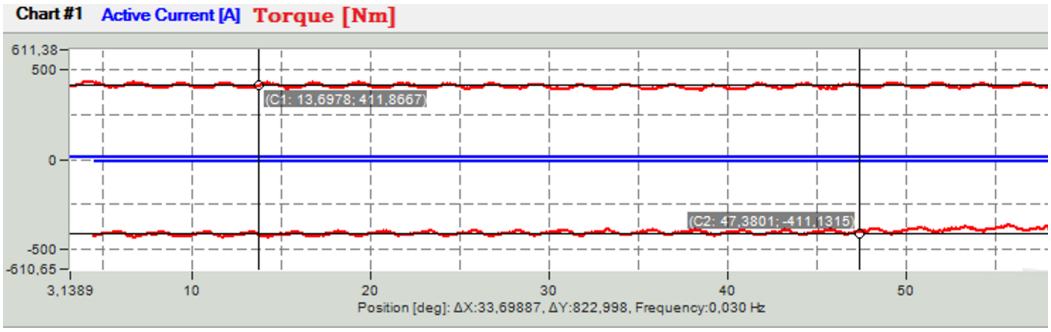
Tests, which are based on this methodology, were planned as their details are demonstrated in Table 3.1. The tests were envisaged to be performed via driving system at constant velocity on motion controller software, i.e., EASII, and logging motor current along with simultaneous gimbal angle. However, in order to validate parameters effecting measurements, such as motor torque constant and motor current sensing accuracy, test results were required to be crosschecked by an external test mean. Measurement crosschecking was carried out via both digital force gauge and mechanical weighing scale. In order to eliminate Back-EMF effect, motor terminals were disconnected from motion controller, and only encoder was remained connected to read velocity on motion control software for ensuring that constant velocity is almost attained during the test. Since the first assembled unit was azimuth torque table, i.e., frameless azimuth motor is enframed with azimuth mechanics and encoder, initial validation tests were performed on it by pulling to turn at nearly constant velocity, while force values, synchronously, were read as demonstrated by Figure 3.2a and Figure 3.2b. For 3.5 °/s, dragging tests results are convergent on 650 N, and 410 Nm torque is yielded with the level arm of 630 mm. Almost the same is result is obtained when azimuth torque table is driven on motion controller (Figure 3.2c), thus, motion control software environment is verified. Since azimuth torque table was leveled, averaging cancels out cogging effects, and the factors, which could create springness effect such as moving cable or hose, are not installed, 410 Nm is sole friction torque.



(a) Test by Pulling with Mechanical Weighing Scale



(b) Test by Pulling with Digital Force Gauge



(c) Test by Driving on Motion Controller

Figure 3.2: Test Technique Verification on Azimuth Torque Table

Since the torque value of 400 Nm was considered as quite high when considering motor selection assumptions along with current bearing and seal datasheets, a problem was thought to exist, and additional tests were performed. Herein, the repeats yielded the same results, and from the tests at 10 °/s and 20 °/s, torque values of 530 Nm and 680 Nm were measured, respectively. Frictional characteristics could be modeled with $T_f = 15\omega + 380$ Nm. In addition to high friction, its high dependency on rotational velocity was unexpected due the selected components, which were known not to show significant viscous friction. Therefore, in order to lower friction, torques of retainer bolts were adjusted, and seal configuration were reworked. Eventually, friction levels were decreased to 200 Nm, which was given as nominal value from the supplier, and assembly process proceeded by elevation supports. With elevation supports only, equivalent elevation axis payload on top of them, and ultimate elevation configuration, around 180 tests were performed via EASII, Simulink/xPC target model and gimbal software interface. As a result, convergent and consistent results were obtained. The same was valid in elevation axis, regarding the tests with both dummy payload and actual units. Figure 3.3, Figure 3.4, Figure 3.5, and Figure 3.6 sum all final results up.

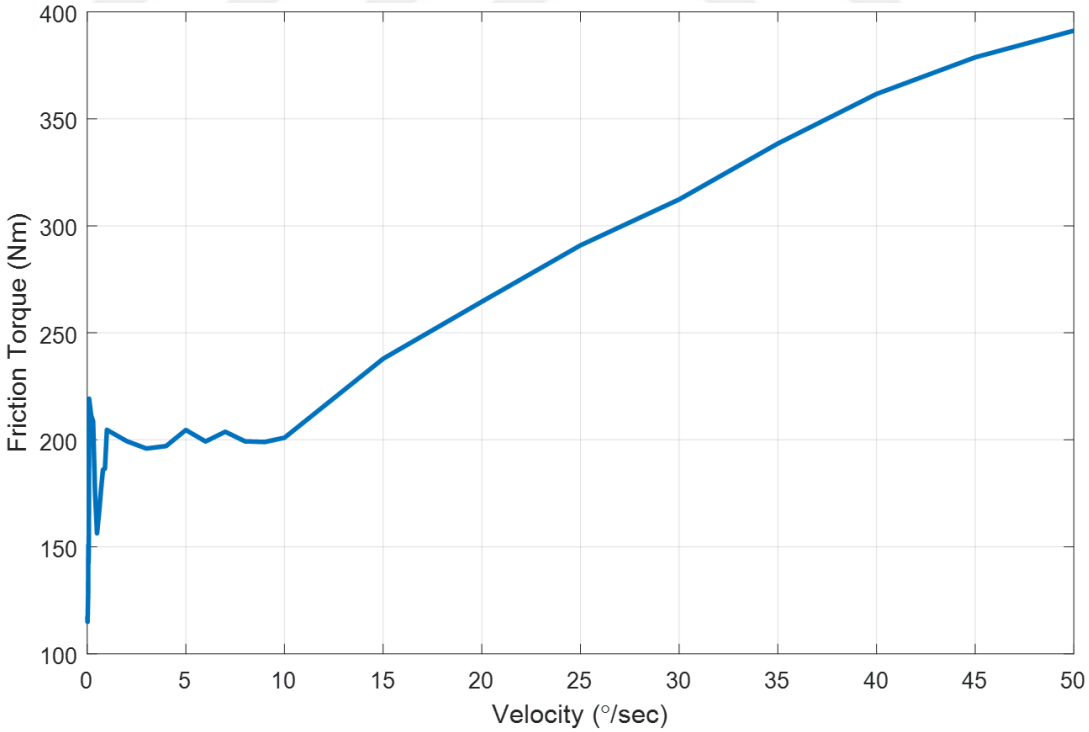


Figure 3.3: Azimuth Friction Torque vs. Angular Velocity

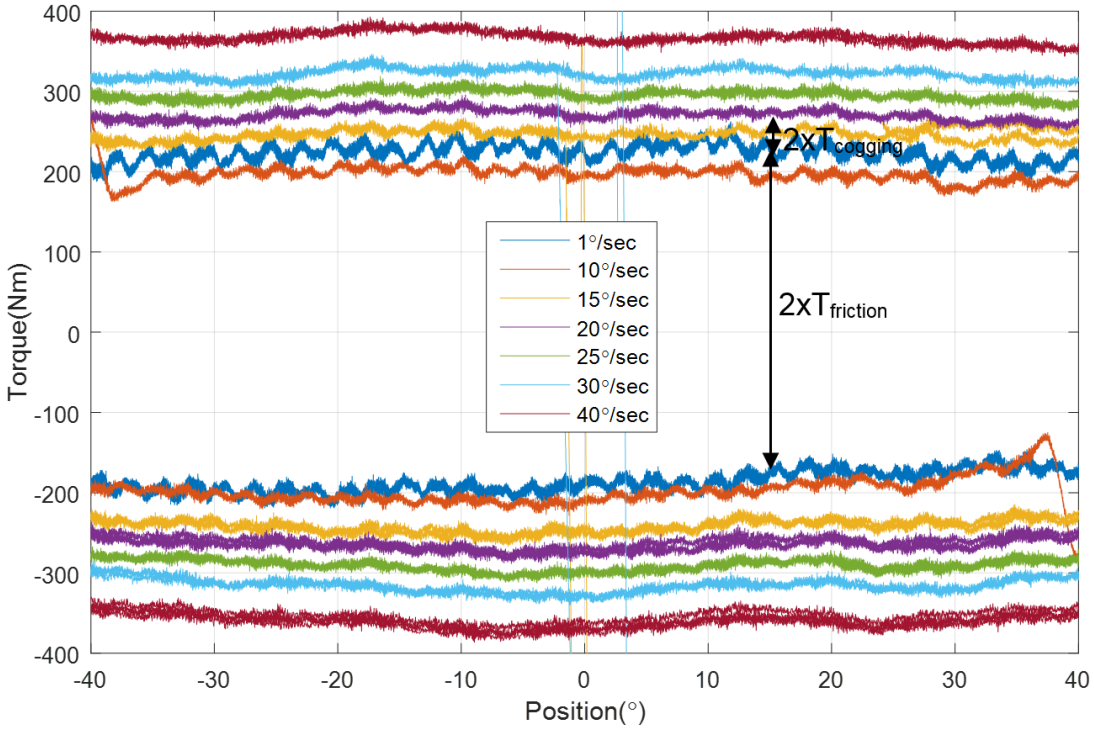


Figure 3.4: Azimuth Hysteresis Curve for Different Angular Velocities

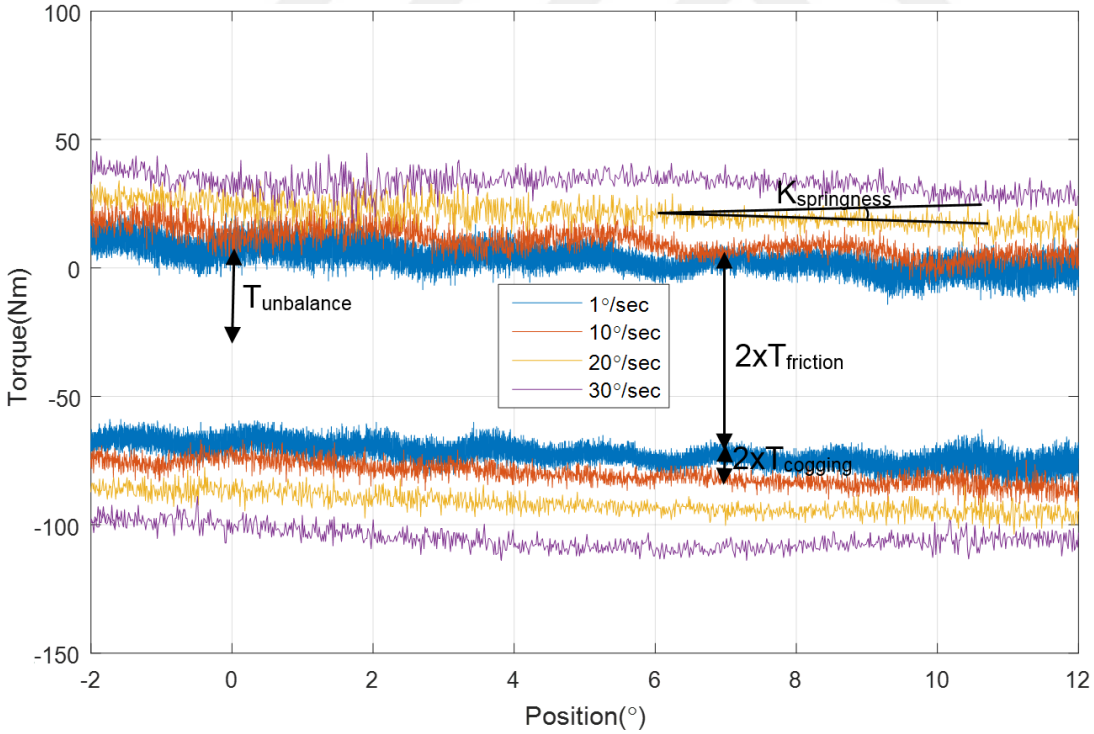


Figure 3.5: Elevation Hysteresis Curve for Different Angular Velocities

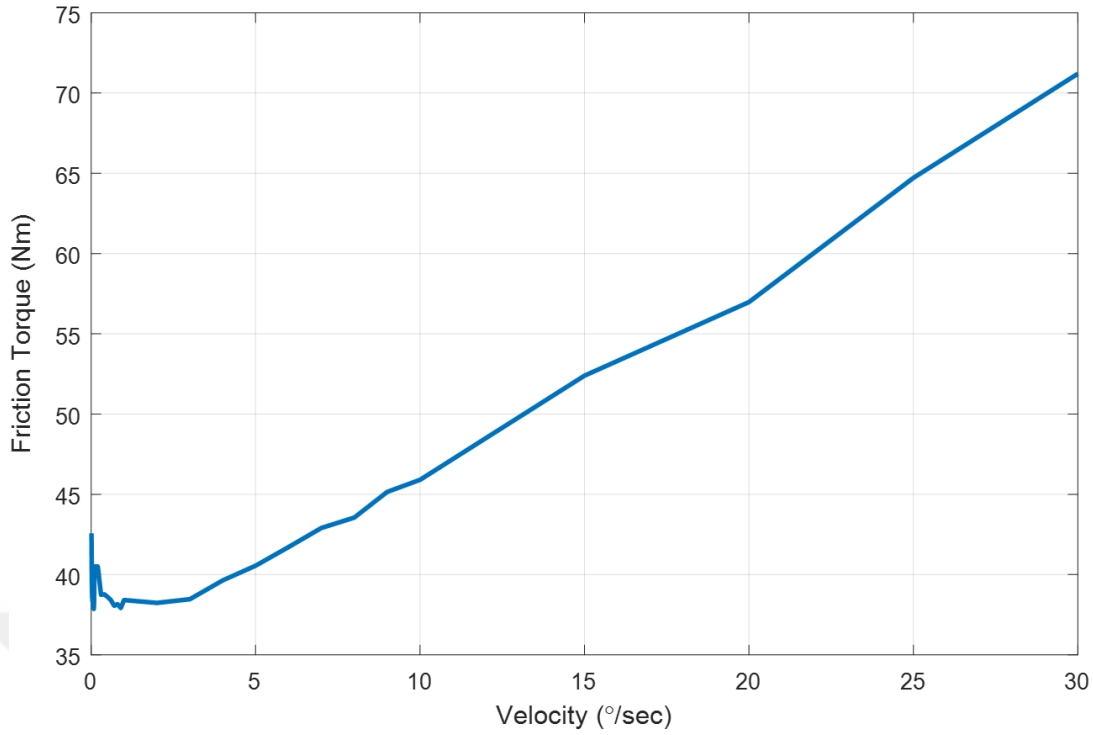


Figure 3.6: Elevation Friction Torque vs. Angular Velocity

All azimuth axis tests were performed on zero slope bench, therefore, unbalance torque was not acting. Since azimuth axis would be operated in a similar manner, T_u could be regarded as zero. Even with final elevation axis configuration, in which all cooling hoses, laser fibers, and cables are installed, thanks to proper routing, no significant springness torque was experienced by azimuth axis. Hence, $K_s\theta$ is zero, too. $\mathcal{T}_{cogging}$ is calculated theoretically as 2.5°, where $\#Sloth$ is 144 and $\#Pole$ is 36. On azimuth hysteresis curve, as expected for low speeds, cogging ripple pattern at period of 2.5°is distinguishable with T_c amplitude of 8.45 Nm. As velocity increases, inertia filters out cogging effects. Last but not least, friction, as the largest torque component, are constant over a large motion range. Time averaged for removing cogging term and mapped onto corresponding constant gross sliding velocity value, complete characterization of frictional behavior is obtained as presented in Figure 3.3.

Although methodology necessitates repeating the tests for several orientations, end even turning the gimbal upside down for complete characterization, i.e., determining CoG offsets, is not feasible. However, the center shift of hysteresis curve gives effective T_u = 14 Nm for operational conditions by means of stationary basement.

As well as longitudinal center shift, shear sway is discernible on hysteresis curve, which indicates springness term. Although all flexible elements were routed appropriately, it was impossible to get rid of all their effects. Regarding the linear fashion in springiness, K_s could be inferred as 54 Nm/θ. $\mathcal{T}_{cogging}$ is calculated theoretically as 3.3°, where $\#Sloth$ is 108 and $\#Pole$ is 18. On elevation hysteresis curve, cogging ripples at period of 3.3°is distinguishable with amplitude of 5.07 Nm. Lastly, mapped onto corresponding constant rates, friction characteristics is presented in Figure 3.6.

3.1.1.2 Dynamic Response Tests

In order to analyze frequency response of dynamic systems, several test inputs such as sinusoidal, white noise, or chirp signal are used. Input-output dynamic relationship is expressed in frequency domain as transfer function. Defining mathematical expression is represented in Equation 3.2, along with visual description (Figure 3.7).

$$PSD_{out}(f) = PSD_{in}(f)|G(f)| \tag{3.2}$$

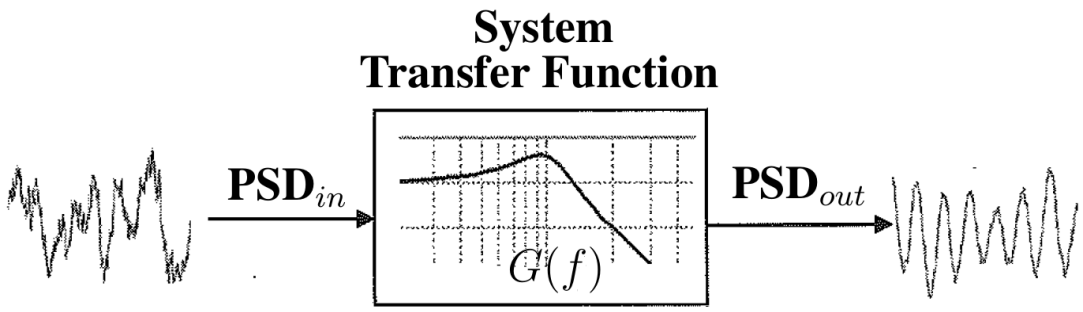


Figure 3.7: Dynamic Linear System Input-Output Relationship

Tests were envisaged to performed by driving axis motor and measuring up to 3 simultaneous transfer functions in a real-time manner on signal analyzer, as the setup is visualized by Figure 3.8. All the analysis was based on the linear system behavior assumption. Had observed the repetitive initial test results, it was concluded that the assumption held, and the tests preceded according to the plans, whose details are represented in Table 3.2, Table 3.3, and Table 3.4.

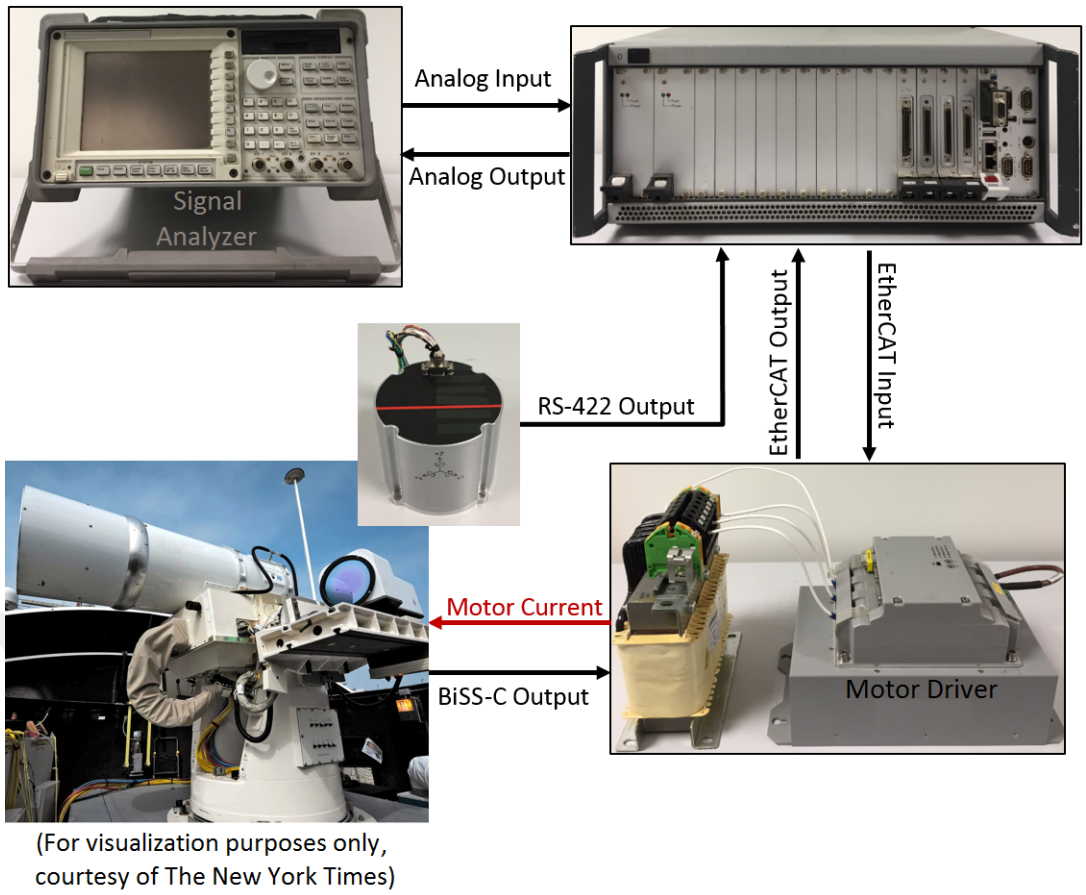


Figure 3.8: Dynamic Response Test Setup

Table 3.2: Kick-off Test Plan on Readily Available Motion Controller

Test Phase	Transfer Function Data Packages	Communication Protocol	Input (V PTP)	
			1	2
1	Closed Loop, Current	EtherCAT	✓	✓
		Analog	✓	✓
2	Open Loop, Torque to Velocity	EtherCAT	✓	✓
	Open Loop, Torque to Position		✓	✓
	Closed Loop, Velocity		✓	✓

Table 3.3: Azimuth Axis Dynamic Response Identification Tests Plan

Transfer Function Data Packages	Elevation Axis Position (°)	Input Level (V PTP)					
		1	2	4	6	8	10
	0	✓	✓	✓	✓	✓	✓
	5				✓	✓	
∗ Closed Loop, Current	10				✓	✓	
	15				✓	✓	
	20				✓	✓	
	25				✓	✓	
	30				✓	✓	
∗ Open Loop, Azimuth	35				✓	✓	
Axis Torque to	40				✓	✓	
Azimuth Axis Velocity	45	✓	✓	✓	✓	✓	✓
	50				✓	✓	
	55				✓	✓	
	60				✓	✓	
	65				✓	✓	
∗ Open Loop, Azimuth	70				✓	✓	
Axis Torque to	75				✓	✓	
Elevation Axis Velocity	80				✓	✓	
	85				✓	✓	
	90	✓	✓	✓	✓	✓	✓
∗ Closed Loop, Velocity	0			✓	✓	✓	✓
∗ Open Loop, Azimuth	45			✓	✓	✓	✓
Axis Velocity to Position	90	✓	✓	✓	✓	✓	✓

In test setup, analog sine sweep input, generated by signal analyzer, was commanded as current, open and closed loop velocity demands. Since signal analyzer do not support EtherCAT protocol, xPC Target real-time computer was used as analog to EtherCAT converter for current loop tests. In velocity loop tests, it carried out additional functionalities such as reading RS-422 output format gyro, converting data into ana-

log as well, and implementing control action, in particular for closed loop operation. Although motion controllers were selected, due to the latency on their shipment, with an available a servo drive on azimuth axis tests began. Since the available drive supports analog format along with EtherCAT, opportunities of benchmarking and prior verification of test infrastructure were caught.

Table 3.4: Elevation Axis Dynamic Response Identification Tests Plan

Transfer Function Data Packages	Elevation Axis Position (°)	Input Level (V PTP) 1	2	4	6	8	10
∗ Closed Loop, Current	0	✓	✓	✓	✓	✓	✓
	5				✓	✓	
∗ Open Loop, Elevation	15				✓	✓	
Axis Torque to	26				✓	✓	
Elevation Axis Velocity	35				✓	✓	
	40				✓	✓	
∗ Open Loop, Elevation	56				✓	✓	
Axis Torque to	68				✓	✓	
Azimuth Axis Velocity	75				✓	✓	
∗ Closed Loop, Velocity	0	✓	✓	✓	✓	✓	✓
∗ Open Loop, Elevation	45	✓	✓	✓	✓	✓	✓
Axis Velocity to Position	90		✓	✓	✓	✓	✓

Firstly, analog input, generated by analyzer, was directly echoed on xPC Target real-time computer in order to verify all analog path. These tests were repeated for models running both 1 kHz and 4 kHz. After, analog input, as current demand, was sent to the drive on real-time computer, and motor current analog feedback was read, reversely, with models at 1 kHz and 4 kHz. Subsequently, via EtherCAT current commands, closed current loop were tested with several base times, cycle tick numbers and xPC target model sample times. Results related with test phase#1 is presented in Figure 3.9. Magnitude losses around 500 Hz for the tests at 1 kHz are due to Nyquist criteria.

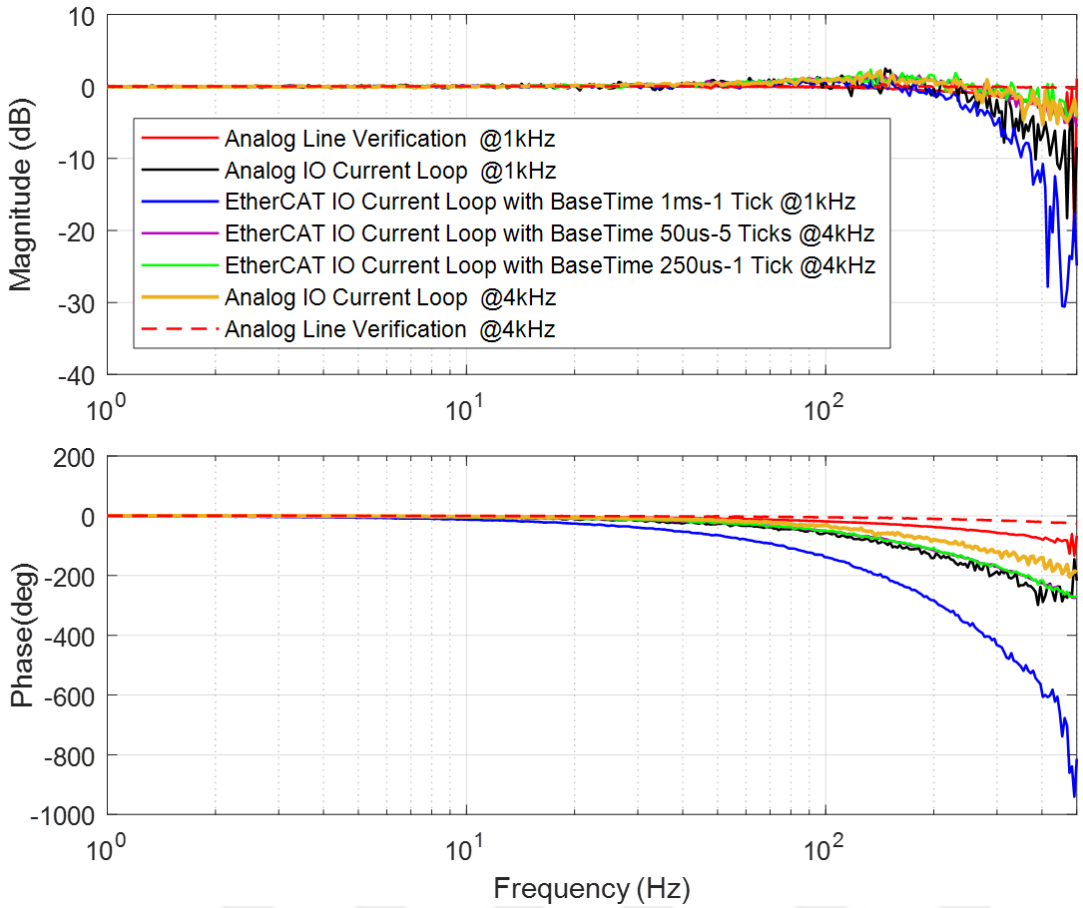


Figure 3.9: Results of Benchmark and Verification Tests via the Available Drive

In addition to magnitude losses, phase losses are also discernible and stem from several delay sources. Negative phase contribution of the transport lag ($G(j\omega) = e^{-j\omega T}$) is derived as Equation 3.3 in degrees. According to this formulation, for both 1 kHz and 4 kHz models, time delay (T) on just analog path is calculated 0.5 sample period. In other words, real-time computer could finish all required calculations and communication within half sample time. When driver with analog IO is taken into account, end to end process times are calculated as 1.313 ms and 836 μs, respectively, with the models at 1 kHz and 4 kHz. Analyzer to driver path took 0.5 sample period, however, due to slower analog communication dynamics of driver, these levels were yielded.

$$\angle G(j\omega) = -57.3^{\circ}\omega T \tag{3.3}$$

As anticipated, 50 μsec base time with 5 cycle ticks was achieved the same performance with 250 μsec base time with 1 cycle tick, and, eventually, 4 kHz cycle time was implemented. When motor driver with EtherCAT IO is taken into account, end to end process times are calculated as 3.5 ms and 1.1 ms, respectively, with the models at 1 kHz and 4 kHz. EtherCAT communication, as dominant delay factor, caused more latency when compared with analog IO. However, as sample rate is increased, EtherCAT performance was to converge on Analog. Besides, although latency was larger, experiencing EtherCAT networks creation on TwinCAT, running xPC target model with EtherCAT communication on xPC Target computer, and observing that current EtherCAT test infrastructure operated reliably were valuable outcomes. Further communication tests and optimization steps were left to be performed on the selected drivers. According to the Kick-off tests plan phase#2, all tests were completed, however, since, exactly the same responses were observed with both the available and selected drives, only to the tests, which were performed via the selected drives, coverage is given. Test results of the selected drive is presented in Figure 3.10.

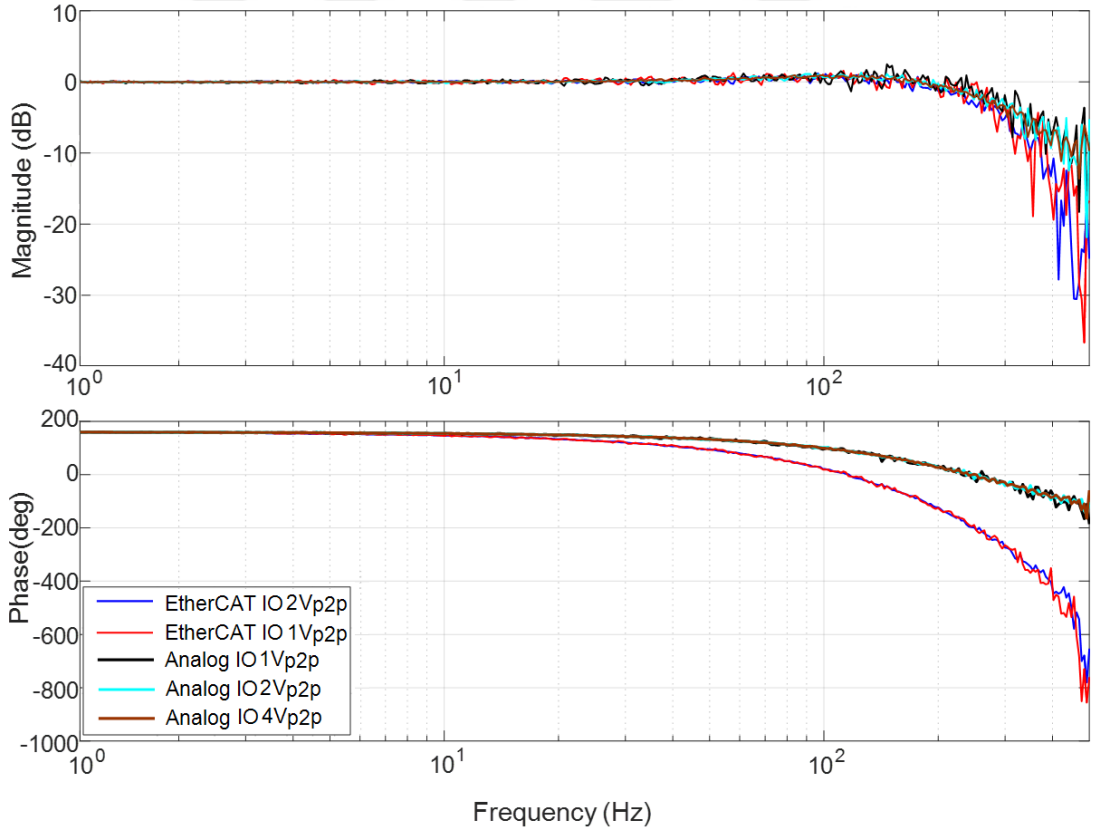


Figure 3.10: Results of Benchmark and Latency Tests via the Selected Drive

Regarding latency values, the selected driver is quite similar to the available driver, and they are independent from input amplitude. EtherCAT latency, between analyzer output to input, is measured as 3 ms on azimuth axis current closed-loop bode diagram (Figure 3.10). As well as the available driver, latency readings are done on low frequency interval for the selected drive, in order not to be intervened with driver internal current loop phase losses. During all the tests, moderate current loops, whose bandwidths are around 1 kHz, were present. In order to further investigate latency dynamics, with oscilloscope and current probe some additional tests were held. In this context, step input, applied by signal analyzer, along with current probe on motor phases were, simultaneously, monitored via oscilloscope. By this way, time between step current demand to current rise on motor wingdings were aimed to measured. As measurement details are presented Figure 3.11, one way latency is measured as 1.5 ms. Hence, it is concluded that, for both from and to analyzer directions, even latency values of 1.5 ms exist. Ensuring that, test infrastructure with reliable EtherCAT communication is available and latencies could be lowered via increased current loop bandwidth along with sightline manager sample rate, velocity loop tests proceeded.

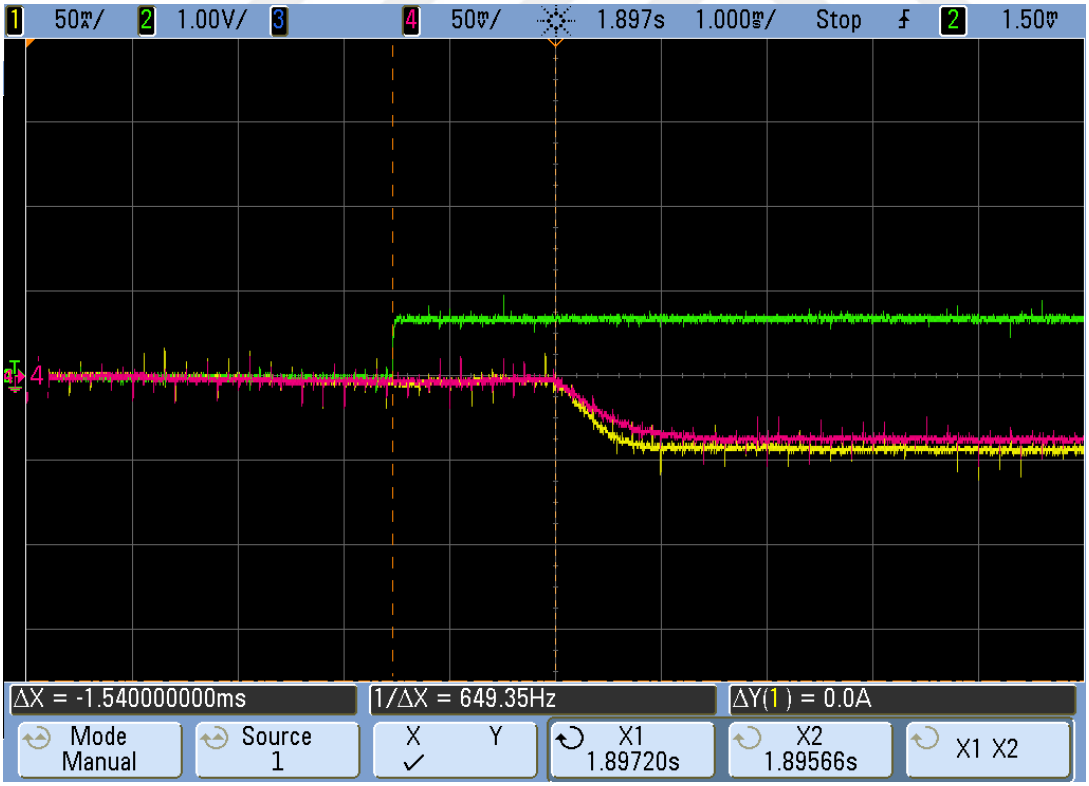


Figure 3.11: The Result of Latency Test on the Selected Drive via Current Probe

In torque demand input to velocity output transfer function tests, Analyzer output was scaled such that 1 V equals to 1 A. 1 V and 2 V peak to peak (PTP) current demand could not excite azimuth axis, input torque level fell below friction, and dynamic response magnitude remained at the level of noise within low frequency regime. Hence, although they took place in test plan at the beginning, remaining ones were canceled. Then, for 0°elevation axis orientation, repeated tests were performed on azimuth axis with 4 VPTP, 6 VPTP, 8 VPTP, and 10 VPTP sine-sweep current demands. Independent from input amplitude, the same structural dynamics were observed to be effective, as shown in Figure 3.12. When the same test set repeated at 45°and 90°elevation angles, input magnitude independency of structural dynamics remained valid. Thus, as nominal values, only tests with 6 and 8 VPTP were preferred to perform hereafter.

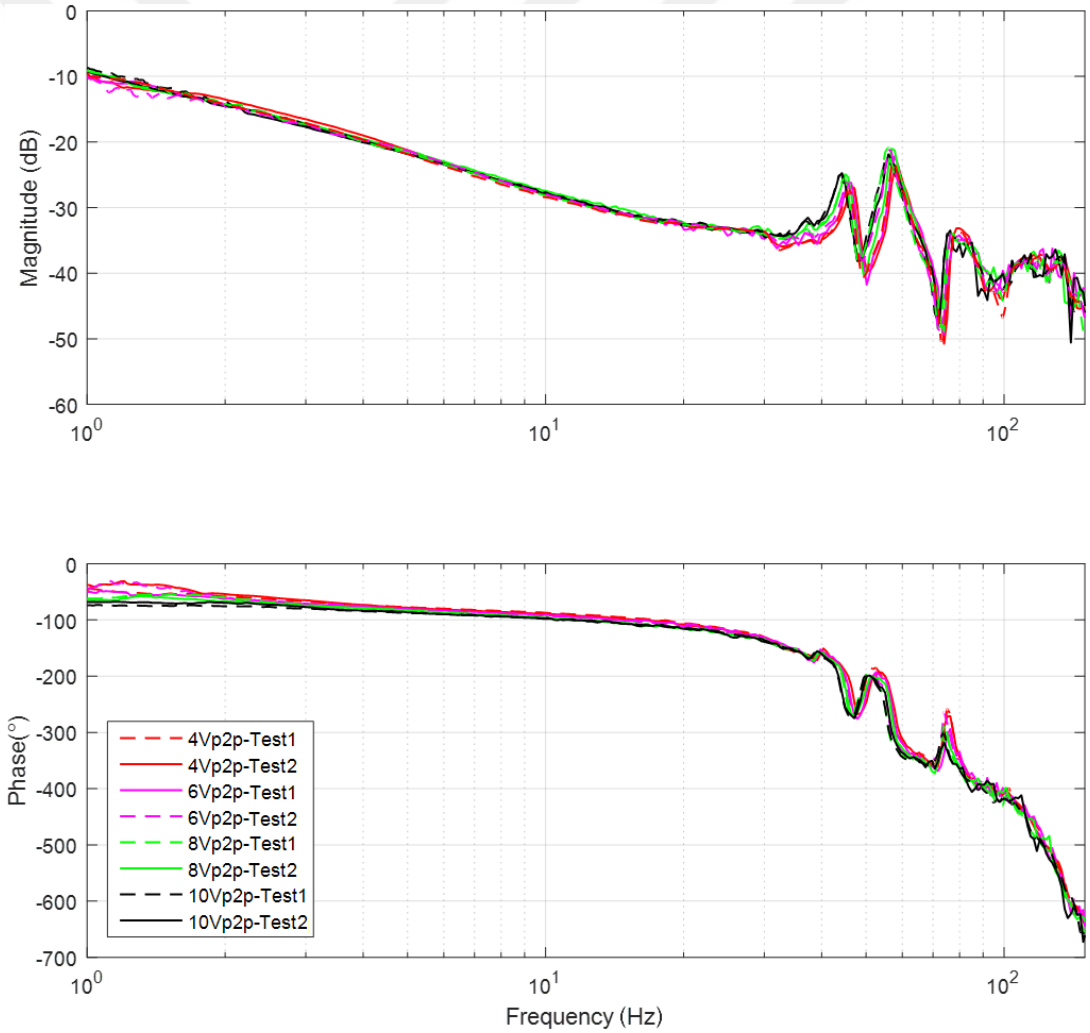


Figure 3.12: Azimuth Axis Torque to Velocity Transfer Functions (Elevation @0°)

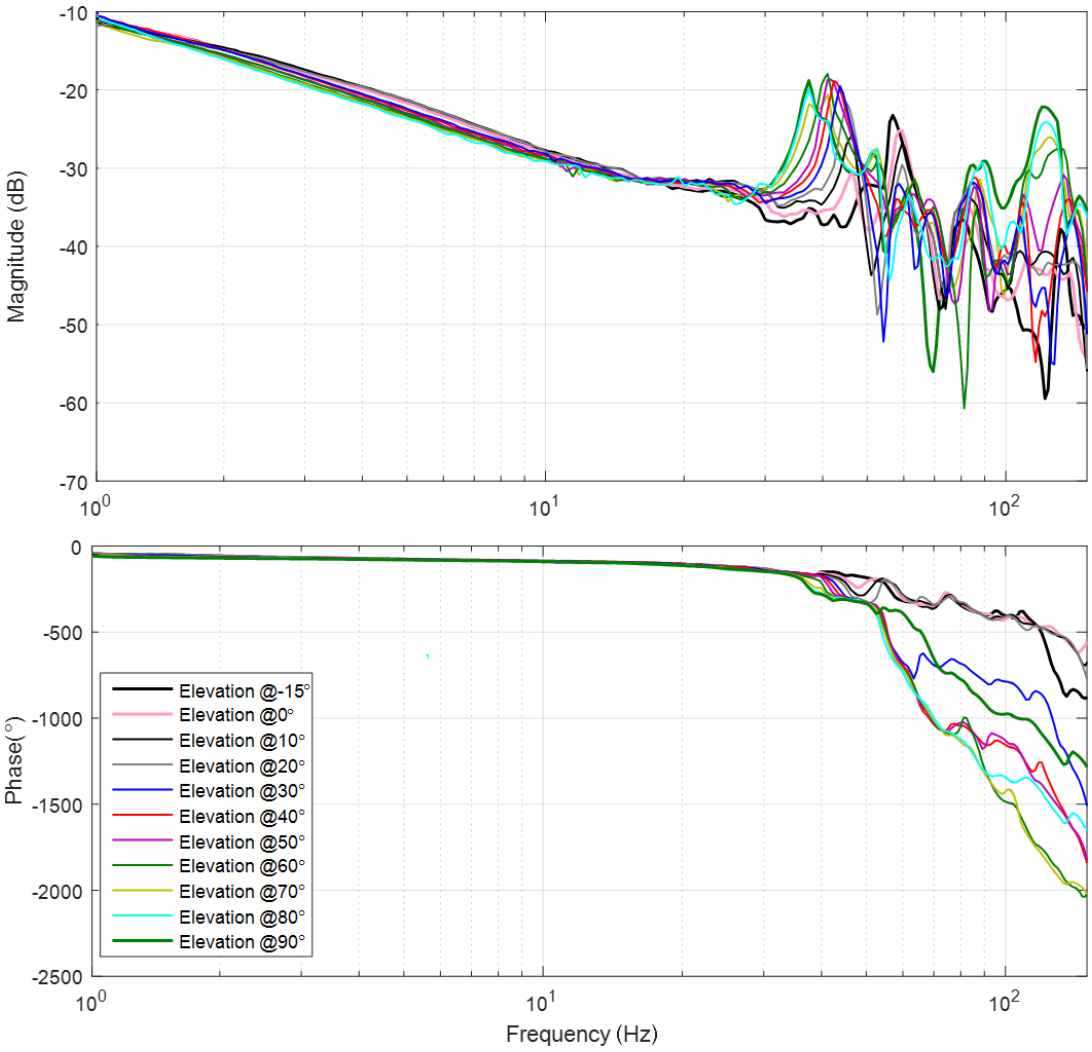


Figure 3.13: Azimuth Axis Torque to Velocity Transfer Functions
(For Elevation Angles 10°Apart)

Azimuth Axis torque to velocity transfer function tests, as planned, were performed for elevation axis orientations 5°apart between -15°to 90°. In order to simplify demonstration, only the results of tests at 6 VPTP input level with 10°elevation angle increments are presented in Figure 3.13. It is observed that resonant peaks are disappeared or their locations were shifted, in a repeatable manner, with respect to elevation axis orientation. FEA results in the servomechanism design section indicate the same dynamics. Stress distribution variations with elevation axis motion and resultant stress hardening/softening mechanisms could actuate cubic stiffness term and, in company with inertia alterations, cause position-varying response characteristics.

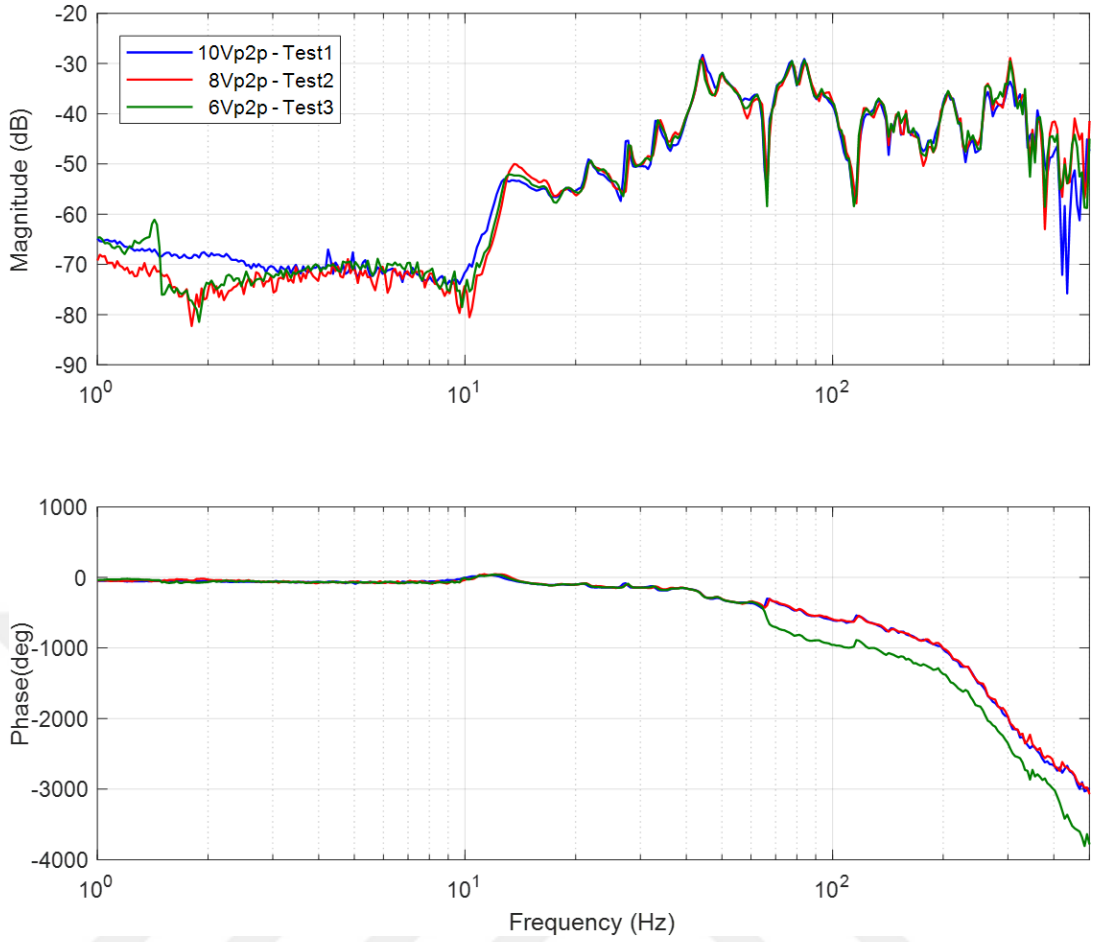


Figure 3.14: Azimuth Axis Torque to Elevation Axis Velocity Cross Axis Transfer Functions

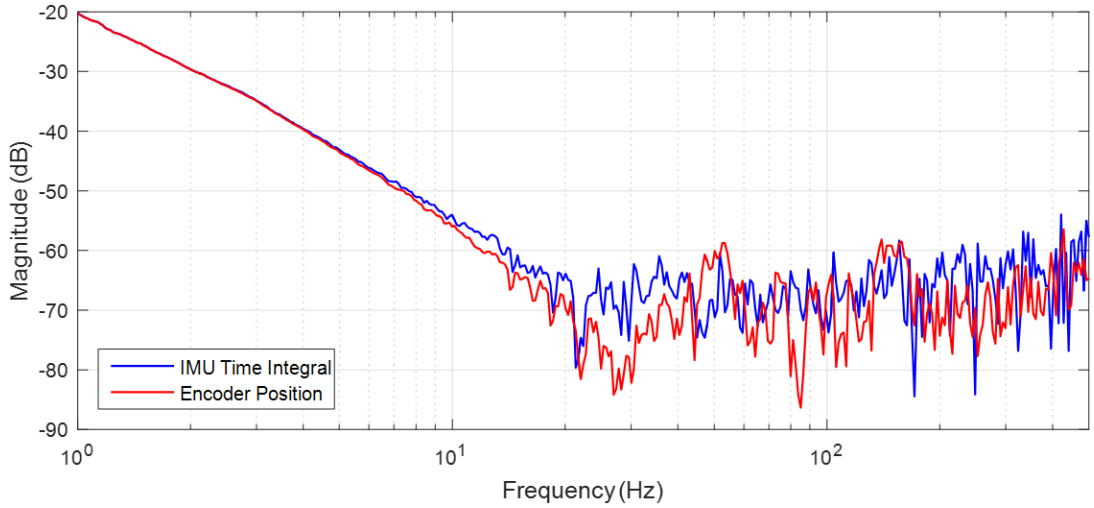


Figure 3.15: Azimuth Axis Torque to Position Transfer Functions

Torque to velocity transfer functions, as core test results, yielded valuable data for modeling and indicated consistent structural dynamics. Azimuth torque to elevation velocity transfer function tests, as well, indicated notable characteristics that cross-axis interactions were quite low. Up to 10 Hz and for significant input amplitudes, no azimuth axis excitation is reflected on elevation axis, at 0°orientation (Figure 3.14). Although frequency regime beyond 10 Hz exhibits more inter-axis coupling due to resonating behavior, by 3%, interaction levels still are not worth considering.

For azimuth velocity closed loop transfer function (CLTF) tests, a cursory P controller was applied. Thereby, controller implementation on test infrastructure was examined, and synthesized open loop plant transfer functions from closed loop tests were able to be compared with foregoing original tests. Comparison eventuated in congruence of test-resultant and synthesized OLTF. OLTF is derived from CLTF via equation 3.4.

$$\mathbf{OLTF} = \frac{\mathbf{1} - \mathbf{CLTF}}{\mathbf{CLTF}} \tag{3.4}$$

Azimuth axis velocity input to position output tests were performed using both encoder position readings and derived position data from IMU gyro time integral. Inspecting encoder and IMU coaxiality along with IMU coordinate transformation with elevation angle is one of the outputs obtained via this test set. Demonstrated by Figure 3.15, low frequency congruence of IMU gyro time integral and encoder signals corroborate tolerances and kinematics conversions. On structural dynamics wise, test set provide output, too. Since, encoder and IMU are located 1300 mm apart, looking over the synchronous responses sensed by them could provide insight and cross-checking about structure vibration characteristics in-between. For instance, the amplification in 20-30 Hz band could indicate a mode shape executed on elevation frame, and this dynamics is consistent with elevation axis analyses and tests.

Elevation axis velocity OLTF tests were performed in a different fashion than azimuth tests. Although, offset torque was applied in order to overcome, unbalance caused elevation axis drift. In order to compensate its effect and keep elevation angle around specified positions throughout the tests, in CLTF form tests were carried out and, eventually, OLTF was derived. Herein, not to distort originality, loose PI control was used. Priorly, OLTF synthesizing, as azimuth case, was verified by comparison.

The comparison was made between synthesized and test product OLTFs (Figure 3.16). In order to maintain elevation orientation around predefined angle, unbalance torque offset were being adjusted with difficulty, throughout the OLTF test. As a result, obtaining convergent and consistent results, the methodology was verified. Thus, elevation axis torque to velocity OLTF tests at several elevation angles proceeded.

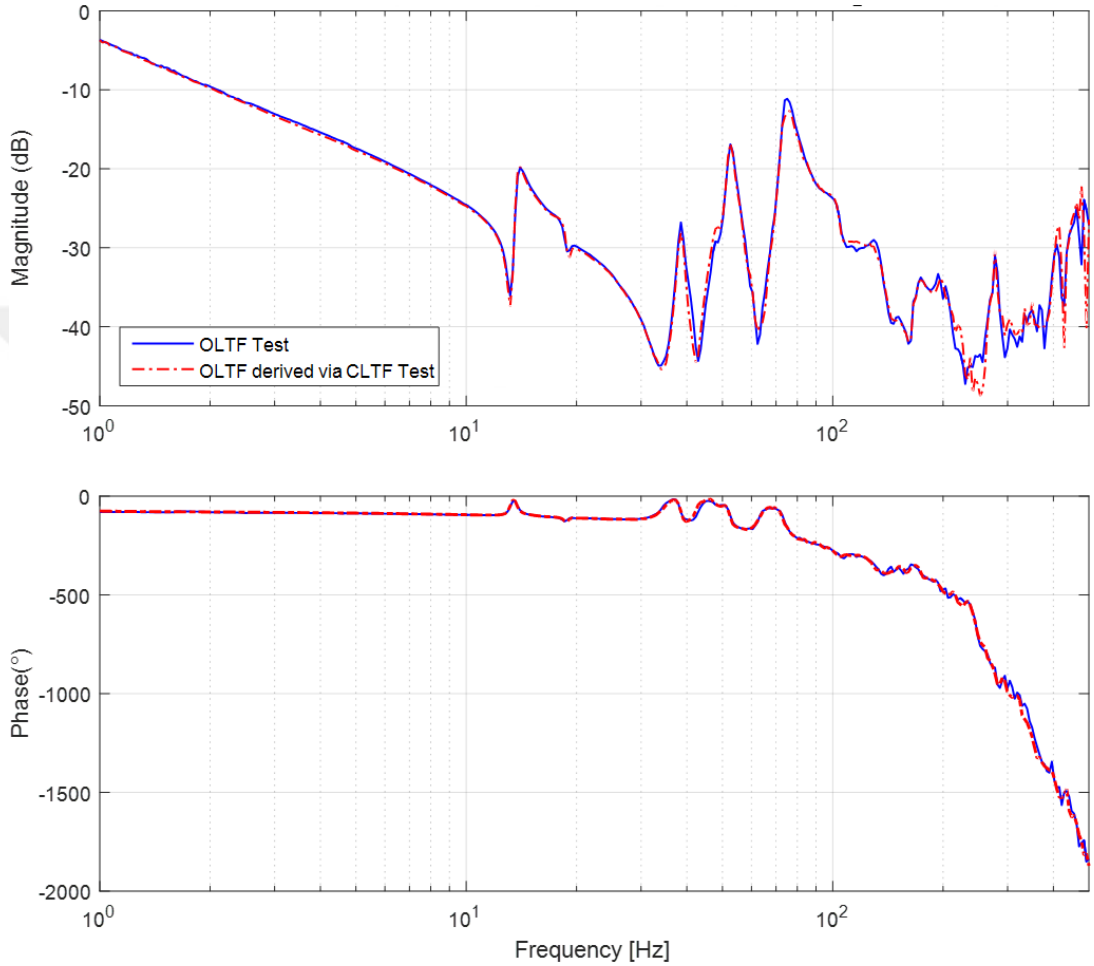


Figure 3.16: Comparison of Synthesized and Test Product Elevation Axis Torque to Velocity Transfer Functions

Elevation axis torque to velocity OLTF test results are presented in Figure 3.17 for elevation angles with approximately 10°increments. Since, the transfer functions are not dependent on input amplitude, in a similar manner with azimuth axis, only to the results, belong to 6 VPTP tests, place is given. Although it is not as significant as the one of azimuth axis, elevation angle dependent vibration characteristics still exists.

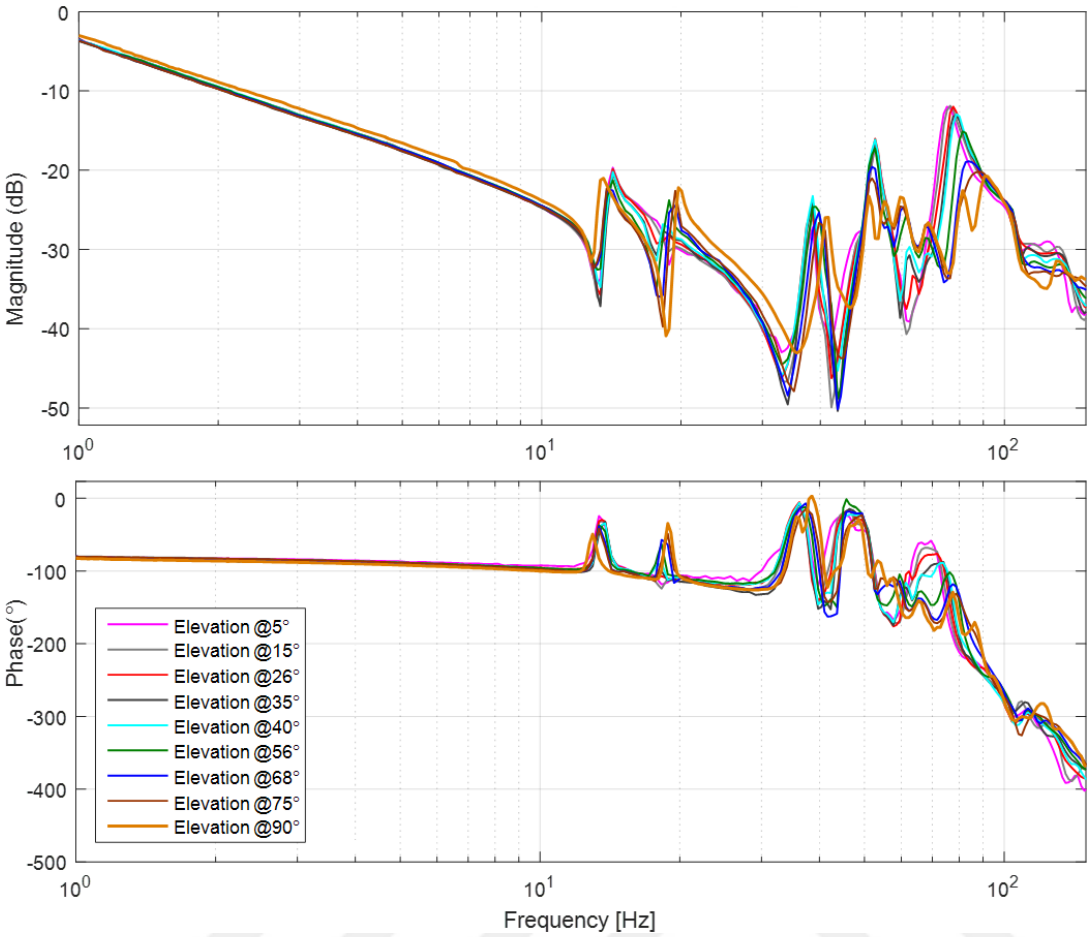


Figure 3.17: Elevation Axis Torque to Velocity Transfer Functions

(For Elevation Angles Approximately 10°Apart)

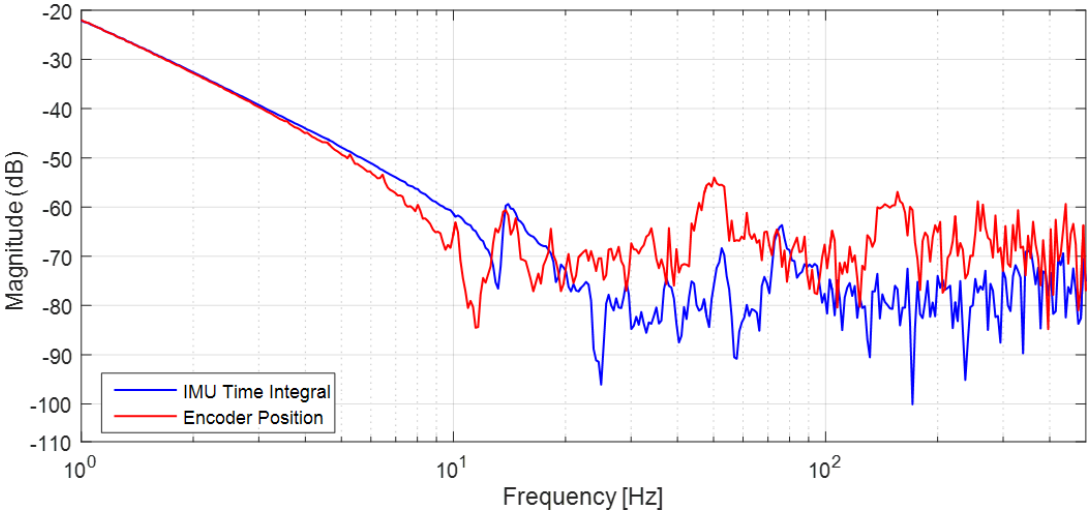


Figure 3.18: Elevation Axis Torque to Position Transfer Functions

Less effective inertia variations, stiffer support by virtue of two bearing arrangements, and lighter payload are considered as determinant factors on attenuated elevation angle dependency. According to final FEA results at servomechanism design section, it is anticipated that the first interactive mode is to be around 17-18 Hz and the second one is sliding between 17 and 24 Hz. Considering the first and second resonance peaks on Figure 3.17, total consistency with FEA is revealed. Moreover, among elevation axis torque to position transfer functions (Figure 3.18), the one with IMU gyro time integral output has considerably higher relative response around 10 Hz, which is estimated as first natural frequency via final FEA. Encoder is located to the elevation shaft end, and IMU is placed closer to middle, i.e., on lower right edge of elevation frame. Taking symmetrical vertical bending mode shape at 10 Hz (Figure 2.20a), the relative placement of sensors, and signal levels within frequency region of interest at elevation axis torque to position transfer functions together into consideration, the dynamic that it is a highly damped mode could be deduced. Ending dynamic response subsection, it should be noted that, with both dummy payloads and final units almost the same and already presented structural dynamics were observed.

3.1.2 FSM

FSM primary system identification indexes are impedance test and dynamic response. Impedance test indicates natural frequencies of the mechanism. On factory acceptance (FAT), both impedance and dynamic response tests were performed. Besides, on optical bench and final location in assembly, dynamic response tests were repeated.

3.1.2.1 Impedance Tests

Impedance testing was performed via impedance analyzer with excitation voltage of 1 VPTP between 20 Hz - 2 kHz range by one by for each axis. As presented in Figure 3.19, test results indicate that the first and interactive mode is at 350 Hz for the R_x axis, and at 322 Hz for the R_y axis. Attained values are consistent with producer design definition. Observed higher modes are neglected, because they could not be influential on closed loop control performance due to their low amplitude levels.

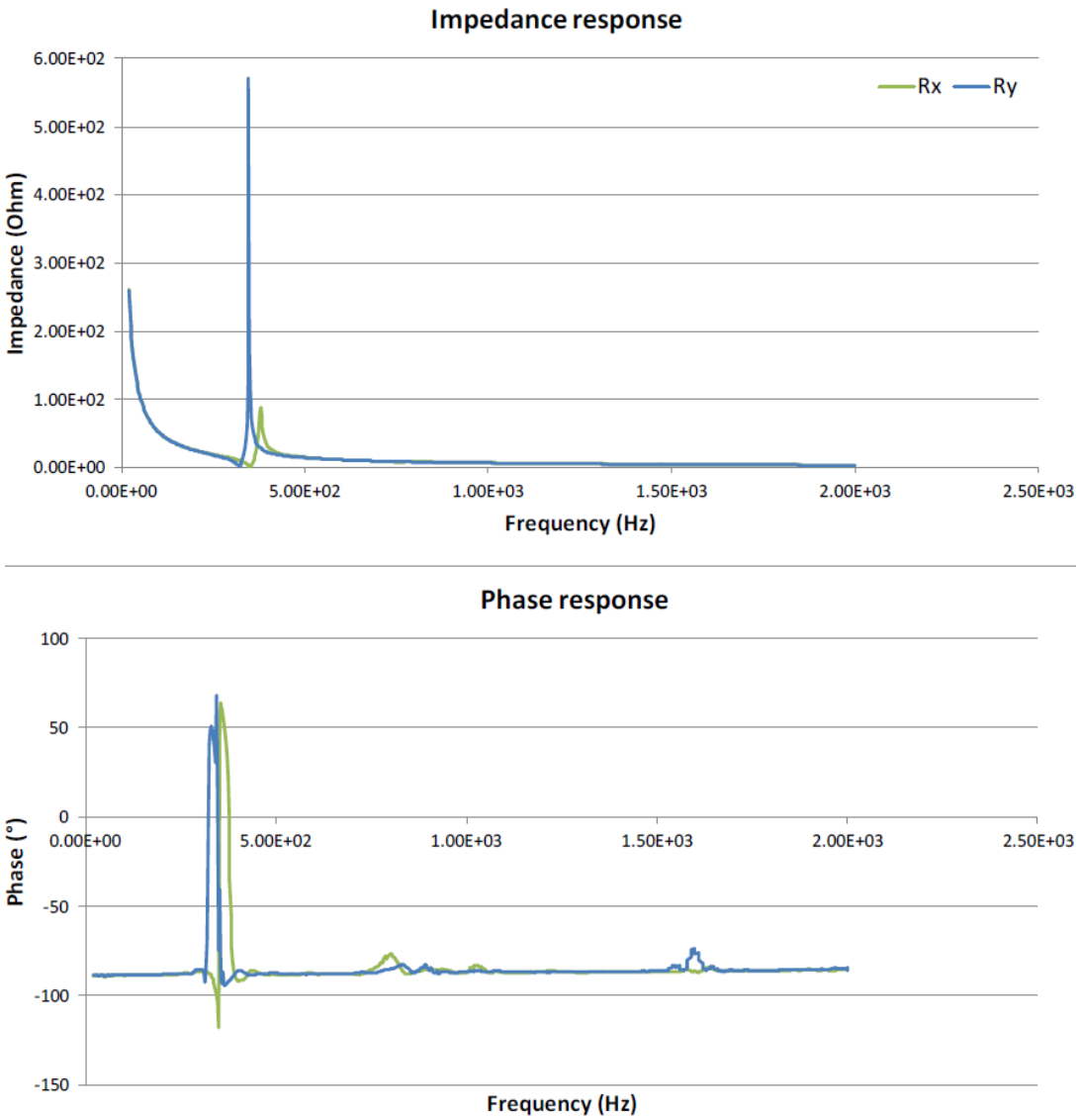


Figure 3.19: Results of the Impedance Measurements for both Axes

3.1.2.2 Dynamic Response Tests

Upon strain gauge calibration, closed loop transfer function of each axis was measured via 1 VPTP sine sweep input, which corresponds to ± 500 μrad stroke. In the tests, PI+I^2 control law was implemented for both axes with the same parameters, i.e., P = 0.08, I = 500, and I^2 = 100000 as proposed via producer. The only difference was the notch cutoff frequency, which is tuned to the mode frequency, as 350 Hz for the R_x axis and 322 Hz for the R_y axis. CLTF FAT results are presented in Figure 3.20.

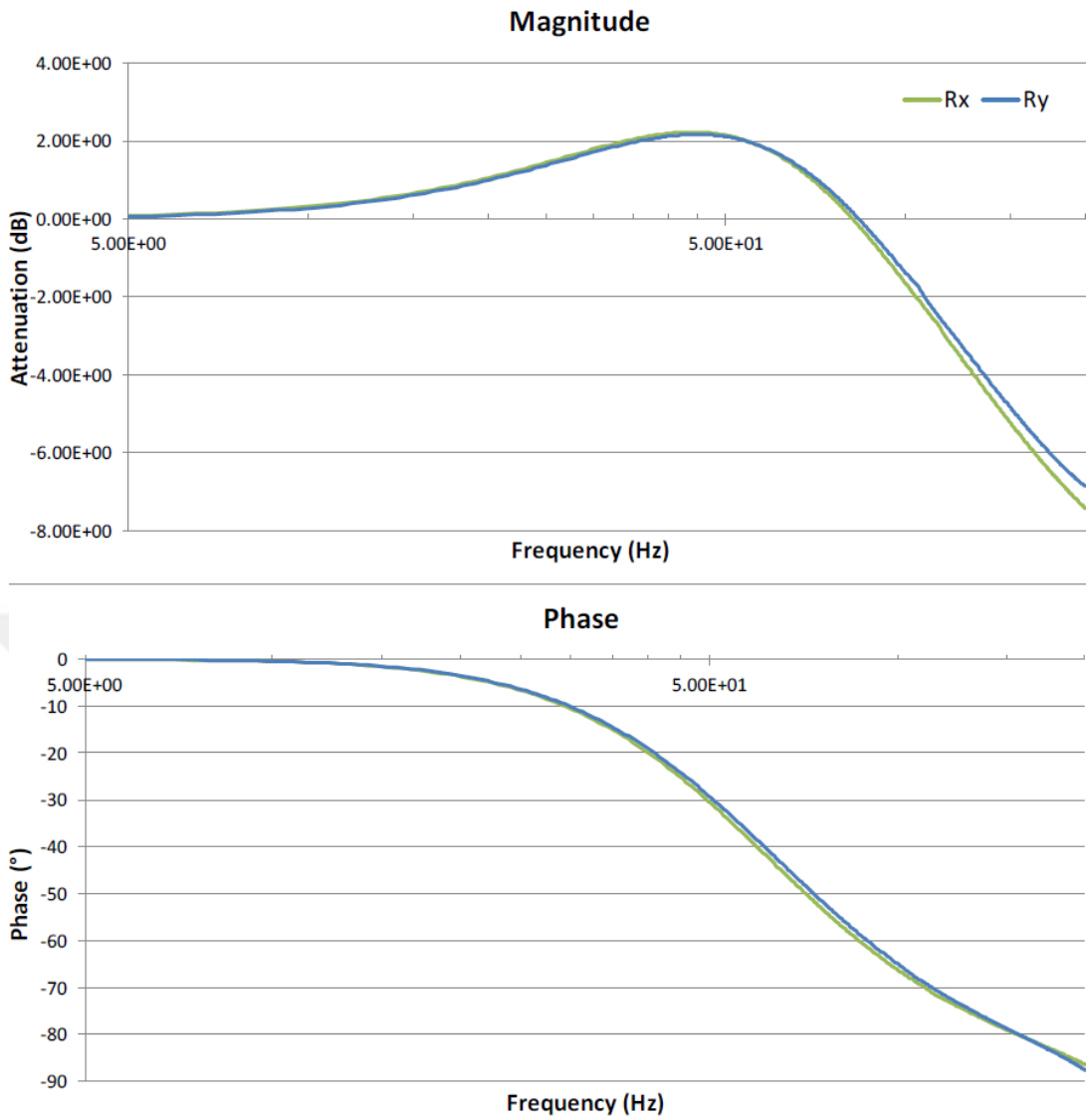


Figure 3.20: R_x and R_y Axes Closed Loop Transfer Functions Performed with 500μrad PTP Sine-sweep Input at FAT

At CLTF FATs, less than 3dB attenuation on the 100Hz was yielded on both axes, which is compliant with the bandwidth requirements. Tests were performed via both on analog and RS-422 channels, and the same performance were achieved. Before integrating into gimbal assembly, FSM was put to a test course of boresight on optical table within active tracker subassembly during embodying. However, due to high torques, exerted via FSM during dynamic response tests, all frame underwent resonance. That is why, remaining dynamic response tests were left to final assembly. Test results on final location in assembly are presented in Figure 3.21 and Figure 3.22.

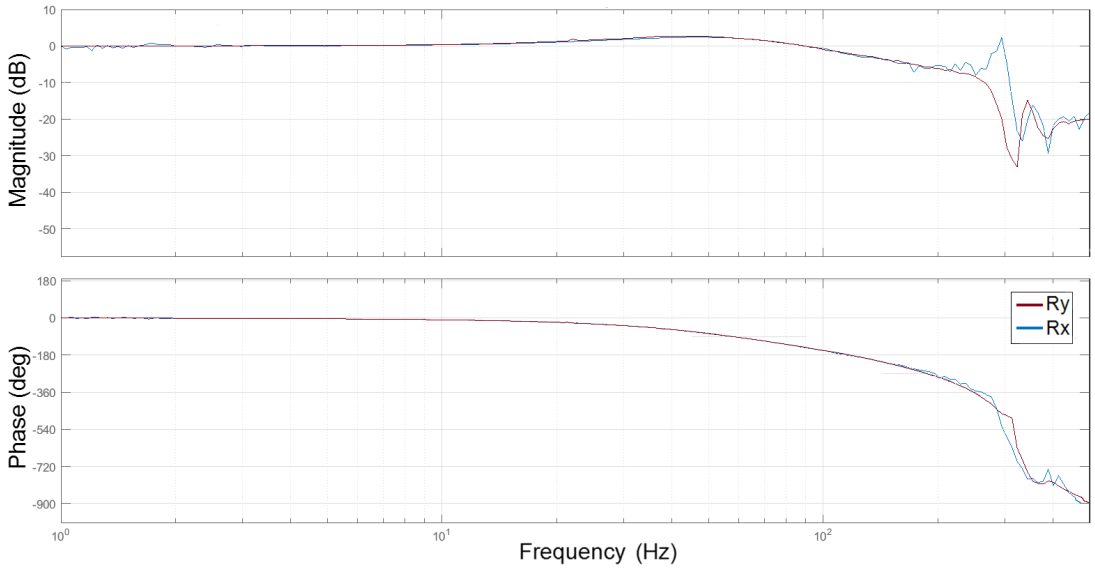


Figure 3.21: R_x and R_y Axes Closed Loop Transfer Functions Performed with 500μrad PTP Sine-sweep Input on Assembly

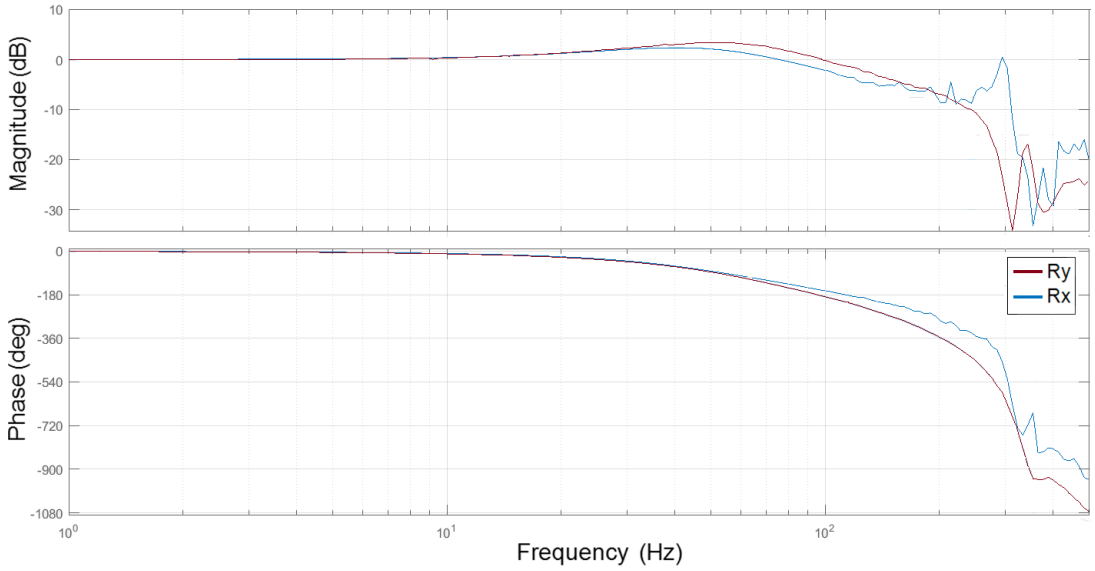


Figure 3.22: R_x and R_y Axes Closed Loop Transfer Functions Performed with 1000μrad PTP Sine-sweep Input on Assembly

On final configuration, Ry and Rx correspond to Elevation and Azimuth axes, respectively. Even up to limit strokes, more than adequate dynamic response performance persisted for both axes. Anisotropic mirror geometry caused the slight difference.

3.2 MODELING

3.2.1 Gimbal

Upon completion of identification tests on gimbal, modeling phase proceeded. Due to multidisciplinary characteristic of the project, from several professions a crowded team was working on. Therefore, it was quite hard to arrange time to carry out functional tests on final system, such as tracking on several target sets. Moreover, safety and logistics affairs further limited potential working times. Thus, necessity of detailed model gained much more importance, beyond assistance to controller design.

3.2.1.1 Friction, Unbalance, Springness and Cogging Modeling

The tests, which were carried by applying ultra-low rate torque at 0.01 A/s and aimed at determining corresponding breakaway torque, indicate the presence of noteworthy presliding displacement and hysteretic behavior (Figure 3.23). Furthermore, assessing low velocity trends of both axes on Figure 3.3 and Figure 3.6, reveals Coulomb and static friction terms along with the Stribeck Effect profile in-between.

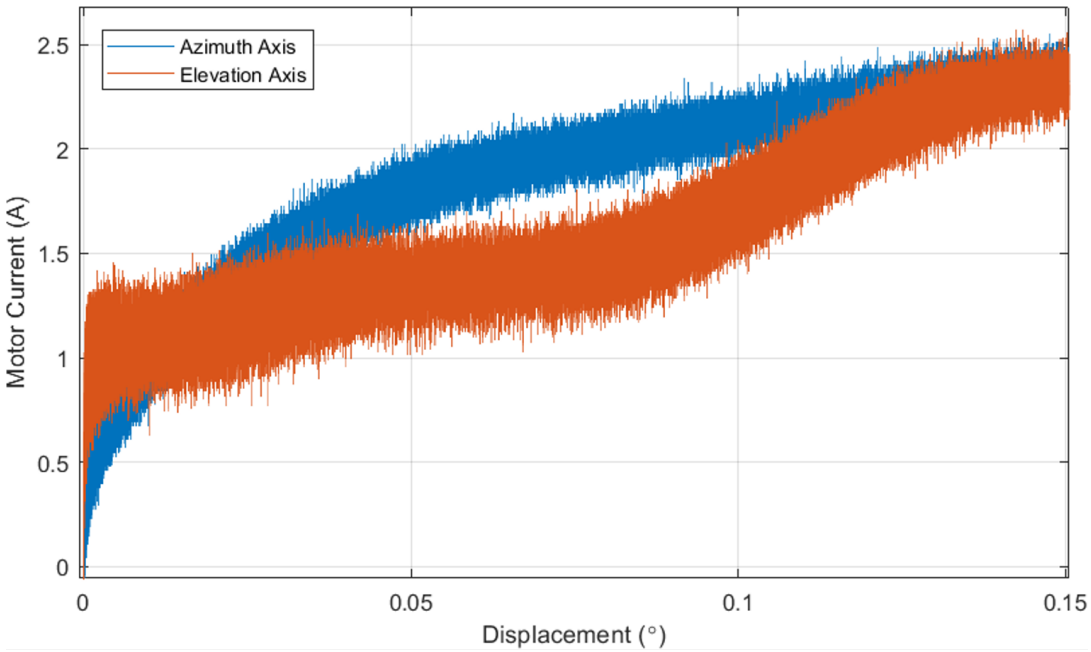


Figure 3.23: Elevation and Azimuth Axes Presiliding Regime Behaviors

With the increase in steady-state gross sliding velocities, higher friction torques arise as concluded from friction torque - velocity mappings. This bias is due to viscous term. As well as velocity dependency, time dependency of friction was observed. By the longer rest periods in stick state, i.e., dwell time, rising static friction phenomenon was experienced in consecutive tests. Lund Institute of Technology and INPG Grenoble (LuGre) friction model covers all abovesaid factors by the help of Equation Set 3.5 and presents a good trade-off between complexity and accuracy [97].

$$T_m = J\ddot{\theta} + T_f(\dot{\theta}, z) \tag{3.5a}$$

$$T_f(\dot{\theta}, z) = \sigma_0 + \sigma_1 \frac{dz}{dt} + \sigma_2 \dot{\theta} \tag{3.5b}$$

$$\frac{dz}{dt} = \dot{\theta} - \sigma_0 \frac{|\dot{\theta}|}{s(\dot{\theta})} z \tag{3.5c}$$

$$s(\dot{\theta}) = T_{Coulomb} + (T_{Static} - T_{Coulomb}) e^{-|\dot{\theta}/\dot{\theta}_s|^\delta} \tag{3.5d}$$

where J is equivalent inertia, θ is the angular displacement, T_m is the motor torque, T_f is friction torque, σ_2 viscous friction coefficient, σ_0 is Bristle stiffness term, σ_1 is Bristle damping term, z is Bristle deformation, $s(\dot{\theta})$ is Stribeck function, θ_s is Stribeck displacement, δ is Stribeck shape factor, T_{Static} is static friction component, and $T_{Coulomb}$ Coulomb friction component. Under steady-state conditions, z is constant, and its time derivative equals to zero. Thus, Equation 3.5c could be rearranged as $z_{ss} = sgn(\dot{\theta}) s(\dot{\theta}) / \sigma_0$. Substituting z_{ss} and Equation 3.5d into Equation 3.5b, rate dependent steady-state friction ($T_{f(ss)}(\dot{\theta})$) is obtained as presented with Equation 3.6.

$$T_{f(ss)}(\dot{\theta}) = \left(T_{Coulomb} + (T_{Static} - T_{Coulomb}) e^{-|\dot{\theta}/\dot{\theta}_s|^\delta} \right) sgn(\dot{\theta}) + \sigma_2 \dot{\theta} \tag{3.6}$$

$T_{f(ss)}(\dot{\theta})$ corresponds to friction torque - velocity mappings, on where parameter identification for T_{Static} and $T_{Coulomb}$ were practiced at zero velocity and saddle points, respectively. $\dot{\theta}_s$ falls into close vicinity of saddle point. σ_2 is the slope at gross-sliding regime. unitless δ is observed to be taken from 0.5 up to 2.5 in literature. Estimated parameters are presented in Table 3.5, and corresponding $T_{f(ss)}(\dot{\theta})$ fittings are demonstrated in Figure 3.24 and Figure 3.25.

Table 3.5: Estimated Steady State Friction Parameters

Axis	$T_{Coulomb}$ (Nm)	T_{Static} (Nm)	$\dot{\theta}_s$ (rad/s)	σ_2 (Nm·s/rad)	δ
Azimuth	167.750	210.000	0.120	273.600	2.500
Elevation	34.500	43.125	0.012	68.400	0.850

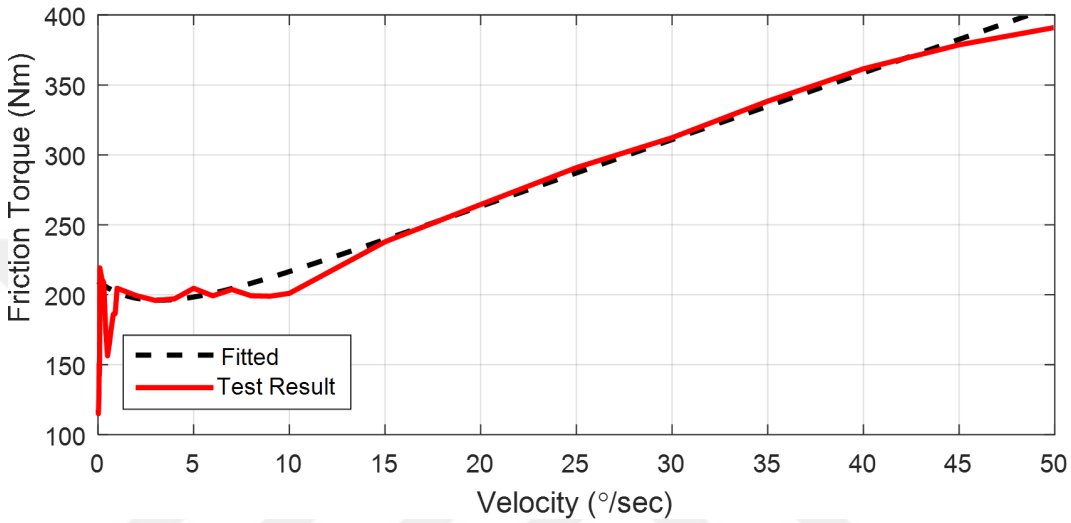


Figure 3.24: Azimuth Axis Friction Torque vs. Velocity Mappings

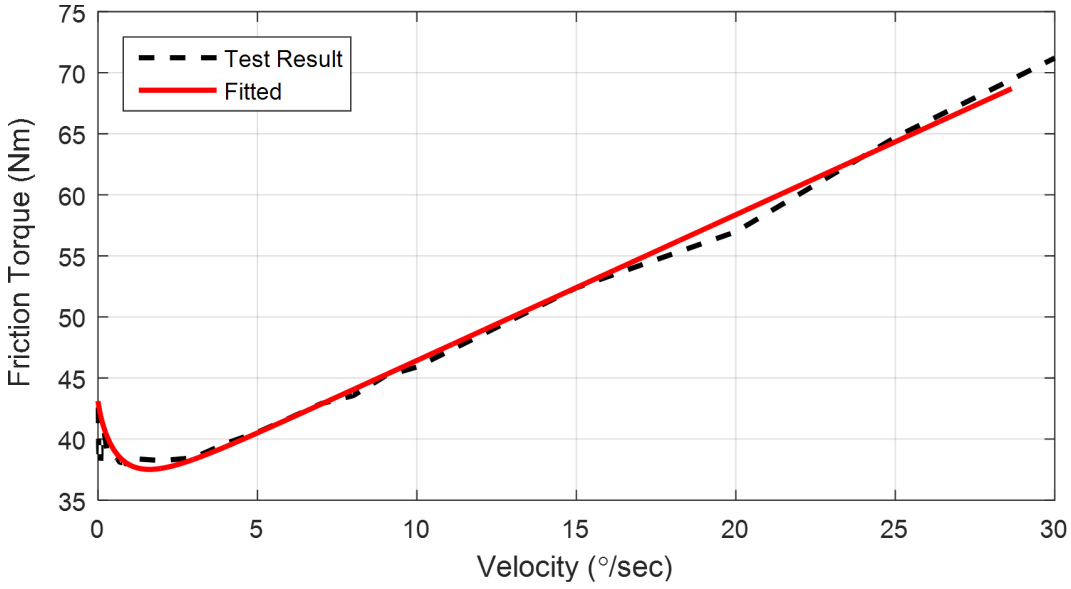


Figure 3.25: Elevation Axis Friction Torque vs. Velocity Mappings

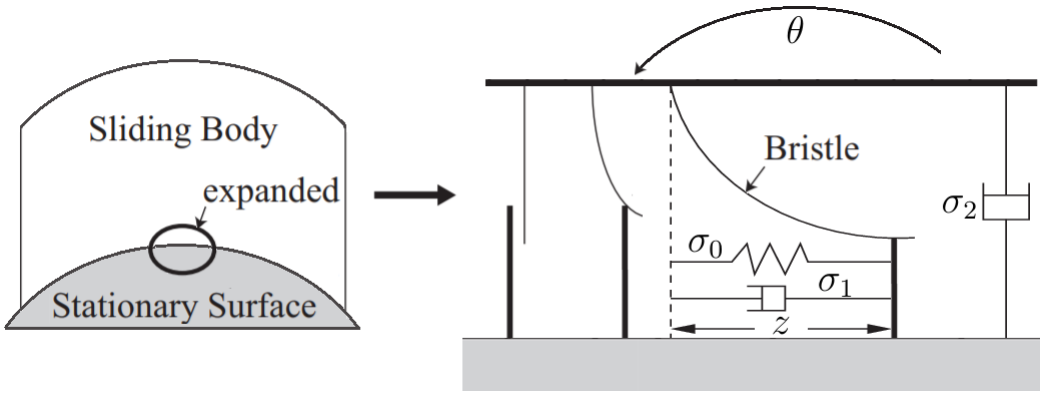


Figure 3.26: Bristle Interpretation of Friction Micromechanism with LuGre Model

In the LuGre model, presiliding regime behavior is modeled via elastic bristles, which are distributed on frictional surfaces in a random manner as visualized by the Figure 3.26. Until the onset of gross sliding, bristles act as if springs under compression, and against slowly increasing ramp torque input, the governing dynamic could be expressed via adapted version of Hooke's law, i.e., $\Delta T_m = \sigma_0 \Delta z$. Hence from the initial slopes of presliding regime curves (Figure 3.23), Bristle stiffnesses (σ_0) are calculated as 90000 Nm/rad and 50000 Nm/rad for azimuth and elevation axes, respectively.

In presiliding regime $\dot{\theta}$ is equal to $\dot{z}$. Thus, $T_m = J\ddot{\theta} + (\sigma_2 + \sigma_1)\dot{\theta} + \sigma_0\theta$ force equation holds. Converting into Laplace domain and equating to general form second order system, Relation 3.7 is obtained. Comparing peer terms yields $\omega_n = \sqrt{\sigma_0/J}$ and, ultimately, $\sigma_1 = 2\xi\omega_n J - \sigma_2 = 2\xi\sqrt{\sigma_0 J} - \sigma_2$. As inferred from CAD model and verified by low frequency torque to velocity transfer function slope, $J_a = 1200$ kgm^2 and $J_e = 975$ kgm^2. Considering damped nature of presiliding and a similar system, ξ is taken as 0.8 [97]. Hence, Bristle damping values (σ_1) are calculated as 16354 Nm/rad and 8322 Nm/rad for azimuth and elevation axes, respectively.

$$\frac{\theta(s)}{T_m(s)} = \frac{1}{Js^2 + (\sigma_2 + \sigma_1)s + \sigma_0} = \frac{K\omega_n}{s^2 + 2\xi\omega_n s + \omega_n^2} \tag{3.7}$$

By the determination of required 6 parameters, friction characteristics of both axes $T_f(\dot{\theta}, z)$ were modeled with Simulink as represented in Figure 3.27.

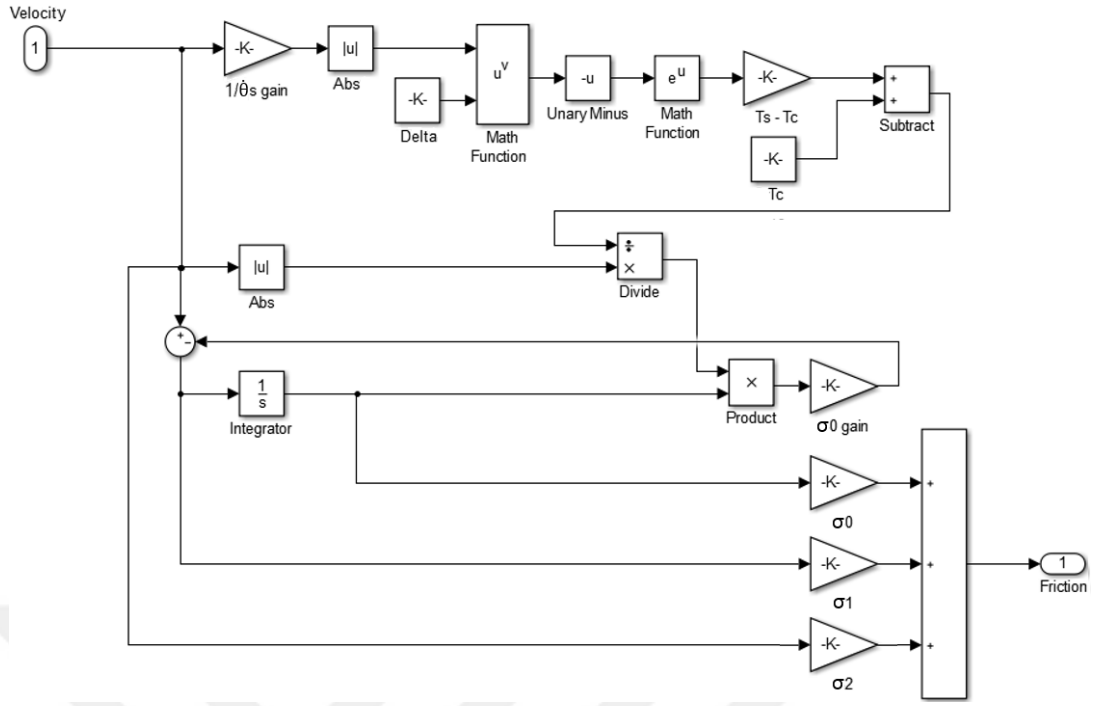


Figure 3.27: The LuGre Friction Model Simulink Implementation

Cogging torque exhibits absolute position dependent sinusoidal characteristic. Accordingly, T_c is modeled as $A_c \sin(\mathcal{T}_{cogging}\theta)$ where A_c is amplitude, and unit of θ in degrees. Pertaining to elevation axis, unbalance and springness torques are absolute position dependent, as well. Due to level arm length change as a function of cosine, unbalance torque (T_u) is modeled as $A_u \cos(\theta)$ with amplitude term A_u. Directly proportional to angular position, springness torque is act as $K_s\theta$. Related Simulink model branches for elevation axis is demonstrated in Figure 3.28.

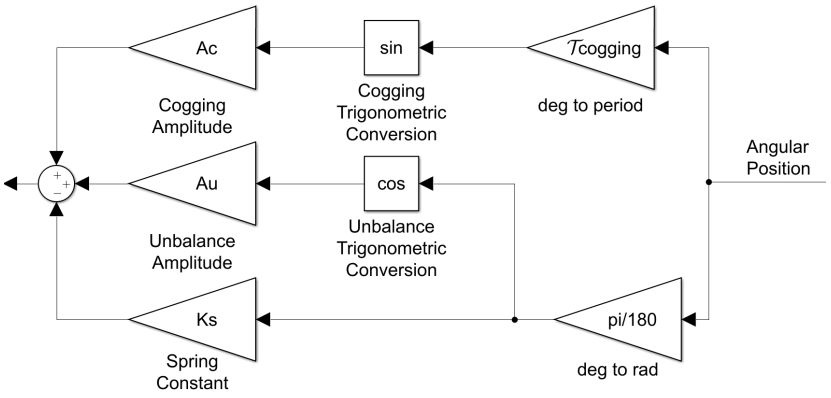


Figure 3.28: Cogging, Unbalance, and Springness Models Simulink Implementation

3.2.1.2 Dynamic Response Modeling

Adequate modeling of vibrational dynamics could be achieved via reduction to truncated second order general order transfer functions. Between motor excitation to response at any point on flexible structure, such as IMU, could be derived via relation, Equation 3.8. The modal participation factor ($Pcoff_n$) reflects the contribution level of a specific mode to overall response under excitation in a particular direction. FEA results could good $Pcoff_n$ initial guesses. Natural frequencies (ω_n) are definable on torque to velocity transfer functions, corresponding to magnitude peaks. Based on the width of resonant peak around its center, structural damping factor ξ could be assigned, typically, between 0.01 and 0.1. Manually fitted torque to velocity TFs, for elevation axis and at around 0°, are demonstrated in Figure 3.29 and Figure 3.30.

$$\frac{\ddot{\theta}_{output}}{\ddot{\theta}_{input}} = \sum_{n=1}^{\#\ of\ modes} \frac{Pcoff_n}{s^2 + 2s\xi\omega_n + \omega_n^2} \tag{3.8}$$

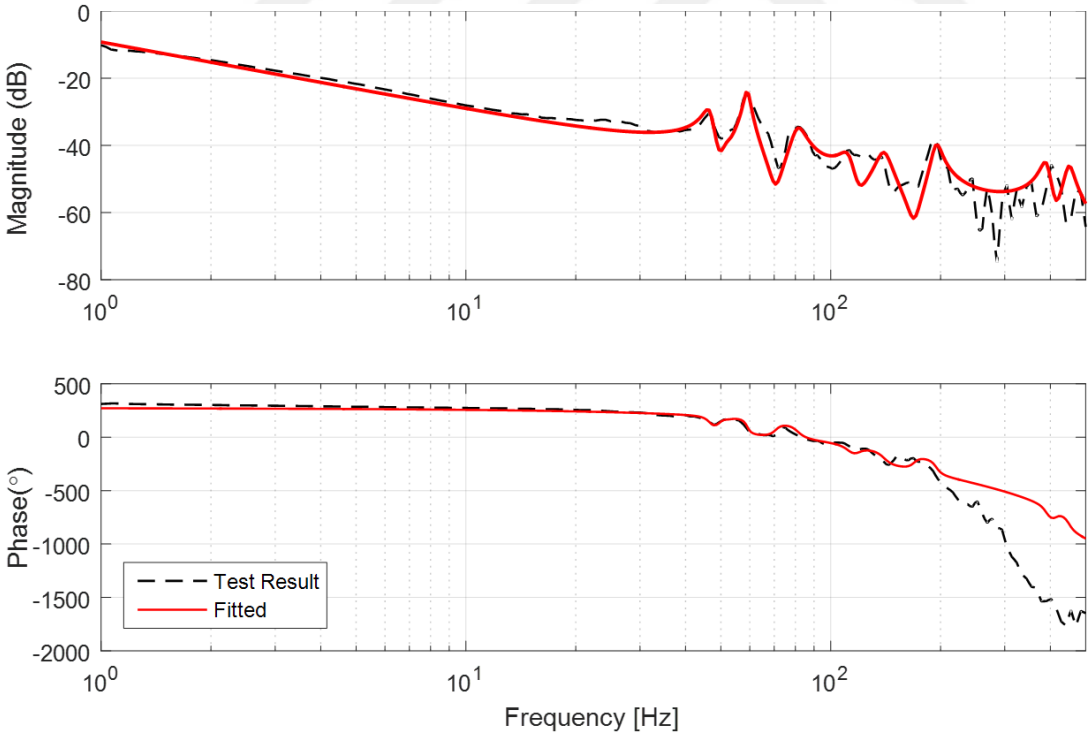


Figure 3.29: Comparison of Fitted and Test Product Azimuth Axis Torque to Velocity Transfer Functions

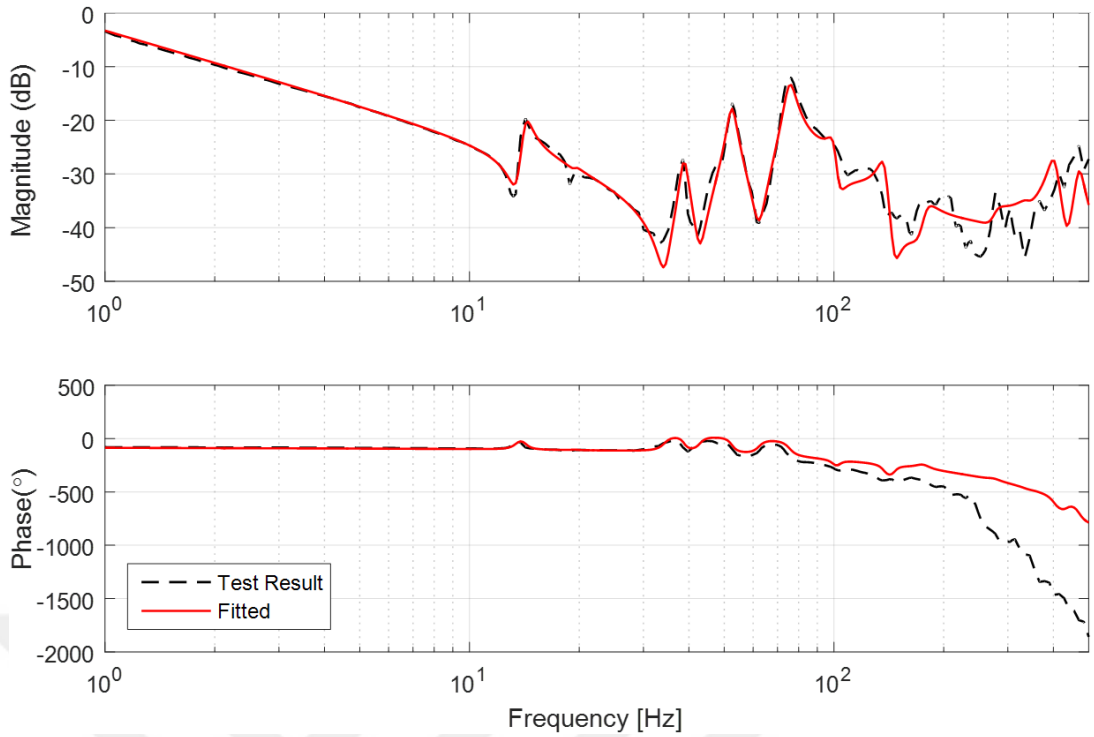


Figure 3.30: Comparison of Fitted and Test Product
Elevation Axis Torque to Velocity Transfer Functions

In a similar fashion, torque to angular velocity OLTF fittings were carried out at pretested elevation angles for both elevation and azimuth axes. Following this, elevation angle relationships between $Pcoff_n$ and ω_n were inferred for each specific resonant mode and fed into transfer function with varying coefficients (Figure 3.31). Exemplary $Pcoff_n$ vs. elevation angle correlations are presented in Figure 3.32.

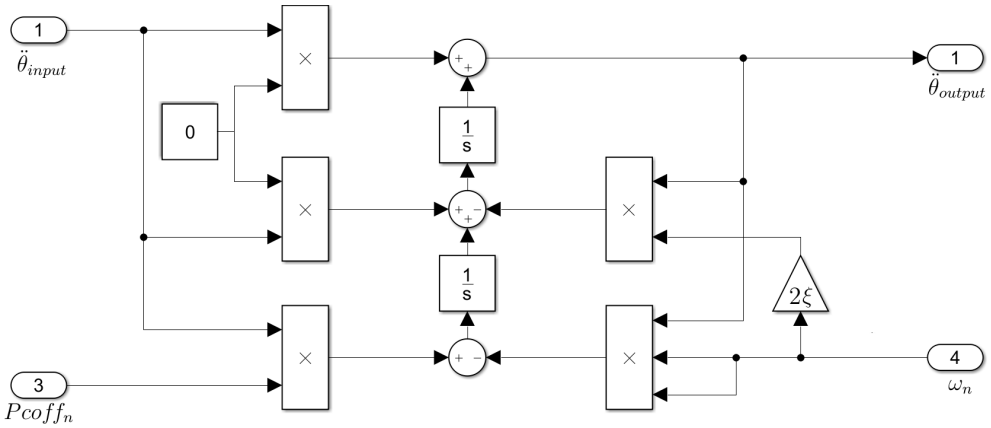


Figure 3.31: Simulink Transfer Function Model with Varying Coefficients

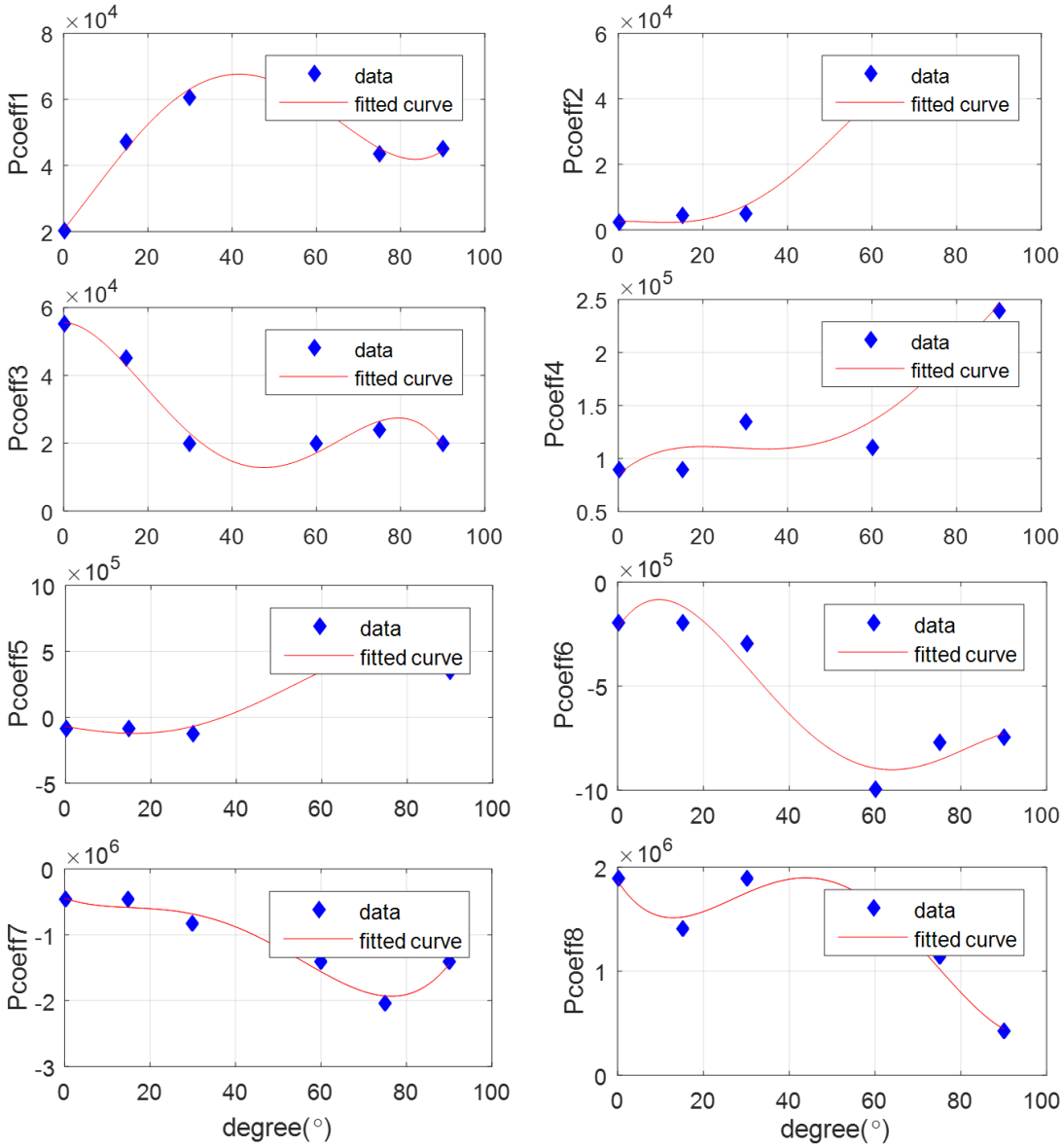


Figure 3.32: $Pcoff_n$ vs. Elevation Angle Fitted Curves for Azimuth Axis

Since velocity response was measured by gyro for identification, its dynamics were already reflected on fitted gimbal TF, except from latency. Latency is modeled via $e^{-st_{delay}}$ transport lag multiplication of fitted TF. Adding 1.5 ms delay on both forward and backward paths of plant model, better phase convergence could be achieved. However, lags arise from electronics and based on operation mode, different values would be dominant. Therefore, detailed coverage is left to oncoming sections. Thus, gimbal model took the final form (Figure 3.33). For expressing model performance, some test and simulation data comparisons are presented in Figures 3.34 and 3.34.

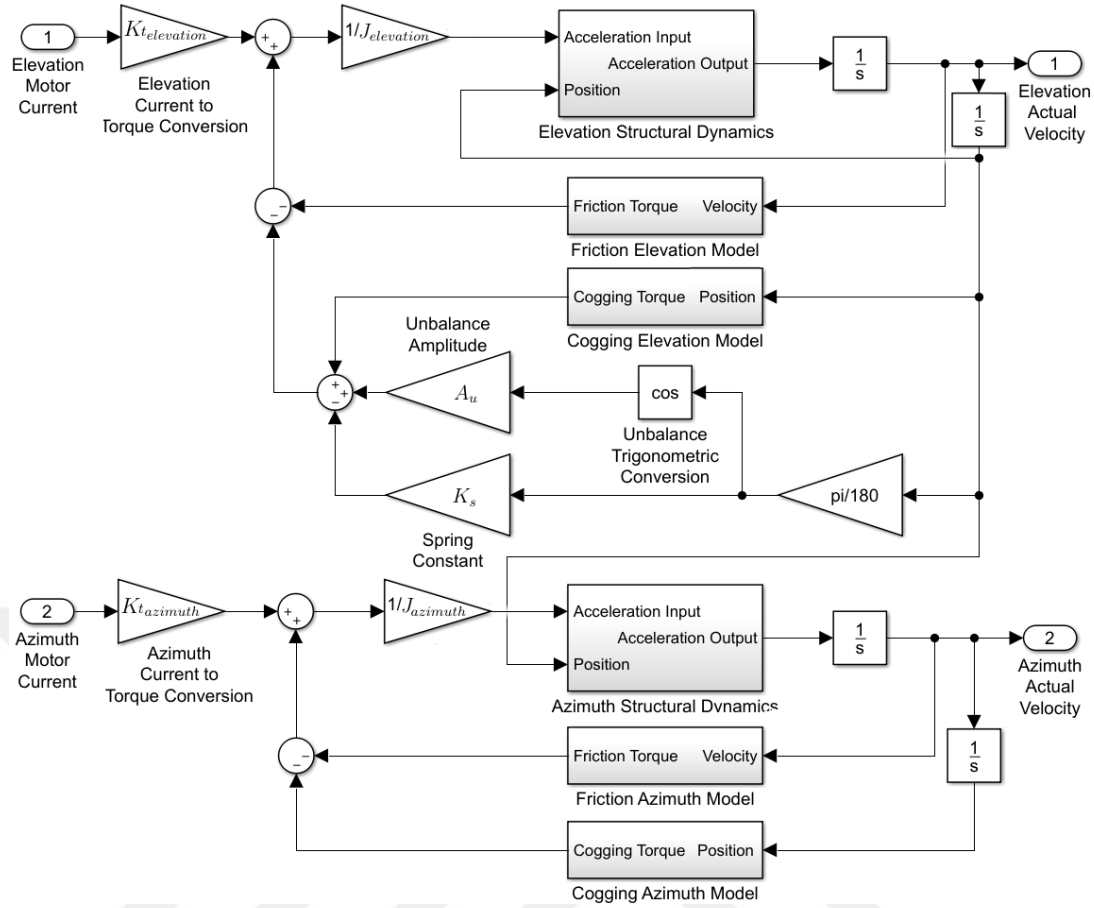


Figure 3.33: Final Version of 2-Axis Simulink Gimbal Model

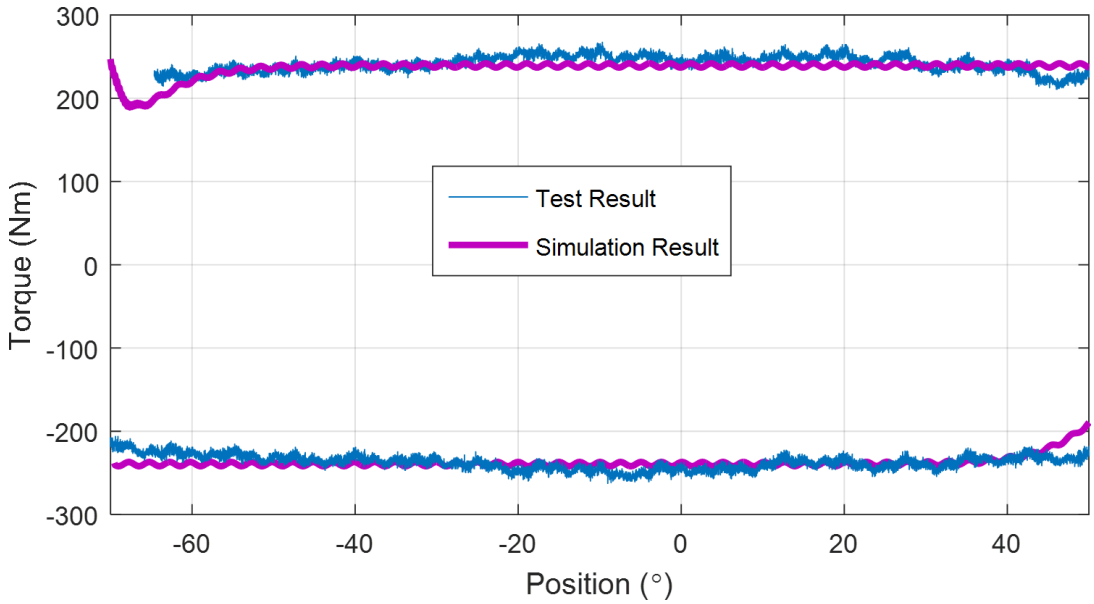


Figure 3.34: Azimuth Axis Hysteresis Curve Comparison at Constant 15 °/s Rate

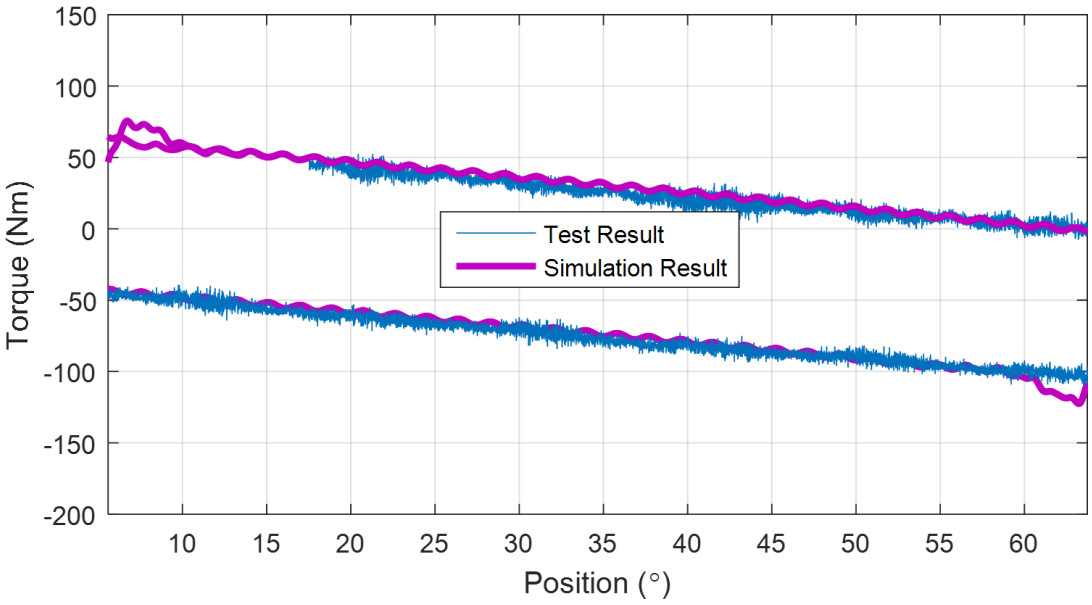
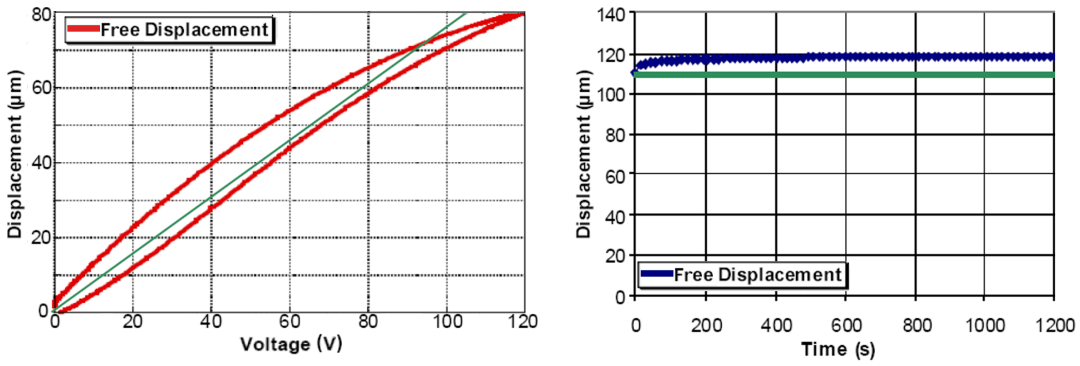


Figure 3.35: Elevation Axis Hysteresis Curve Comparison at Constant 15 °/s Rate

3.2.2 FSM

Electromechanic characteristics of piezoelectric materials are, mainly, modeled by Equation Pair 3.9, where S strain, T stress, D induction, E field, s^E constant field compliance, d piezoelectric strain per unit field, and ε^T constant stress permittivity.

$$D = d \times T + \varepsilon^T \times E \quad \& \quad S = s^E \times T + d \times E \tag{3.9}$$



(a) Hysteresis

(b) Drift (Creep)

Figure 3.36: Additional Effects on Piezoelectric Effector Performance [98]

Not knowing material properties, it is not possible to model with this detail level. Besides, on actuator level, additional factors, such as hysteresis, creep, and preloading side effects, could degrade model accuracy radically. Hysteretic nonlinearities could deviate linear modeling accuracy up to 15% as presented in Figure 3.36a. Also, creep could cause difference of around 5-10% between linear simulation results and reality (Figure 3.36b). In addition to these, preloading arrangements result in numerous phenomena, such as friction, stiction, and stress-concentration (Figure 3.37) [98].

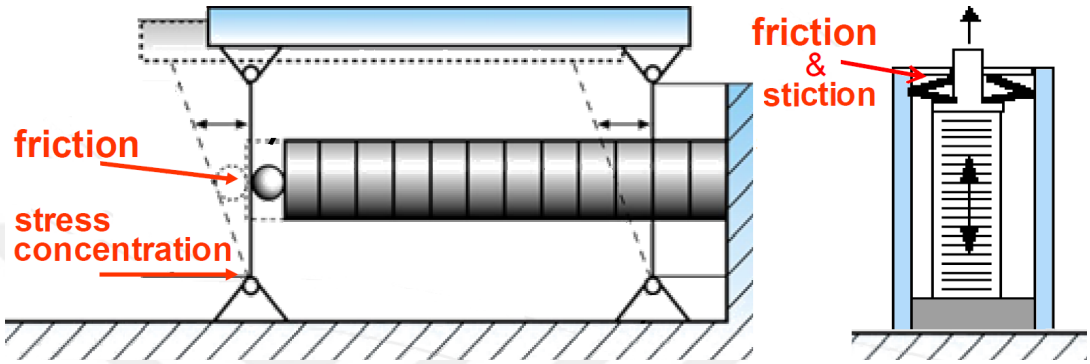


Figure 3.37: Drawbacks of Several Preloading Mechanisms [98]

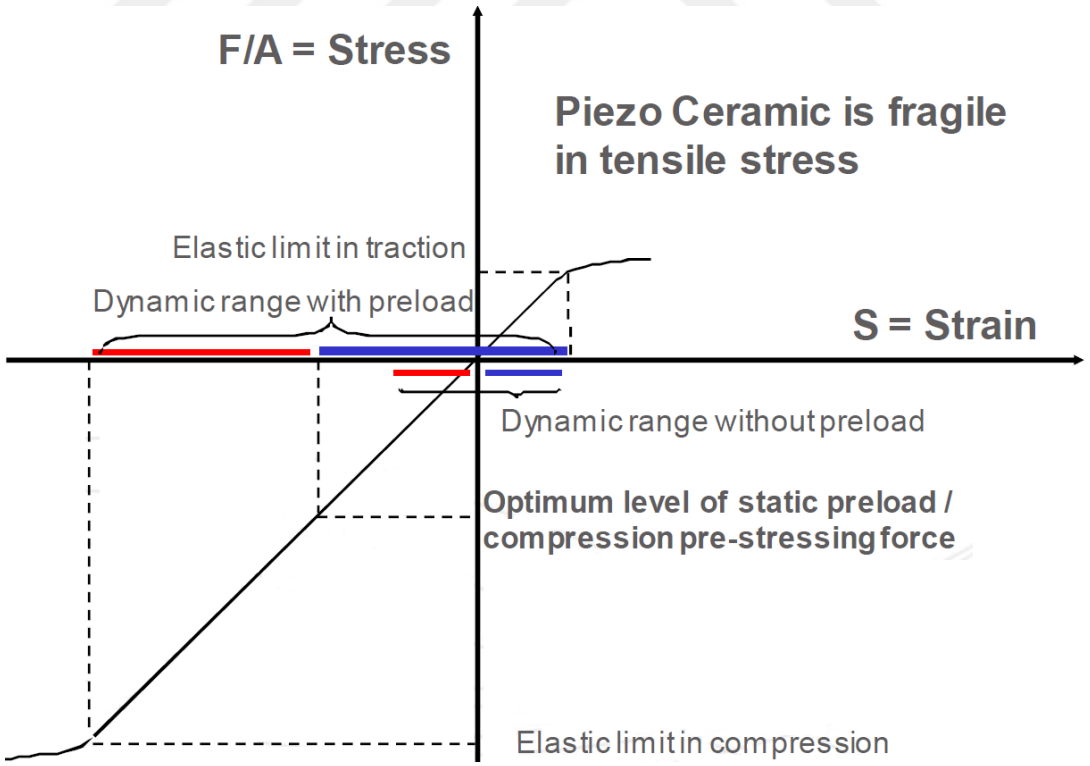


Figure 3.38: Piezo Ceramic Stress-Strain Diagram [98]

Because of their brittle nature, piezomaterials could not resist to tension, and they have to work under compression. For this reason, preloading is a must, and despite its all side effects, it could extend dynamic motion range in a considerable manner, as represented in Figure 3.38 [98]. Eventually, considering all complicated characteristics, instead of detailed modeling, reflecting key dynamics were found adequate. Herein, the most common practice was assessed to be modeling only dynamic response and via 2nd order transfer function, as related literature reviewed [5][38]. Moreover, since closed loop operation with strain gauges already compensates effects of both hysteresis and creep, beyond for only controller design, realistic performance assessment could also be performed via 2nd order modeling approach.

3.2.2.1 Dynamic Response Modeling

For the canonical 2nd order form with the test resultant natural frequencies and the best fit providing damping ratios, plant transfer functions of elevation ($G_{el}(s)$) and azimuth ($G_{az}(s)$) axes are calculated as represented with TF Set 3.10 .

$$G_{az}(s) = \frac{\omega_{az}^2}{s^2 + 2\xi_{az}\omega_{az}s + \omega_{az}^2} = \frac{4093280.25}{s^2 + 1456.70s + 4093280.25} \tag{3.10a}$$

$$G_{el}(s) = \frac{\omega_{el}^2}{s^2 + 2\xi_{el}\omega_{el}s + \omega_{el}^2} = \frac{4836106.15}{s^2 + 1583.40s + 4836106.15} \tag{3.10b}$$

Herein, beyond piezo actuator level, modeling total closed loop response of FSM is more reasonable, because independent from system operation mode FSM is operating more like a stand-alone unit. Considering unit characteristics derived from datasheets, strain gauge conditioner and linear amplifier were modeled as low pass filters. Although their contribution to overall dynamics is quite low, in order to be coherent they were modeled, as well. Electronic factors such as controller signal to noise ratio and joint strain gauge - conditioner ADC errors pose nominal resolution of 0.2 μrad, which is modeled with quantization errors. Saturation dynamics were utilized in order to limit total strokes, as the design rules. For 2.4 A peak and equivalent 30.2 μF capacitance, current saturation dynamics were also reflected upon model just to monitor and assess in terms of amplifier capacities. Thus, FSM model took the final form as exemplary elevation axis submodel is presented in Figure 3.33. In or-

der to demonstrate the model performance, comparison of test and simulation results against combination of harmonics input, which is stipulated to producer as success criteria for including probable disturbance contributors, is presented in Figure 3.34.

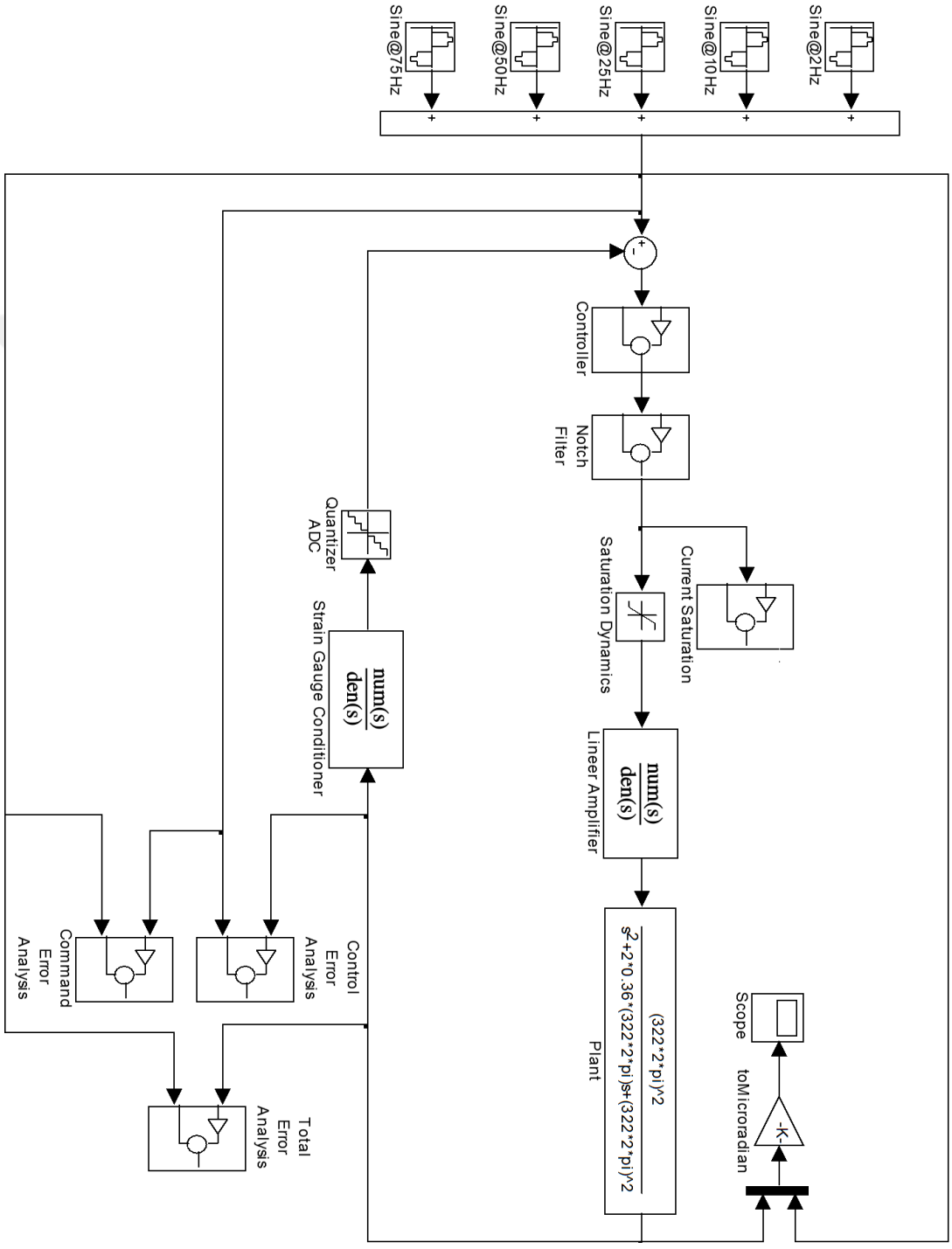


Figure 3.39: Final Version of Elevation Axis FSM Simulink Model

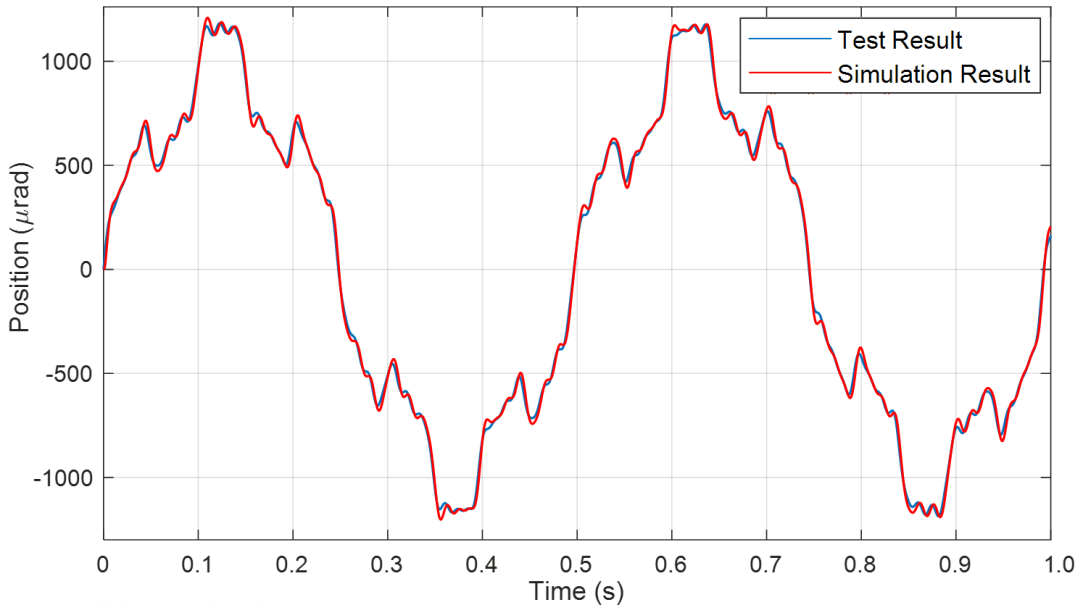


Figure 3.40: Comparison of FSM Elevation Axis Model Output and Test Result

3.2.3 Atmospheric Disturbance

In FSM selection section, atmospheric disturbance modeling via Tyler approximation was performed, and $PSD(f)$ was derived. Since simulation environment is built on time-domain, synthesizing from $PSD(f)$ data is done via inverse fast Fourier transform (Equation 3.11). Another and direct time-domain modeling approach is based on dividing atmospheric medium between laser source and target as a lens array, thus, producing related phase screens, that present optical aberrations. Accordingly, optical design team conducted a demanding analysis on Zemax OpticStudio to simulate atmospheric disturbance. Comparison of the atmospheric turbulence time data, which were derived from both approaches for 20 m/s effective wind speed and C_n^2 of 10^{-14} $m^{-2/3}$, are presented in Figure 3.41. Order of magnitude and general trends seem similar in both curves. Although phase screens give more accurate results, it is toilsome and necessitates wide optic knowledge. Tyler approximation is practical, and cross-checking indicated that it is also sufficient on control engineering wise.

$$Inverse\ FFT \rightarrow x(n) = \frac{1}{N}\sum_{m=0}^{N-1}[X_{real}(m) + jX_{imag}(m)]e^{\frac{2\pi mnj}{N}} \tag{3.11}$$

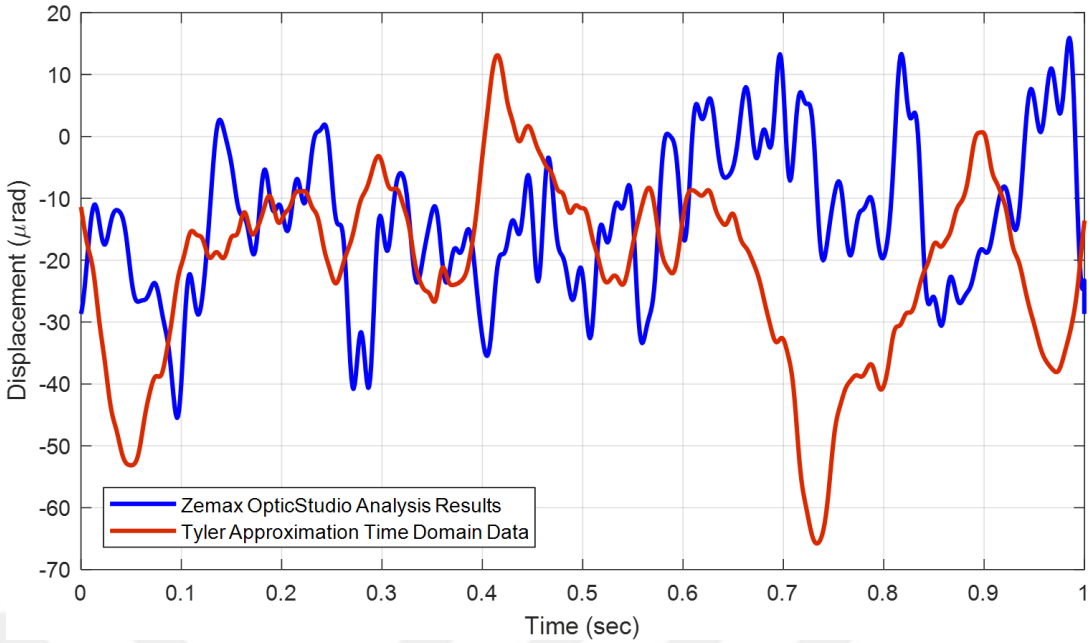


Figure 3.41: Comparsion of Phase Screens Analysis and Tyler Approximation on Atmospheric Turbulence Time Data Generation

3.2.4 Cameras and Target Tracking Algorithms

Output of the tracker algorithm, running on thermal image, drives gimbal and provides coarse tracking. Single image capturing period is defined as exposure time in IR cameras. Upon exposure, the frame is written on tracker hardware Random Access Memory (RAM) and algorithm execution runs, coordinately. Put it differently, between true motion and related tracking algorithm output, there is a significant latency. In addition to latency, half pixel PTP random jitter degrades tracking accuracy, as well. Course tracker Simulink segment, in which these factors are put into action, is demonstrated in Figure 3.42. In addition to these, target geometry, relative motion, etc. factors matter on tracker performance, however, by adjusting track gate size or applying a different algorithm, performance loss due to these could be enhanced. On the contrary, modeled dynamics were optimized and invariable. Moreover, according to analyses on offline videos of potential targets, target position reporting errors fell within subpixel random jitter envelope.

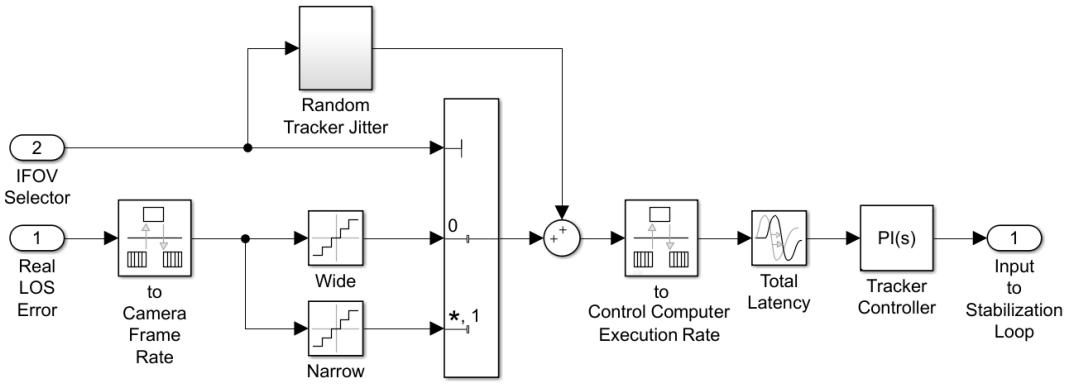


Figure 3.42: Course Video Tracker Simulink Model Segment

In the course tracker model segment, real LoS error corresponds to actual displacement between target aimpoint and camera frame centroid. Frame capturing is simulated via *to Camera Frame Rate* rate transition block. Wide and narrow FOVs have different IFOVs, and subpixel uncertainties. This phenomenon behaves as if quantization error. Half pixel random jitter is added at the following step. Tracking system total latency is modelled as transport delay. Since the control computer runs at 2 kHz, sample rate is transitioned, and tracker controller is implemented, subsequently.

Deploying a fast camera, a fast steering mirror, and fast tracker dynamics, fine tracking functionality is implemented. CCD camera frame rates could be increased up to 400 Hz. For true motion to tracker message issue elapsed time of 7.5 ms and 200 Hz fine tracking system frequency a timing routine is represented in Figure 3.43.

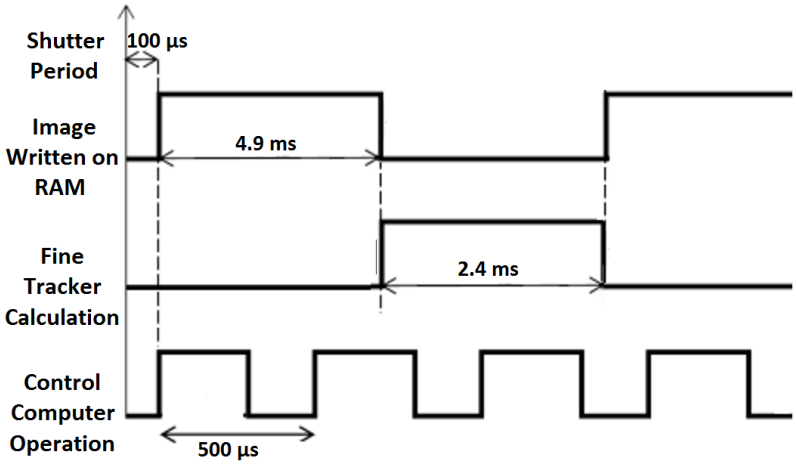


Figure 3.43: Timing Routine for Fine Tracking System

Similar to IR camera exposure time, for CCD image sensors shutter speed governs capturing, which could take 100 µs. Since camera is considerably fast, tracker computer capacity is determinative on fine tracker operation frequency. After several trials, achievable maximum frequency is specified. Trials were carried out on still gimbal via driving FSM with varying sinusoidal inputs and observing corresponding camera - track algorithm duo response against a static target, as exemplary result for fine tracking system operating at 100 Hz is demonstrated in Figure 3.44.

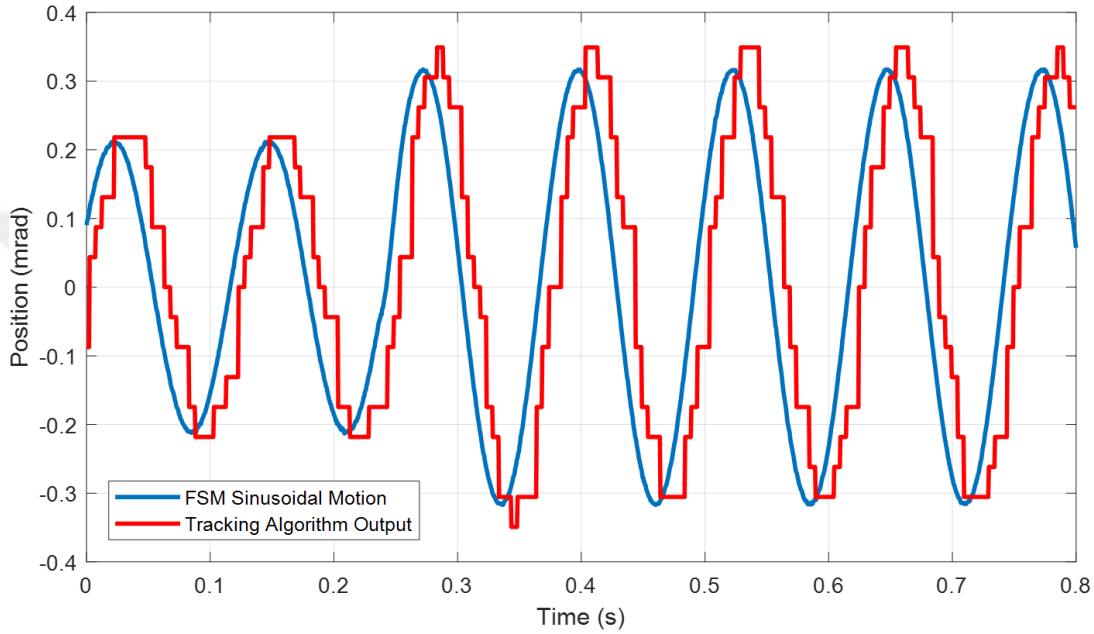


Figure 3.44: Fine Tracker Algorithm Output against Disturbance Created by FSM

By the application of same algorithm, fine and course tracker models are the same except from parameter differences such as total latency and camera frame rate. Exposure time could be changed in order to enhance target visibility, however this is not a dynamically changing parameter, and would only effect total latency up to 1 ms.

3.2.5 Targets

Target tracking scenarios of the project are moving pressurized tank on rail and drone. Assessing target tracking capability on a controlled manner, on-rail target was envisaged. Drone was preferred as a realistic and more challenging target scenario.

3.2.5.1 Pressurized Tank on Rail

Artillery munitions such as mortar have ballistic trajectories, which is in parabolic form and mostly depending on muzzle velocity along with air drag. Small portions of the time of flight along their long range could be approximated as linear motions. Taking advantage of this disposition and ease of installation, as a common practice, on rail moving target was utilized (Figure 3.45). By means of their well-controlled operability, on rail target sets could allow repeatable tests. EOD system target engageability could diminish to 1.13 m/s at 85 m from the relation $\dot{s} \approx L\dot{\theta}$, keeping the same tracking velocity $\dot{\theta}_{azimuth}$ = 0.764 °/s. Driving back and forth at 1 m/s, target motion profile was acquired via placing IMU onto it as processed velocity data presented in Figure 3.46. Sway direction is throughout the rails and corresponds to EOD azimuth tracking coverage. Due to irregularities on rail surface, moving target jumps and heave velocity component with high frequency content arises. Acquired data was inserted into Simulink offline simulation model with Repeating Sequence block.



Figure 3.45: Pressurized Tank as Moving Target on Rail System

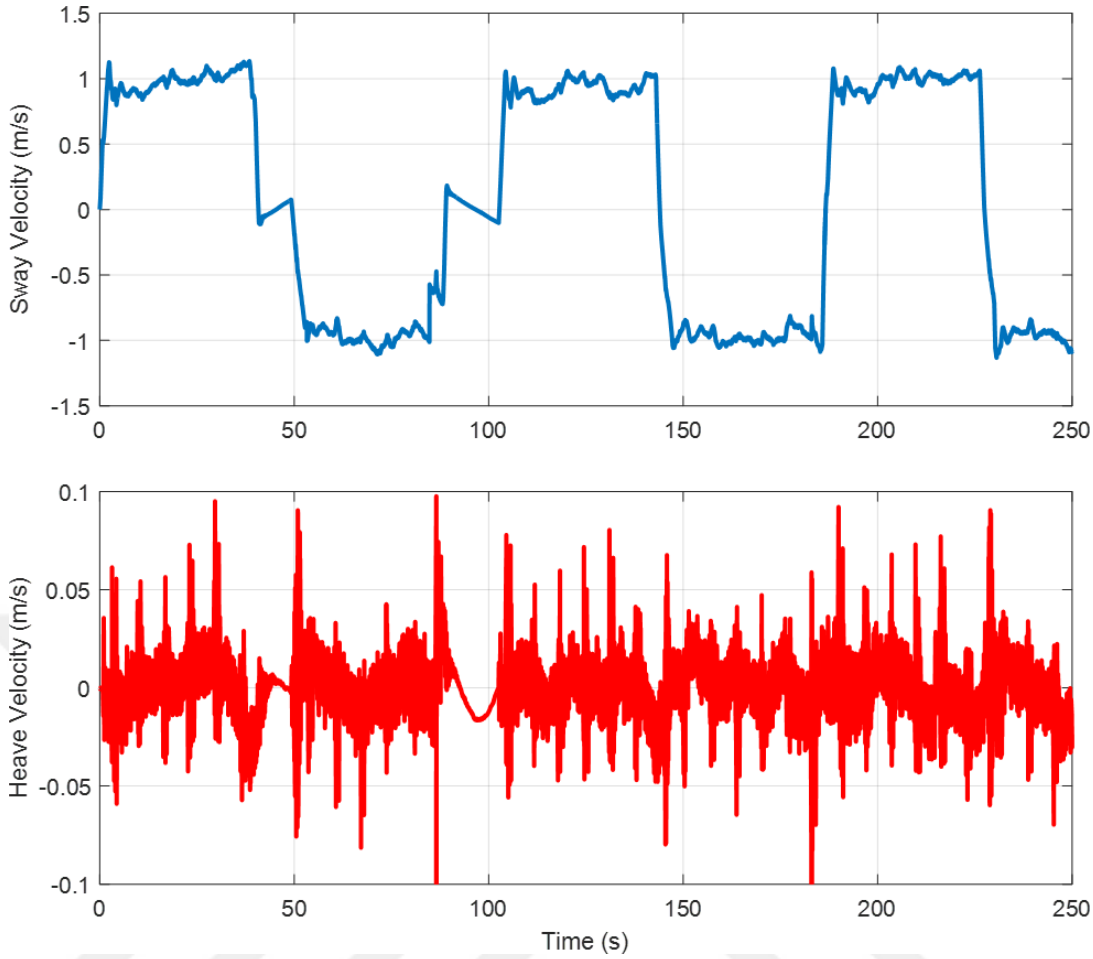


Figure 3.46: On Rail Target Velocity Profile

3.2.5.2 Drone

Deploying directed energy weapons against drone threats has become widespread. In addition to be a more realistic target scenario, posing more elevational tracking load, compared with target on rail, makes drone motion profile more complete tracking performance assessment tool. Initially hovered on top of rail at 85 m altitude, drone began moving along it while descending and went back to starting position in the end over the reverse path, which is demonstrated in Figure 3.47, within motion profile data acquisition. Processed velocity data is presented in Figure 3.48. Due to cross wind, some lateral jumps are present on sway direction, whereas gaining and losing altitude occurs in smooth trends as observed on heave data .As well as on rail target profile, drone data was applied in the Simulink model as repeating sequence.

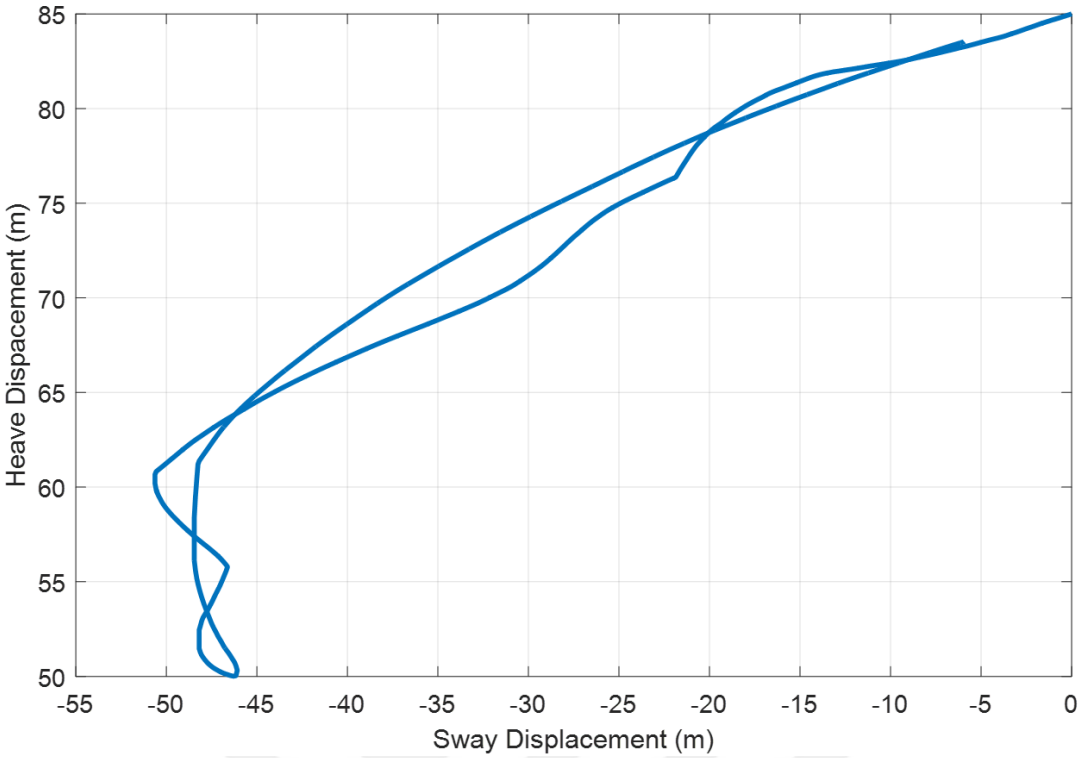


Figure 3.47: Drone Path During Data Acquisition

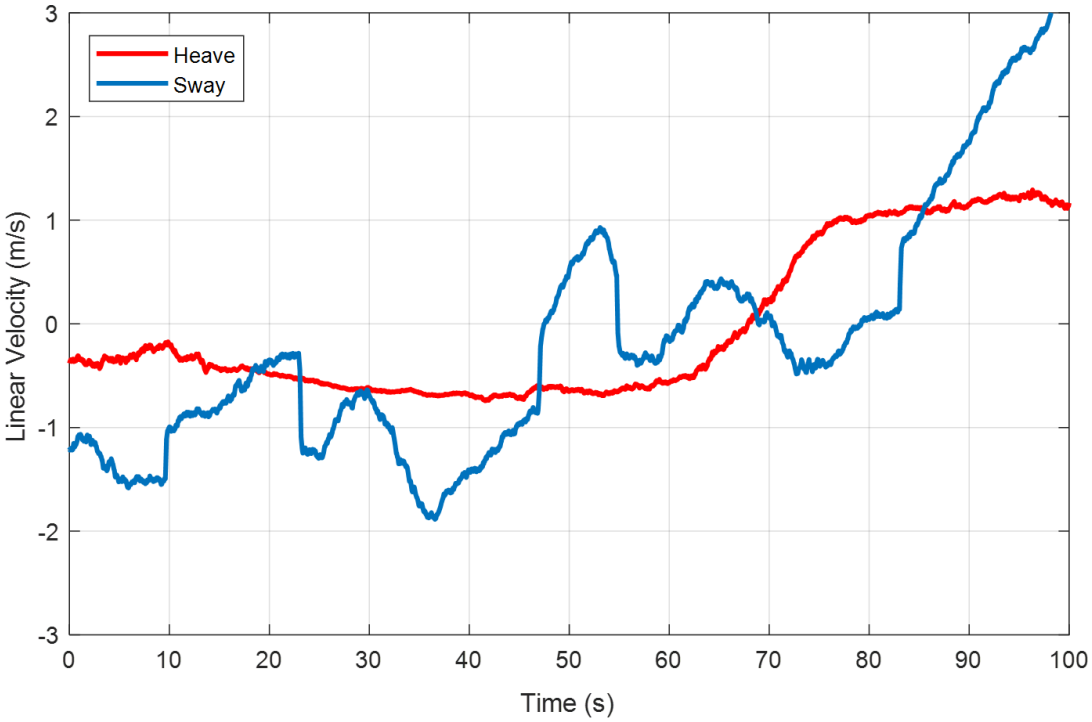


Figure 3.48: Drone Velocity Profile

CHAPTER 4

CONTROL

Cascade control structure involves two controllers, and primary controller output is the input for secondary one. Implementing 3-4 times faster inner loop, significantly better performance could be reached when compared with single-loop control system. Cascading inner velocity loop with outer track or position loop is a common EOD control topology. Velocity, position, and tracker controller designs are detailed below.

4.1 Velocity Controller Design

4.1.1 Elevation Axis

Elevation axis plant was modeled up to 8th natural frequency and has transfer function of 17th order. In order to remove steady state error along with track ramp input with constant error, system type is required to be changed from 0 to 1 by adding free integrator on OLTF. For this purpose PI controllers are widely used in electro-mechanical system control as mentioned in control strategies section. Considering that there was no significant nonlinear term except from elevation angle dependency, controller design practices began with initial assumption of PI sufficiency. If PI controller could not perform as required, it would be upgraded to switching parameter PI based on elevation angle, as plan B. Herein, speaking of required, no definite requirements were defined specifically for velocity loops, hence, stability and bandwidth requirements were derived based on engineering rule of thumbs at that level. Primary processes are tracking and position loops, and in order to enhance their performance, PI controller could be re-tuned, recursively. As highlighted in preliminary servomechanism design, fundamental system limitation on adequate bandwidth is perceived as first in-

teractive mode, which limits bandwidth to its 1/3 or less. Accordingly, velocity loop bandwidth expectancy was 8 Hz. However, since higher resonant poles contain larger energy levels than expected, they act as main limit in this case and could necessitate leveling bandwidth projection down in order to attenuate high frequency oscillations' coupling onto overall system response. Supposing that ideal video tracker is available, which reports target position with absolute accuracy and zero latency, then ideal tracker controller yields to be pure time-derivative for converting target velocity induced on EOD axes as input to velocity loop, in case of no base disturbance. This case sets the upper performance expectancy limit on velocity loop bandwidth, because as tracking dynamics filters out high order terms, workload on velocity loop comprising of high frequency target motions diminishes. When target sets are examined, at the joining points of 7 m long rails, target moving at 1 m/s experiences upward 3 Hz jerk, which dampens out in 1.5 s as observed in Figure 4.1. High frequency component and residual steady state error compensation is on FSM by means of fine tracking, however, course tracking system is required to assist by removing lower frequency trends. Hence, velocity loop bandwidth projection comes along as 3.5 Hz, nominally with a margin. Oscillations at 0.5 Hz are present in drone heave profile. Drone flight trends and limits of structural dynamics both cohere with derived bandwidth.

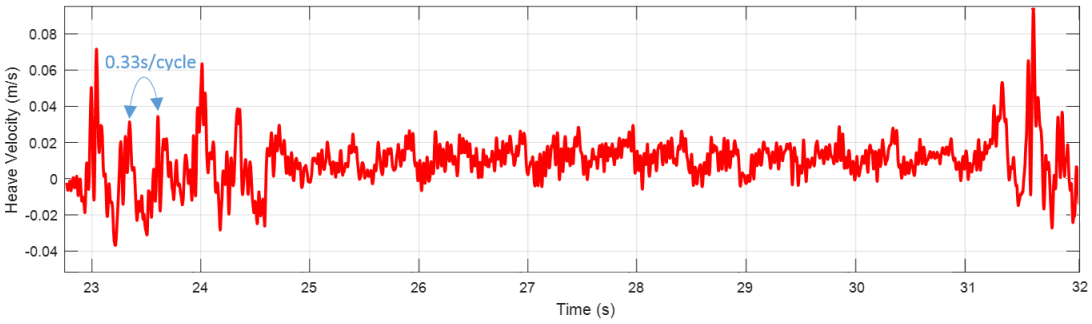


Figure 4.1: Detail View of On Rail Target Velocity Profile

In order to accommodate uncertainties at least 6 dB gain margin and as an indication of system damping more than 45°phase margin are stability related rule of thumbs. Covering all the requirements derived so far, a PI controller was designed on bode plot, graphically, via MATLAB Control Designer app (Figure 4.2) for the best fit of test resultant elevation angle torque to velocity transfer functions (Figure 4.3).

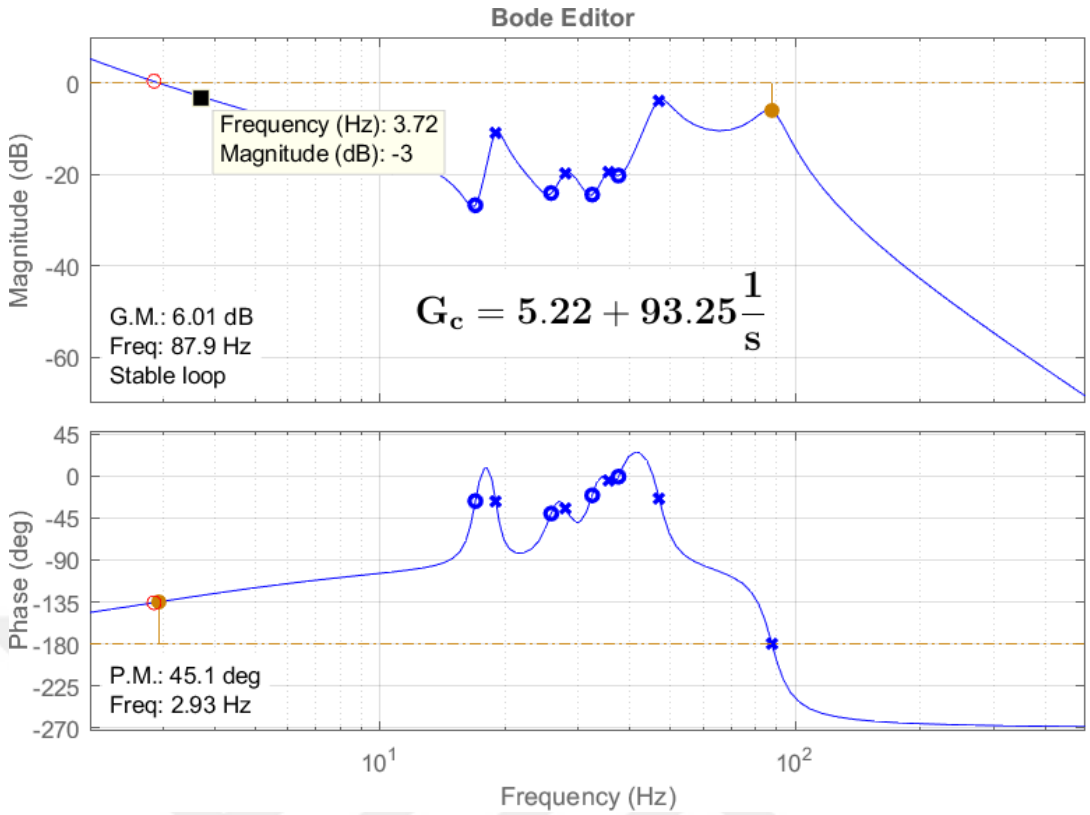


Figure 4.2: MATLAB Control System Designer app Bode Plot Editor Interface

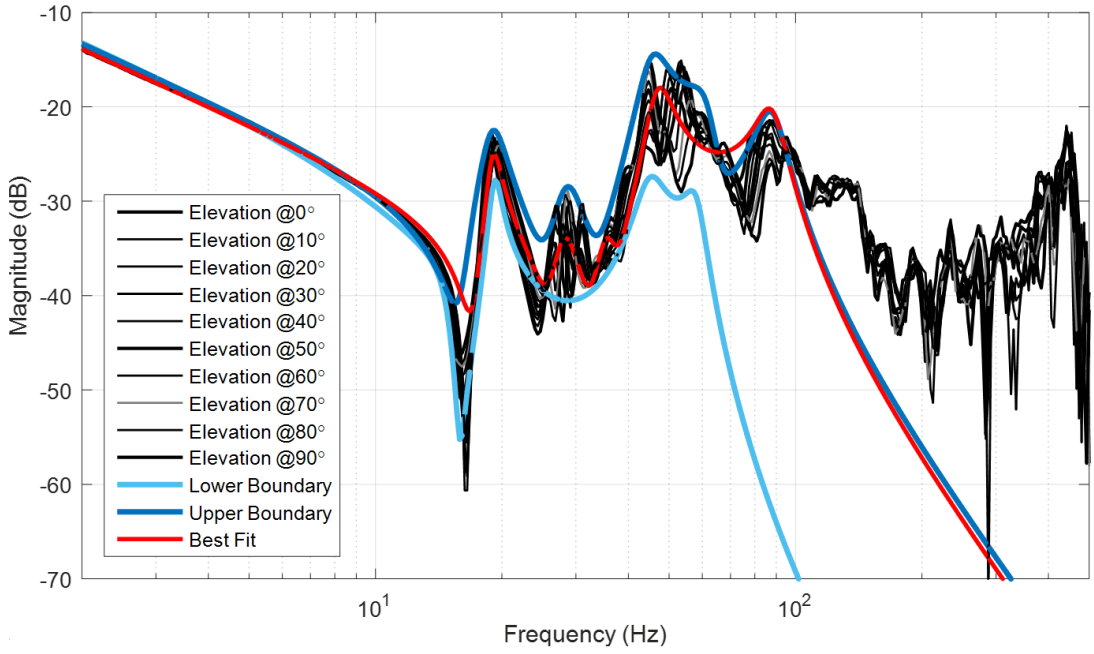


Figure 4.3: Elevation Axis Torque to Velocity Transfer Functions

By the synthesized controller law achieved stability margins and open-loop bandwidths are evaluated for TF fittings at elevation angles 10°apart and envelope boundaries for assuring full angular span stability and performance (Table 4.1). Within all operational elevation range, closed loop system is stable and have more than adequate bandwidth. Actually, boundary responses do not have physical correspondence, however they indicate an envelope of stability. Low phase margin at lower bound is due to lack of fitting convergence at low frequency phase regime and could be neglected.

Table 4.1: Velocity Controller Performance with Respect to Elevation Angles

Elevation Angle (°)	Open Loop Bandwidth (Hz)	Phase Margin (°)	Gain Margin (dB)
Lower Bound	3.55	12.70	9.17
-10°	3.86	46.70	6.71
0°	3.75	45.80	6.93
10°	3.74	45.60	7.14
20°	3.84	46.20	7.27
30°	3.77	45.90	7.48
40°	3.85	46.50	7.41
50°	3.75	45.80	10.10
60°	3.77	46.10	9.81
70°	3.87	46.90	9.47
80°	3.79	46.20	11.60
90°	3.95	47.50	9.49
Upper Bound	4.18	49.00	5.82

4.1.2 Azimuth Axis

As presented in Figure 3.13 elevation axis rotation causes first vibration mode shift between 34 and 43 Hz along with energy level change. Moreover, catching almost the same magnitude with the first one, second mode moves between 44 and 57 Hz. Although the rest exhibits minor natural frequency deviations, their magnitudes fluctu-

ate, considerably. Thus, in the same manner with elevation axis, bandwidth projection falls below 11 Hz. Stemming from ideal tracker assumption, if the agilest first order sway acceleration dynamics of drone is considered, in order to track its trajectory accordingly, required bandwidth could be approximately calculated from the relationship between rise time and bandwidth for a low-pass system, i.e., $f_{3dB} \approx 0.35/\tau_r$ as 3.5 Hz as same as elevation axis bandwidth, where nominal rise time (τ_r) is inferred to be 0.1 s from Figure 4.4. On rail target experiences even less steep velocity reversals. Thus, azimuth velocity loop bandwidth requirement is regarded as 3.5 Hz.

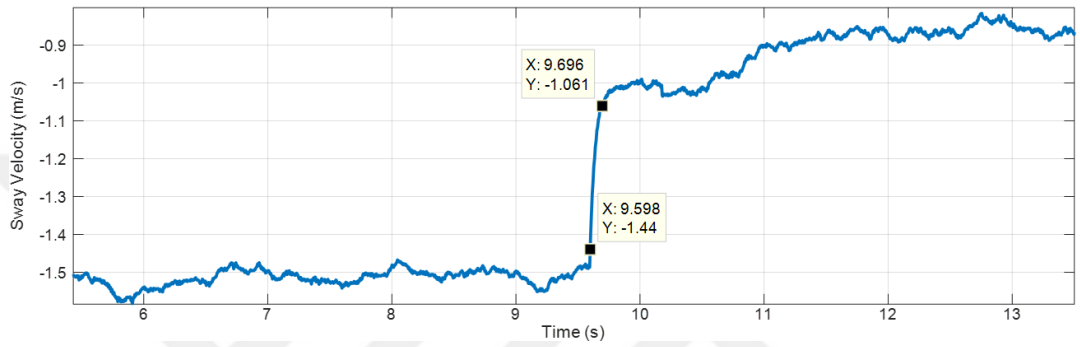


Figure 4.4: Detail View of Drone Velocity Profile

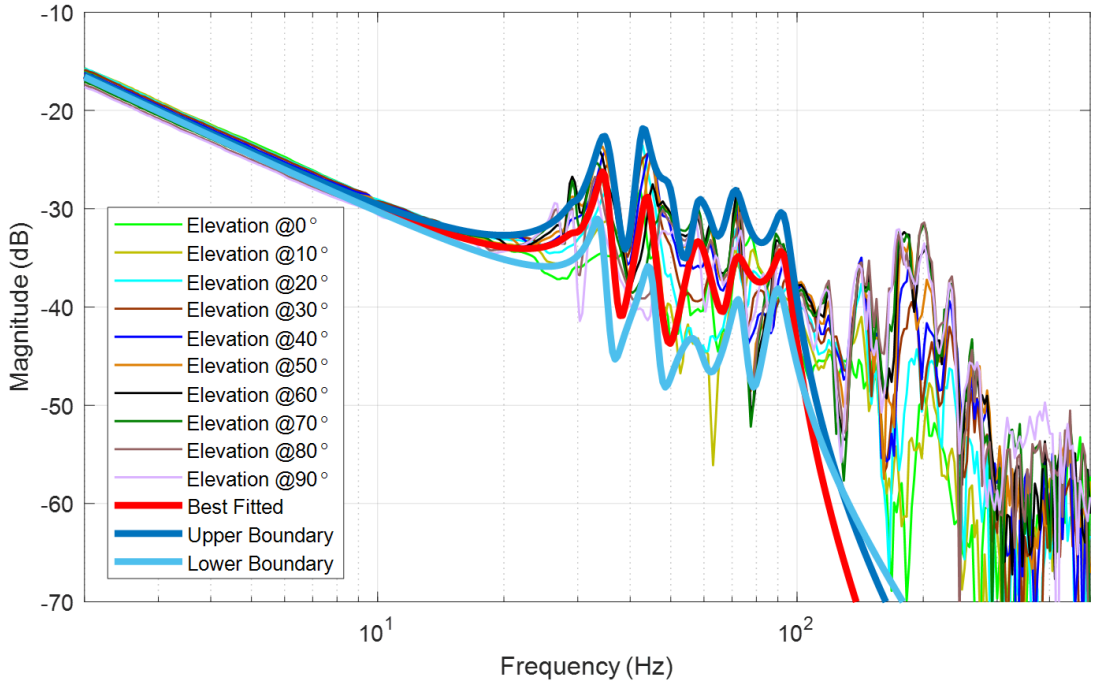


Figure 4.5: Azimuth Axis Torque to Velocity Transfer Functions

Due to first order dynamics, initial phase of acceleration is ramp input. During this interval PI controller could assure trajectory tracking with constant error. As destination velocity is being reached, input profile becomes more convergent to step input, and tracking error decreases to zero. Experiencing decreasing offset, only when target sharply accelerates, does not pose considerable performance deficiency as long as target is not lost on view, and since constant velocity intervals are sufficient for engaging and destroying the target. Furthermore, increasing system type to 2 for tracking ramping could bring along stability concerns. Taking azimuth axis linear behavior with the elevation angle dependency exception, into consideration as well, controller design was initiated with PI law. For synthesizing, the best fit of azimuth torque to velocity transfer functions at 10°apart elevation angles were derived, as depicted in Figure 4.5. Boundaries were also drawn for stability analysis. Together with stability-related requirements, PI controller synthesis was conducted on bode plot, graphically, via MATLAB Control Designer app as depicted in Figure 4.6. Elevation angle dependent stability margins and achieved bandwidths are demonstrated on Table 4.2.

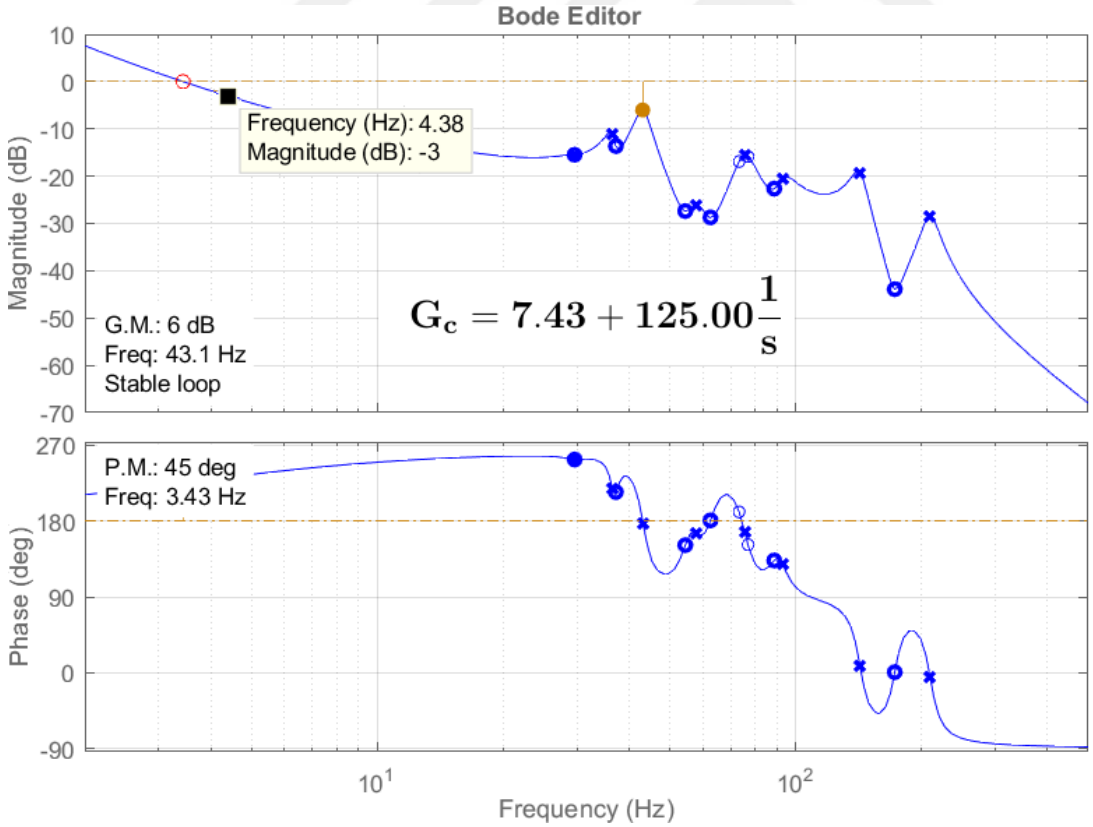


Figure 4.6: MATLAB Control System Designer app Bode Plot Editor Interface

Table 4.2: Velocity Controller Performance with Respect to Elevation Angles

Elevation Angle (°)	Open Loop Bandwidth (Hz)	Phase Margin (°)	Gain Margin (dB)
Lower Bound	3.81	48.30	17.00
-10°	4.05	49.70	14.20
0°	4.15	50.40	11.70
10°	4.41	51.90	6.82
20°	4.11	50.10	6.02
30°	4.28	50.50	7.42
40°	3.69	46.70	7.25
50°	3.84	47.80	6.80
60°	3.60	46.00	7.15
70°	3.75	47.10	8.03
80°	3.48	44.90	9.95
90°	3.59	46.10	12.20
Upper Bound	3.86	48.30	5.91

4.2 Position Controller Design

Cascaded position control topology is represented in Figure 4.7. Inner closed velocity loop and free integrator constitutes a type 1 unit feedback system. Hence in order to compensate steady state error, proportional controllers are sufficient for both axes.

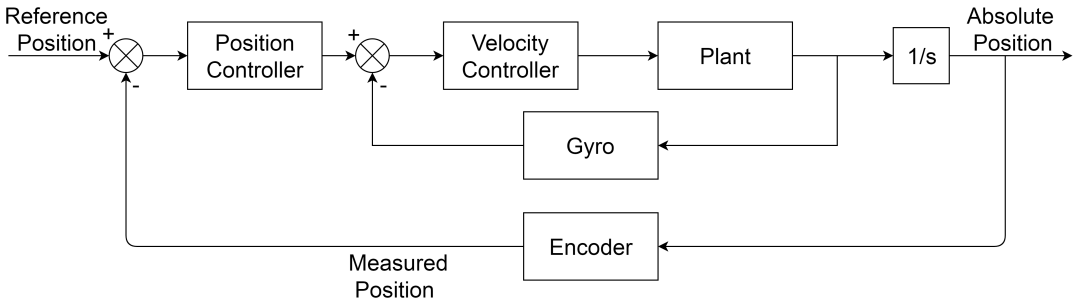


Figure 4.7: Cascaded Position Control Loop Topology

Herein, highlighted in servomechanism design, design requirements are stated for reference input tracking and positioning accuracy as 100 µrad and 50 µrad, respectively. Moreover, for both axes, since required and mechanical limits match, overshoot is undesirable. Since the moves toward limits are subject to current, acceleration, and velocity limitations, synthesized linear controller would be tested against nonlinear factors which act as presented in Figure 4.8.

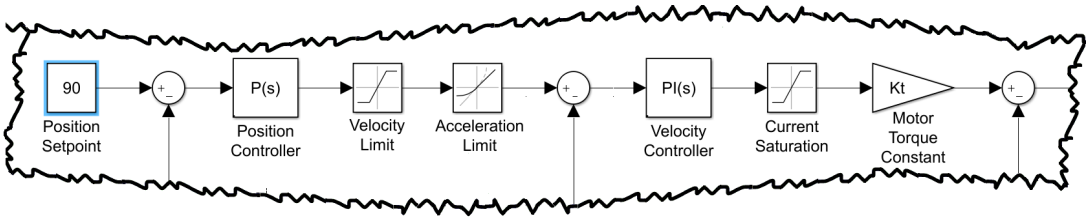


Figure 4.8: Position Loop Forward Path Nonlinear Terms

4.2.1 Elevation Axis

Elevation axis position P controller synthesis was conducted on step response, graphically, with the aid of MATLAB Linear Analysis Tool, and comparison between system model including nonlinear dynamics and linear responses are presented in Figure 4.9. Except from small deviations, similar and satisfactory trends are traced. Covered all angular span, positioning accuracy becomes approximately 0.2 µrad (Figure 4.10).

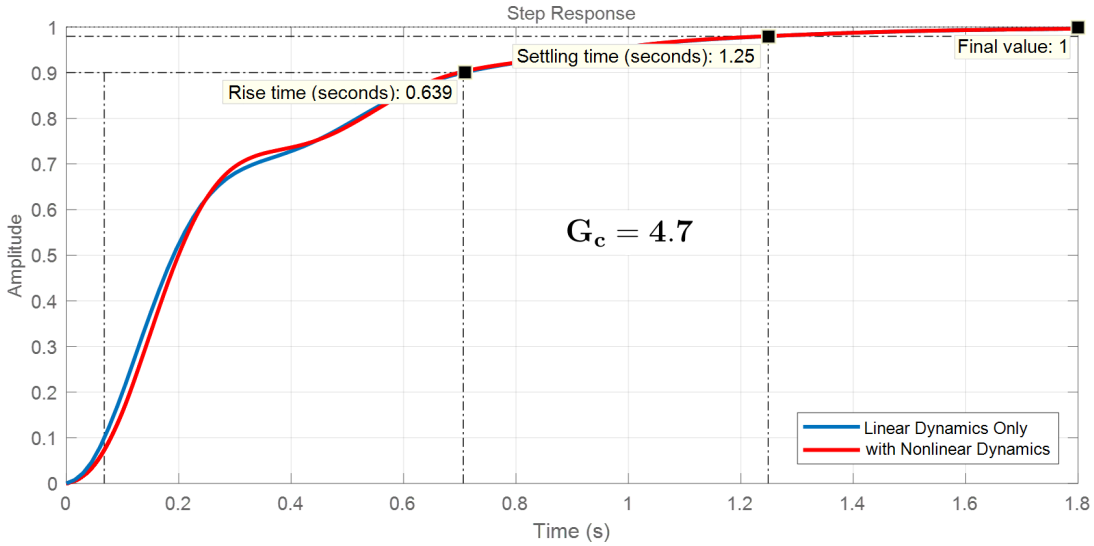


Figure 4.9: Elevation Axis Position Loop Step Response

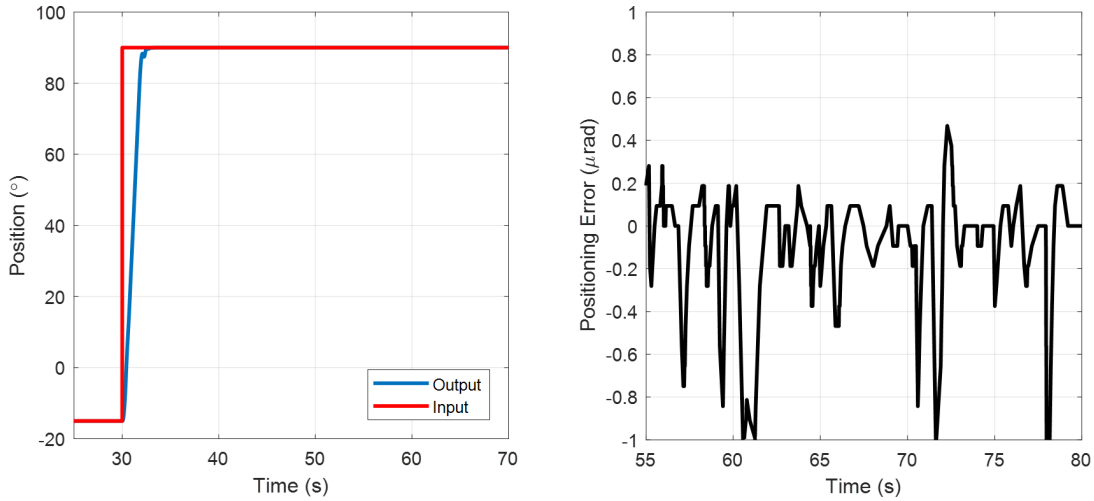


Figure 4.10: Elevation Axis Positioning Accuracy

In order to asses position input tracking accuracy, ideal on rail target profile induced on azimuth axis is applied to elevation axis, as well. In order to be coherent and keeping in the vicinity of unique predefined motion profile of the project, tests were performed on real unit in this way as the results are demonstrated in Figure 4.11. Command tracking accuracy is considerably less than the requirement of 125 μrad.

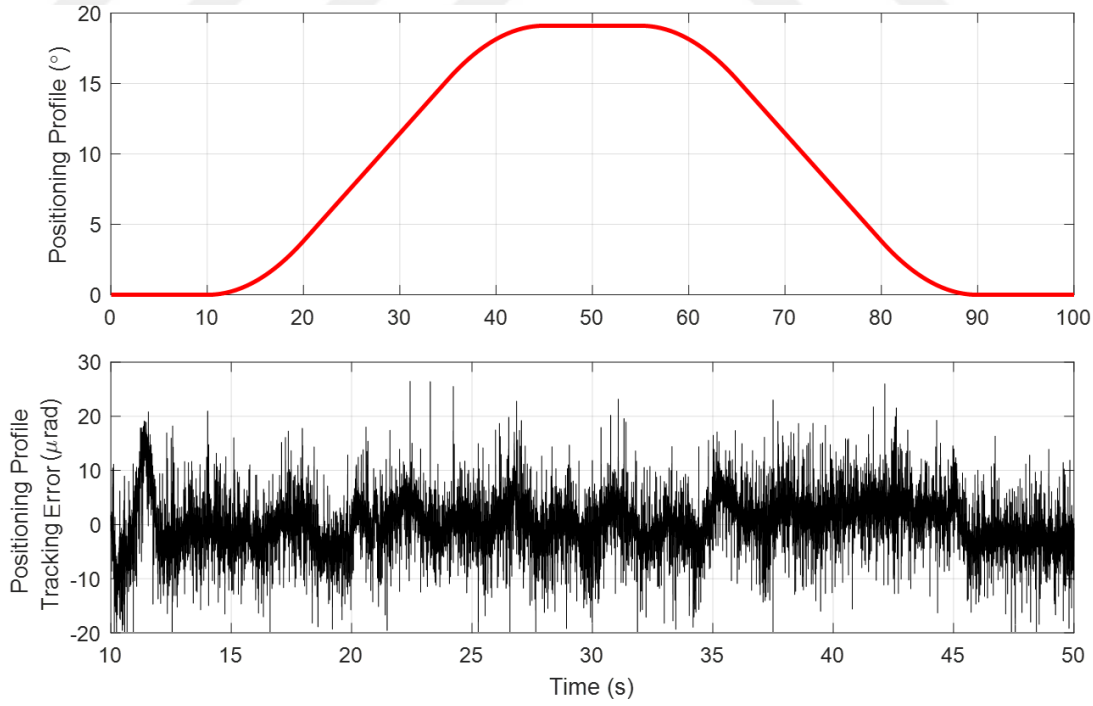


Figure 4.11: Elevation Axis Position Profile Tracking Accuracy

4.2.2 Azimuth Axis

Azimuth axis proportional position controller synthesis was actualized at 0°elevation angle in the same manner with elevation axis peer and slight difference between step responses of linearized and nonlinear models is demonstrated in Figure 4.12. Time response characteristics assessment versus elevation angles is presented via Table 4.3.

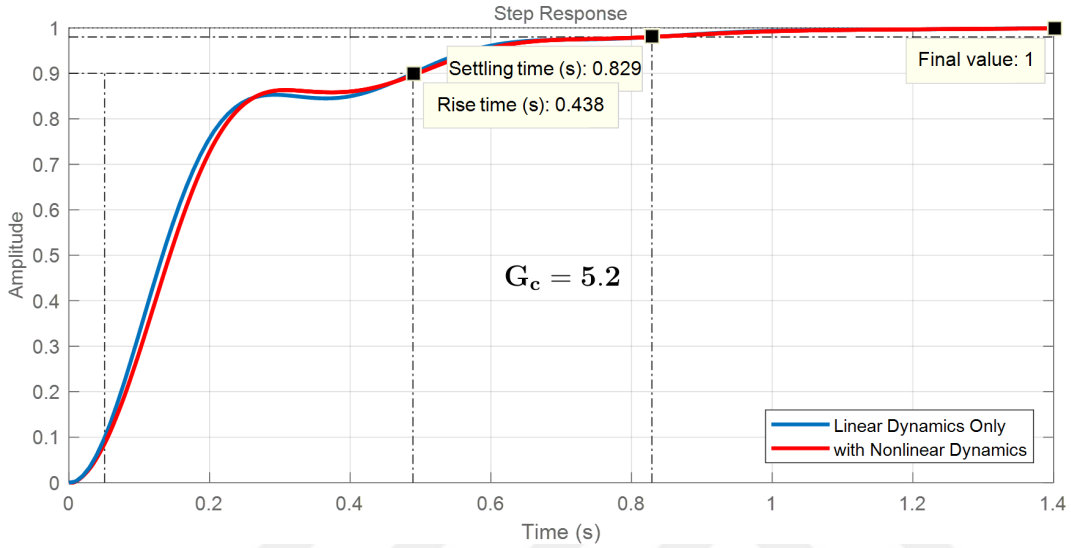


Figure 4.12: Azimuth Axis Position Loop Step Response

Table 4.3: Position Controller Performance with Respect to Elevation Angles

Elevation Angle (°)	Rise Time (s)	Setting Time (s)	Final Value
-10°	0.443	0.839	1
10°	0.438	0.828	1
20°	0.438	0.829	1
30°	0.442	0.838	1
40°	0.451	0.857	1
50°	0.461	0.882	1
60°	0.467	0.899	1
70°	0.468	0.901	1
80°	0.469	0.904	1
90°	0.472	0.953	1

Compelling axis with limit velocities and accelerations on the back and forth moves between mechanical limits, reached 1σRMS positioning accuracy falls within encoder resolution. Furthermore, position profile tracking tests yield accuracy level of 10 μrad (1σRMS), and the resultant error trend, which is presented on Figure 4.13.

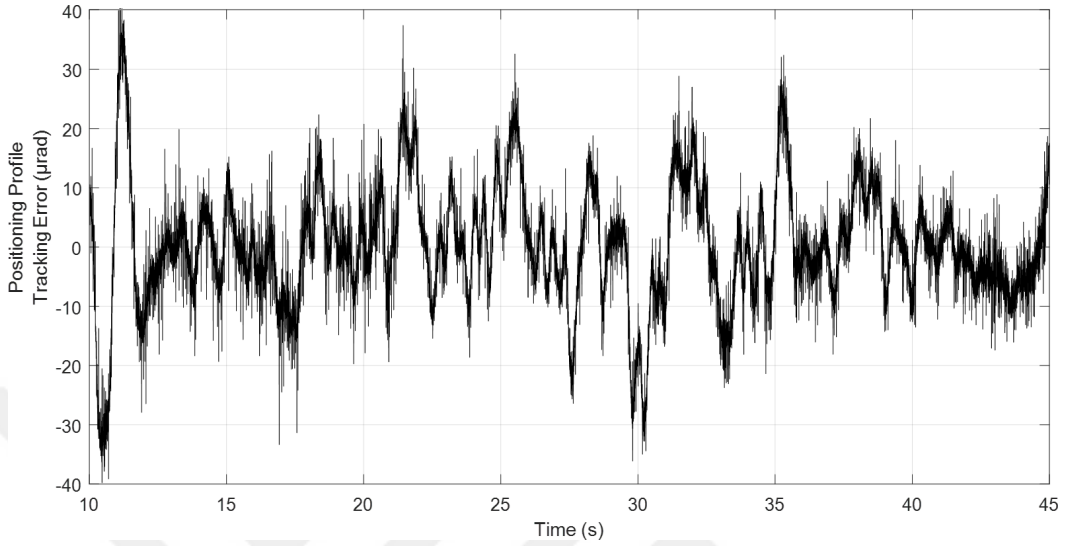


Figure 4.13: Azimuth Axis Position Profile Tracking Accuracy

4.3 Coarse Tracking Controller Design

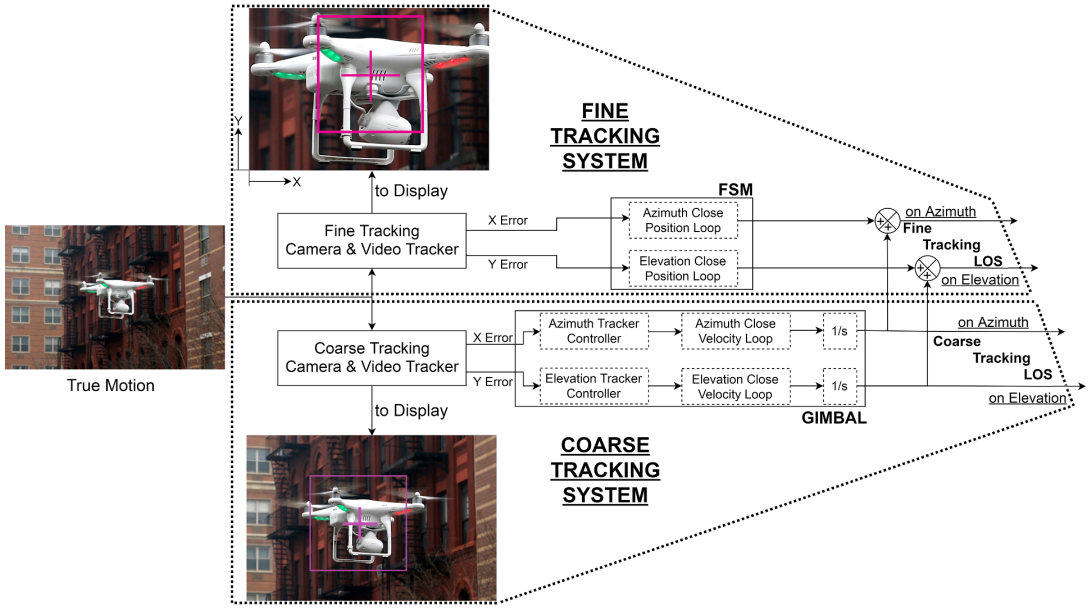


Figure 4.14: Target Tracking Architecture

Target tracking architecture is demonstrated by Figure 4.14. As highlighted before, fine tracking system compensates residual error of coarse tracking action and atmospheric turbulence. Since video tracker outputs angular deflection of LoS from selected aimpoint on target, and fine tracking system end effector FSM already operates, solely, in position mode, tracker output is commanded directly to FSM as position input. In the coarse tracker case, regarded as position error, deflection becomes input to tracker controller. Aforementioned ideal tracker assumption is accompanied by exact target velocity deduction via time-differentiation and reduces tracking problem into velocity profile chasing one. However, since track error is reported at discrete instances in reality, taking derivative yields a quite noisy pattern, and applying simple low pass filter could not upgrade performance to satisfactory levels most of the times. For synthesizing velocity data, some elaborate techniques are available in the literature, such as tracking differentiators. Although real-time differentiators take an important place on high performance of control systems and fits for in-question velocity profile derivation purpose, which is, principally, for utilizing higher bandwidth characteristics of velocity loops, their deployment were considered as more than necessary in the first phase. Shifting attention from prefiltering for velocity loop to tracker controller synthesis in correspondence with positional loop nature of tracker, initiating design with PI controller is a common practice. Different from proportional controllers, designed previously for position loops, here, PI control laws are required to raise system order to 2 for handling constant velocity target motion without steady state error. In velocity controller design section bandwidth requirement was derived as 3.5 Hz for both axes. When cascade control rule of thumb of 3-4 times faster inner loop than outer one for optimal performance is brought in mind, course tracking system bandwidth should be more than 1 Hz. Yet another derived requirement is maximum 100 μrad target tracking accuracy. The underlying reason is that, target acceleration intervals, which result in error peaking, constitute roughly 5% of total cycle, and assuming the tracking trend for the rest is almost Gaussian noise, nominal PTP amplitude becomes around 4 fold RMS value. With optical conversion, the largest excursion is expected from FSM azimuth axis by 3.5355 times fine video tracker output for covering coarse tracking residuals. 1σRMS coarse track error is required to be less than 106 μrad, in order not to hit FSM to its limits on coarse track error peaks when limited by FSM motion range is considered.

4.3.1 Elevation Axis

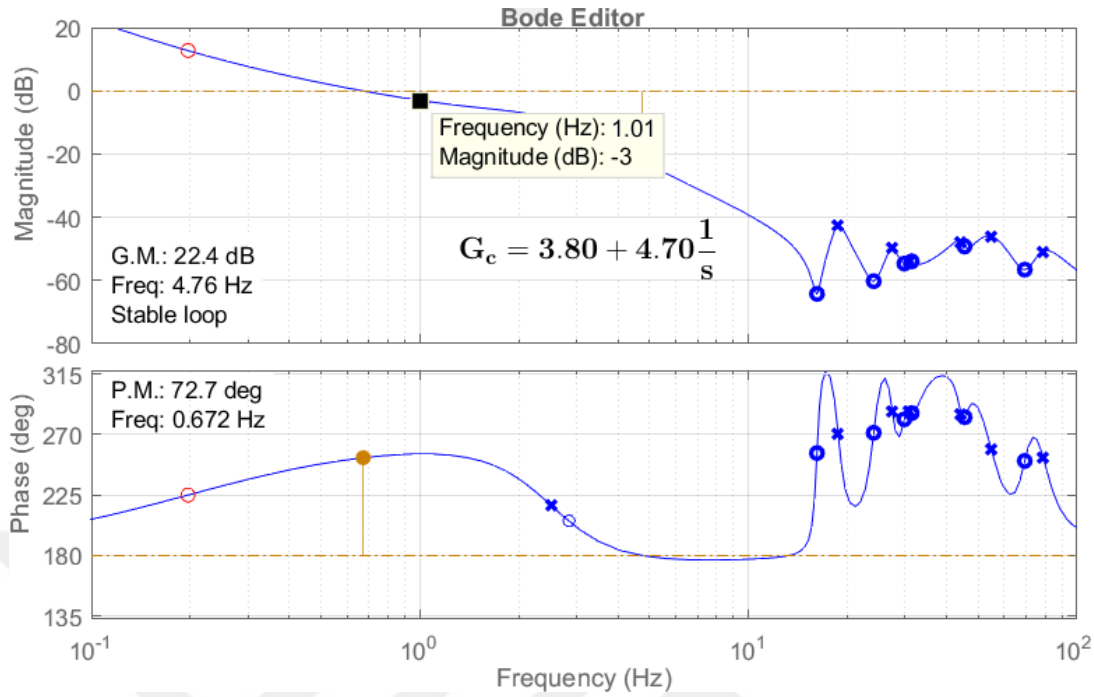


Figure 4.15: MATLAB Control System Designer app Bode Plot Editor Interface

Table 4.4: Coarse Tracker Controller Performance with Respect to Elevation Angles

Elevation Angle (°)	Open Loop Bandwidth (Hz)	Phase Margin (°)	Gain Margin (dB)
-10°	1.01	72.70	22.40
10°	1.02	72.70	20.90
20°	1.02	72.70	21.00
30°	1.01	72.70	21.50
40°	1.01	72.70	21.80
50°	1.02	72.70	21.30
60°	1.02	72.70	20.50
70°	1.03	72.70	20.30
80°	1.02	72.70	21.40
90°	1.00	72.70	23.90

Elevation axis coarse tracker open loop response with synthesized controller is represented in Figure 4.15. Elevation angle dependency of achieved bandwidth and stability margins are tabulated in Table 4.4. Different from velocity loops, much more margins were left due to time response characteristics. As approaching to margin rule of thumb values, overshoot and oscillation decay periods were observed to get larger.

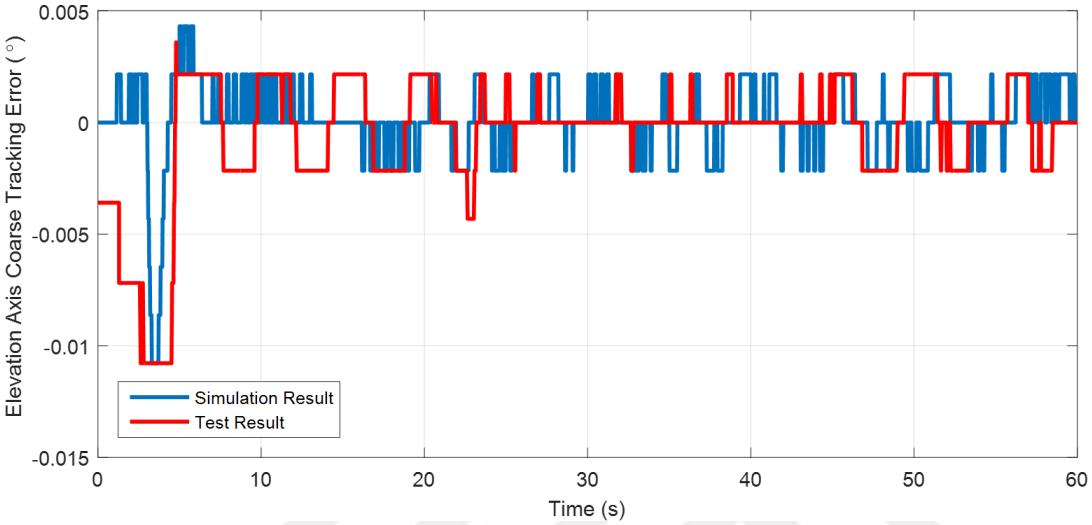


Figure 4.16: Elevation Axis Coarse Tracking System Error Against on-Rail Target

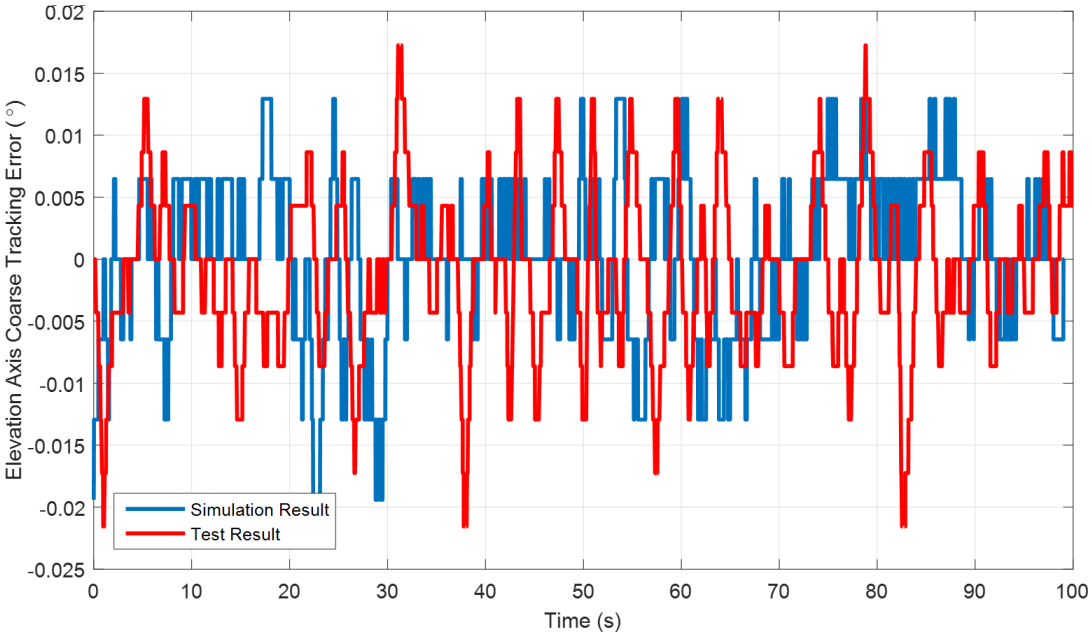


Figure 4.17: Elevation Axis Coarse Tracking System Error Against Drone Threat

Optimizing both for required bandwidth and reasonable oscillatory behavior yielded the synthesized PI compensator. Coarse tracking performance against on-Rail target and drone threat were assessed both on model and real-time test, as the results are demonstrated on Figure 4.16 and Figure 4.17, respectively. Target motion profiles, which were used in model, were acquired beforehand and targets, particularly drone, moved somehow variously in real-time tests although the same pattern was tried to be caught. Not exactly matched simulation and test results are, fundamentally, due to asynchrony and slight profile deviations. However, peak amplitudes, peaking profile, steady state trends seem quite similar and convergent such that 1σRMS coarse track error against on-Rail target is measured as 26.56 µrad, while simulation model yields 23.55 µrad. Furthermore, against drone threat coarse tracking accuracy was measured as 97.57 µrad and calculated on simulation model as 97.17 µrad. Keeping 1σRMS coarse track error under 100 µrad is another requirement fulfillment. The largest error amplitude is observed to be 350 µrad, and with optical conversion this could be compensated via 873 µrad FSM stroke. Hence, even error peaks remain within correcting range of fine tracking system, which is also discernible on fine tracker error plots, Figure 4.18 and Figure 4.19. By the aid of fine tracker, 1σRMS on-Rail target tracking error was decreased to 0.94 µrad on model and 1.09 µrad as test result. Besides, drone tracking error shrank to 2.17 µrad on model and 1.98 µrad in the test. Lastly, to know that stairwise look of the plots are due to comparison of video tracker outputs, which are subjected to quantization in proportion to camera pixel pitch.

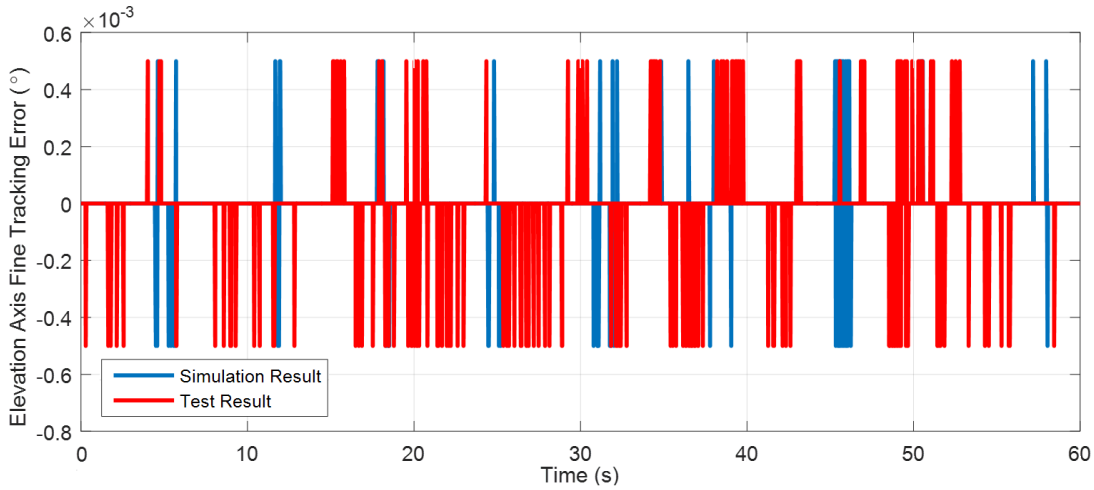


Figure 4.18: Elevation Axis Fine Tracking System Error Against on-Rail Target

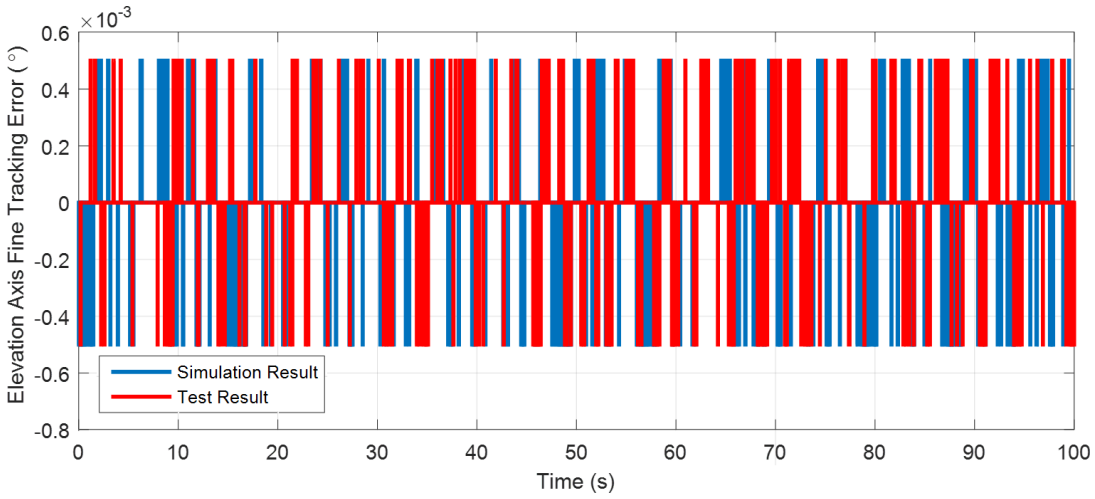


Figure 4.19: Elevation Axis Fine Tracking System Error Against Drone Threat

4.3.2 Azimuth Axis

Open loop response with PI controller, synthesized at 0°elevation, is represented in Figure 4.20. Elevational dependency of achieved bandwidths and stability margins are tabulated in Table 4.5. In the same manner with elevation axis, as a result of preventing highly oscillatory transients, margins, higher than required, were attained.

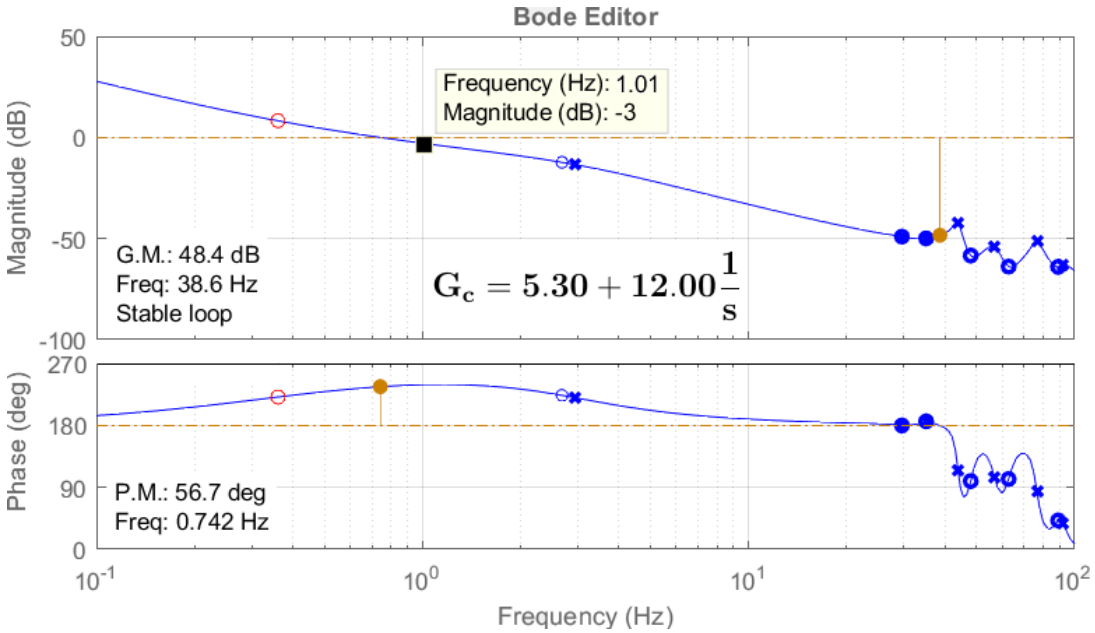


Figure 4.20: MATLAB Control System Designer app Bode Plot Editor Interface

Table 4.5: Coarse Tracker Controller Performance with Respect to Elevation Angles

Elevation Angle (°)	Open Loop Bandwidth (Hz)	Phase Margin (°)	Gain Margin (dB)
-10°	1.02	56.60	43.90
10°	1.02	56.60	44.90
20°	1.02	56.60	44.90
30°	1.02	56.60	43.90
40°	1.03	56.50	42.80
50°	1.03	56.50	36.40
60°	1.04	56.50	41.40
70°	1.04	56.50	41.20
80°	1.04	56.50	41.20
90°	1.05	56.40	37.50

Coarse tracking simulation and test results seem convergent when overall trends are regarded. Peak shapes and heights along with steady regime patterns are quite similar.

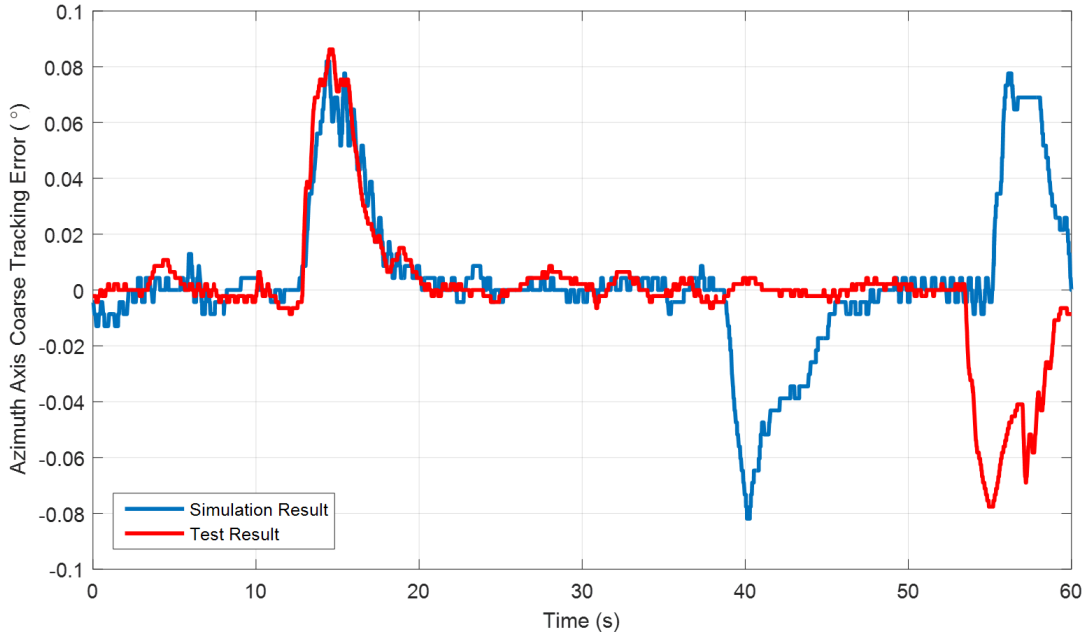


Figure 4.21: Azimuth Axis Coarse Tracking System Error Against on-Rail Target

Test and simulation results of on-Rail target coarse tracking is demonstrated with Figure 4.21. 1σRMS error during constant velocity interval (second 20 to 38) was measured as 48.58 µrad by the tests, and simulation results yielded 52.12 µrad. Since on-Rail target did not perform a predefined positioning routine, and reversals were commanded manually, unmatched peaks are present. However, although some peaks are shifted relatively, they are almost identical with the same peak value of 0.08°.

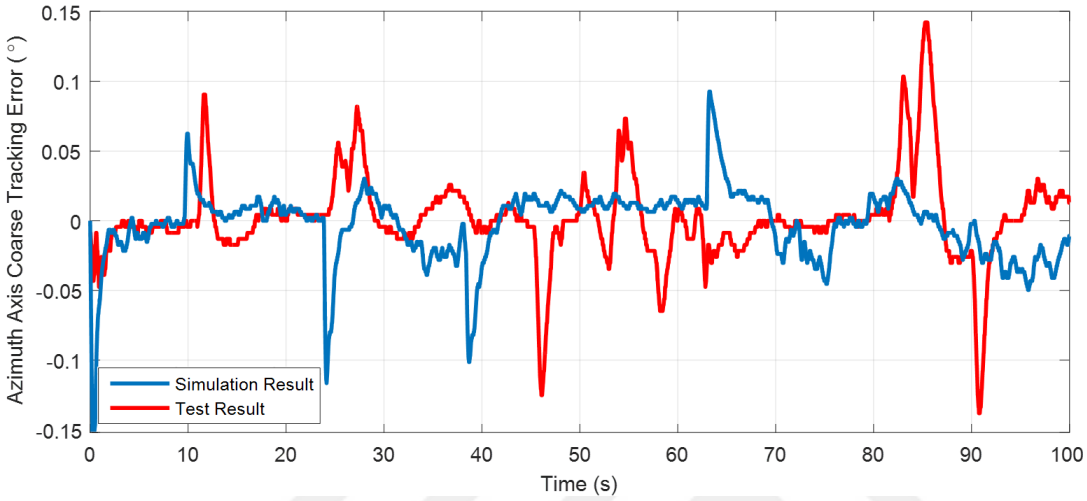


Figure 4.22: Azimuth Axis Coarse Tracking System Error Against Drone Threat

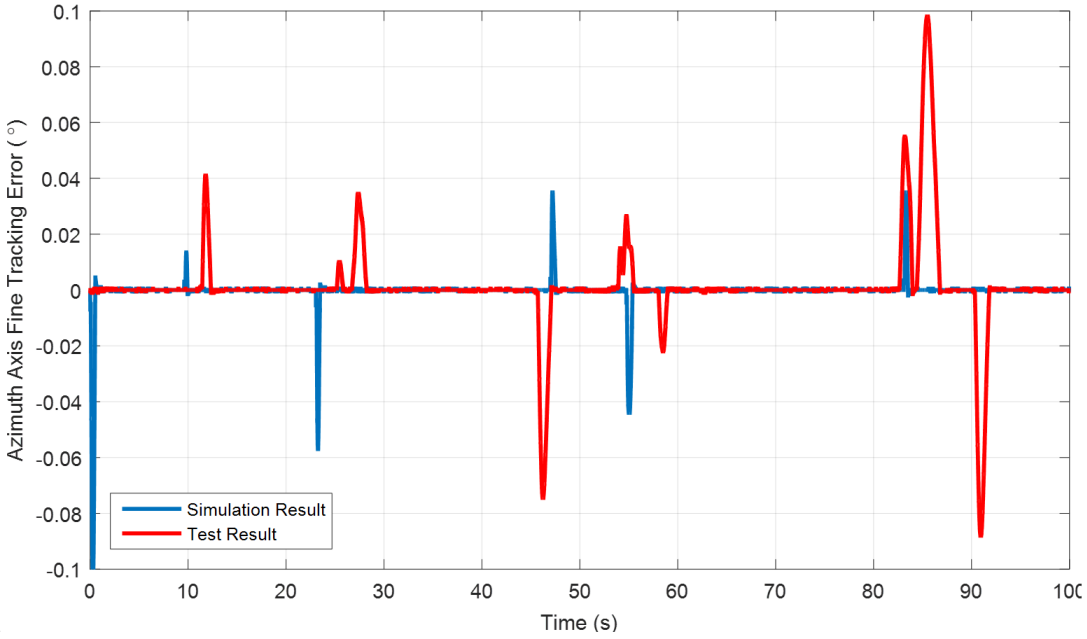


Figure 4.23: Azimuth Axis Fine Tracking System Error Against Drone Threat

Test and simulation results of drone threat coarse tracking is demonstrated in Figure 4.22. Excluding error jumps, the test results reveal 73.05 µrad tracking accuracy. Simulation results approximate closely to the tests with 67.42 µrad 1σRMS track error. However, effects of sudden drone maneuvers are noticeable as error jumps, which severely degraded RMS accuracy. This state indicates both the looseness of derived requirements and importance of fine track assistance. In order to demonstrate clearly the benefit of fine tracking assistance to coarse track by comparison, fine track error plot (Figure 4.23) is placed right below coarse track correspondent. Fine tracker seem to compensate all residual errors except from peaks, such that between second 60 and 80, 1σRMS fine tracking error is measured as 2.57 µrad by the test and calculated as 3.13 µrad from the simulation. However, on the peaks, since FSM reached to motion limits, it could not take any correcting action. Considering that with the aid of fine tracking system, more than 10 seconds of nearly errorless intervals are present, in order to destroy the target even 6 seconds are enough, and the target is not lost from the scene at error jumps, overall system performance was found acceptable, hence, improving the performance of azimuth coarse tracker controller was not found necessary. Revisiting on-Rail target tracking affair, as observed from fine tracking accuracy plot (Figure 4.24), error peaking seems less catastrophic than drone. Also, RMS error levels are drawn to order of 2 µrad magnitudes in each of test and simulation results.

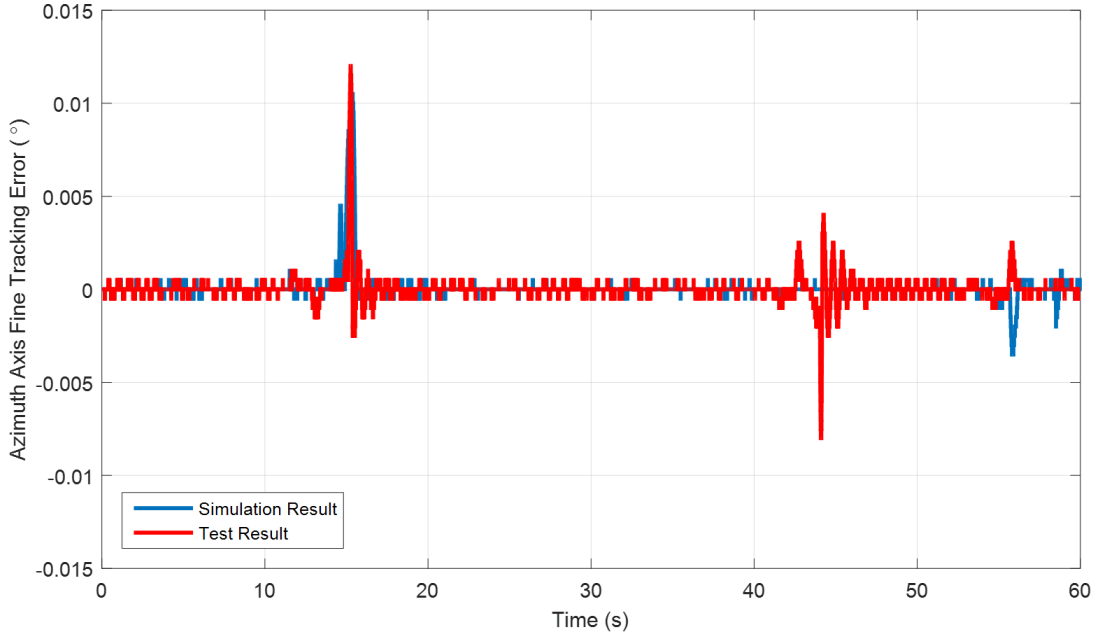


Figure 4.24: Azimuth Axis Fine Tracking System Error Against on-Rail Target

4.4 Atmospheric Disturbance Compensation

Measurement was performed via fine video tracker on a distant target at C_n^2 value of 5×10^{-14} $m^{-2/3}$ with 25 m/s wind speed. Both Tyler approximation and measurement results yield, approximately, the same f_G reading of 10 Hz. By means of FSM corrective actions, below 10 Hz, i.e., tip-tilt component, of atmospheric disturbance was rejected in each of simulation and test as the results are presented on Figure 4.25.

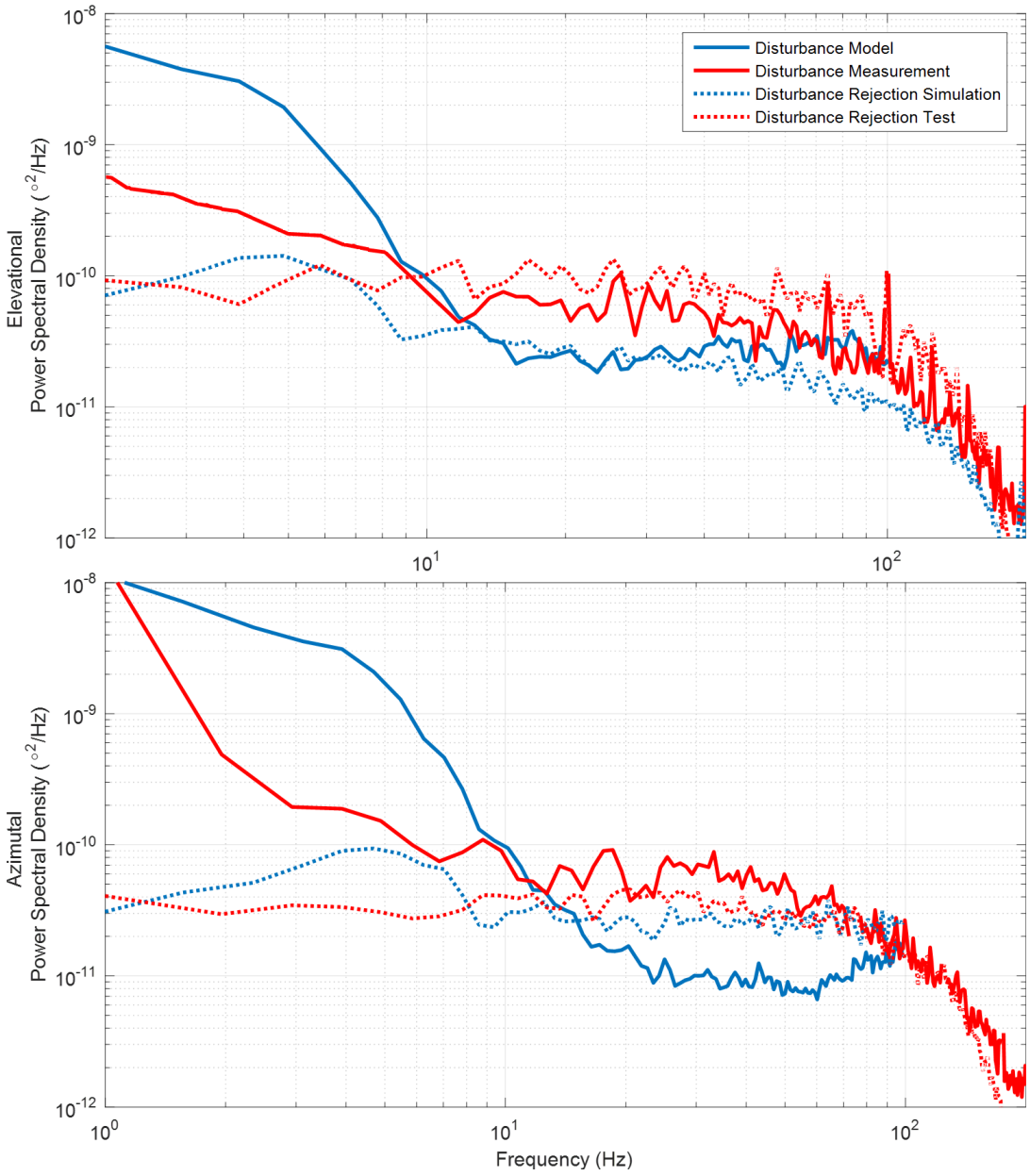


Figure 4.25: Compensation of Atmospheric Disturbance Components

CHAPTER 5

CONCLUSIONS

There has been great progress in the field of directed energy systems recently. Keeping pace with and even leading the technology are the necessities of our time and major outcome of the project. Acquiring knowledge on the novel concepts such as 4-axes gimbal design of this size, practice on FSM, concurrent tracking systems implementation and atmospheric disturbance handling is yet another invaluable gain.

Extensive literature review provided the opportunity of knowledge refreshment in a variety of fields under actuation systems and control strategies. Deciding on the most appropriate EOD configuration, choosing the compatible sensors, sizing the right actuators, embodied system after required tests became possible under the light of gathered data. Furthermore, principle functionalities of EOD is directing laser beam onto target and carrying all optical payload in a stiff manner, hence, having knowledge on laser fundamentals and optical trains were essential. Detailed literature research enabled mature design on these aspects, as well. In addition to assistance in design, literature research also provided broad insight on system identification and modeling.

Gimbal identification was performed in two phases, namely, dynamic response tests and disturbance torque component measurements. Tests at various conditions and instances yielded almost the same OLTFs. The only dependency was observed as elevational. Disturbance torque measurements were repeated from the beginning of assembly to site tests for both problem diagnostics beforehand and identifying the axes. At the end of the day, minimal mechanical problems were faced with, overcome all, and eventually friction, unbalance, cogging, and cable restraint torque levels were yielded compliant to design. FSM identification was actualized in dynamics response tests along with impedance analyses, and its conformity to design was verified.

Thriven identification data allow detailed gimbal and FSM modeling. Gimbal axes modeled up to eight resonant peaks, and model frequency responses were matched with identification test results in both phase and magnitude manner. For azimuth axis, friction, with the LuGre approach, and cogging models were verified via constant ±15 °/s velocity test resultant hysteresis curve. In addition to LuGre friction and cogging components, elevation model included unbalance and springness terms, and their integral response confirmed with hysteresis test at constant ±15 °/s velocity, as well. Superposing latency dynamics of sensors, drivers, and control computer, performance and stability of a velocity and position controllers were assessed. Hereupon, with cascaded coarse tracking system model target tracking performance against on-rail and drone targets were analyzed and the results are compared with real-time test outputs. As model and test results converged, system could fulfilled required coarse tracking functionality, and with fine tracking aid, engagement performance escalated, significantly. Test and analysis results or any other detail related to fulfilled requirements are widely covered in control or system identification and modeling chapters.

In conclusion, requirement driven servo design and component selection processes came in fruition. Predefined and derived requirements were fulfilled and tracking systems operated against potential threat in an effective manner. However elaborate identification and following field tests still provided some insights on future enhancements. For instance, EOD was designed in a gyro-stabilized manner and compatibility with marine environment. Bringing system to maturity on a naval platform with upgrades such as adjusting control topology to conform sea states up to 6, trackability of various target sets with even steeper maneuver patterns, and integrating to a radar for better target acquisition is considered as doorways of future works. Herein, analyzing scenario and platform based system effectiveness beforehand is crucial for taking corrective design changes on time, if required. Yet another future work has been determined as replacement of FSM with motor driven stabilized head-mirror. Acknowledging 10 fold of f_G as required bandwidth for atmospheric tip-tilt correction is far beyond servo rule of thumb, and it is mainly due to keep phase loss low. However piezoactuators are export items, and large-payload versions are, generally, subject to export license. Application of phase leading control laws and appropriate mechanical design could enable adaptation of standard head mirror instead of FSM.

REFERENCES

[1] US Army Armament Research, Development, and Engineering Center, *FIRE CONTROL SYSTEMS—GENERAL (MIL-HDBK-799 (AR))*, 1996.

[2] R. J. Dunn, "Operational implications of laser weapons," tech. rep., Northrop Grumman Corporation, 2005.

[3] `https://www.cgtrader.com/3d-models/military/armor/laser-weapon-system-us-navy`. [Online; accessed June 21,2019].

[4] P. H. Merritt and J. R. Albertine, "Beam control for high-energy laser devices," 2013.

[5] D. Kim, J. J. Kim, D. Frist, M. Nagashima, and B. Agrawal, "High energy laser testbed for accurate beam pointing control," tech. rep., Naval Postgraduate School, Monterey, CA, 2009.

[6] S. C. Singh, H. Zeng, C. Guo, and W. Cai, *Nanomaterials: Processing and Characterization with Lasers*. Wiley-VCH Verlag GmbH, 2012.

[7] W. T. Silfvast, *Lasers*. Elsevier Science, 2001.

[8] M. Csele, *Fundamentals of light sources and lasers*. Wiley-Interscience, 2004.

[9] K. Thyagarajan and A. Ghatak, *Lasers Fundamentals and Applications*. Graduate Texts in Physics, Springer US, 2 ed., 2011.

[10] `https://shop.monash.edu/media/catalog/product/cache/c687aa7517cf01e65c009f6943c2b1e9/l/a/laser-cutting.jpg`. [Online; accessed June 22,2019].

[11] `https://spie.org/Images/Graphics/Newsroom/Imported-2010/PRO_lasersMedicine/laser_nci.jpg`. [Online; accessed June 22,2019].

[12] http://jacobsschool.ucsd.edu/cosmos/2016/cluster5/images/free_space_fig1.png. [Online; accessed June 22,2019].

[13] H. Kaushal and G. Kaddoum, "Applications of lasers for tactical military operations," *IEEE Access*, September 2017.

[14] J. Cook, "High-energy laser weapons since the early 1960s," *Optical Engineering*, vol. 52, February 2013.

[15] R. D. McGinnis and A. Skolnick, "High-energy laser weapons for the fleet," *Journal of Directed Energy*, vol. 1, Fall 2003.

[16] D. Kiel, "Is this the time for a high-energy laser weapon program?," *Optical Engineering*, vol. 52, February 2013.

[17] http://large.stanford.edu/courses/2016/ph240/holmvik2/images/f1big.jpg. [Online; accessed June 23,2019].

[18] C. N. Ang, "Analysis of high energy laser weapon employment from a navy ship," master's thesis, NAVAL POSTGRADUATE SCHOOL, MONTEREY, CALIFORNIA, September 2012.

[19] B. Mohring, L. Tassini, R. Protz, and J. Zoz, "Beam-guidance optics for high-power fiber laser systems," in *Laser Technology for Defense and Security IX*, SPIE, May 2013.

[20] D. P. Greenwood and C. A. Primmerman, "Adaptive optics research at lincoln laboratory," *THE LINCOLN LABORATORY JOURNAL*, vol. 5, 1992.

[21] https://www.edmundoptics.com/contentassets/6c90e61974354a2bbb3dc59149548897/fig-3b-aod.gif. [Online; accessed June 25,2019].

[22] P.-Y. Madec, "Overview of deformable mirror technologies for adaptive optics and astronomy," in *Adaptive Optics Systems III*, SPIE, 2012.

[23] J. W. Hardy, *Adaptive Optics for Astronomical Telescopes*. Oxford Series in Optical and Imaging Science, Oxford University Press Inc., 1998.

[24] B. Stoklasa, L. Motka, J. Rehacek, Z. Hradil, and L. L. Sanchez-Soto, "Wavefront sensing reveals optical coherence," *NATURE COMMUNICATIONS*, vol. 5, 2014.

[25] Spiricon Laser Beam Diagnostics, Inc., 2600 North Main St. Logan, Utah, USA 84341, *Hartmann Wavefront Analyzer Tutorial*, 2004.

[26] B. M. Welsh, B. L. Ellerbroek, M. C. Roggemann, and T. L. Pennington, "Fundamental performance comparison of a hartmann and a shearing interferometer wave-front sensor," *APPLIED OPTICS*, vol. 34, 1995.

[27] J. Silva, E. Brunner, A. Polo, C. Visser, and M. Verhaegen, "Wavefront reconstruction using intensity measurements for real-time adaptive optics," in *2014 European Control Conference (ECC)*, IEEE, 2014.

[28] Edmund Optics Inc., *What are Beamsplitters?* [Retrieved from https://www.edmundoptics.com/resources/application-notes/optics/what-are-beamsplitters/, accessed June 27,2019].

[29] R. R. Parenti, *System Design and Optimization*, ch. 2. MARCEL DEKKER, INC., 2000.

[30] C. Grigorov, "Evaluation of coarse-and fine-pointing methods for optical free space communication," master's thesis, Lulea University of Technology, Luleå, Sweden, 2008.

[31] A. Berta, L. R. Hedding, C. Hoffman, and M. Messaros, "Development of a commercial line of high-performance fast-steering mirrors," in *Optical Scanning: Design and Application*, SPIE, 1999.

[32] CEDRAT-TECHNOLOGIES, "Piezo mechanisms brochure." `https://www.cedrat-technologies.com/fileadmin/user_upload/CTEC/Technologies/Actuators/Brochure-FSM.pdf`. [Online; accessed June 29,2019].

[33] L. L. Howell, *Compliant Mechanisms*. Wiley-Interscience, 2001.

[34] P. Bai, S. Wang, Q. Cao, and W. Yue, "Brief review: Development of fast steering mirror (fsm)," in *International Conference on Mechanism Science and Control Engineering (MSCE 2014)*, 2014.

[35] T. Maillard, F. Claeyssen, R. LeLetty, O. Sosnicki, A. Pages, Vazquez, and A. Carazo, "Piezomechatronic-based systems in aircraft, space, and defense applications," in *Space Exploration Technologies II*, SPIE, 2009.

[36] Q. Zhou, P. BenTzvi, and D. Fan, "Design and analysis of a fast steering mirror for precision laser beams steering," *Sensors & Transducers*, vol. 5, 2019.

[37] L. M. Germann, "Specification of fine-steering mirrors for line-of-sight stabilization systems," in *Active and Adaptive Optical Components*, SPIE, 1992.

[38] M. N. Sweeney, G. A. Rynkowski, M. Ketabchi, and R. Crowley, "Design considerations for fast-steering mirrors (fsms)," in *Optical Scanning 2002*, SPIE, 2002.

[39] A. Mäkynen, "Position-sensitive devices and sensor systems for optical tracking and displacement sensing applications," master's thesis, Faculty of Technology, University of Oulu, Oulu, Finland, 2000.

[40] T. Tang, C. Deng, T. Yang, D. Zhong, G. Ren, Y. Huang, and C. Fu, "Error-based observer of a charge couple device tracking loop for fast steering mirror," *Sensors*, vol. 17, February 2017.

[41] Y. Wang, D. Li, R. Wang, C. Jin, S. Wang, Q. Mu, L. Xuan, Z. Cao, and Z. Wang, "High-bandwidth fine tracking system for optical communication with double closed-loop control method," *Optical Engineering*, vol. 58, 2019.

[42] `https://www.omegaeng.cz/prodinfo/images/StrainGage_Graphic1.gif`. [Online; accessed July 01,2019].

[43] A. J. Fleming, "A review of nanometer resolution position sensors: Operation and performance," *Sensors and Actuators A: Physical*, vol. 190, 2013.

[44] `https://www.cedrat-technologies.com/uploads/tx_templavoila/SG_WEB.jpg`. [Online; accessed August 09,2019].

[45] https://www.allaboutcircuits.com/uploads/articles/full-bridge-strain-gauge-circuit.jpg. [Online; accessed August 09,2019].

[46] G. Schitter, R. W. Stark, and A. Stemmer, "Sensors for closed-loop piezo control: strain gauges versus optical sensors," *INSTITUTE OF PHYSICS PUBLISHING*, vol. 13, 2002.

[47] A. Glindemann, "Relevant parameters for tip tilt systems on large telescopes," *Publications of Astronomical Society of the Pacific*, vol. 109, 1997.

[48] C. Liu, S. Chen, X. Li, and H. Xian, "Performance evaluation of adaptive optics for atmospheric coherent laser communications," *OPTICS EXPRESS*, vol. 22, 2014.

[49] R. K. TYSON, *INTRODUCTION TO ADAPTIVE OPTICS*. No. 41 in TUTORIAL TEXTS SERIES, SPIE—The International Society for Optical Engineering, 2000.

[50] A. Tunick, N. Tikhonov, M. Vorontsov, and G. Carhart, "Characterization of optical turbulence (cn2) data measured at the arl alot facility," tech. rep., Army Research Laboratory, 2005.

[51] R. K. Tyson and B. W. Frazier, *Adaptive Optics*. No. 24 in Field Guide, Bellingham, Washington USA: SPIE, 2 ed., 2012.

[52] D. P. Greenwood, "Bandwidth specification for adaptive optics systems," *Journal of the Optical Society of America*, vol. 67, 1977.

[53] A. Glindemann, S. Hippler, T. Berkefeld, and W. Hackenberg, "Adaptive optics on large telescopes," *Experimental Astronomy*, vol. 10, 2000.

[54] G. P. Perram, M. A. Marciniak, and M. Goda, "High energy laser weapons: technology overview," in *Laser Technologies for Defense and Security*, SPIE, 2004.

[55] C. R. Fussman, "High energy laser propagation in various atmospheric conditions utilizing a new, accelerated scaling code," master's thesis, Naval Postgraduate School, Monterey, CA, 2014.

[56] A. P. Minton, "Recent applications of light scattering measurement in the biological and biopharmaceutical sciences," *Analytical Biochemistry*, vol. 501, 2016.

[57] D. Meschede, *Optics, Light and Lasers: The Practical Approach to Modern Aspects of Photonics and Laser Physics*. WILEY-VCH, 2 ed., 2007.

[58] B. Zohuri, *Directed Energy Weapons*. Springer International Publishing, 2016.

[59] V. V. Ter-Mikirtychev, *Fundamentals of Fiber Lasers and Fiber Amplifiers*. Springer International Publishing, 2014.

[60] R. Clarke, "Techniques for laser combining," tech. rep., LumOptica Limited, 2015.

[61] P. Sprangle, A. Ting, J. Peñano, R. Fischer, and B. Hafizi, "Incoherent combining and atmospheric propagation of high-power fiber lasers for directed-energy applications," *IEEE JOURNAL OF QUANTUM ELECTRONICS*, vol. 45, 2009.

[62] S. K. Saha, *DIFFRACTION-LIMITED IMAGING WITH LARGE AND MODERATE TELESCOPES*. World Scientific Publishing Co. Pte. Ltd., 2007.

[63] J. Cheng, *The Principles of Astronomical Telescope Design*. No. 360 in Astrophysics and Space Science Library, Springer-Verlag New York, 2009.

[64] J. HILKERT, "Inertially stabilized platform technology concepts and principles," *IEEE CONTROL SYSTEMS MAGAZINE*, vol. 28, 2008.

[65] P. Merritt, T. Howard, and R. Brunson, "Acquisition, Tracking, Pointing, and Beam Control Technology." Short Course, 2009.

[66] S.-H. Kim, *Electric Motor Control: DC, AC, and BLDC Motors*. Elsevier Science, 2017.

[67] P. J. Kennedy and R. Kennedy, *Line of Sight Stabilization Primer*. Peter J. Kennedy, 2008.

[68] J. HILKERT, *STABILIZATION, POINTING AND TRACKING SYSTEM TECHNOLOGY HANDBOOK*. TEXAS INSTRUMENTS INCORPORATED, 1989.

[69] D. P. KOTHARI and I. J. NAGRATH, *ELECTRIC MACHINES*. Tata McGraw-Hill Education, 1990.

[70] W. Leonhard, *Control of Electrical Drives*. Power Systems, Springer-Verlag Berlin Heidelberg, 2001.

[71] G. K. Dubey, *Fundamentals of Electrical Drives*. Alpha Science International Ltd., 2001.

[72] T. L. M. Bartelt, *Industrial Automated Systems Instrumentation and Motion Control*. Delmar Cengage Learning, 2010.

[73] M. A. Laughton and D. F. Warne, *Power Semiconductor Devices*, ch. 17. Elsevier, 2003.

[74] B. Drury, *Control Techniques Drives and Controls Handbook (2nd Edition)*. Institution of Engineering and Technology, 2009.

[75] S. Lee, T. Lemley, and G. Keohane, "A comparison study of the commutation methods for the three-phase permanent magnet brushless dc motor," in *Electrical Manufacturing Technical Conference 2009: Electrical Manufacturing and Coil Winding Expo*, pp. 49–55, 2009.

[76] Renesas Electronics Corporation. `https://www.renesas.com/img/solutions/key-technology/motor-control/motor-algorithms/algorithm_wheel.jpg`. [Online; accessed July 18,2019].

[77] S. L. Herman, *Industrial Motor Control (5th Edition)*. Thomson Delmar Learning, 2005.

[78] H. Marais, "RS-485/RS-422 circuit implementation guide," tech. rep., Analog Devices, Inc., Norwood, MA, 2008.

[79] EtherCAT Technology Group, "Ethercat Overview & ETG Introduction (Brochure)." `https://www.ethercat.org/download/documents/ETG_Brochure_EN.pdf`, 2018.

[80] W. Voss, *A Comprehensible Guide to Servo Motor Sizing*. Copperhill Technologies Corporation, 2007.

[81] J. M. Hilkert, "Precision Stabilized Pointing & Tracking Systems System Configuration, analysis & Design." Short Course, 2011.

[82] J. Nazzaro, "What you should know about frameless motors," tech. rep., Electromechanical Automation North America, Parker Hannifin., Charlotte, NC, 2014. [Online; accessed July 25,2019].

[83] V. N. Branets, B. E. Landau, Y. N. Korkishko, D. Lynch, and V. Y. Raspopov, *GYROSCOPIC DEVICES AND SENSORS*, ch. 6, pp. 167–244. Sensors Technology, Momentum Press, LCC, 2013.

[84] KVH Industries, "Guide to comparing gyro and imu technologies – micro-electro-mechanical systems and fiber optic gyros," tech. rep., KVH Industries, Inc, 2018.

[85] L. B. Pupo, "Characterization of errors and noises in mems inertial sensors using allan variance method," master's thesis, Universat Politècnica de Catalunya Department de Teoria del Senyal i Comunicacions, Barcelona, 2014.

[86] V. M. N. Passaro, A. Cuccovillo, L. Vaiani, M. De Carlo, and C. E. Campanella, "Gyroscope technology and applications: A review in the industrial perspective," *Sensors*, vol. 17(10), 2017.

[87] A. S. Morris and R. Langari, *Measurement and Instrumentation: Theory and Application*. Elsevier Inc. Academic Press, 2012.

[88] TR-Electronic GmbH, "Absolute Rotary Encoders Overview." `http://trelectronic.com/sites/default/files/brochures/Brochure-PDF/Absolute-Rotary-Encoders.pdf`, 2015.

[89] J. Wagner and J. Burgemeister, "Piezoelectric accelerometers theory and application," tech. rep., Metra Mess- und Frequenztechnik, Radebeul / Germany, 2012.

[90] J. He and Z.-F. Fu, *Modal Analysis*. Butterworth-Heinemann, 2001.

[91] Texsas Instruments Defense Systems & Electronics Group, "Control Systems Technology - Servomechanism Design." Short Course, 1985.

[92] T. Hindle, T. Davis, and J. Fischer, "Isolation, pointing, and suppression (ips) system for high performance spacecraft," in *Industrial and Commercial Applications of Smart Structures Technologies*, vol. 6527, SPIE, 2007.

[93] K. J. Åström and T. Hagglund, "The future of PID control," *Control Engineering Practice*, vol. 9, 2001.

[94] B. Li, D. Hullender, and M. DiRenzo, "Nonlinear Induced Disturbance Rejection in Inertial Stabilization Systems," *IEEE TRANSACTIONS ON CONTROL SYSTEMS TECHNOLOGY*, vol. 6, 1998.

[95] O. Bosgra, H. Kwakernaak, and G. Meinsma, *Design Methods for Control Systems*. Dutch Institute of Systems and Control, 2008.

[96] J. M. Hilkert and B. Pautler, "A reduced-order disturbance observer applied to inertially stabilized Line-of-Sight control," in *Acquisition, Tracking, Pointing, and Laser Systems Technologies XXV*, vol. 8052, SPIE, 2011.

[97] T. S. Kumar and R. N. Banava, "Identification of Friction in the 50/80 cm ARIES Schmidt Telescope Using the Lugre Model," in *Proceedings of the International Federation of Automatic Control 18th World Congress*, 2011.

[98] "Piezo Actuators Training." Short Course, 2014.

APPENDIX A

REMAINING SIMULATION MODEL DETAILS

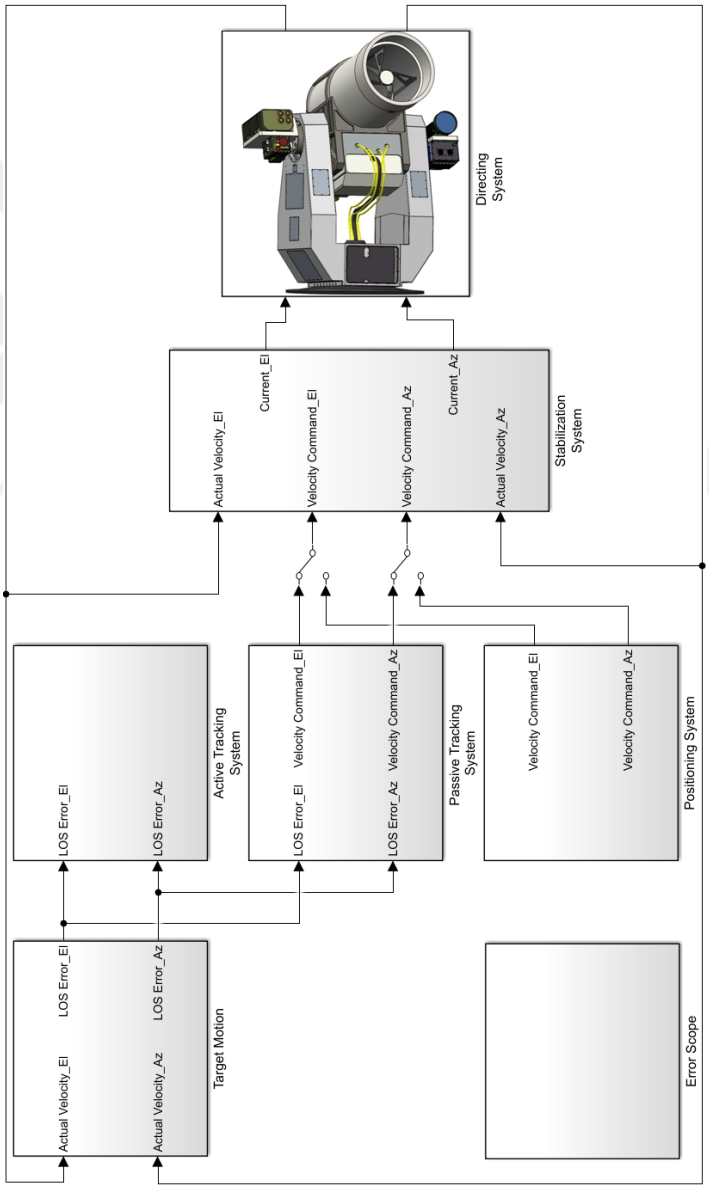
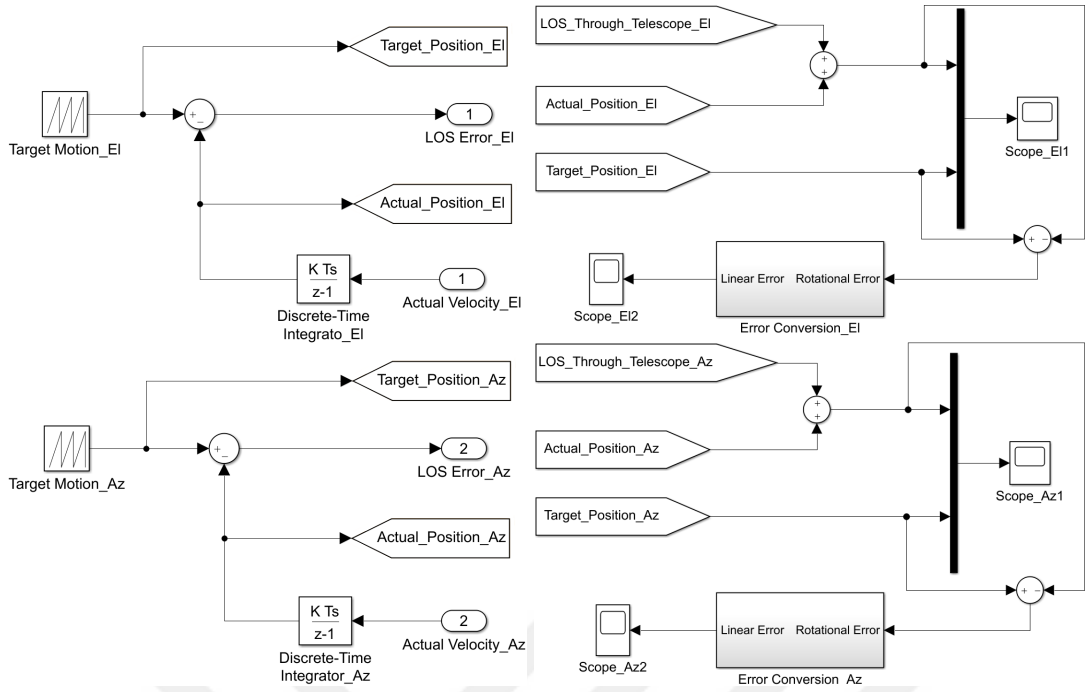


Figure A.1: Simulink EOD Simulation Model General View



(a) Target Motion (b) Error Scopes

Figure A.2: Model Inlet and Outlet Means

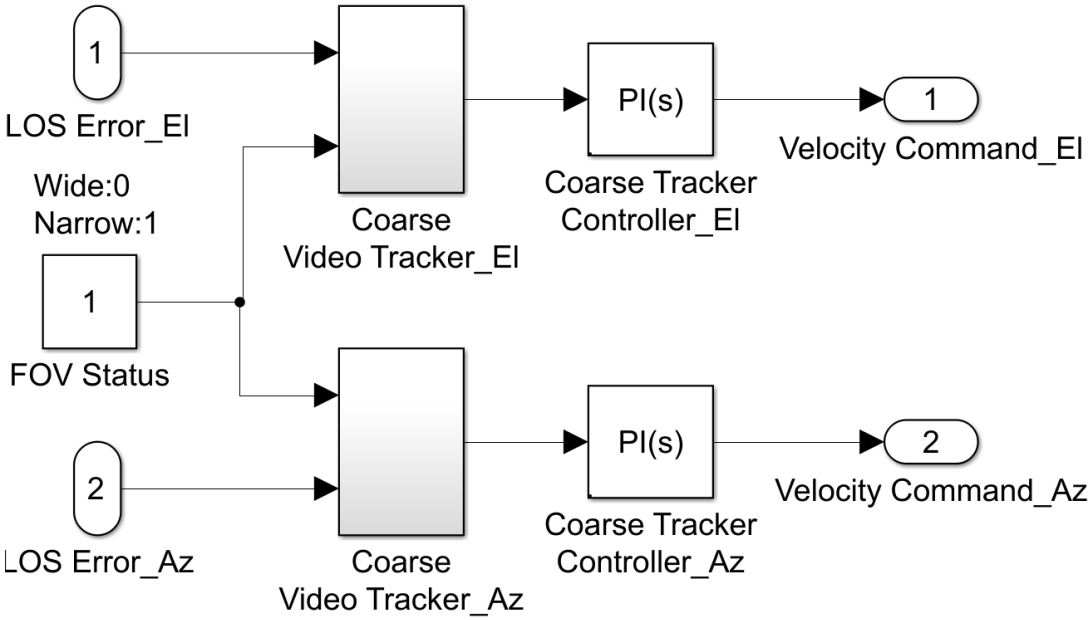


Figure A.3: Coarse Tracking System (Except From End Effector)

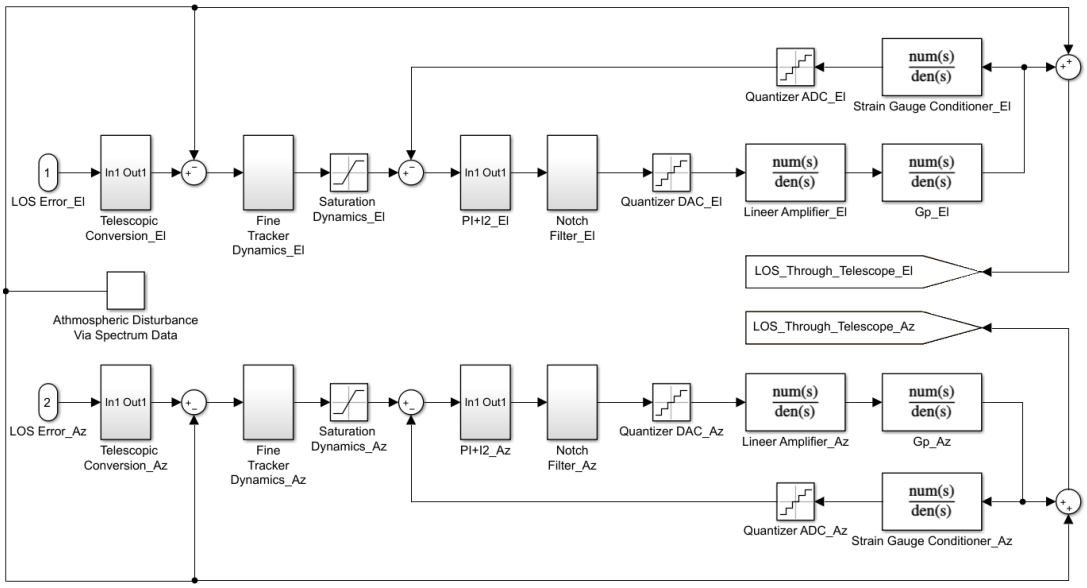


Figure A.4: Fine Tracking System

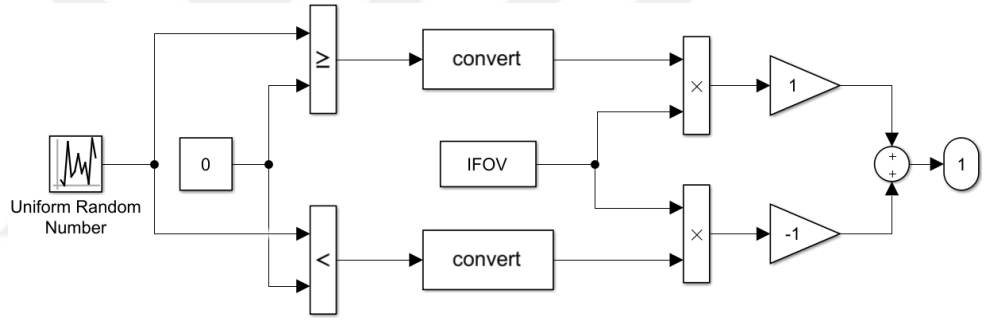


Figure A.5: Tracker Random Jitter Model

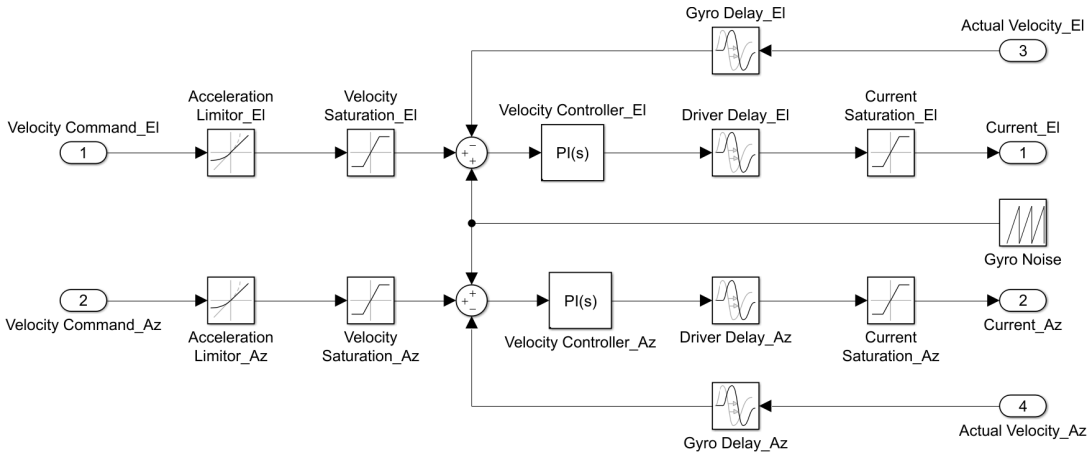


Figure A.6: Stabilization System Model

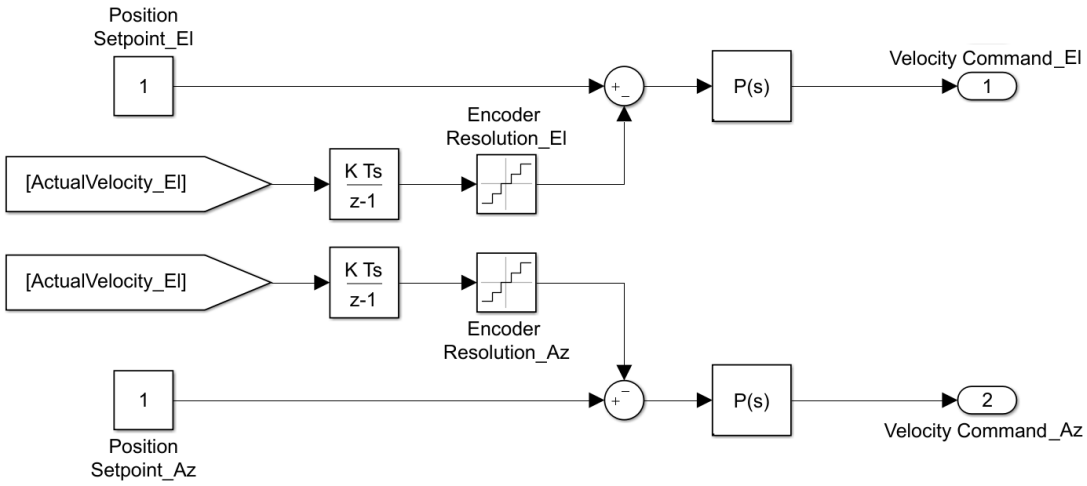


Figure A.7: Positioning System Model

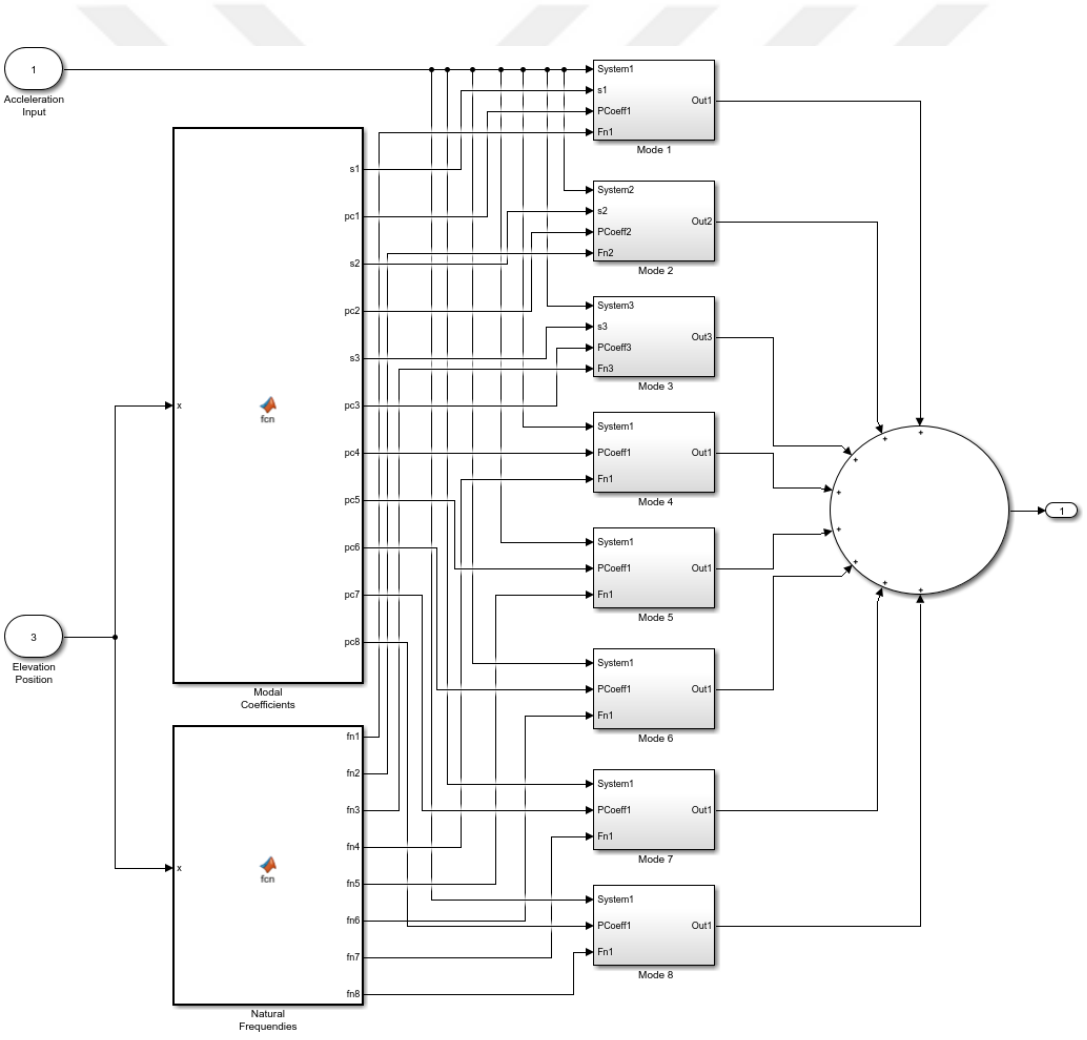


Figure A.8: Elevation Angle Dependent Structural Dynamics

APPENDIX B

AZIMUTH VELOCITY MEASUREMENT EULER TRANSFORMATION

Since gyro is mounted on elevation axis, elevational rotations would deviate azimuth axis velocity measurements. In order correct azimuth axis velocity in a real-time manner with elevation encoder reading, Euler transformation is applied based on rotation transformationB.1 with model segment FigureB.1. Herein, ω_X, ω_Y, and ω_Z are velocity measurements on IMU axes. ω_{El} and ω_{Az} are velocity components, transformed onto EOD axes. θ_{El} is elevational angular position as encoder reading.

$$\begin{bmatrix} 0.707 & -0.707 & 0 \\ 0.707\cos(\theta_{El}) & 0.707\cos(\theta_{El}) & \sin(\theta_{El}) \end{bmatrix} \cdot \begin{bmatrix} \omega_X \\ \omega_Y \\ \omega_Z \end{bmatrix} = \begin{bmatrix} \omega_{El} \\ \omega_{Az} \end{bmatrix} \tag{B.1}$$

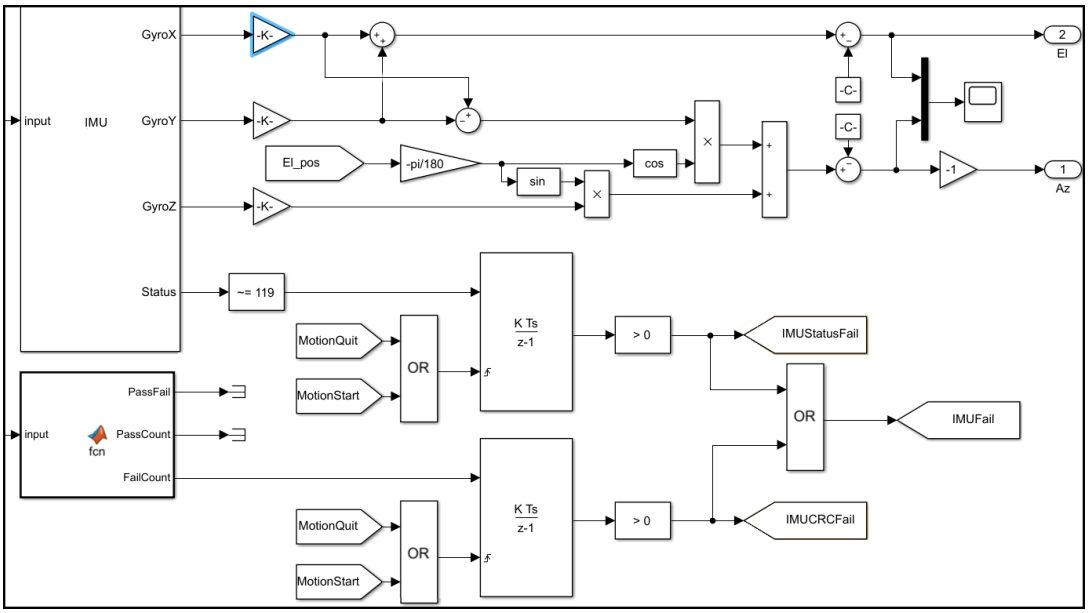


Figure B.1: Real-time IMU Axis Transformation Model Segment